MEASUREMENT OF SURFACE DISPLACEMENTS AND STRAINS BY THE DOUBLE APERTURE SPECKLE SHEARING CAMERA

by

JAN BRDICKO

B.Sc., University of Illinois, 1970
M.A.Sc., University of British Columbia, 1972

A THESIS SUBMITTED IN PARTIAL FULFILMENT
OF THE REQUIREMENTS FOR THE DEGREE OF
DOCTOR OF PHILOSOPHY

in

THE FACULTY OF GRADUATE STUDIES
(Department of Civil Engineering)

We accept this thesis as conforming
to the required standard

THE UNIVERSITY OF BRITISH COLUMBIA

October, 1977

In presenting this thesis in partial fulfilment of the requirements for an advanced degree at the University of British Columbia, I agree that the Library shall make it freely available for reference and study. I further agree that permission for extensive copying of this thesis for scholarly purposes may be granted by the Head of my Department or by his representatives. It is understood that copying or publication of this thesis for financial gain shall not be allowed without my written permission.

Department of Civil Engineering

The University of British Columbia
2075 Wesbrook Place
Vancouver, Canada
V6T 1W5

Date October 11 1977

MEASUREMENT OF SURFACE DISPLACEMENTS AND STRAINS BY THE DOUBLE APERTURE SPECKLE SHEARING CAMERA

ABSTRACT

In the testing of materials, structures and structural components it is often desired to determine the surface displacement and strain fields due to some external loading. Numerous optical techniques have been developed for this purpose and successfully used in particular applications. Unfortunately, when the surface deformation is quite large, as is usually the case in practical testing, most of these methods fail and only a few suitable optical interferometric techniques will work.

Two of the recently developed techniques that seem to work are based on laser speckle interferometry. The first technique was described in 1972 by Duffy [1] who showed that a Double Aperture Speckle Camera (DASC) is suitable for measurement of a reasonably large in-plane displacement having its direction parallel to the line connecting the two apertures of the camera. A second technique was described in 1973 by Hung [3] . He showed that a Double Aperture Speckle Shearing Camera (DASSC) may be used to measure both the in and out-of-plane strains of planar surfaces.

Duffy has not considered the fringe formation by DASC due to the displacement normal to the surface and the displacement normal to the line connecting the two apertures of DASC. Hung, in turn, has not considered the effect on fringe formation of either the in and out-of-plane displacements, or the in-plane strain, which is the partial derivative $w,_y$ (see Fig. 3.11 for the definition of $w,_y$).

Because of the great potential of DASC and DASSC stemming from their ability to measure displacements and strains over many orders of magnitude, a considerable effort was made to determine the fringe formation of the two

cameras due to all displacements and strains occuring in a general deformation of a specimen surface.

The theoretical analysis of models of DASC and DASSC was performed and resulted in two "new" equations describing the fringe formation by these cameras. The equations take into account the effect of all displacements and strains on the fringe formation; in addition, the equations are "symmetric" and the equation governing DASSC reduces to the one governing DASC for the lateral shear set equal to zero. The accuracy of these equations was then verified by a number of simple experiments. Various ways of using the two cameras were proposed so that the unknown displacements and strains in the specimen surface may be calculated from the least number of fringe patterns. Computer programs based on these proposed methods were written and used in several experiments. In all instances the actual and the calculated displacements and strains agreed quite well.

TABLE OF CONTENTS

CHAPTER Page

LIST OF TABLES

LIST OF FIGURES

NOTATION

The meaning of symbols is defined in the text where they are introduced. The summation convention applies to subscripted variables with lower case indices with the range of the subscripts usually indicated.

ACKNOWLEDGEMENTS

The author would like to sincerely thank to his advisors, Dr. M. D. Olson and Dr. C. R. Hazell, for their helpful advice and guidance given during the course of the research and preparation of this thesis. He also wishes to thank to Dr. D. L. Anderson for his assistance during the research work.

The author also wishes to thank to Mr. L. E. Dery, Mr. Phil Hurren, Mr. John Hoar and Mr. Dick Postgate for their valuable technical assistance.

This study was made possible through a research grant provided by the National Research Council of Canada.

1. INTRODUCTION

1.1 Background

There are many experimental techniques [7,...,11] for determining the displacements and strains in materials or structural components subjected to various loads. Certain tests, for various reasons, must be noncontacting, i.e. it is not possible to use stress coatings, photo-elastic coatings, strain gages, displacement gages or other contact probes. In such instances optical interferometry may often be used successfully. Its previous use in practical testing had been hindered by its excessive sensitivity, the need for complicated and expensive instrumentation and its susceptibility to disturbing effects of environment. While some shortcomings remain, the use of optical interferometry has spread dramatically since the invention of the laser in the 1960's. Numerous optical interferometric techniques using laser generated coherent light were developed and proved extremely valuable for specific applications. Most of the techniques that have been developed for the measurement of displacements to date are, unfortunately, only suitable for the measurement of very small displacements. Alternatively some techniques have been developed to measure large displacements along the line of sight. Therefore, there has existed a need to develop a technique for the measurement of the displacements and strains of the magnitudes encountered in practical testing.

Duffy [1,2] described the double aperture camera and showed that it is suitable for the measurement of reasonably large in-plane displacements. Hung [3,4,5,6] has shown that a somewhat modified double aperture camera, DASSC, may be used to measure in and out-of-plane strains. Other researchers have proven the feasibility of different methods for measuring displacements and strains, but these methods seemed less powerful and promising than Hung's.

This thesis objective, in 1974, was to examine the mechanism of failure

of wooden beams subjected to various loads and, at that time, Hung's method appeared to be the most suitable noncontacting experimental technique available. Subsequently, DASSC was built and its performance tested on a calibration specimen. The surface strains were then calculated from the fringe patterns produced by the camera in the way suggested by Hung. Unfortunately, the calculated strains and the actual surface strains (determined by strain gages and dial gages) were in a considerable disagreement. A decision was made to find the cause of this disagreement, and the subsequent theoretical analysis of DASSC resulted in a new equation governing the fringe formation. The accuracy of the new equation was then thoroughly tested both experimentally and by computer simulation. However, the above analysis had been very time consuming and left little time for the actual investigation of the failure mechanism of wooden beams. The research which was done, though, has given some insight into the behaviour of wood and provides a starting point for other researchers considering this area of study with the use of DASSC.

Literature Survey

Because both optical interferometry and even coherent light interferometry encompass such a great number of various techniques it is not possible to review all of them. Instead, only the best known techniques suitable for measurement of displacements and strains in planar surfaces are investigated with special emphasis in the review attached to speckle interferometry.

Hopefully, the review of all techniques relevant to the research presented in this thesis is complete. If an omission has been made, it is quite unintentional. The techniques are reviewed in chronological order, starting with holographic interferometry and ending with DASSC.

1.2 Holographic Interferometry

One of the first demonstrations of holographic interferometry was done by Powell and Stetson [12] in the early 1960's. The technique is similar to conventional holography, except that two exposures (and, hence, two holograms) of the object are recorded on the same holographic plate; the surface of the object is deformed or displaced between the two exposures. Upon reconstruction of the hologram, two three-dimensional images of the object are formed, interfere with each other, and produce a set of fringes. The fringes represent areas of the same change in total optical path length and, with knowledge of the parameters of the experimental setup, a component of the surface displacement along a line of sight may be calculated. Since three displacement components must be calculated to determine the surface deformation, in general, three holograms are needed. The surface strains may then be obtained by differentiation of the displacements.

Since 1965 holographic interferometry has been applied successfully to a study of transient and steady vibration [12,...19] and in a wide variety of materials testing [20,23,24,29,30,31,32] . Special techniques were developed for the measurement of the wave propagation using pulsed lasers [25,26] . By illuminating the specimen surface by two beams inclined at equal angles to the surface normal, or by other means, experimenters were able to develop several holographic techniques for the measurement of in-plane displacements [27,28,33] . A number of techniques for the measurement of in-plane strain were developed as well [34,35,36] .

The main advantage of holographic interferometry is its ability to work with an arbitrary three dimensional surface. Another advantage is, in many cases, its high sensitivity as the fringes usually represent displacements of the order of 1×10^{-5} in. Unfortunately, such a high sensitivity makes this method unsuitable for ordinary engineering testing where displacements

of the order of 1×10^{-3} in. and 1×10^{-2} in. are commonly encountered. All holographic techniques are also quite sensitive to the disturbing effects of the environment. Finally, a major problem associated with using holography to obtain numerical measurements stems from the fact that the fringes may not be localized [21,22] on the specimen surface and, consequently, the fringe positions cannot be clearly established.

1.3 Holographic Contouring Techniques

There are several holographic interferometric techniques suitable for measurement of relatively large static or dynamic changes in the shape of an object. In the absence of large in-plane motion, the fringes produced by these techniques are related to the out-of-plane displacements of the object. The methods known as contouring techniques, [37,40,41,42] are based on producing an illuminated volume of space in which the apparent illumination of any point in that space is some function of position alone. If the function is known, the shape of the illuminated area of the object can be determined. Most optical field contouring techniques result in sinusoidal functions of position. Although in theory the sensitivity of such a continuous function is unlimited, in practice a sensitivity of one-half of the period is used.

There are numerous ways in which contours can be formed [38,39] . Two holograms can be recorded on the same plate. The object can be illuminated with two wavelengths simultaneously, with only one wavelength but from two directions, or with one wavelength but with a medium of different retractive index surrounding the object. Alternatively, the hologram can be recorded with one wavelength, developed and replaced, and both it and the object illuminated with a second wavelength. The interference between the wave appearing to originate from the image (magnified because of the shift in wavelength) and the wave actually coming from the object itself causes

contours to appear on the image. Similar results are obtained if the hologram is recorded while the object is in a medium of one refractive index, and the hologram and the object then illuminated while the object is in another medium.

All of these techniques generate Moire-type of fringes which are related to the change in shape of the object; the techniques are usually insensitive to the in-plane displacements. Out-of-plane displacements cannot be calculated from these fringes if deformation of the object involves large in-plane displacements.

1.4 Measurement of Displacements by Speckle Interferometry

Anyone working with lasers is familiar with the speckle phenomenon which causes a grainy appearence of the laser illuminated surface. Laser speckle (or speckle pattern) is formed when coherent light is either scattered from a diffusely reflecting surface or propagates through a medium with random refractive index fluctuations. The speckle size is usually defined as the statistical average distance between adjacent regions of maximum and minimum brightness. If a diffusely reflecting surface is imaged by a lens on a screen, the speckle size D_s is related to the effective numerical aperture NA of the lens by

$$D_s \simeq .6 \frac{\lambda}{NA}$$

The speckle pattern depends on the properties of the scattering surface and this fact is utilized by speckle interferometers which relate the fringes created by changes in the speckle pattern to the surface deformation. Speckle interferometers may be classified as those suitable for measurement of displacements smaller than speckle size and those suitable for measurement of displacements larger than speckle size. Alternatively, the speckle

interferometers could be classified according to the type of light fields that the interferometers employ, i.e., either as interferometers combining speckle and uniform fields or as interferometers combining two speckle fields. The main advantage of speckle interferometers is their ability to vary their sensitivity by changing speckle size and other optical parameters; it is also claimed that these interferometers measure the in-plane displacements of the tested surface independently of any displacement taking place in the direction normal to the object surface.

There are a great number of interferometric techniques utilizing laser speckle [1,2,3,4,5,6,44,45,46,47] . These techniques are used for displacement measurements, steady state vibration analysis and qualitative testing. An excellent up-to-date review of existing techniques using speckle interferometry for measurement of displacements and strains has been done by A.E.Ennos [43] . Several of the numerous techniques will now be briefly described.

The speckle interferometer described by Leendertz [49] uses two illuminating beams incident at equal angles on either side of the normal to the object surface; the illuminated surface is then imaged by a lens on a photographic plate. The two speckle patterns, one due to each illuminating beam, interfere coherently, producing fringes according to the rule

$$2u \sin\theta_i = n\lambda$$

where u, θ_i , n , and λ are defined as

u ... in plane displacement

θ_i ... angle of illumination

n ... fringe number

λ ... wavelength of illuminating light

The sensitivity of the interferometer may be changed primarily by changing the angle θ_i. The maximum allowable in-plane displacement u must be smaller than the apparent speckle diameter. Fringes produced by this interferometer are of low visibility.

Duffy [1,2] has proven the feasibility of a double aperture speckle interferometer. One beam is needed to illuminate the object surface, and the surface is imaged on a photographic plate by a lens having two radially opposed circular apertures in its entrance pupil. To each aperture corresponds a particular speckle pattern, and the two patterns interfere coherently in the photographic plate emulsion to produce a fine grating-like grid over an area of each speckle. In a double exposure method two grids are formed over the area of speckle, one grid corresponding to the undeformed surface and the other to the deformed surface. The two grids add either constructively or destructively. The constructive addition preserves the grid-like structure of the speckle whereas this structure vanishes in destructive addition. The addition takes place over all speckles comprising the "speckled" image of the object, and generates fringes related to the surface in-plane displacement in the direction of the line connecting the two apertures. However, optical filtering is necessary to view these fringes. This is done by illuminating the photographic plate with parallel light and viewing in the direction of the first order diffracted beams. Using the notation shown in Fig. 3.11 and employed throughout this thesis Duffy showed that a small displacement v along the y-axis causes fringes according to

$$v(y,z) = -\frac{\lambda x_s}{D} n(y,z) \tag{1.1}$$

Duffy did not consider the effect on fringe formation by displacements u and w which may occur in addition to the displacement v. This method is less sensitive than the preceeding one and the fringes are of high

visibility. It, too, is limited to the measurement of displacements smaller than the object speckle size and the system is further handicapped by its failure to work when slope changes exceed a certain magnitude; in addition, long exposures are necessary if small apertures are used.

Duffy has also described an alternative technique which uses one illuminating beam and a lens with a single aperture to image the surface on a photographic plate. A double exposure is used to record surface deformation. This recording contains all spatial frequencies from zero to the highest frequency which the aperture limited lens is capable of passing. Through the use of a double aperture screen optical filtering of the recording is used to produce fringes related to the displacements along the line connecting the two apertures; the sensitivity is determined by the separation of the apertures. The advantage of this method is that the sensitivity can be chosen after the deformation of the object was recorded to obtain the most desirable fringe spacing. The disadvantage is that only a small part of the surface can be viewed at a time.

Ennos [48] has demonstrated a speckle interferometric technique which produces fringes when the lateral component of surface displacement is greater than the object speckle size. The object is illuminated by one beam and a double exposure photograph, one each before and after straining, is recorded on high resolution film. The optical transform of this recording is a pattern of parallel fringes of angular distribution α given as

$$\frac{v}{m}\sin\alpha = n\lambda$$

where m is the demagnification factor.

The examination of the recording on a point by point basis thus yields the magnitude and direction of the lateral movement of the object surface. Alternatively, the recorded image may be spatially filtered to yield a

contour map showing the surface displacement along a chosen direction. The technique is insensitive to displacements in the direction of the line of sight; however, it too fails to work when slope changes are large. The number of fringes that the method generates is limited and the fringes are usually of low visibility.

1.5 Measurement of Strains by Speckle Interferometry

There seems to be, at present, only one speckle interferometer capable of direct measurements of surface strains. It is called the Double Aperture Speckle Shearing Camera (DASSC) and is described by Hung in several papers [3,4,5,6]. The camera is the same as DASC used by Duffy except for the lateral shear which is produced either by placing inclined glass blocks in front of apertures or by defocussing, i.e. , positioning the photographic plate a small distance away from the focal plane of the lens. Regardless of how the lateral shear is produced, Hung showed that the fringes are formed according to

$$\Delta y_s(1 + \cos\theta_x)u,_y + \Delta y_s\cos\theta_y v,_y = - \lambda n(y,z) \qquad (1.2)$$

with the notation being that of Fig. 3.11. Hung has not considered the effect on fringe formation by the displacements u,v and w and the strain $w,_y$ all of which, in general, are present in a specimen deformation. He then solved equation (1.2) for $u,_y$ and $v,_y$ "algebraically" from two fringe patterns.

1.6 Limits of Investigation

The work presented in this thesis is devoted solely to the theoretical and experimental investigation of the use of DASC and DASSC for the measurement of displacements and strains in planar surfaces. The theoretical investigation of the fringe formation by DASC and DASSC is restricted to the

analysis of the simplest possible models of the two cameras. In the analysis the following assumptions (restrictions) are made:

a) A small area of the specimen surface may be represented by a point source of light in the analysis of DASC and by two point sources (reflectors) when DASSC is considered.

b) The imaging lens(es) is negligibly thin, free of aberrations and coincident with the aperture plane.

c) The only significant diffraction occurring in the camera takes place in the aperture(s).

d) The specimen illumination is collimated, monochromatic and perfectly coherent.

e) The recording medium (photographic plate emulsion) is negligibly thin and records the intensity of the incident light in a linear fashion.

f) The two cameras are used only in the double exposure method.

The results of the theoretical investigation are two equations describing the fringe formation by the models of DASC and DASSC. Then, various ways in which the unknown displacements and strains may be determined from the smallest number of "photographs" made by the two cameras are considered. In general, the recorded fringe patterns represent partial differential equations which are solved here only by the finite difference method. Lastly some special cases are considered leading either to a set of algebraic equations or to an ordinary first order differential equation with a variable coefficient.

The experimental work is limited to seven experiments involving various specimens, all with planar surfaces coated with a flat white paint to approximate the diffusely reflecting surface. Light of wavelength 5145 Å provided by an argon gas laser was the only illumination used. The field

of view (defined as $\sqrt{y^2 + z^2}/x_s$) is smaller than 1 : 5 and in most cases less than 1 : 10 . All the fringe patterns are obtained by the Fourier filtering of the photographic plate(s) made by the two cameras.

2. THEORETICAL PRELIMINARIES

2.1 Introduction

The basic concepts of geometrical and wave optics are reviewed in the first part of this chapter to familiarize the reader having little or no background in optics with those aspects of optics which are used later in the analysis of DASC and DASSC. Those readers acquainted with optics and, in particular, interferometry may wish to proceed directly to Section 2.13 where the basic concepts of a general coherent interferometer are developed, although a brief review of the whole chapter might be helpful, as the terminology and notation introduced here is used in the subsequent chapters. The chapter starts with a discussion of light waves and their representation and behaviour, such as reflection,diffraction and interference. The coherence of light is then defined and developed, an examination of some of the imaging properties of a thin lens follows and, in addition, various types of specimen surfaces are defined. In the last part of this chapter the properties of a general coherent interferometer are derived. Some of the material presented there is original and is essential for the analysis of DASC and DASSC.

So that this chapter may be kept to a reasonable length, many topics are discussed only briefly and, hence, the presentation may be at times overly simplistic. However, most topics presented here are well known and are discussed in depth in numerous textbooks and source books on optics [50,....,56,60,61].

2.2 Light

Visible light is a form of electromagnetic energy usually described

as electromagnetic waves. The behaviour of light is governed by Maxwell's electromagnetic theory and quantum theory; Maxwell's theory describes the wave-like aspects of light, while quantum theory describes the particle-like nature of light.

Even though light is an electromagnetic nature it will be represented here, without loss of generality, by its electric component only. This is done both to simplify the notation and because the photographic plate emulsion, used as a recording medium, is sensitive only to the intensity of the electric field component of incident light.

2.3 Geometrical Optics

There is a class of optical phenomena which may be described without taking into account any hypotheses concerning the wave nature of light or its interaction with material bodies. This division of optics concerned with the image formation by optical systems is called geometrical optics since its description is founded almost entirely on geometrical relations. The laws of geometrical optics may be stated as follows:

1. Light is propagated in straight lines in homogeneous medium.
2. Two independent beams of light may intersect each other and thereafter be propagated as independent beams.
3. The angle of incidence of light upon a reflecting surface is equal to the angle of reflection.
4. On refraction, as is shown in Fig. 2.1, the ratio of the sine of the angle of incidence to the sine of the angle of refraction is constant, depending only on the nature of the media. This relationship is known as Snell's law and is given by

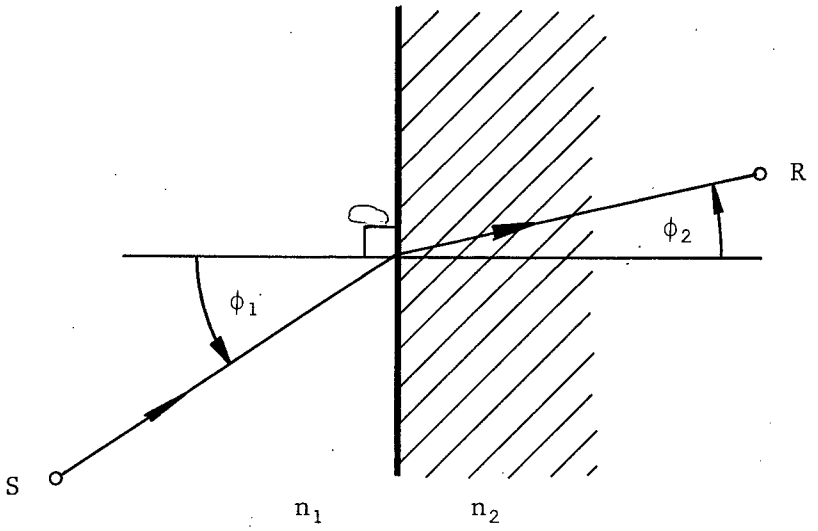

Fig. 2.1 Refraction of light.

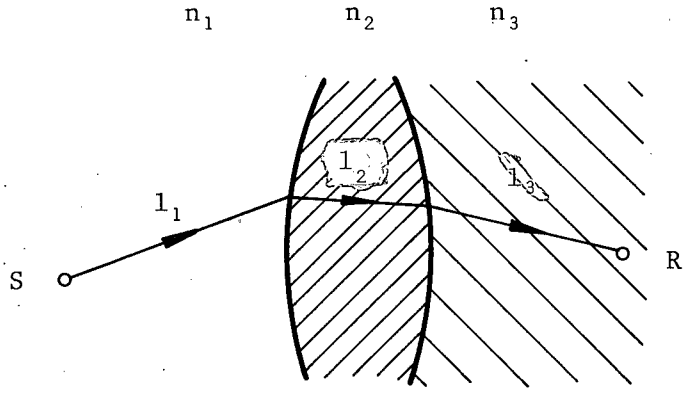

Fig. 2.2 Optical path length of a ray.

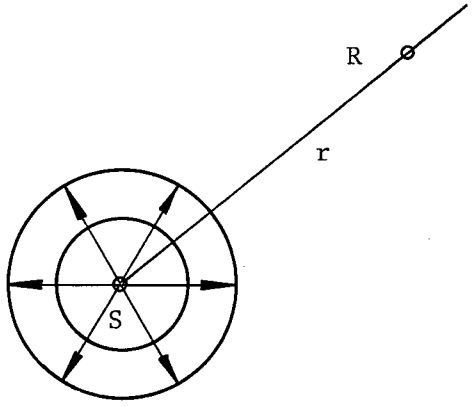

Fig. 2.3 Point source.

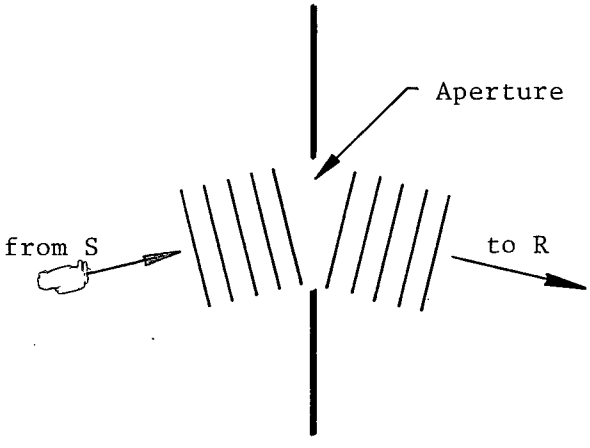

Fig. 2.4 Fraunhofer diffraction by an aperture.

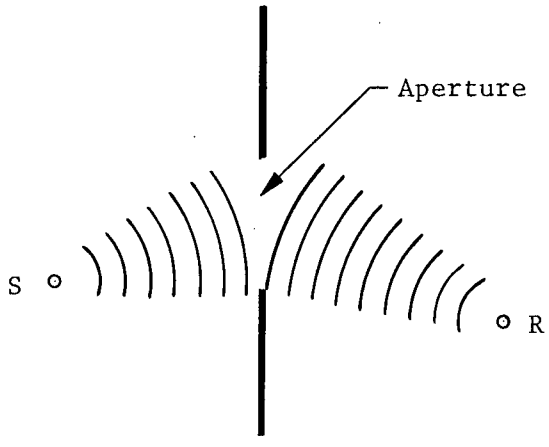

Fig. 2.5 Fresnel diffraction by an aperture.

$$n_1 \sin\phi_1 = n_2 \sin\phi_2 \tag{2.1}$$

where n_1 and n_2 are the indices of refraction of the media.

2.4 The Ray

The ray may be defined as the path along which light travels or, alternatively, it may be said that the ray is the direction in which the wave motion propagates. The optical length of a ray of length l in a medium of index n is defined as the product nl. For example, the optical length SR shown in Fig. 2.2, is given as

$$SR = n_1 l_1 + n_2 l_2 + n_3 l_3$$

2.5 Fermat's Principle

This principle, sometimes called the law of extreme path, states that the path taken by light in passing between two points is that which it will traverse in the least time.

2.6 Point Source of Light

It can be shown that, in free space, the electric field component of light, E(r,t), emitted by a point source S radiating uniformly in all directions may be expressed as

$$E(r,t) = \frac{1}{r} f(r - ct) \tag{2.2}$$

where r denotes the distance from the point source , t denotes time, and c is the speed of wave propagation. The point source S is shown in Fig. 2.3, with R being the receiving point where E(r,t) is measured. Solution (2.2) satisfies Maxwell's equations everywhere except at r = 0. This singularity is unimportant since any real source cannot have a zero

radius. The form of f depends on the nature of the source; if the source radiates a monochromatic wave then f is of the form

$$f(r - ct) = a \cos\left[k(r - ct) + \psi\right] \tag{2.3}$$

where

a ... amplitude of radiation

ψ ... phase angle determined from the value of $E(r,t)$ at $r = r_0$ and $t = t_0$

k ... wave number

λ ... wavelength of radiation

ω ... angular frequency

and k, c, λ, and ω are related as

$$k = \frac{2\pi}{\lambda} \tag{2.4}$$

$$\omega = kc \tag{2.5}$$

Using equations (2.3), (2.4), and (2.5) we may write the electric field at $R(r)$ in the form

$$E(r,t) = \frac{a}{r} \cos(kr - \omega t + \psi) \tag{2.6}$$

Equation (2.6) describes a circularly polarized electric field. If the field is polarized in any other way it is necessary to introduce vector notation:

$\hat{n}$ ... unit vector normal to wavefront

$\overline{k}$ ... propagation vector defined as: $\overline{k} = k\hat{n}$

$\overline{r}$ ... position vector

$\hat{\hat{e}}$ ... unit vector normal to propagation vector and oriented so that it lies in the plane of polarization.

With this notation a polarized electric field due to a point source may be written as

$$\overline{E}(r,t) = \frac{a}{r}\,\hat{e}\,\cos(\overline{k}\cdot\overline{r} - \omega t + \psi) \tag{2.7a}$$

and, in general, the polarized electric field may be described by

$$\overline{E}(\overline{r},t) = E(\overline{r})\,\hat{e}\cos(\overline{k}\cdot\overline{r} - \omega t + \psi) \tag{2.7b}$$

where $E(\overline{r})$ is the amplitude of electric field at $\overline{r}$.

2.7 The Principle of Linear Superposition

The theory of optical interference is based essentially on the principle of linear superposition of electromagnetic fields. According to this principle, the electric field $\overline{E}$ produced at a point in empty space due to n different sources is equal to the vector sum.

$$\overline{E} = \overline{E}_1 + \overline{E}_2 + \ldots. + \overline{E}_n \tag{2.8}$$

The same principle holds for the magnetic field. In the presence of matter, however, the principle of linear superposition is only approximately true.

2.8 Diffraction

When waves pass through an aperture or past the edge of an obstacle they always spread to some extent into the region which is not directly exposed to the oncoming waves. This phenomenon is called diffraction. In the study of diffraction it is customary to distinguish between two general cases known as Fraunhofer diffraction and Fresnel diffraction. Fraunhofer diffraction, shown in Fig. 2.4, occurs when the source of light and the screen on which the diffraction pattern is observed are effectively at infinite distances from the aperture causing the diffraction. If either the source or the screen, or both, are at finite distances from the aperture then Fresnel diffraction occurs. An example of Fresnel

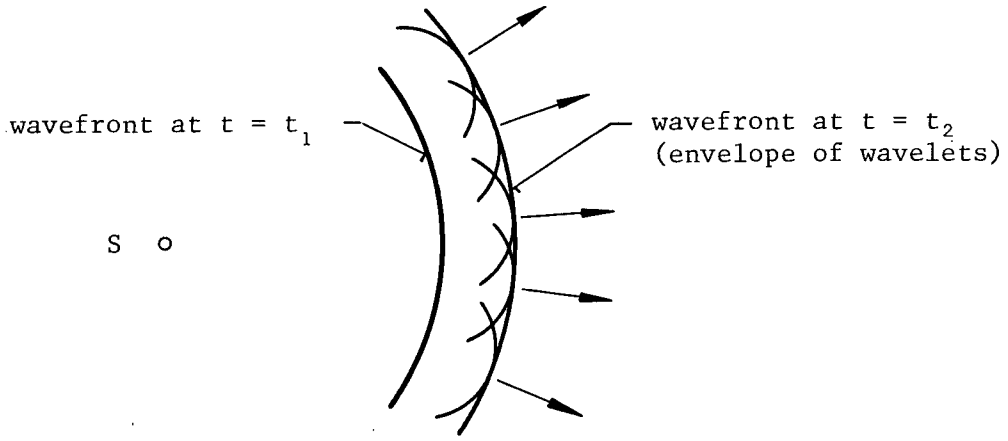

Fig. 2.6 Illustration of the Huygen's principle.

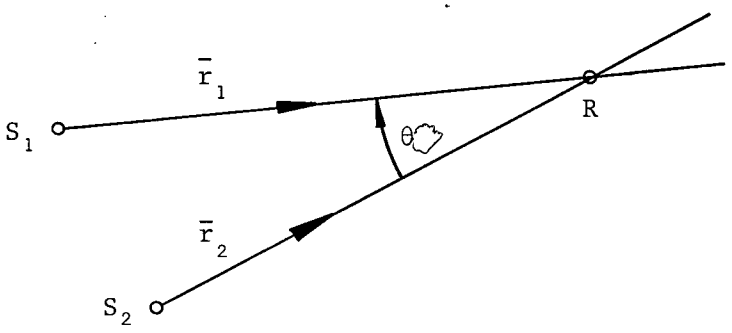

Fig. 2.7 Coherence of light.

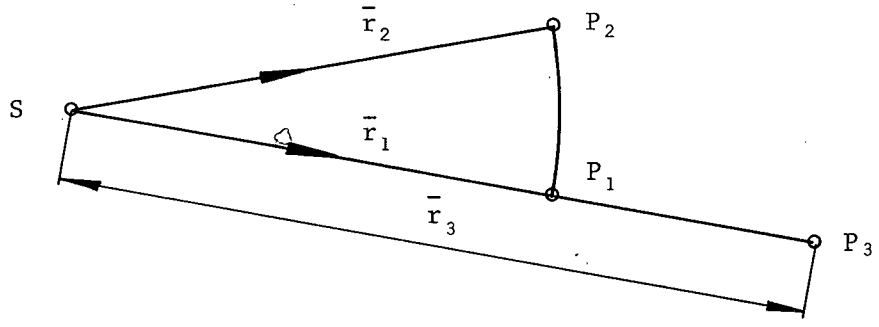

Fig. 2.8 Longitudinal and lateral coherence of electric fields.

diffraction is shown in Fig. 2.5.

There is no sharp line of distinction between the two cases of diffraction and, if it is at all possible, the Fresnel diffraction is approximated by the Fraunhofer diffraction as the Fraunhofer case is much simpler to treat theoretically. The approximation is appropriate only if the actual optical path from the source to the screen and the optical path given by the Fraunhofer approximation differ by much less than the wavelength of light.

2.9 Huygen's Principle

This principle says that each point on a wavefront may be considered as being instantaneously and continuously the origin of a new spherical wavefront moving outward from that point. The secondary wavelets from all points along the wavefront overlap and the superposition of all of them accounts for the forward motion of the original wavefront. This principle is useful in the explanation of diffraction and the determination of diffraction patterns of various apertures. The illustration of the Huygen's principle is shown in Fig. 2.6.

2.10 Coherence

In discussing the idea of coherence of light it is convenient to consider two identical point sources S_1 and S_2 at different locations, each radiating harmonic travelling waves of the same frequency ω, as is shown in Fig. 2.7, and generating an electric field at point R

$$\overline{E}_1 = \frac{a_1}{r_1} \hat{e}_1 \cos (kr_1 - \omega t + \psi_1)$$

$$\overline{E}_2 = \frac{a_2}{r_2} \hat{e}_2 \cos (kr_2 - \omega t + \psi_2)$$

The resultant electric field at R is given by the principle of superposition as

$$\overline{E} = \overline{E}_1 + \overline{E}_2$$

The instantaneous intensity at R is given by

$$I(t) = |\overline{E}|^2 = (\overline{E}_1 + \overline{E}_2)\cdot(\overline{E}_1 + \overline{E}_2) = |\overline{E}_1|^2 + |\overline{E}_2|^2 + 2\overline{E}_1\cdot\overline{E}_2$$

and the intensity recorded over "exposure" time $T \gg \tau$, (τ being the period of light wave), is derived in Appendix A as

$$I_r = \frac{T}{2}\left(\frac{a_1}{r_1}\right)^2 + \frac{T}{2}\left(\frac{a_2}{r_2}\right)^2 + \frac{T}{2}\,2\left(\frac{a_1}{r_1}\right)\left(\frac{a_2}{r_2}\right)(\hat{e}_1\cdot\hat{e}_2)\cos(kr_1 - kr_2 + \psi_1 - \psi_2)$$

$$= I_1 + I_2 + 2\sqrt{I_1 I_2}\,(\hat{e}_1\cdot\hat{e}_2)\cos(kr_1 - kr_2 + \psi_1 - \psi_2) \qquad (2.9)$$

The term $2\sqrt{I_1 I_2}\,(\hat{e}_1\cdot\hat{e}_2)\cos(kr_1 - kr_2 + \psi_1 - \psi_2)$ is called the interference term, and its presence causes the resultant intensity to be greater than or less than the sum of $I_1 + I_2$. In the derivation of equation (2.9) it was assumed that the phase difference $\psi_1 - \psi_2$ did not change during the "exposure" time. If the two sources behave in such a way, they are said to be mutually coherent. If the phase difference $\psi_1 - \psi_2$ does change in a random fashion with time during the "exposure", then the mean value of the cosine term would be zero and the two sources would be called mutually incoherent.

The product of the unit vectors $\hat{e}_1\cdot\hat{e}_2$ depends on the relative polarization of the two electric fields. If the polarization of these two fields are mutually orthogonal, then $\hat{e}_1 \cdot \hat{e}_2 = 0$. In many instances the two propagation vectors, $\overline{k}_1$ and $\overline{k}_2$, are nearly parallel (θ is very small) and, if the two fields are circularly polarized or are polarized in the same way, then $\hat{e}_1\cdot\hat{e}_2 = 1$ and equation (2.9) is reduced to the form

$$I_r = I_1 + I_2 + 2\sqrt{I_1 I_2}\cos(kr_1 - kr_2 + \psi_1 - \psi_2) \qquad (2.10)$$

Since the argument of the cosine depends on r_1 and r_2, periodic spatial variations in intensity occur; these variations are the familiar fringes that are seen when two mutually coherent beams of light interfere. If the two independent sources are not purely monochromatic but have, instead, a dominant frequency and the same finite frequency bandwidth $\Delta\nu$, then the relative phase difference $\psi_1 - \psi_2$ will remain constant over a time of the order of $(\Delta\nu)^{-1}$. This time is usually referred to as the coherence time, and the distance that the radiation traverses in the coherence time is called the coherence length.

Often the two sources may be "locked" in phase with one another if they are "driven" by a common driving force. In this case, even though the phase constant of each source may change in a random manner in time $(\Delta\nu)^{-1}$, where $\Delta\nu$ is now the bandwidth of the common driving force, the relative phase difference will remain constant.

There are several more aspects to the coherence of light that need to be mentioned here. In Fig. 2.8, S is a point source of monochromatic radiation. The two points, P_1 and P_3, lie in the same direction from the source; they differ only in their distance from S . The electric field at P_1 is E_1 and the field at P_3 is E_3. The coherence between the fields E_1 and E_3 measures the longitudinal spatial coherence at the field. Point P_2 is at the same distance from S as P_1 , but it lies in a different direction. In this case the coherence between fields E_1 at P_1 and E_2 at P_2 measures the lateral spatial coherence of the field.

2.11 Imaging Properties of a Thin Lens

A lens is a most common element occuring in optical systems. It is made of a transparent, optically dense material, usually glass, having an

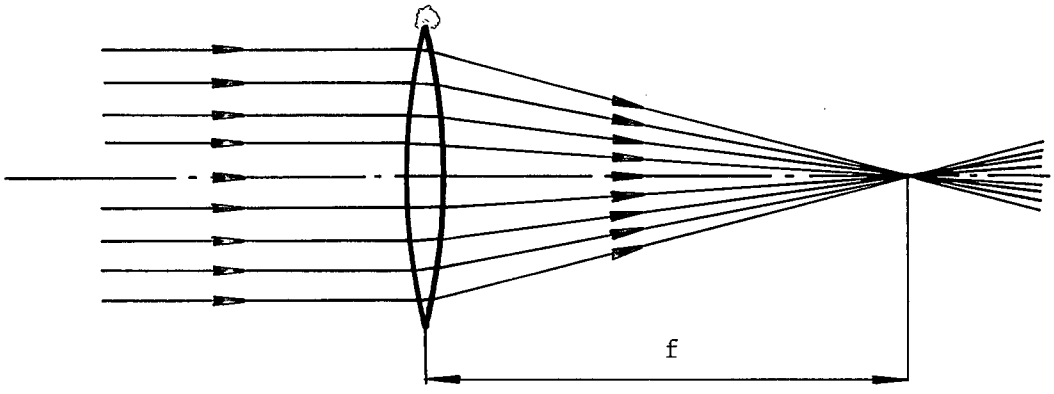

Fig. 2.9 Focal length of a thin lens

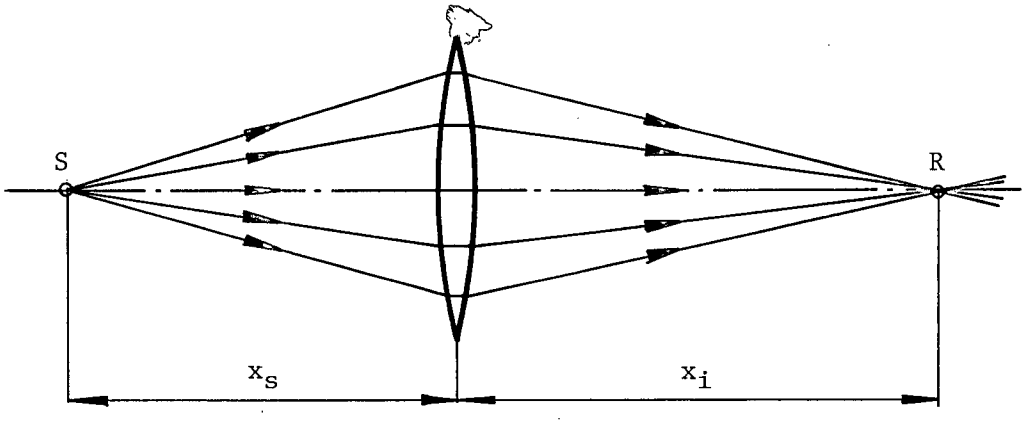

Fig. 2.10 Image formation by a thin lens.

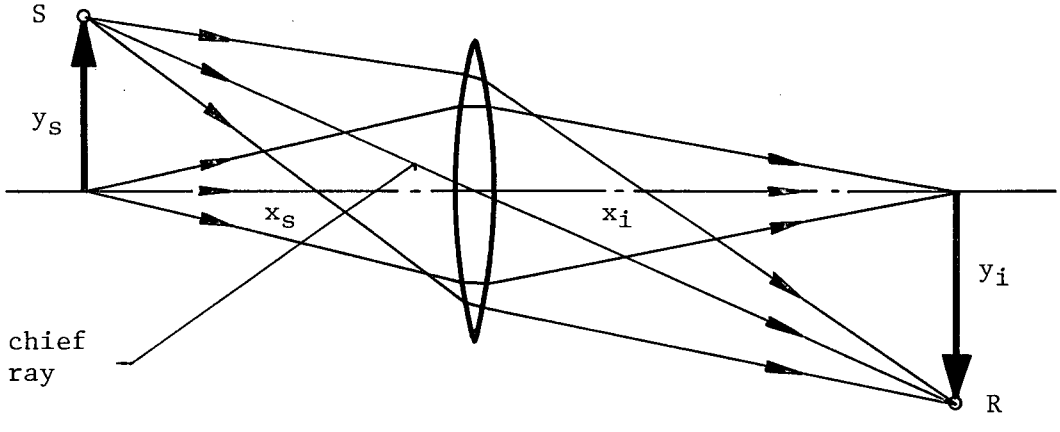

Fig. 2.11 Lateral magnification by a thin lens.

index of refraction greater than one. Usually the two surfaces of a lens are spherical. In a simple thin lens the line through the center of the lens joining the centers of curvature of the lens surface is called the optical axis. The imaging "power" of a lens is defined by its focal length f, which is the distance from the lens at which all incident rays parallel to the optical axis will meet after passing through the lens as is shown in Fig. 2.9 . If a thin lens is used to image a source point at distance x_s from the lens, then the image will be formed at distance x_i behind the lens, as is shown in Fig. 2.10 . The two distances x_s and x_i are related to the focal length f by the equation

$$\frac{1}{x_s} + \frac{1}{x_i} = \frac{1}{f} \tag{2.11}$$

An important imaging property of a thin lens is that all rays emitted by S and passing through the lens to the receiving point R are of equal (or nearly equal) optical path length.

The image size of an object is usually different from the actual size of the object. This imaging property of a thin lens is called the lateral magnification m . By considering the geometry of Fig. 2.11 , equation (2.12) relating the object size and the image size to the lens parameters is obtained.

$$-\frac{y_i}{y_s} = \frac{x_i}{x_s} = m \tag{2.12}$$

The minus sign in the equation (2.12) means that the image of an object is inverted.

2.12 Aberrations in Optical Systems

Optical systems in which thin spherical lenses are used have a number of aberrations or faults which impair or limit the imaging quality of the

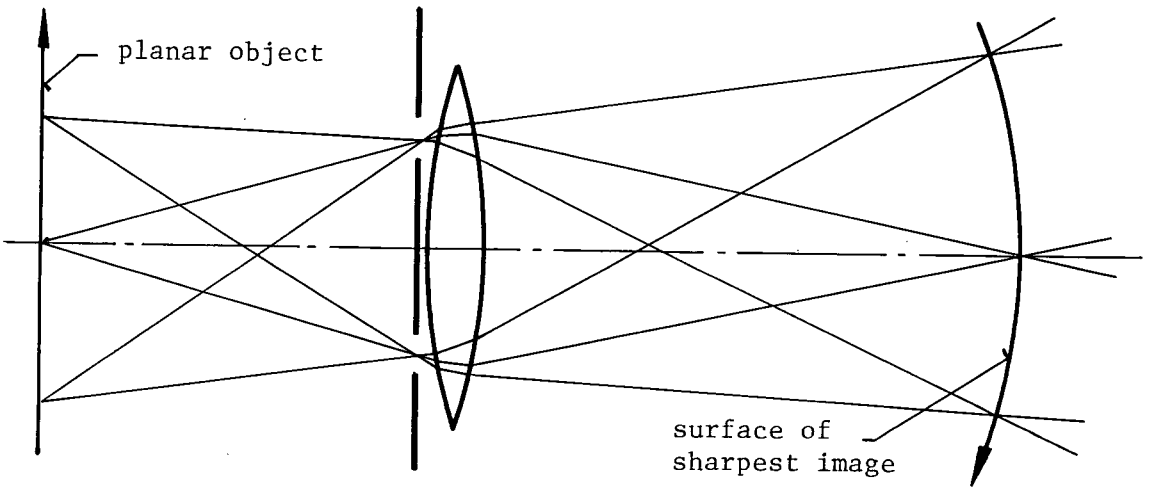

Fig. 2.12 Curvature of field aberration of a thin lens.

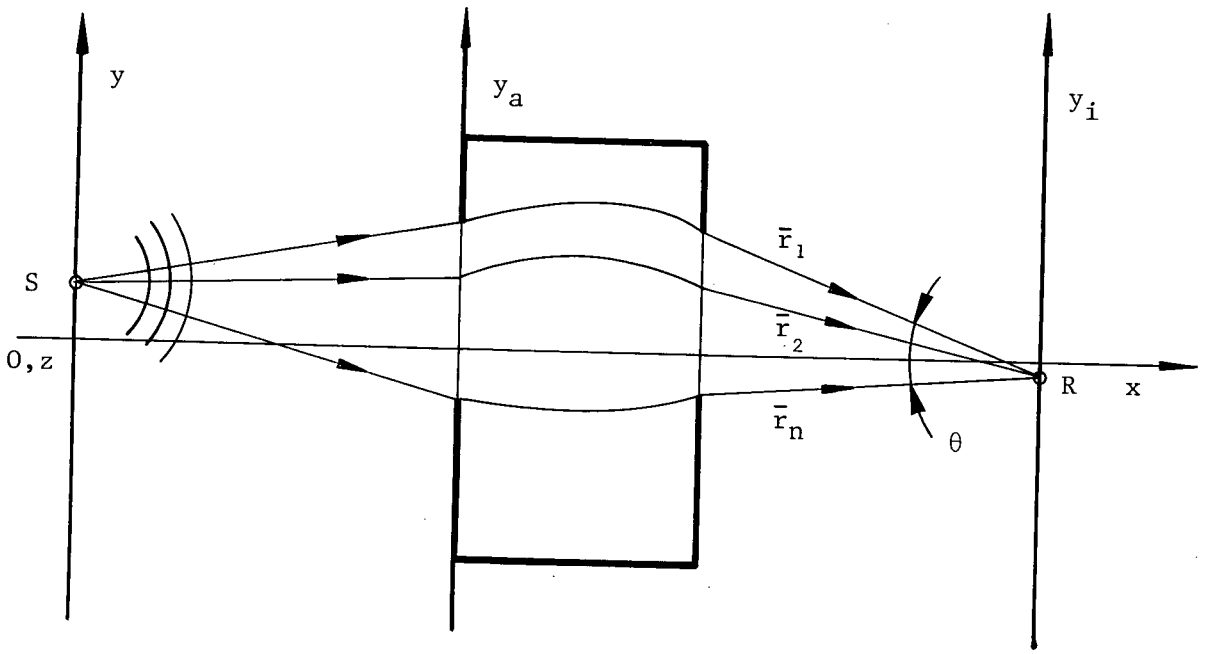

Fig. 2.13 Generalized coherent interferometer.

system. The most common aberrations are spherical aberration, astigmatism, comma, curvature of the image field, distortion of the image, and chromatic aberration. All aberrations are analyzed in great detail in a number of optics textbooks and other.

The only aberration that needs to be mentioned here is curvature of the field. It arises if the object is an extended plane; in that case the astigmatic images will not be planes but curved surfaces. For object points on or near the optical axis, there will be sharp point-to-point representation in the image plane, but, as the distance from the axis is increased, the sharpness of the image will decrease. Each point of the object will be represented by a blurred patch, the size of which will be greater for greater distances from the axis. Even if the defects of spherical aberration, astigmatism, and comma are corrected, this patch will be the clsest approach to a sharp point focus. The surface containing the best possible focus for all parts of the image will not be a plane but a surface of revolution of a curved line about the axis. An example of this aberration in a system using a lens with two relatively small apertures in its entrance pupil is shown in Fig. 2.12 . The curvature of field aberration may be corrected if more than one thin lens is used.

2.13 Generalized Coherent Interferometer

We will consider here a coherent interferometer with one point source

of polarized monochromatic coherent light. The schematic of the interferometer is shown in Fig. 2.16 . S is the point source of light, and $\bar{r}_1$,$\bar{r}_2$, ... $\bar{r}_n$ are the light rays passing through the interferometer and reaching the receiving point R. In Section 2.6 , it was shown that these rays may be described by equation (2.7a). Our task is to determine the expression for the intensity of light which would be recorded at the receiving point over some "exposure" time T much greater than the period of light radiated by the source. The analysis will eventually be restricted to the case where all rays reaching the receiving point are nearly parallel so that the scalar description of light may be used. The resultant electric field at the receiving point is given by the principle of superposition as

$$\bar{E}_r(t) = \sum_{i=1}^{n} \frac{a}{r_i} \hat{e}_i \cos(\bar{k}_i \cdot \bar{r}_i - \omega t + \psi) \tag{2.13}$$

The phase angle ψ and the amplitude a are the same for all rays since they originate from one source. For a continuous field, the number of rays is infinite and, hence, the summation sign in equation (2.13) must be replaced by the integral sign. Equation (2.14) results.

$$\bar{E}_r(t) = \int_A \frac{a}{r(y,z)} \hat{e}(y,z) \cos\left[\bar{k}(y,z) \cdot \bar{r}(y,z) - \omega t + \psi\right] dA \tag{2.14}$$

The integration extends over the area A(y,z) of the aperture(s), with the understanding that the integration is to include only those parts of the aperture area which are traversed by those rays eventually reaching the receiving point. The optical path length of a ray, and the propagation vector are expressed as functions of the coordinates (y,z) of the aperture in the entrance pupil of the interferometer. The intensity recorded at R over "exposure" time T is given by

$$I_r = \int_0^T |\bar{E}_r(t)|^2 dt \tag{2.15}$$

Let us now consider an interferometer where the light rays reaching the receiving point R are nearly parallel and polarized in the same way. In addition the optical path lengths of the rays are almost equal so that the "mean" optical path length r_0 may be defined as the optical path length of a typical ray. With these assumptions, and using r_0 , we may closely approximate equation (2.14) by

$$E_r(t) \simeq \frac{a}{r_0} \int_A \cos\left[kr(y,z) - \omega t + \psi\right] dA \tag{2.16}$$

It is now convenient to introduce the path length variation $r_e(y,z)$ defined as

$$r_e(y,z) = r(y,z) - r_0 \tag{2.17}$$

In Appendix B equations (2.15),(2.16), and (2.17) were used to derive equations (2.18) and (2.19) giving I_r as

$$I_r = \left(\frac{a}{r_0}\right)^2 \frac{T}{2} \left[\left(\int_A \cos kr_e(y,z)\, dA \right)^2 + \left(\int_A \sin kr_e(y,z)\, dA \right)^2 \right] \tag{2.18}$$

With the use of complex notation, equation (2.18) may be written as

$$I_r = \left(\frac{a}{r_0}\right)^2 \frac{T}{2} \left(\int_A e^{ikr_e(y,z)} dA \right) \left(\int_A e^{-ikr_e(y,z)} dA \right) \tag{2.19}$$

It should be noted that the intensity I_r depends, in general, on the positions of the source point S and the receiving point R, since any change in their positions will cause a change in optical path length variation $r_e(y,z)$.

The recorded intensity I_r often varies in some reasonable fashion

with y_i, z_i thus producing a pattern of dark and bright fringes usually referred to as an "interference pattern". If the image formation or characteristics of the interferometer are known, it may be possible to obtain some information about the source of light from the interference pattern, and indeed, most interferometers are used in this way. Various techniques are used to produce interference patterns which provide information about the source (with respect to the object's size, position, displacement, etc.). Reseachers usually strive to design an "ideal" interferometer which would be sensitive to only one particular aspect of the source or object behaviour which is of interest, while being completely insensitive to the other aspects. Unfortunately, in most cases this cannot be achieved, and the object behaviour which is of interest must be "extracted" from the interference pattern by an additional data processing, filtering, etc.

3. ANALYSIS OF THE FRINGE FORMATION BY DASC AND DASSC

3.1 Preliminary Remarks

In Chapter 2 the principles of physical optics were reviewed, and the equations describing the image formation by the generalized coherent interferometer were derived. Using these results, we will now examine the image formation of three particular interferometers. In the study, the actual interferometers are represented by their mathematical models, and the object surface is represented by one or two points. The equations describing the image formation by these mathematical models are approximate, but should approach the image formation of real interferometers with sufficient accuracy for practical testing.

The chapter starts with an analysis of image formation by a camera having one small circular aperture in its entrance pupil. The basic principles, notation, and approximations which are made here are then used throughout this chapter. The analysis of the Double Aperture Speckle Camera (DASC) and Double Aperture Speckle Shearing Camera (DASSC) follows, and the equations governing the fringe formation by these two cameras in the double exposure process are derived.

3.2 Image Formation by a Single Aperture Camera

The model of the camera is shown in Fig. 3.1 . The cartesian coordinate system x,y,z is set up with x-axis coincident with the optical axis of the system and the y and z-axes in the source plane. The point source $S(y_S,z_S)$ radiates a monochromatic, coherent light of wavelength λ and amplitude a at the unit distance from S. The aberration free lens has a focal length f, diameter D_L, and is negligibly thin as compared to the distances x_s and x_i . Placing the lens immediately to the right of the aperture plane permits one to say that both the aperture plane and the lens

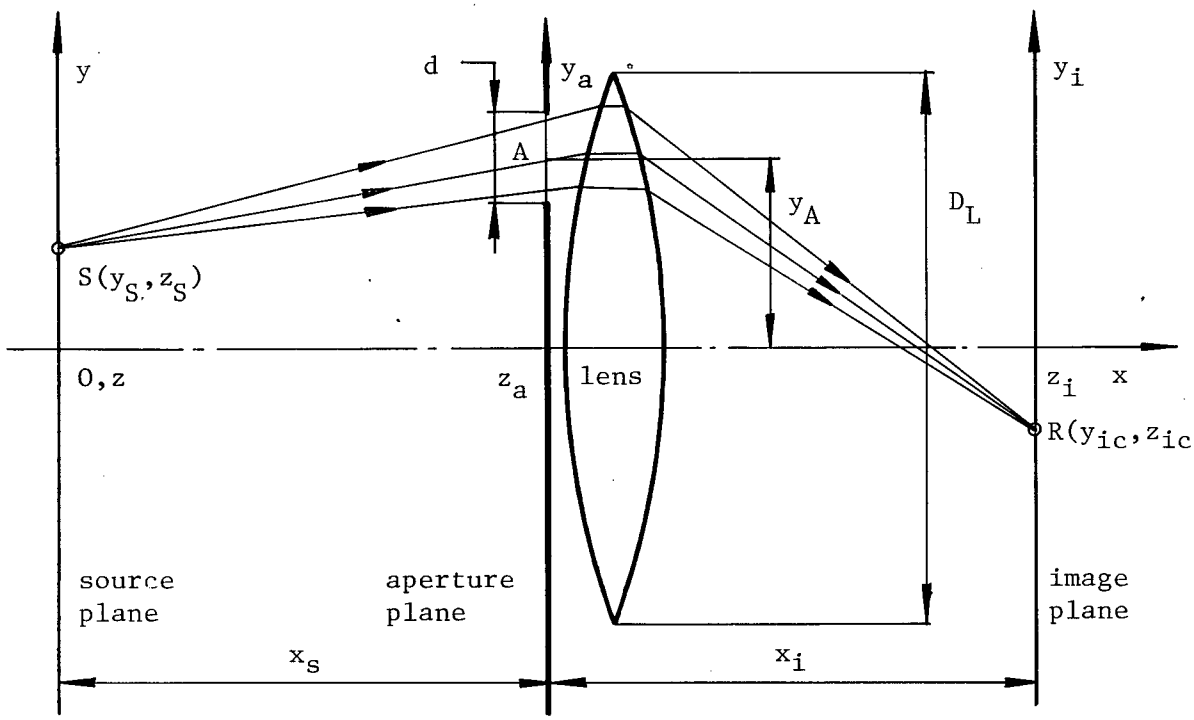

Fig. 3.1 Single aperture camera.

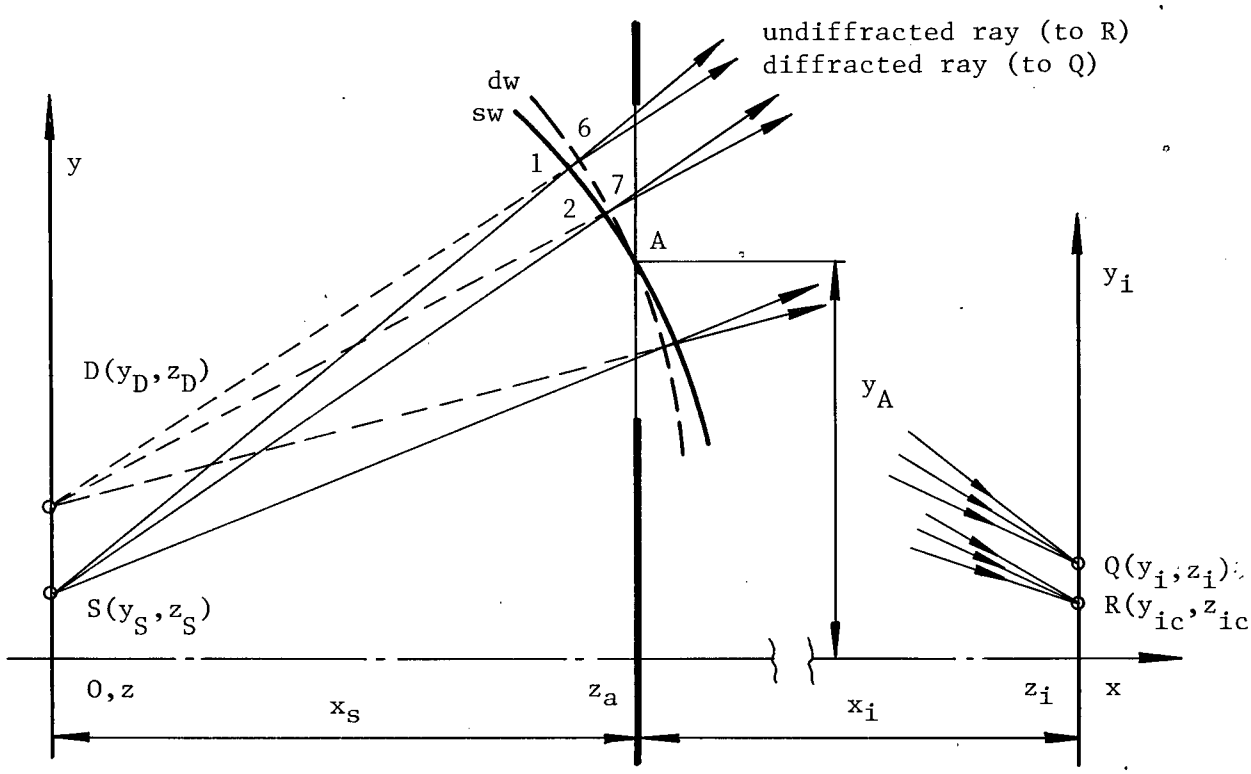

Fig. 3.2 Diffraction in a single aperture camera.

are at approximately the same distance x_s from the source plane. The aperture plane is opaque, infinite in extent, and contains a circular aperture of a diameter d with its center at $(y_A,0)$. The geometric image of $S(y_S,z_S)$ is in the image plane at $R(y_{ic},z_{ic})$. It is assumed that the aperture diameter d is very much smaller that the lens diameter D_L and, hence, the only significant diffraction in the camera occurs in the aperture itself. This diffraction causes the image, R, of S to be "blurred" rather than being a point. We wish to determine the recorded intensity distribution I_r around the geometric image R.

One of the imaging properties of a thin lens is that the optical path lengths of all undiffracted rays from a point source to its geometric image are equal. Thus in Fig. 3.2, which shows the diffraction in the camera, all rays from S to R are of equal optical length, that is $\overline{S\text{-}1\text{-}R} = \overline{S\text{-}2\text{-}R} = \ldots$. Since the source wavefront sw reaching the aperture is spherical, $\overline{S\text{-}1} = \overline{S\text{-}2} = \ldots$ and, correspondingly, $\overline{1\text{-}R} = \overline{2\text{-}R} = \ldots$. If there were another point source at $D(y_D,z_D)$, similar arguments would hold; but of course $\overline{S\text{-}R} \neq \overline{D\text{-}Q}$, where $Q(y_i,z_i)$ would be the image of D. Let us consider a diffracted spherical wavefront dw of such curvature and orientation that it would appear to originate from the point D. The optical path lengths from the wavefront dw to the virtual image of D at Q are all equal, that is $\overline{6\text{-}Q} = \overline{7\text{-}Q} = \ldots$. However, the diffracted wavefront dw is derived from the spherical, constant phase , source wavefront sw and, therefore, in general is not a wavefront of constant phase. At point 6 dw leads sw by the distance $\overline{1\text{-}6}$, at point 7 it leads sw by the distance $\overline{2\text{-}7}$ and so on. The distances $\overline{1\text{-}6}$, $\overline{2\text{-}7}$, ...may be expressed in terms of the system geometry, and the intensity at point Q due to the diffracted wavefront dw can be calculated according to the equation (2.18). The analysis is restricted to those systems where

$$x_s, x_i \gg y_i, y_S, y_D, z_i, z_S, z_D, d, D, y_A \tag{3.1}$$

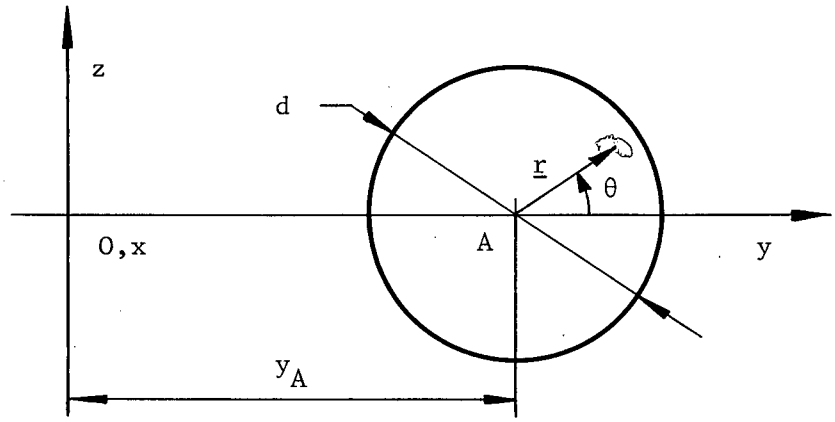

Fig. 3.3 Coordinate system of the circular aperture.

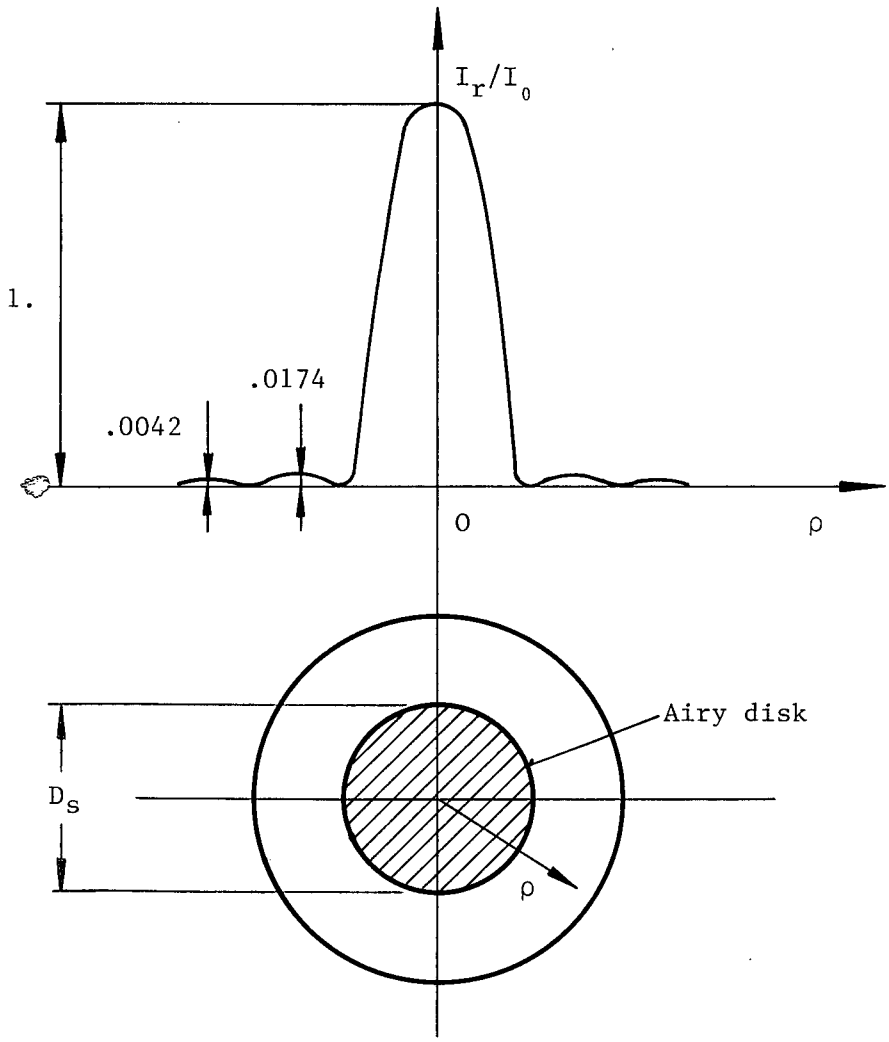

Fig. 3.4 Diffraction pattern of a single circular aperture.

Let us now determine an approximate expression for the optical path length variation $r_e(y,z)$ which was defined in Chapter 2 as

$$r_e(y,z) = r(y,z) - r_0 \tag{2.17}$$

Here $r(y,z)$ is the optical path length from the point source $S(y_S,z_S)$ in the source plane, through a point (y,z) in the aperture plane, to the image point $Q(y_i,z_i)$ in the image plane; it is given by

$$r(y,z) = \overline{S-A} + \overline{dw-sw} + \overline{A-Q} \tag{3.2}$$

where $\overline{dw-sw}$ is the distance by which the diffracted wavefront dw leads the source wavefront sw and A is the aperture centre. For example, $r(y,z)$ for the ray 1 is

$$r_1(y,z) = \overline{S-1} + \overline{1-6} + \overline{6-Q} = \overline{S-A} + \overline{dw_1-sw} + \overline{A-Q}$$

If we choose r_0 as

$$r_0 = \overline{S-A} + \overline{A-Q} \tag{3.3}$$

then the substitution of equations (3.1) and (3.2) in equation (3.3) yields

$$r_e(y,z) = \overline{dw-sw} \tag{3.4}$$

It is shown in Appendix C that because of equation (3.1) the optical path length variation r_e is very closely approximated by

$$r_e = \underline{r}\left[\left[\left(1 - \frac{3y_S^2}{2x_S^2}\right)\Delta y - \frac{y_S z_S}{x_S^2}\Delta z\right]\cos\theta + \left[\left(1 - \frac{3z_S^2}{2x_S^2}\right)\Delta z - \frac{z_S y_S}{x_S^2}\Delta y\right]\sin\theta\right] \tag{3.5}$$

The radius $\underline{r}$ and angle θ of equation (3.5) are shown in Fig. 3.3, and Δy and Δz are defined as

$$\Delta y = \frac{y_D - y_S}{x_S} \qquad \Delta z = \frac{z_D - z_S}{x_S} \tag{3.6}$$

In Appendix F it is shown that all rays reaching a point in the image plane

are nearly parallel, thereby making it possible to disregard the vector nature of light in the calculation of the light intensity at that point and consequently, equation (2.19) may be used to calculate I_r . The intensity is calculated in Appendix D from equation (2.19) with r_0 given by equation (3.3) and $r_e(y,z)$ given by equation (3.5). The integration is done over the circular area A of the aperture with the result

$$I_r(\rho) = I_0 \left(\frac{2J_1(\rho)}{\rho}\right)^2 \tag{3.7}$$

where I_0 and ρ are given by

$$I_0 = \left(\frac{a}{r_0}\right)^2 \frac{T}{2} \left(\frac{\pi d^2}{4}\right)^2 \tag{3.8}$$

$$\rho = \frac{kd}{2x_i}\sqrt{(y_i - y_{ic})^2 + (z_i - z_{ic})^2} \tag{3.9}$$

Equation (3.7) describes the recorded intensity distribution I_r as a function of the image plane coordinates y_i and z_i . J_1 is the first order Bessel function of the first kind. The amplitude of the distribution is proportional to the square of the aperture area $\pi d^2/4$ and to the amplitude 'a' of the radiation. It decreases with the square of the source-image distance r_0 . I_r is linearly proportional to the exposure time T. The distribution is of the shape shown in Fig. 3.4 and is symmetric about the geometric image $R(y_{ic},z_{ic})$ of the source point; here it also attains its maximum value. The first minimum in the distribution occurs when $\rho = 3.83$, and the area within this perimeter minimum is known as the Airy disk. Its diameter D_s is given in terms of the system geometry by equation (3.10) derived in Appendix E .

$$D_s = 2.44\,\lambda \frac{x_i}{d} \tag{3.10}$$

The apparent diameter of the Airy disk in the source plane is given by

$$D_{ss} = 2.44\,\lambda \frac{x_s}{d} \tag{3.11}$$

As is shown in Fig. 3.4 , the values of the maxima of the intensity distribution decrease rapidly with increasing distance from the centre of the pattern and, hence, the diffraction pattern of the circular aperture may be approximated by the Airy disk alone.

The results of this section may be summarized by the following: When the camera with a single circular aperture in its entrance pupil is used to image a point source of monochromatic coherent light, the image of the point source is essentially a circle, sometimes referred to as a speckle, of diameter D_s .

3.3 Image Formation by a Double Aperture Speckle Camera (DASC)

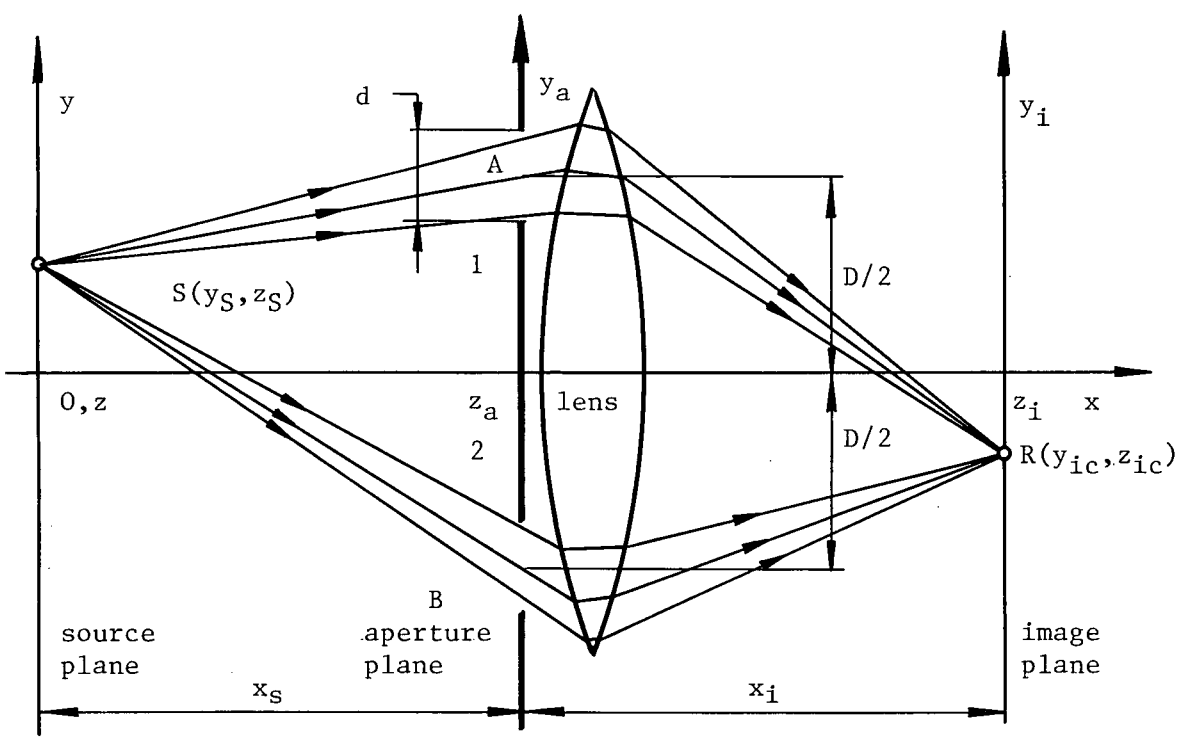

Fig. 3.5 Double aperture camera.

The model of DASC is shown in Fig. 3.5 . With the exception of the two apertures, it has the same geometry as the single aperture camera. The two apertures are circular, of diameter d, and their centers are at $(x_s,-D/2,0)$ and $(x_s,+D/2,0)$ where D is the separation of aperture centers. Again we wish to determine the recorded intensity distribution around $R(y_{ic},z_{ic})$, the geometric image of S .

The diffraction process in the two apertures is shown in Fig. 3.6 . The optical path length variations, r_{e_1} for aperture 1 and r_{e_2} for aperture 2, are derived in Appendix G as

$$r_{e_1} = r_e$$

$$r_{e_2} = r_e - D\delta$$

r_e is given by equation (3.5) and δ is given by equation (3.13). Because of the assumptions stated in equation (3.1), the electric field unit vectors are nearly parallel and equation (2.19) may again be used to calculate the recorded intensity distribution I_r . The calculations are done in Appendix H with the result

$$I_r = 4I_0 \left(\frac{2J_1(\rho)}{\rho}\right)^2 \cos^2\frac{kD\delta}{2} \tag{3.12}$$

In equation (3.12) I_0 is given by equation (3.8), ρ by equation (3.9), and δ by

$$\delta = -\frac{y_i - y_{ic}}{x_i} \tag{3.13}$$

Equation (3.12) describes the recorded intensity distribution in the image plane as a function of the image coordinates (y_i,z_i) . The amplitude of the distribution is proportional to the square of the area of the two apertures $2\frac{\pi d^2}{4}$ and to the amplitude 'a' of the radiation. It diminishes with the square of the distance r_0 from the source to its image and is linearly proportional to the exposure time T . An example of the typical shape of

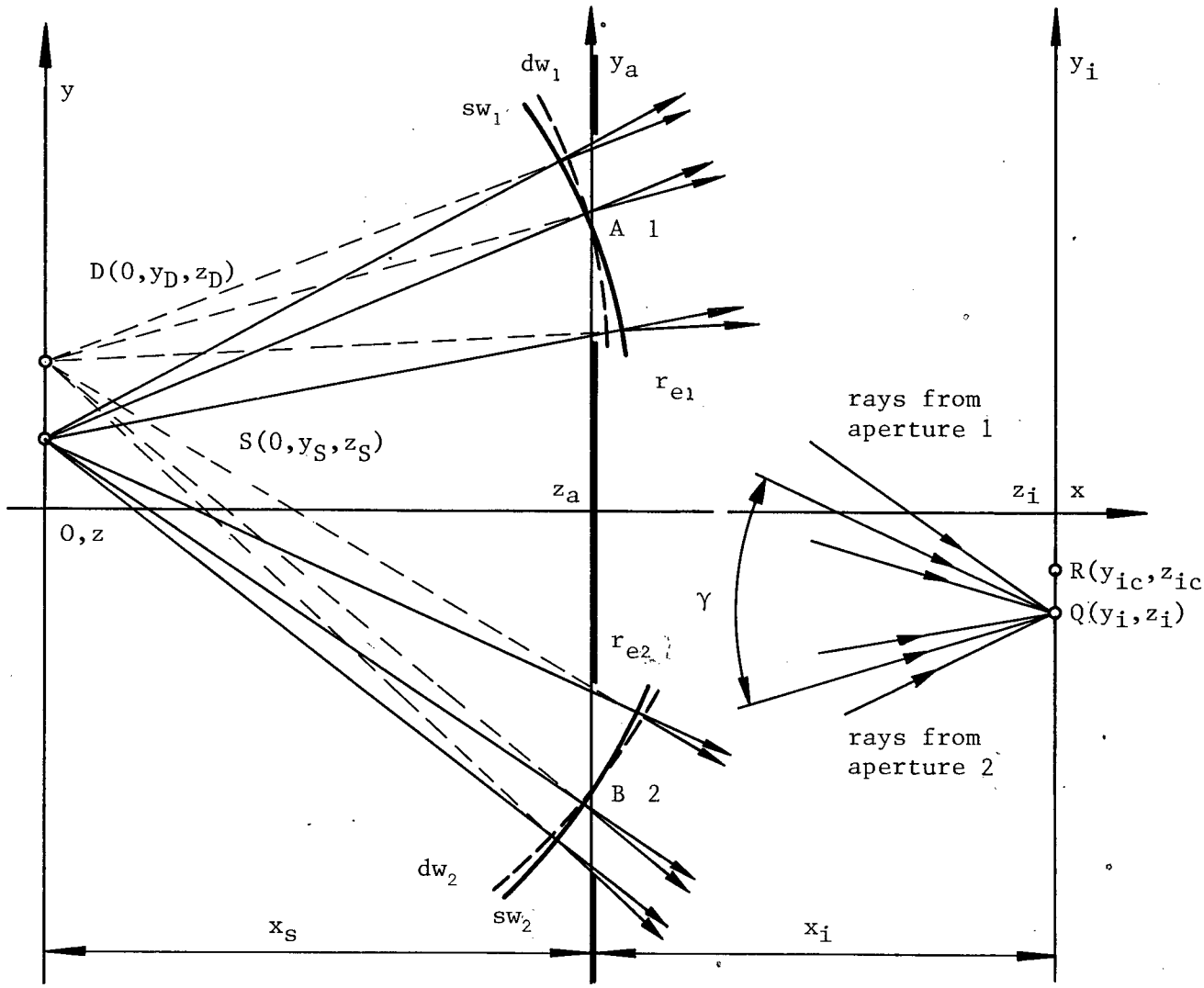

Fig. 3.6 Diffraction in a double aperture camera.

the distribution is shown in Fig. 3.7 for the case of $D/d = 4$.

The envelope of the intensity distribution is of the same shape as that for the single aperture case shown in Fig. 3.4 . However, because the intensity distribution is modulated by the cosine term of higher frequency, it causes the grid-like appearance of the speckle. This grid is normal to the y_i coordinate and is centered on and symmetric about the geometric image

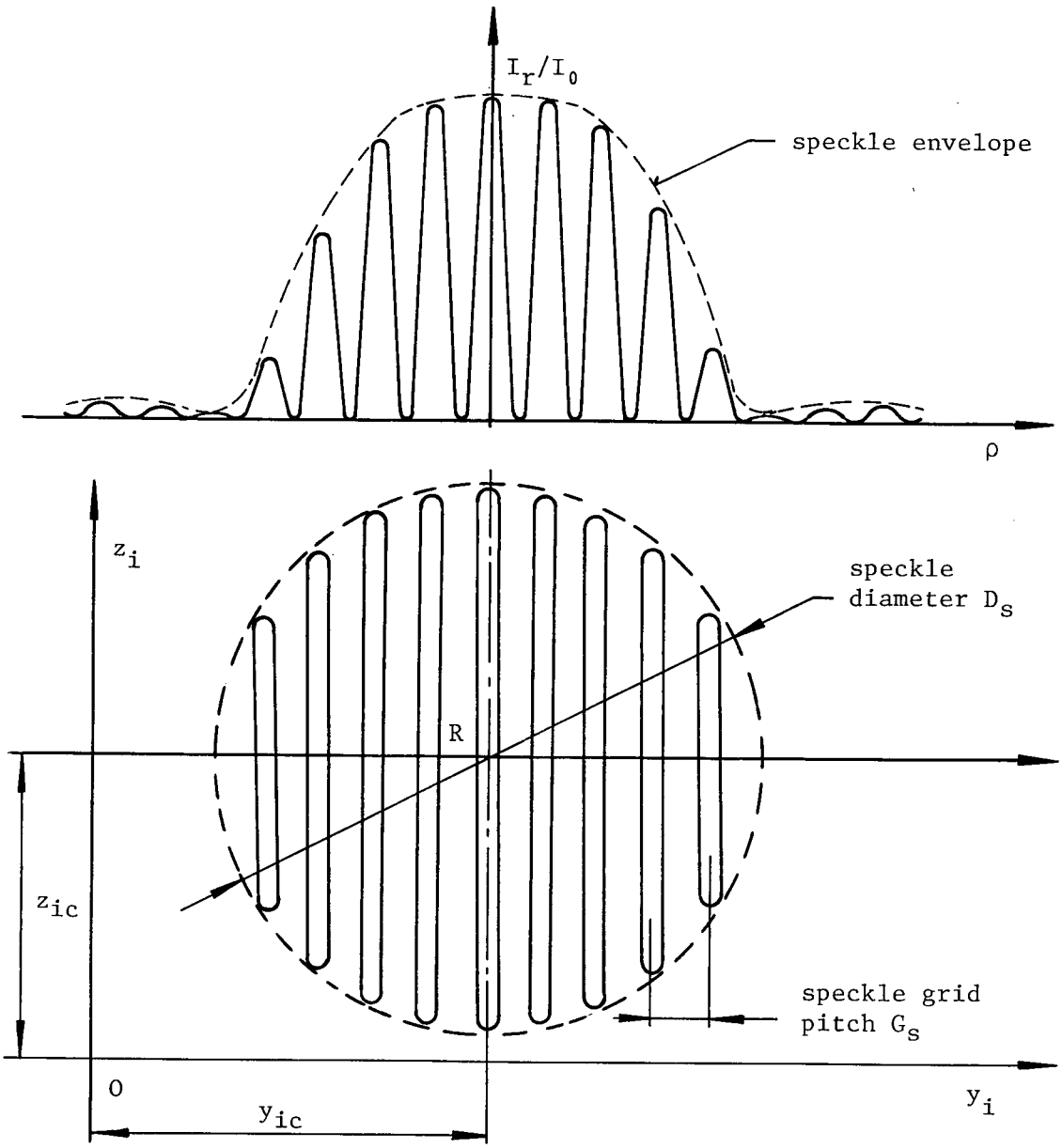

Fig. 3.7 Diffraction pattern of two circular apertures.

of the source point. The speckle diameter D_s is the same as that in case of the single aperture, i.e.

$$D_s = 2.44\,\lambda \frac{x_i}{d} \tag{3.10}$$

The "grid pitch" G_s in the image plane is given by two successive zeros of the modulating cosine term and is calculated in Appendix I as

$$G_s = \lambda \frac{x_i}{D} \tag{3.14}$$

The apparent "grid pitch" G_{ss} in the source plane is given by

$$G_{ss} = \lambda \frac{x_s}{D} \tag{3.15}$$

The result of this section may be summarized as follows: When a camera with two radially opposed circular apertures in its entrance pupil is used to image a point source of monochromatic coherent light, the image of the point source is essentially a speckle of diameter D_s modulated by a grid of pitch G_s which is perpendicular to the line connecting the centers of the two apertures.

3.4 Formation of Moire Fringes by DASC

The equation governing the formation of Moire-type fringes by DASC in the double exposure process are derived here. The equations relate the magnitude of the in-plane and out-of-plane motion of a point source and the parameters of the system to the Moire fringe number n .

During the first exposure the coordinates of a point source S are $(0,y_S,z_S)$. We know from the preceeding section that the recorded image of S

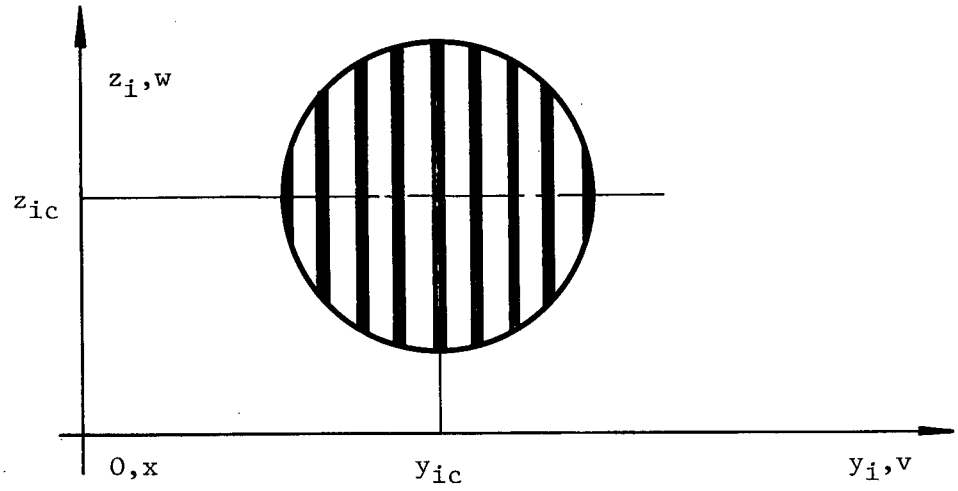

Fig. 3.8 Elevation of the first exposure speckle

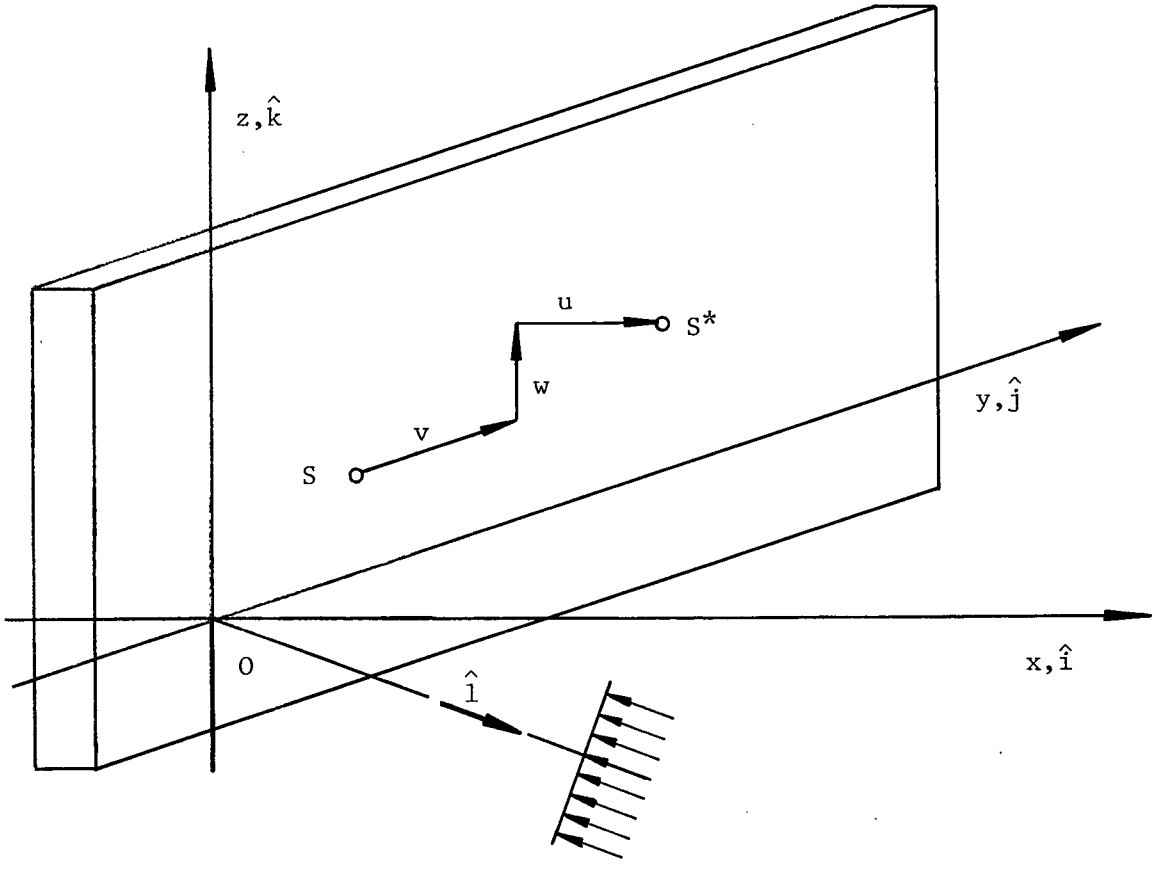

Fig. 3.9 General deformation of the specimen surface.

formed by the DASC is centered about the geometric image of S in the image plane at the point $R(y_{ic}, z_{ic})$ where the coordinates y_{ic} and z_{ic} are given by equation (2.12) as

$$y_{ic} = -\frac{x_i}{x_s} y_S \qquad z_{ic} = -\frac{x_i}{x_s} z_S$$

The image is a speckle of diameter D_S and is modulated by a grid of pitch G_S perpendicular to the y-axis. The elevation of this speckle is shown in Fig. 3.8 .

Between the first and second exposure of the double exposure recording method the specimen is deformed in a general manner. Point S , which represents the specimen surface, is therefore displaced both in and out-of-plane and its new coordinates are $(u, y_S + v, z_S + w)$ as shown in Fig. 3.9 . The three components comprising the displacement vector of S are u,v and w oriented along x,y and z-axes respectively. The optical path length variations, r_{e_1} and r_{e_2}, occuring during the second exposure are derived to within an accuracy of $\lambda/30$ in Appendix J as

$$r_{e_1} = \underline{r}\left[(E_1 + F)\cos\theta + E_2 \sin\theta\right]$$

$$r_{e_2} = \underline{r}\left[(E_1 - F)\cos\theta + E_2 \sin\theta\right] - D(\delta - \xi)$$

where E_1, E_2, F and ξ are defined in Appendix J with ξ given as

$$\xi = \frac{u}{X_{S0}}\left[\frac{y_S}{X_{S0}}\left(\frac{x_s}{X_{S0}} + \frac{u}{X_{S0}}\right) - \frac{2}{D}\frac{x_s}{X_{S0}}\left(v\frac{y_S}{X_{S0}} + w\frac{z_S}{X_{S0}}\right)\right] + \frac{v}{X_{S0}}\left(1 - \frac{y_S^2}{X_{S0}^2}\right) - \frac{w}{X_{S0}}\frac{y_S z_S}{X_{S0}^2} \tag{3.16}$$

I_r is calculated in Appendix K with the result

$$I_r = 4I_0\left[\left(\frac{J_1(\rho_1)}{\rho_1} - \frac{J_1(\rho_2)}{\rho_2}\right)^2 + \underbrace{\left(\frac{2J_1(\rho_1)}{\rho_1}\right)\left(\frac{2J_1(\rho_2)}{\rho_2}\right)\cos^2\frac{kD(\delta - \xi)}{2}}_{\text{speckle grid term}}\right] \tag{3.17}$$

where ρ_1 and ρ_2 are given as

$$\rho_1 = \frac{kd}{2}\sqrt{(E_1 + F)^2 + E_2^2}$$

$$\rho_2 = \frac{kd}{2}\sqrt{(E_1 - F)^2 + E_2^2}$$

The term $\left(\frac{J_1(\rho_1)}{\rho_1} - \frac{J_1(\rho_2)}{\rho_2}\right)^2$ is of much lower "frequency" than the speckle grid term and its magnitude is usually smaller than that of the term $\left(\frac{2J_1(\rho_1)}{\rho_1}\right)\left(\frac{2J_1(\rho_2)}{\rho_2}\right)$. Since we are interested in the recorded intensity pattern, I_r , acting as a diffraction grating, the former term may be thought of as a low frequency "background noise" which does not appreciably affect the diffractive efficiency of the speckle grid described by the term

$$\left(\frac{2J_1(\rho_1)}{\rho_1}\right)\left(\frac{2J_1(\rho_2)}{\rho_2}\right)\cos^2\frac{kD(\delta - \xi)}{2}$$

Comparison of the speckle grid terms recorded during the first and second exposures reveals that the speckle grid recorded during the second exposure has been "shifted" by the amount ξ with respect to its first exposure position. This "shift" and the simplified plan view of the speckles recorded in the two exposures is shown in Fig. 3.10 .

In the double exposure method the images of the object in the positions which it occupied during the two exposures are both recorded on the same photographic plate. Usually the two exposures are of equal duration and, hence, the resultant image intensity distribution is the sum of the two distributions, as is shown in Fig. 3.10 . The two speckles overlap, and in the overlaping area the two grids, each belonging to one speckle, add. This addition is defined here as constructive when the high intensity regions of one speckle overlap the high intensity regions of the other speckle. This occurs when

$$\text{speckle grid shift} = nG_s \qquad n = 0, \pm 1, \pm 2, \ldots$$

In a similar manner, the addition is defined as destructive when the high intensity regions of one speckle overlap the low intensity regions of the other speckle; this destructive addition occurs when

$$\text{speckle grid shift} = nG_s \qquad n = \pm\frac{1}{2}, \pm\frac{3}{2}, \ldots$$

Thus, "n" indicates the type of addition which takes place in a double exposure method. In general, n is continuous and the product nG_s is equal to the shift between the two grids caused by the deformation of the specimen surface. In particular we may write

$$\text{speckle grid shift} = y_{ig_2} - y_{ig_1} = nG_s \quad n \text{ continuous} \tag{3.18}$$

In equation (3.18) y_{igj} is the speckle grid "center" position during the j-th exposure. Equation (3.18) is solved for n in Appendix L with the result

$$n = -\frac{D}{\lambda x_s}\left[\left(1 - \frac{y_S^2}{X_{S0}^2}\right)^{-1}\left[u\left(\frac{y_S}{X_{S0}}\frac{x_s + u}{X_{S0}} - \frac{2x_s}{D}\frac{vy_S + wz_S}{X_{S0}^2}\right) - w\frac{y_S z_S}{X_{S0}^2}\right] + v\right] \tag{3.19}$$

where X_{S0} is defined as $\qquad X_{S0}^2 = x_S^2 + y_S^2 + z_S^2 + y_A^2$

Equation (3.19) may be closely approximated by

$$n \simeq -\frac{D}{\lambda x_s}\left(\frac{y_S}{x_s}u + v - \frac{y_S z_S}{x_s^2}w\right) \tag{3.20}$$

The accuracy of equation (3.20) should be sufficient for any laboratory testing; both equations (3.19) and (3.20) are applicable as long as the speckles recorded during the two exposures overlap and, to ensure this, the displacements must be sufficiently small. Equation (3.21), which restricts the size of the surface displacements, was derived in Appendix M as

$$\left[\left(v + u\,\frac{y_S \pm D/2}{x_S}\right)^2 + \left(w + u\,\frac{z_S}{x_S}\right)^2\right]^{\frac{1}{2}} < \frac{D_{ss}}{2} = 1.22\,\lambda\,\frac{x_s}{d} \qquad (3.21)$$

The addition of the speckles recorded during the two exposures is shown in Fig. 3.10 . The out-of-plane component u of the displacement vector causes the second exposure speckle envelope to "divide" into two circles 2_A and 2_B . The Moire fringes are formed by the addition of the speckle grids created during the first and second exposures. This addition takes place in the area which is common to speckles (circles) $1, 2_A$, and 2_B .

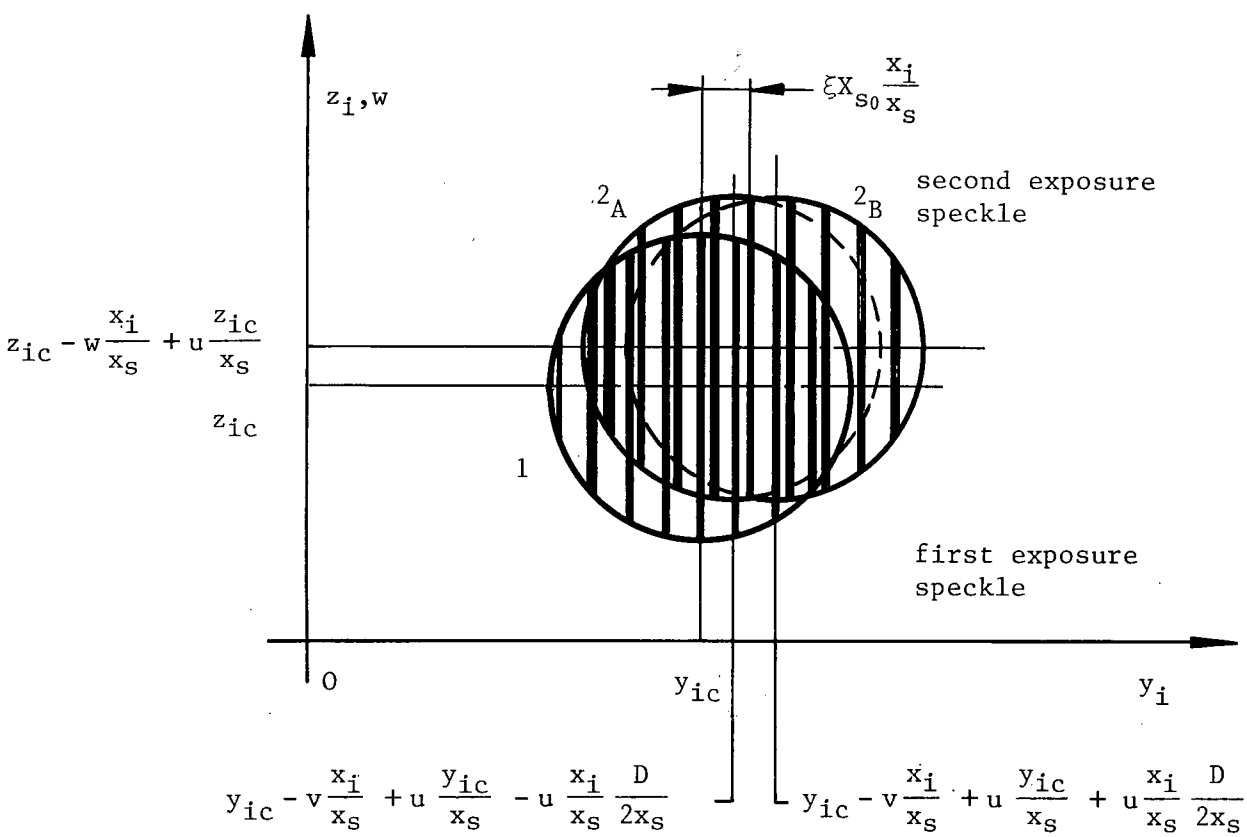

Fig. 3.10 Elevation of the first (1) and the second ($2_A, 2_B$) exposure speckles.

The result of this section may be summarized by the following: When DASC is used to record the displacement field of a specimen surface illuminated by a laser light, Moire fringes will be produced according to equation (3.20) or, more accurately, according to equation (3.19). The surface displacements must be sufficiently small to satisfy equation (3.21).

3.5 Image Formation by DASSC

The double aperture speckle shearing camera (DASSC) is similar to DASC except for the lateral shear of the images. This lateral shear may be achieved either by placing inclined glass plates in front of the apertures or by "defocusing". Both methods of producing the lateral shear were tried and the defocusing method was found to be more convenient for practical material testing, mainly because of the ease with which the size and the sign of the lateral shear may be adjusted to suit a specific test. The schematic of DASSC employing defocusing to produce the lateral shear is shown in Fig. 3.11 . With the exception of the position of the photographic plate, the geometry of DASSC is the same as that of DASC shown in Fig. 3.5 .

To determine the equation governing the formation of Moire fringes by this camera we will represent the surface of a specimen by two point sources. The diffraction process that actually occurs in DASSC is closely represented by the model shown in Fig. 3.12 . The schematic shows the specimen plane y,z and the image plane y_i, z_i which are familiar from the prior analysis of DASC. There are, however, two more planes in the system. One is called the "photo" plane Y_i, Z_i and it coincides with the emulsion of the photographic plate located the distance γ_i from the image (focal) plane; the other plane Y,Z is called the object plane, which is an imaginary plane located at $x = -\gamma$, where γ is such that the object plane would be focused by the system lens on the photo plane. The system lens(es) is represented

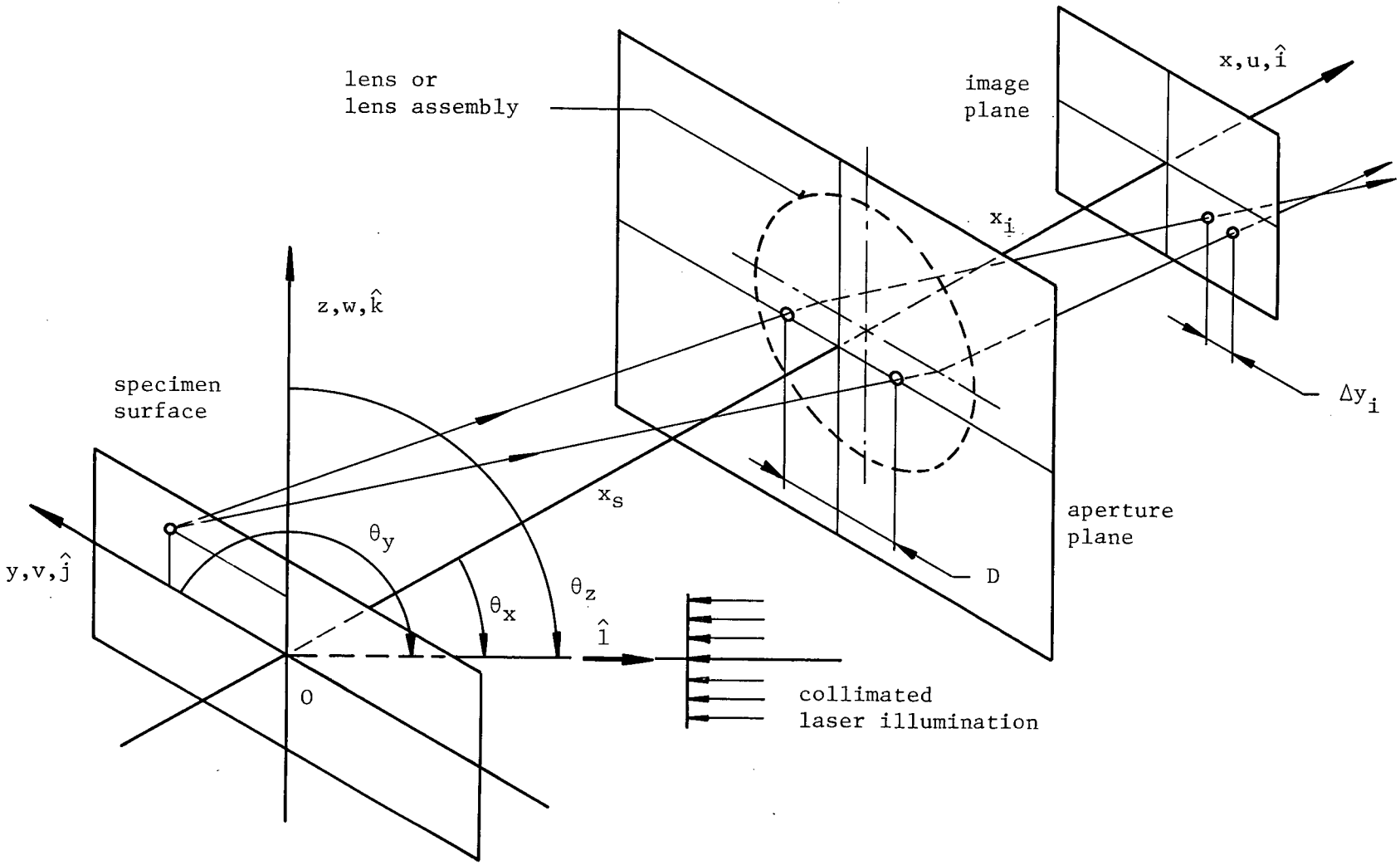

Fig. 3.11 The schematic of DASSC.

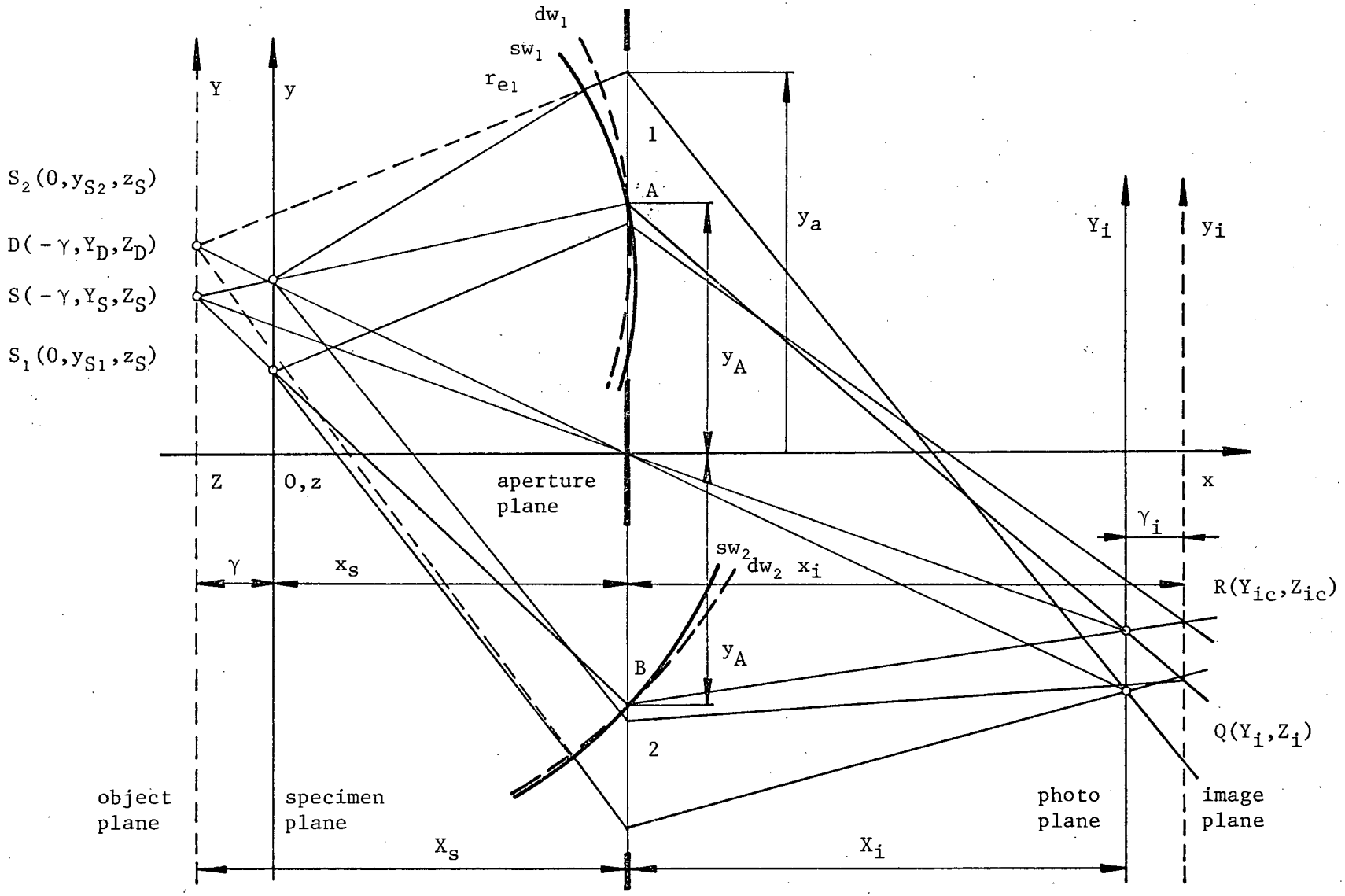

Fig. 3.12 Diffraction in DASSC.

by a thin lens so that the axial distances are related according to equation (2.11) as

$$\frac{1}{x_s} + \frac{1}{x_i} = \frac{1}{f} = \frac{1}{X_s} + \frac{1}{X_i} \tag{2.11}$$

where X_s and X_i are defined as

$$X_s = x_s + \gamma$$

$$X_i = x_i - \gamma_i$$

Let us consider an imaginary point source $S(-\gamma, Y_S, Z_S)$ in the object plane. The geometric image of S is in the photo plane at $R(Y_{ic}, Z_{ic})$. If S were a real point source, then the intensity distribution around R at $Q(Y_i, Z_i)$ would be found by considering an apparent source at $D(-\gamma, Y_D, Z_D)$, the geometric image of which would be at Q . This is what was done in the analysis of DASC previously. In the case of DASSC, the specimen surface is represented by two real point sources $S_1(0, y_{S1}, z_S)$ and $S_2(0, y_{S2}, z_S)$. S_2 lies where the line from S to the center of aperture 1 (at $y = y_A = D/2$) intersects the specimen plane, and S_1 lies where the line from S to the center of aperture 2 (at $y = -y_A = -D/2$) intersects the specimen plane. The two real point sources S_1 and S_2 are separated by the distance $\Delta y_s = y_{S2} - y_{S1}$. The choice of positions of S_1 and S_2 is based on the experience gained in the analysis of DASC. It is anticipated (and confirmed later) that the somewhat blurred image of S_2 made by light passing through aperture 1 is centered about R; as is the image of S_1 made by light passing through aperture 2 . It is reasonable to expect that the intensity distribution around R will depend greatly on the magnitude of the apparent speckle diameter D_{ss} and the separation Δy_s of the two real sources S_1 and S_2; therefore, two cases will be considered.

The first case occurs when $\Delta y_s > D_{ss}$. From the analysis of DASC it is known that the intensity distribution around the geometric image of a point source is of negligible magnitude at distances greater than $D_s/2$ from the

geometric image. The intensity distribution around R will therefore be produced essentially by the interference of the light radiated by S_2 and passing through aperture 1 with the light radiated by S_1 and passing through aperture 2 . The interference pattern that is produced is shown in Fig. 3.13 and is similar to the one produced by DASC shown in Fig.3.7 .

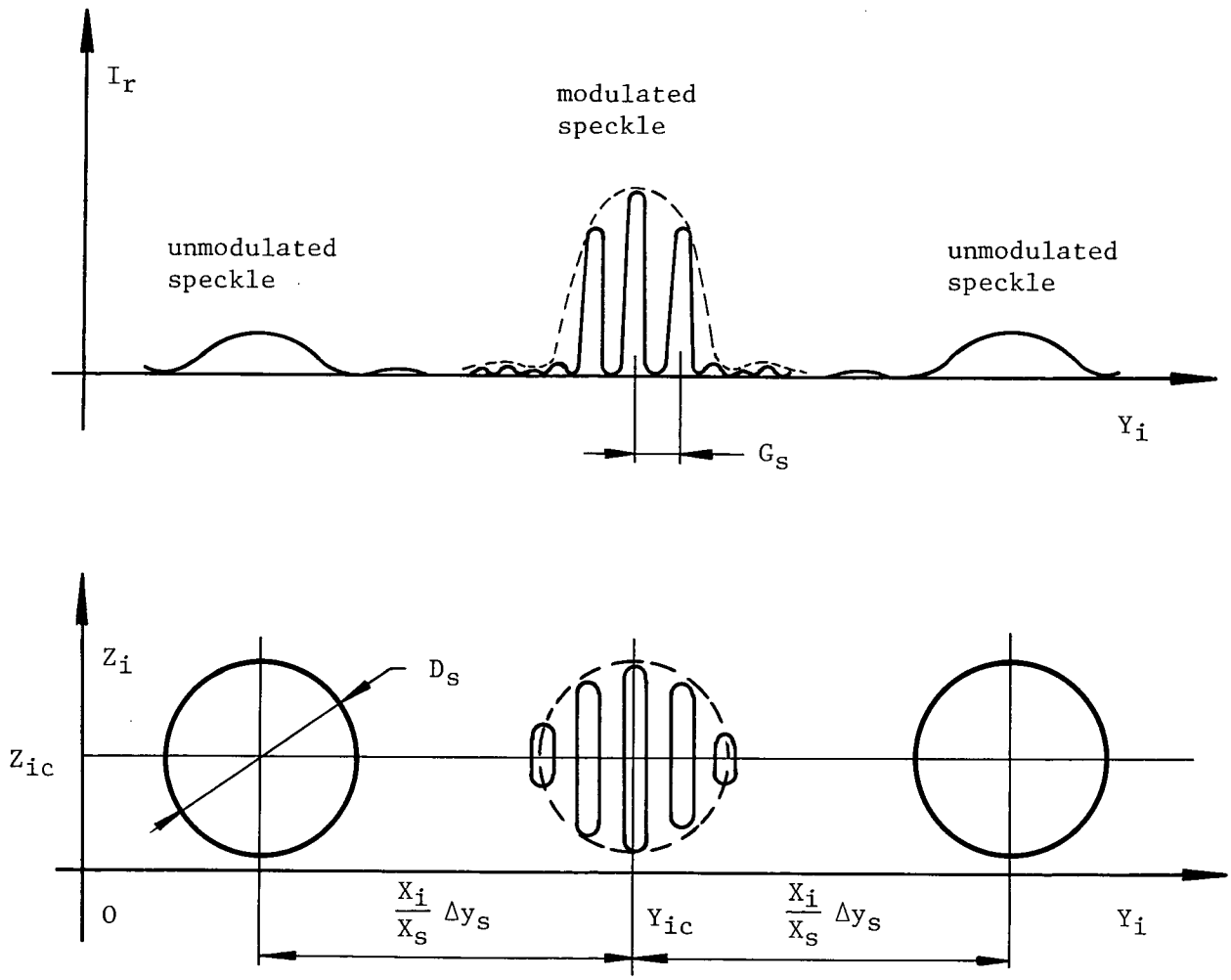

Fig. 3.13 Intensity distribution I_r for DASSC with $\Delta y_s > D_{ss}$.

Because of defocusing, the envelope of the pattern has changed; however, the speckle grid of pitch G_s is still present. Light radiated by S_2 and passing through aperture 2 and light radiated by S_1 and passing through aperture 1

are both imaged as "blurred" unmodulated speckles similar to the speckle shown in Fig. 3.4 produced by a single aperture camera. These two speckles are not of interest in as much as they do not diffract light once the recording is developed.

In the calculation of the intensity distribution I_r, computations similar to those done previously were made. The derivation of I_r is, however, more tedious as two point sources must be considered and some non-linear terms representing "blurring" of images may not be neglected. The calculation of the optical path length variation is performed in Appendix N, and the intensity distributions are determined in Appendix O . The following notation was used:

sw_{ij} ... source wavefront originating from S_j and reaching aperture i

dw_i ... wavefront appearing to originate from $D(-\gamma, Y_D, Z_D)$ and caused by diffraction of a source wavefront in aperture i

r_{eij} ... the optical path-length variation of rays radiated by source j and passing through aperture i

The mean optical path length r_0 was chosen arbitrarily as

$$r_0 = \overline{S_2 - sw_{12}} + \overline{dw_1 - Q} \tag{3.22}$$

r_{e12} and r_{e21} are derived in Appendix N to an accuracy of $\lambda/30$ or better as

$$r_{e12} = q\underline{r}^2 + \underline{r}(K_1\cos\theta + K_2\sin\theta) \equiv r_e$$

$$r_{e21} = q\underline{r}^2 + \underline{r}(K_1\cos\theta + K_2\sin\theta) - Dp$$

where q, K_1, K_2, and p are defined in Appendix N and I_r is calculated in Appendix O as

$$I_r = \left(\frac{a}{r_0}\right)^2 \frac{T}{2} \underbrace{\left[\left(\int_0^{d/2}\int_0^{2\pi} e^{ikr_e}\,\underline{r}\,d\underline{r}\,d\theta\right)\cdot\left(\int_0^{d/2}\int_0^{2\pi} e^{-ikr_e}\,\underline{r}\,d\underline{r}\,d\theta\right)\right]}_{\text{speckle envelope term}} \underbrace{4\cos^2\frac{kDp}{2}}_{\text{speckle grid term}} \tag{3.23}$$

The integrals comprising the speckle envelope term cannot be evaluated directly. While some approximate solutions are certainly possible, just a one step integration by parts done in Appendix O yields results from which it appears that the speckle envelope term is made up of terms having a much lower frequency than the speckle grid term. This is especially true for a small defocussing. In as much as the speckle grid is our main interest, equation (3.23) describes the recorded I_r sufficiently well. Fig. 3.13 shows I_r for this case; the drawing is only an approximation of I_r , and its sole purpose is to show graphically what I_r might be like and to aid in the discussion of the image formation by DASSC.

Let us now consider the situation where $\Delta y_s < D_{ss}$. In this case light radiated by S_1 and passing through apertures 1 and 2 and light radiated by S_2 and passing through apertures 1 and 2 all interfere with one another and contribute to I_r . Since $\Delta y_s < D_{ss}$, the parameter q is sufficiently small so that it may be neglected in expressions for r_{e12} and r_{e21} . In Appendix N r_{e11} and r_{e22} are derived and the four optical path length differences are given as

$$r_{e11} = \underline{r}\left[\left(K_1 + \beta_1\frac{D}{X_s}\right)\cos\theta + K_2\sin\theta\right] - \alpha_A + \alpha_s$$

$$r_{e12} = \underline{r}(K_1\cos\theta + K_2\sin\theta)$$

$$r_{e21} = \underline{r}(K_1\cos\theta + K_2\sin\theta) - Dp$$

$$r_{e22} = \underline{r}\left[\left(K_1 - \beta_1\frac{D}{X_s}\right)\cos\theta + K_2\sin\theta\right] - Dp + \alpha_A + \alpha_s$$

Also define ρ as

$$\rho = \frac{kd}{2}\sqrt{K_1^2 + K_2^2}$$

The parameters α_A and α_s are defined in Appendix N, and the parameters β_1, P_1, and P_2 are defined in Appendix O. I_r is derived in Appendix O as

$$I_r = \left(\frac{a}{r_0}\right)^2 \frac{T}{2} \left(\sum_{\substack{m=1,2 \\ n=1,2}} \int_0^{d/2} \int_0^{2\pi} e^{ikr_{emn}} \underline{r}\, d\underline{r}\, d\theta \right) \left(\sum_{\substack{m=1,2 \\ n=1,2}} \int_0^{d/2} \int_0^{2\pi} e^{-ikr_{emn}} \underline{r}\, d\underline{r}\, d\theta \right)$$

$$\simeq 16 I_0 \left(\frac{J_1(\rho)}{\rho}\right)^2 \left(P_1 + \underbrace{P_2 \cos^2 \frac{k}{2}(Dp - \alpha_A)}_{\text{speckle grid term}}\right) \qquad (3.24)$$

From equation (3.24) it is evident that the speckle grid with the same frequency as in the previous case is again present. The speckle envelope and the actual intensity variation are rather complicated in shape; this fact is not of great interest to us, however, since we are mainly interested in the diffractive properties of the recorded I_r. Since the speckle grid term is present, the intensity pattern I_r may again be closely approximated by a diffraction grating of pitch G_s over the speckle area.

3.6 Formation of Moire Fringes by DASSC

In this section an equation is derived governing the formation of Moire fringes by the DASSC in a double exposure process. This equation relates the Moire fringe number n to the in and out-of-plane displacements and strains of a surface represented by two points.

In the analysis of image formation by DASC the surface was represented by a point source of light. Even though this point source was in fact illuminated by a laser, the change in the distance between the point and the

laser had no effect on the recorded I_r. This conclusion is arrived at as follows:

Define the terms:

r_L ... optical path length from the laser to the point S on the specimen surface

Δr_L ... increase in r_L due to the displacement of S

r_1 ... optical path length from S to point Q in the image plane through aperture 1

r_2 ... optical path length from S to point Q in the image plane through aperture 2

r_{e1} ... increase in r_1 due to the displacement of S

r_{e2} ... increase in r_2 due to the displacement of S

The difference in the lengths of the two optical paths (one through each aperture) from the laser to the point Q in the image plane is given by

$\Delta_1 = (r_L + r_1) - (r_L + r_2)$ ... difference during the first exposure

$\Delta_2 = (r_L + \Delta r_L + r_1 + r_{e1}) - (r_L + \Delta r_L + r_2 + r_{e2})$ ... difference during the second exposure

The relative change between the two optical paths due to the displacement of S during the time between the two exposures is given by

$$\Delta_{12} = \Delta_2 - \Delta_1 = (r_1 + r_{e1}) - (r_2 + r_{e2}) - (r_1 - r_2) = r_{e1} - r_{e2}$$

Since it is Δ_{12} that determines the relative shift between the speckle grids recorded during the two exposures, it may be concluded that the distance from the point S on the specimen to the laser and the change in this distance due to the displacement of S has no effect on the Moire Fringe formation of DASC.

The situation is somewhat different in the case of DASSC. The specimen

surface is represented by two point sources S_1 and S_2 illuminated by one driving force - the laser. This time, the changes in distances between each of the point sources S_1 and S_2 and the laser, arising from the surface displacements and strains, will have to be considered in determining the fringe formation.

Define the terms:

r_{L1} ... optical path length from the laser to S_1 on the specimen surface

r_{L2} ... optical path length from the laser to S_2 on the specimen surface

Δr_{L1} ... increase in r_{L1} due to the displacement of S_1

Δr_{L2} ... increase in r_{L2} due to the displacement of S_2

r_{ij} ... optical path length from S_j to Q in the image plane through aperture i

r_{eij} ... increase in r_{ij} due to the displacement of S_j

It is sufficient, for now, to look at the case where $\Delta y_s > D_{ss}$ and, therefore, we need to consider only two optical paths. One path is from the laser to S_1 and from S_1 through aperture 2 to Q in the image plane. The other path is from the laser to S_2 and from S_2 through aperture 1 to Q in the image plane. As before, let us define Δ_1 and Δ_2 as the differences between these two paths in the two exposures and Δ_{12} as the relative change between the two optical paths.

$$\Delta_1 = (r_{L1} + r_{21}) - (r_{L2} + r_{12})$$

$$\Delta_2 = (r_{L1} + \Delta r_{L1} + r_{21} + r_{e21}) - (r_{L2} + \Delta r_{L2} + r_{12} + r_{e12})$$

$$\Delta_{12} = \Delta_2 - \Delta_1 = \Delta r_{L1} - \Delta r_{L2} + r_{e21} - r_{e12}$$

A similar Δ_{12} could be formulated for the case $\Delta y_s < D_{ss}$. It is not necessary to do so, however, as the only purpose of the above exercise was to show the need to consider the changes in distances between points on the specimen surface and the laser in the analysis of fringe formation by the DASSC. It should be noted that the actual distances between the laser and points S_1 and S_2 are of no importance and, hence, will be arbitrarily defined as zero; therefore, equation (3.24) need not be altered.

When a specimen is deformed, its surface is, in general, displaced and strained both in and out-of-plane. The deformation changes the coordinates of the two points S_1 and S_2 , representing the surface, as follows

$$S_1(0, y_{S_1}, z_S) \rightarrow S_1^*(u, y_{S_1} + v, z_S + w)$$

$$S_2(0, y_{S_2}, z_S) \rightarrow S_2^*(u + \delta u, y_{S_2} + v + \delta v, z_S + w + \delta w)$$

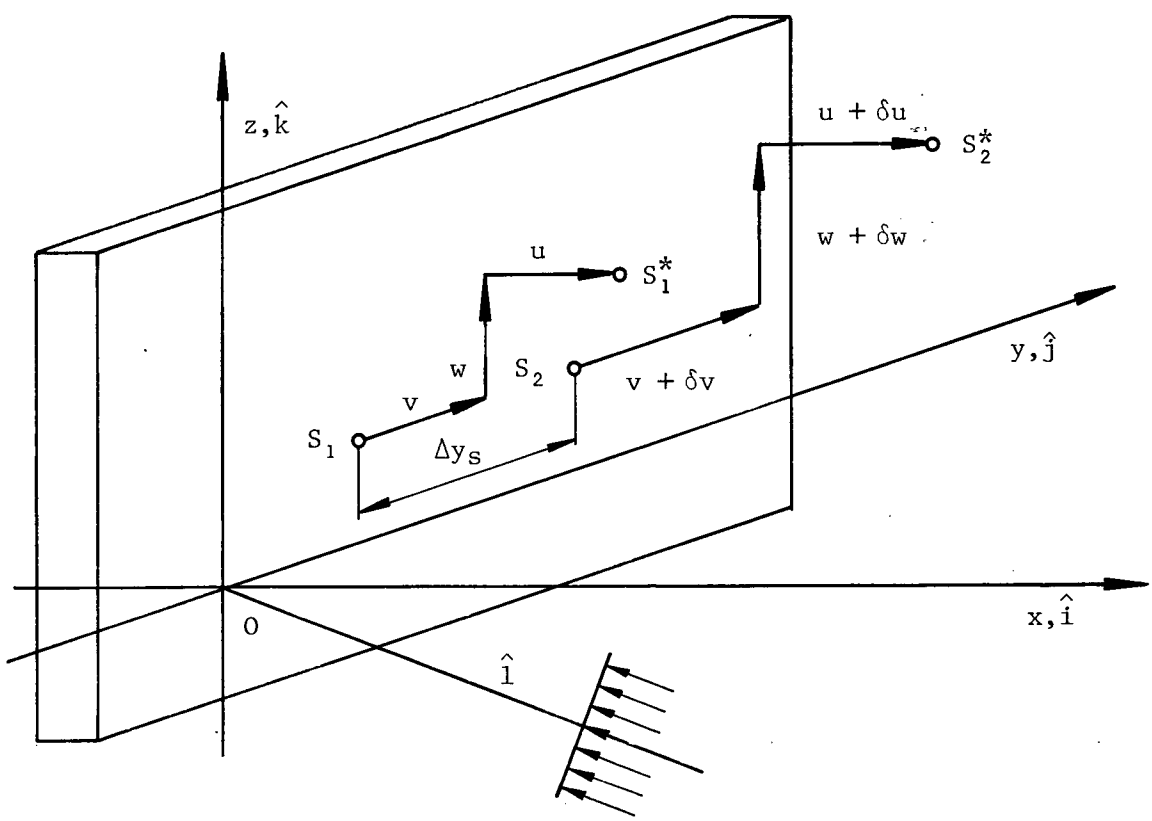

Fig. 3.14 General deformation of the specimen surface.

where δu , δv , and δw are defined as

$$\delta u = \frac{\partial u}{\partial y} \Delta y_s \qquad \delta v = \frac{\partial v}{\partial y} \Delta y_s \qquad \delta w = \frac{\partial w}{\partial y} \Delta y_s$$

Fig. 3.14 shows the specimen surface with the two points S_1 and S_2 during the two exposures. The surface is illuminated by a collimated laser light with its orientation defined by the "illumination" vector . The illumination vector $\hat{l}$ is a unit vector perpendicular to the illuminating plane wavefront and oriented from the specimen surface toward the laser. It makes angles θ_x, θ_y and θ_z with the x, y and z axes respectively; consequently $\hat{l}$ may be written as

$$\hat{l} = \cos\theta_x \hat{i} + \cos\theta_y \hat{j} + \cos\theta_z \hat{k}$$

Due to the displacements and strains, the increments Δr_{L1} and Δr_{L2} are given by

$$\Delta r_{L1} = (u\hat{i} + v\hat{j} + w\hat{k})\cdot(-\hat{l}) = -u\cos\theta_x - v\cos\theta_y - w\cos\theta_z$$

$$\Delta r_{L2} = \left[(u + \delta u)\hat{i} + (v + \delta v)\hat{j} + (w + \delta w)\hat{k}\right]\cdot(-\hat{l})$$

$$= -(u + \delta u)\cos\theta_x - (v + \delta v)\cos\theta_y - (w + \delta w)\cos\theta_z$$

$$= \Delta r_{L1} - \delta u \cos\theta_x - \delta v \cos\theta_y - \delta w \cos\theta_z$$

We are now in a position to calculate r_{eij} and I_r ; first, the case $\Delta y_s > D_{ss}$ is considered. r_{e12} and r_{e21} , accurate to $\lambda/10$, are derived in Appendix P as

$$r_{e12} = \frac{\beta_1 \underline{r}^2}{2X_S} + \underline{r}\left[\left(\frac{Y_D - Y_S}{X_S} - \frac{Y_S - y_A}{X_S}\frac{u + \delta u}{X_S} - (1 + \beta_1)\frac{v + \delta v}{X_S}\right)\cos\theta + \right.$$

$$\left. + \left(\frac{Z_D - Z_S}{X_S} - \frac{Z_S}{X_S}\frac{u + \delta u}{X_S} - (1 + \beta_1)\frac{w + \delta w}{X_S}\right)\sin\theta\right] +$$

$$+ \Delta r_{L_1} - \delta u \cos\theta_x - \delta v \cos\theta_y - \delta w \cos\theta_z$$

$$r_{e21} = \frac{\beta_1 \underline{r}^2}{2X_S} + \underline{r}\left[\left(\frac{Y_D - Y_S}{X_S} - \frac{Y_S + y_A}{X_S}\frac{u}{X_S} - (1 + \beta_1)\frac{v}{X_S}\right)\cos\theta + \left(\frac{Z_D - Z_S}{X_S} - \right.\right.$$

$$\left.\left. - \frac{Z_S}{X_S}\frac{u}{X_S} - (1 + \beta_1)\frac{w}{X_S}\right)\sin\theta\right] + \Delta r_{L_1} - D(p - \xi^*)$$

where ξ^* is defined in Appendix P . Note that now when we are considering DASSC the optical path length variations r_{eij} are functions of both the displacements and their increments related to the surface strains, whereas when DASC was considered r_{eij} were functions of displacements only. I_r is calculated in Appendix Q as

$$I_r = \left(\frac{a}{\underline{r}_0}\right)^2 \frac{T}{2}\left[R_1 + R_2\cos^2\frac{k}{2}\left(D(p - \xi^*) + \Delta^*\right) + \right.$$

$$\left. + R_3 \sin k\left(D(p - \xi^*) + \Delta^*\right)\right] \qquad (3.25)$$

I_r consists of three terms containing R_1 ,R_2 and R_3 defined in Appendix Q and Δ^* is defined in Appendix P. The first term R_1 may be thought of as a low frequency background noise; the second term R_2 is likely to have the largest magnitude of the three terms and is modulated by the cosine term producing the speckle grid; finally, the third term R_3 is likely to be of lower magnitude than the second term and it is also modulated by a grid

producing term (but) of twice the frequency than the second term. Therefore, in the sense of I_r acting as a diffraction grating of pitch G_s, it is described by the term

$$\cos^2\frac{k}{2}\left[D(p - \xi^*) + \Delta^*\right] = \cos^2\frac{kD}{2}\left[p - \xi^* + \frac{\Delta^*}{D}\right]$$

In the above speckle grid term, the presence of ξ^* and Δ^* is due to the specimen deformation that took place between the two exposures. Through a comparison of the speckle grid terms in the two exposures it is obvious that the second exposure speckle grid has been "shifted" by an amount $\xi^* - \frac{\Delta^*}{D}$ with respect to the first exposure grid. From this "shift" of the speckle grid the Moire number is calculated in Appendix R as

$$n(y,z) = -\frac{D}{\lambda X_s}\left(\frac{y}{x_s}u + v - \frac{yz}{x_s^2}w\right) - \frac{\Delta y_s}{\lambda}\left[(1 + \cos\theta_x)u,_y - \right.$$

$$\left. - \left(\frac{y - D/2}{x_s} - \cos\theta_y\right)v,_y - \left(\frac{z}{x_s} - \cos\theta_z\right)w,_y\right] \qquad (3.26)$$

Equation (3.26) is a close approximation of a more complicated "exact" equation derived in Appendix R . The "exact" equation is of little interest to us, though, as it contains a number of higher order terms which contribute negligibly to the equation; the accuracy of equation (3.26) should be sufficient for ordinary laboratory testing. As in the case of DASC, equation (3.26) is valid as long as the speckles recorded during the two exposures overlap. The equations constraining the size of specimen deformation are derived in Appendix S as

$$\left(\frac{y - D/2}{X_s}(u + \delta u) + v + \delta v\right)^2 + \left(\frac{z}{X_s}(u + \delta u) + w + \delta w\right)^2 < \frac{D_{ss}^2}{2} \qquad (3.27a)$$

$$\left(\frac{y + D/2}{X_s} u + v\right)^2 + \left(\frac{z}{X_s} u + w\right)^2 < \left(\frac{D_{ss}}{2}\right)^2 \tag{3.27b}$$

The addition of the speckles recorded in the double exposure process is of the same nature as in DASC and therefore need not be examined again.

Let us now consider the case $\Delta y_s < D_{ss}$. In this case the parameters q and β_1 are so small that r_{e12} and r_{e21}, accurate to $\lambda/10$ and derived for the preceeding case ($\Delta y_s > D_{ss}$), may be approximated as

$$r_{e12} = \underline{r}\left[\left(\frac{Y_D - Y_S}{X_s} - \frac{Y_S - y_A}{X_s}\frac{u + \delta u}{X_s} - \frac{v + \delta v}{X_s}\right)\cos\theta + \left(\frac{Z_D - Z_S}{X_s} - \right.\right.$$

$$\left.\left. - \frac{Z_S}{X_s}\frac{u + \delta u}{X_s} - \frac{w + \delta w}{X_s}\right)\sin\theta\right] + \Delta r_{L1} - \delta u \cos\theta_x - \delta v \cos\theta_y - \delta w \cos\theta_z$$

$$r_{e21} = \underline{r}\left[\left(\frac{Y_D - Y_S}{X_s} - \frac{Y_S + y_A}{X_s}\frac{u}{X_s} - \frac{v}{X_s}\right)\cos\theta + \left(\frac{Z_D - Z_S}{X_s} - \frac{Z_S}{X_s}\frac{u}{X_s} - \frac{w}{X_s}\right)\sin\theta\right] +$$

$$+ \Delta r_{L_1} - D(p - \xi^*)$$

In addition to r_{e12} and r_{e21} , r_{e11} and r_{e22} were derived in Appendix P and the results (accurate to $\lambda/10$) are presented here.

$$r_{e11} = \underline{r}\left[\left(\frac{Y_D - Y_S}{X_s} - \frac{Y_S - y_A}{X_s}\frac{u}{X_s} - \frac{v}{X_s}\right)\cos\theta + \left(\frac{Z_D - Z_S}{X_s} - \frac{Z_S}{X_s}\frac{u}{X_s} - \frac{w}{X_s}\right)\sin\theta\right] +$$

$$+ \Delta r_{L1} - \alpha^* + \beta_{11}$$

$$r_{e22} = \underline{r}\left[\left(\frac{Y_D - Y_S}{X_s} - \frac{Y_S + y_A}{X_s}\frac{u + \delta u}{X_s} - \frac{v + \delta v}{X_s}\right)\cos\theta + \left(\frac{Z_D - Z_S}{X_s} - \right.\right.$$

$$\left.\left. - \frac{Z_S}{X_s}\frac{u + \delta u}{X_s} - \frac{w + \delta w}{X_s}\right)\sin\theta\right] + \Delta r_{L1} + \alpha^* + \beta_{22} - D(p - \xi^*)$$

In the r_{eij} above, the parameters β_{11} and β_{22} are defined in Appendix P . I_r is derived in Appendix Q as

$$I_r = 16I_0\left(\frac{J_1(\rho)}{\rho}\right)^2\left[Q_1 + Q_2\cos^2\frac{k}{2}\left(D(p - \xi^*) - \alpha^* + \frac{\beta_{11} - \beta_{22}}{2}\right)\right] \tag{3.28}$$

I_r again contains the low frequency background noise term called here Q_1 and another low frequency term Q_2 which is modulated so that the speckle grid is produced again. Q_1 and Q_2 are defined in Appendix Q . The Moire number is obtained in Appendix R by relating the shift between the two exposure speckle grid terms as

$$n(y,z) = -\frac{D}{\lambda X_s}\left[\left(\frac{y}{x_s}u + v - \frac{yz}{x_s^2}w\right) + \Delta y_s\left(\frac{y}{2x_s}u_{,y} + \frac{1}{2}v_{,y} - \frac{yz}{x_s^2}w_{,y}\right)\right] \tag{3.29}$$

Equations similar to equation (3.27) could be derived again. However, as four speckles would have to be considered, four equations of constraint would have to be derived. With the case $\Delta y_s < D_{ss}$ of little practical interest and because the system is so much more sensitive to displacements than to strains, it is sufficient to use equation (3.17), derived for DASC, as a guide.

The results of this section may be summarized by the following: When DASSC is used to record the displacement and strain fields of a laser illuminated specimen surface the Moire fringes will be produced according to equation (3.26) which is applicable as long as the lateral shear $\Delta y_s > D_{ss}$. If $\Delta y_s < D_{ss}$, the Moire fringes will be produced according to equation (3.29). The surface displacements and strains must be sufficiently small to satisfy equation (3.27) for the case $\Delta y_s > D_{ss}$, and equation (3.17) is used as a guide for the $\Delta y_s < D_{ss}$ case.

3.7 Imaging of Real Surfaces by DASC and DASSC

Equations (2.18) and (2.19) were derived for a coherent interferometer with one point source. When a real, diffusely reflecting surface is considered, these, and other equations must be modified to take into account all the light reaching a point (Q) in the image plane. This is done by integrating over the illuminated area of the specimen, and consequently equation (2.14) becomes

$$\bar{E}_r(t) = \int_{A_s}\int_{A_a} \frac{a\ \hat{e}(y_a,z_a)}{r(y,z,y_a,z_a)} \cos\left[\bar{k}(y_a,z_a)\cdot\bar{r}(y,z,y_a,z_a) - \omega t + \psi(y,z)\right] dA_s dA_a \quad (3.30)$$

where A_s is the part of the area of the specimen surface illuminated by a laser light, A_a is the aperture(s) area, y_a, z_a are the aperture coordinates and y,z are the specimen coordinates. Note that $\bar{r}$ and ψ are functions of the specimen surface coordinates. As in Section 2.13 we consider such an interferometer where all the rays reaching point Q are nearly parallel, and r_0 denotes some typical object-image distance. Equation (3.30) is then written as

$$\bar{E}_r(t) = \int_{A_s}\int_{A_a} \frac{a}{r_0} \cos\left[kr(y,z,y_a,z_a) - \omega t + \psi(y,z)\right] dA_s\, dA_a \quad (3.31)$$

Assuming that all the points on the specimen surface reflect (radiate) light with nearly the same amplitude $a \simeq a_0$, the recorded intensity I_r is approximately given by

$$I_r \simeq \left(\frac{a_0}{r_0}\right)^2 \frac{T}{2}\left(\int_{A_s}\int_{A_a} e^{ikr_e}\, dA_s\, dA_a\right)\left(\int_{A_s}\int_{A_a} e^{-ikr_e}\, dA_s\, dA_a\right) \quad (3.32)$$

where $\quad r_e(y,z,y_a,z_a) = r(y,z,y_a,z_a) - r_0$

We know, from the analysis of the image formation by DASC, that the recorded intensity distribution (due to a point source) is of a significant amplitude only within the speckle perimeter D_s . It is therefore sufficient to confine the integration over the specimen surface to an area of approximately diameter D_{ss} about the particular point under consideration. $r_e(y,z,y_a,z_a)$ and $\psi(y,z)$ may then be related to the (microscopic) surface geometry, and specimen illumination, and I_r is calculated from equation (3.32). Unfortunately, in most instances the surface geometry is not known, and since any real surfaces are extremely rough on the scale of an optical wavelength, no smooth-surface approximations are possible and it is necessary to rely on statistics to derive an amplitude, intensity and phase of a speckle.

The statistical properties of laser speckle patterns were studied by J. W. Goodman [43] and others, with results agreeing with the experimental observation that the "speckle pattern moves as the source is moved" [43] . Alternatively, it could be said that when the surface is moved, the speckle pattern moves with it, providing the illumination remains unchanged. Depending on the type of the motion of the speckle, the phase of the speckle observed at a point will change accordingly. The phase variation of the whole speckle then may be approximated by a phase variation of a single "typical" point - a point source(s) used in this chapter. We may therefore assume that equations (3.20) , (3.26) and (3.29) derived for a point source, should also describe the fringe formation by the two cameras when they are used to image real diffusely reflecting surfaces. The results of a number of experiments described in Chapter 6. were found to support the validity of this assumption.

The approximation of the speckle by a point source fails, however, to explain the sensitivity of DASC or DASSC to the out-of-plane tilts of the

specimen surface. It was noted and discussed by A. E. Ennos [43] who determined the maximum allowable surface tilt angle $\delta\Psi$ as

$$\delta\Psi < \frac{M}{(1 + M)F}$$

where F is the aperture ratio of the lens, (f/d), and M is the system magnification. Using the notation of this thesis the maximum permissible surface tilt angle is given by

$$\delta\Psi < \frac{d}{x_i} \tag{3.33}$$

4. CALCULATION OF DISPLACEMENTS AND STRAINS.

4.1 Preliminary Remarks

The objective of Chapter 3 was to derive an expression n(y,z) describing the fringe pattern due to a general deformation of a specimen surface. The objective of this chapter is just the opposite, namely, the derivation of various methods of calculating the unknown surface deformation from a given pattern.

When DASC or DASSC is used to record the deformation of the specimen surface, the end product is a photographic recording or recordings, showing a fringe pattern superimposed on the specimen surface. This fringe pattern is in fact "our" function n(y,z). When testing materials, a reseacher usually has some knowledge about the size of displacements and strains that are likely to occur during the testing. This knowledge may come from the theoretical considerations of the test, from direct measurements, or from similar testing done previously by the reseacher. Knowing that the two cameras form fringes according to equations (3.20) and (3.26) and having some knowledge about the specimen deformation, the reseacher is able to assign numerical values to the fringes that make up the fringe pattern. Often this is a trial and error procedure and, usually, only the fringe centers are numbered and located; if a continuous n(y,z) is desirable, a suitable curve fitting technique may be used. Alternatively, n(y,z) may be determined with reasonable accuracy at any point on the surface with the knowledge that the fringe density variation is close to the $\cos^2$ type of variation. In any case, n(y,z) must be uniquely "numbered" by the reseacher before any calculations of the unknown surface displacements and strains are attempted.

It is desirable to be able to determine the specimen deformation using the smallest possible number of photographs. It will be shown that usually

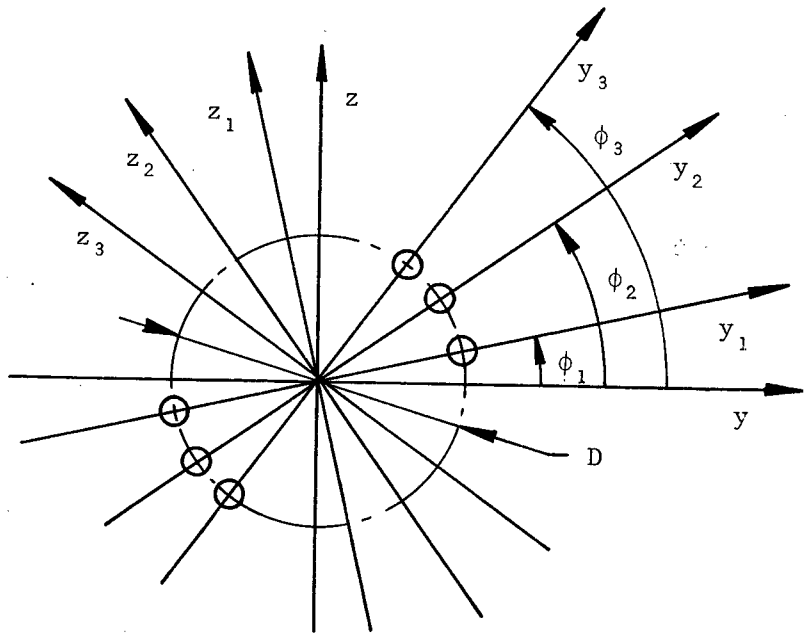

Fig. 4.1 Normal view of the aperture plane.

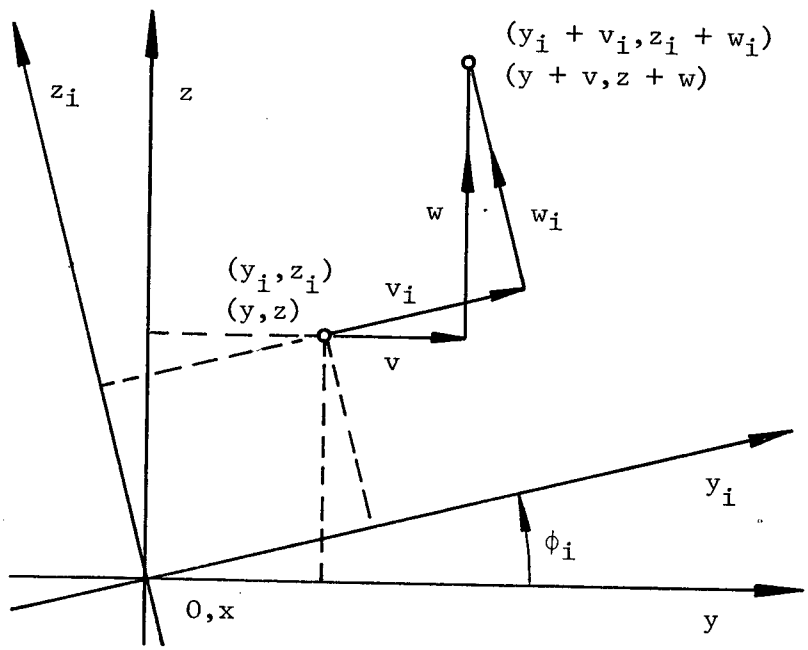

Fig. 4.2 Normal view of the specimen showing coordinate systems y,z and y_i, z_i .

no more than three photographs obtained by DASC or DASSC are needed, and in certain cases of specimen deformation only one or two photographs are sufficient. The calculation of the surface displacements from the photographs obtained by DASC will be discussed first and then calculations involving the use of DASSC will be considered.

4.2 Use of DASC to Measure General Deformation

The fringes are formed by DASC according to equation (3.20) which relates the in and out-of-plane surface displacements u(y,z),v(y,z) and w(y,z) to the fringe pattern function n(y,z).

$$n(y,z) = -\frac{D}{\lambda x_s}\left(\frac{y}{x_s}u + v - \frac{yz}{x_s^2}w\right) \tag{3.20}$$

Treating n(y,z) as a known function, we wish to determine the unknown displacements u,v and w. Since u,v and w are independent, three independent equations like equation (3.20) are required to provide a unique solution. By varying the parameters D,λ and x_s we can obtain different patterns n(y,z); however, these would all be linearly dependent. One possible way of producing three independent patterns n(y,z) is to "photograph" the specimen deformation with a camera having three aperture sets with different rotations in the y,z plane as is shown in Fig. 4.1 .

The surface displacements and the three fringe patterns obtained by recording the specimen deformation through the three sets of apertures are related by equation (4.1).

$$\frac{y_i}{x_s}u_i(y_i,z_i) + v_i(y_i,z_i) - \frac{y_i z_i}{x_s^2}w_i(y_i,z_i) = -\frac{\lambda x_s}{D_i^*}n_i(y_i,z_i) \tag{4.1}$$

$$i = 1,2,3$$

In equation (4.1) u_1 ,v_1 , and w_1 are the three components of the displacement vector along the x,y_1 , and z_1 axes, and similarly u_2 ,v_2 , and w_2 are the displacement components along the x,y_2 , and z_2 axes and so on. D_i^* is the aperture separation D for the case where $\phi = \phi_i$. From Fig. 4.2 it is apparent that the coordinate systems y,z and y_i ,z_i are related as

$$y_i = y \cos\phi_i + z \sin\phi_i \tag{4.2a}$$

$$z_i = - y \sin\phi_i + z \cos\phi_i \tag{4.2b}$$

At the same point on the specimen surface the displacement components u_i ,v_i , and w_i are related to the components u,v and w by

$$u_i(y_i,z_i) = u(y,z) \tag{4.3a}$$

$$v_i(y_i,z_i) = v(y,z)\cos\phi_i + w(y,z)\sin\phi_i \tag{4.3b}$$

$$w_i(y_i,z_i) = - v(y,z)\sin\phi_i + w(y,z)\cos\phi_i \tag{4.3c}$$

where the (y_i,z_i) are related to (y,z) by equations (4.2a) and (4.2b). Substitution of equations (4.2) and (4.3) in equation (4.1) yields

$$a_i u(y,z) + b_i v(y,z) + c_i w(y,z) = N_i(y,z) \qquad i = 1,2,3 \tag{4.4}$$

where a_i ,b_i ,c_i , and N_i are defined as

$$a_i = \frac{y_i}{x_s} \tag{4.5a}$$

$$b_i = \cos\phi_i + \frac{y_i z_i}{x_s^2} \sin\phi_i \tag{4.5b}$$

$$c_i = \sin\phi_i - \frac{y_i z_i}{x_s^2} \cos\phi_i \tag{4.5c}$$

$$N_i(y,z) = - \frac{\lambda x_s}{D_i^*} n_i(y_i,z_i) \tag{4.5d}$$

where, again, the (y_i,z_i) are related to (y,z) by equations (4.2). Provided the determinant of the coefficients of the set of equations (4.4) is not

equal to zero, the set may be solved for the unknown displacements u,v, and w for any value of (y,z). Thus, a minimum of three photographs must be taken and processed to obtain three fringe pattern functions $n_i(y,z)$ to determine the general three dimensional surface deformation.

When the deformation of the specimen is of a special nature, such as plain strain deformation where the out-of-plane displacement vanishes, it may be possible to determine some displacement components from only one or two photographs. The examination of some of these special cases follows.

4.3 Use of DASC to Measure Plane Strain and Plane Stress Deformation

Under these circumstances the out-of-plane displacement u of the specimen surface is zero, or so small compared to the in-plane displacements that it does not contribute significantly to the formation of fringes, and the term $a_i u$ in equation (4.4) may be neglected. Then, only two photographs of the deformation are required through two sets of apertures rotated by ϕ_1 and ϕ_2; v(y,z) and w(y,z) may be solved from equation (4.6)

$$b_i v(y,z) + c_i w(y,z) = N_i(y,z) \qquad i = 1,2 \tag{4.6}$$

If the magnitudes of the in-plane displacements v_i and w_i are of the same order so that $|v_i| >> \left| \frac{y_i z_i}{x_s^2} w_i \right|$ over most of the specimen surface being photographed, the term $\frac{y_i z_i}{x_s^2} w_i$ may be neglected, and v_i can be determined from a single photograph taken by DASC using one set of apertures rotated by ϕ_i . With terms involving u_i and w_i neglected, equation (4.1) becomes

$$v_i(y_i,z_i) \simeq -\frac{\lambda x_s}{D_i^*} n_i(y_i,z_i) \tag{4.7}$$

It is obvious that v_i is given by equation (4.7) with the absolute error equal to the sum of the $\frac{y_i}{x_s} u_i$ and $-\frac{y_i z_i}{x_s^2} w_i$ terms. If this absolute error is

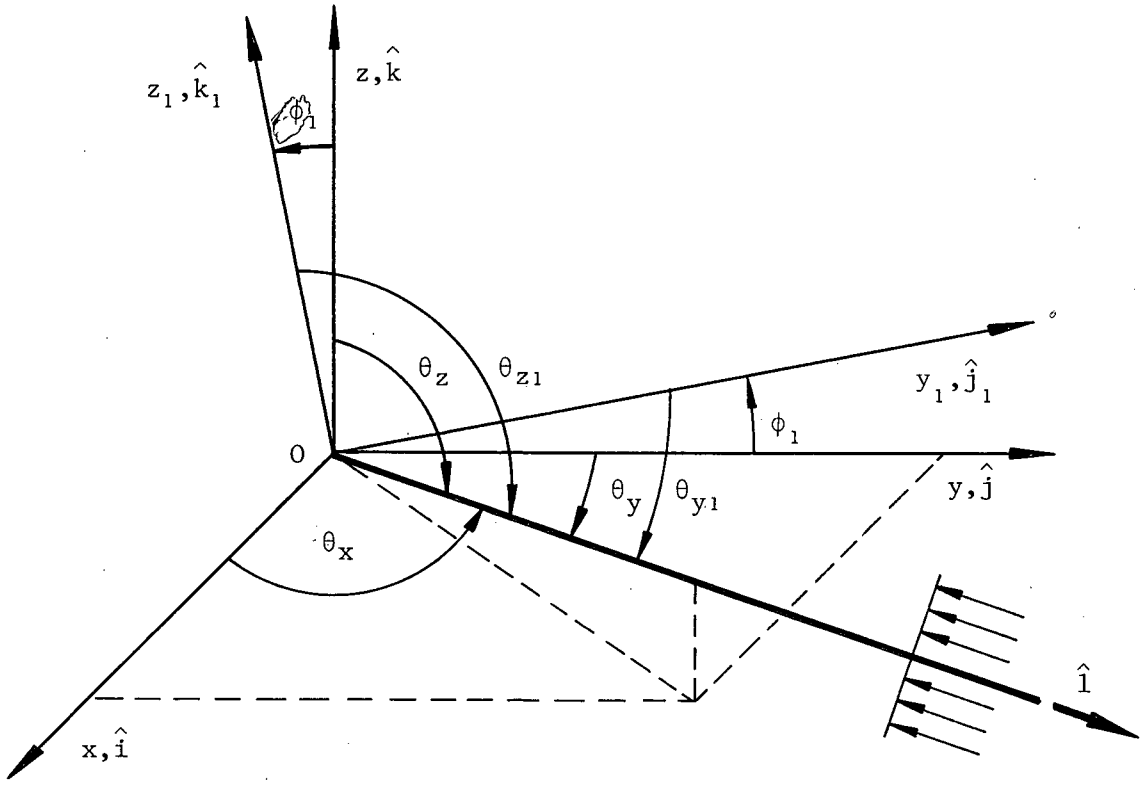

Fig. 4.3 Geometry of specimen illumination.

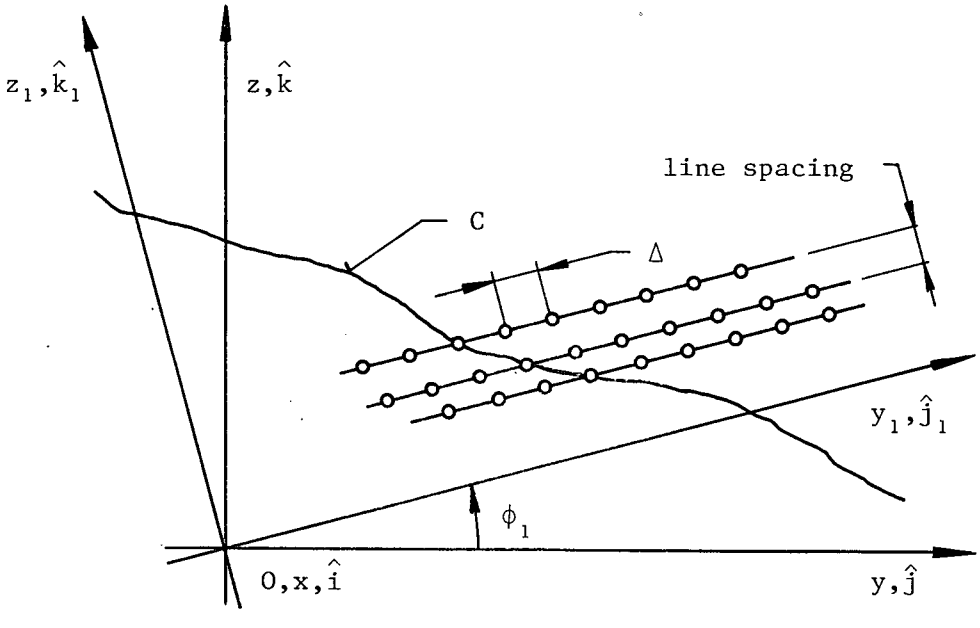

Fig. 4.4 Rotated coordinate system.

acceptable equation (4.7) should be used, with the understanding that it may result in large relative errors at those points of the specimen surface where $v_i(y_i,z_i)$ is small or zero.

While equation (4.7) relates $v_i(y_i,z_i)$ to $n_i(y_i,z_i)$ nothing is determined about the other two displacement components $u_i(y_i,z_i)$ and $w_i(y_i,z_i)$. For the important case of $\phi_i = 0^o$ equation (4.7) becomes

$$v(y,z) \simeq -\frac{\lambda x_s}{D} n(y,z) \tag{4.8a}$$

If w(y,z) is to be determined, rather than v(y,z), an aperture set rotated by $\phi = 90^o$ is used and w(y,z) is determined from

$$w(y,z) \simeq -\frac{\lambda x_s}{D} n(y,z) \tag{4.8b}$$

This time the displacement components u(y,z) and v(y,z) remain undetermined. Similar considerations pertaining to accuracy that were made about equation (4.7) apply to equations (4.8a) and (4.8b).

4.4 Use of DASC to Measure Out-of-Plane Bending

The out-of-plane bending of the specimen surface is usually accompanied by small in-plane displacements. If these displacements contribute negligibly to the formation of fringe patterns, that is if $\left|\frac{y_i}{x_s} u_i(y_i,z_i)\right| >> |v_i(y_i,z_i)|$, $\left|\frac{y_i z_i}{x_s^2} w_i(y_i,z_i)\right|$ over most of the specimen surface being photographed, the two terms involving v_i and w_i may be neglected in equation (4.1). Under these circumstances one can determine the out-of-plane displacement field quite accurately from one photograph of the specimen surface, by using DASC having a set of apertures rotated by $\phi = \phi_i$. With the terms involving v_i and w_i

neglected, equation (4.1) reduces to

$$\frac{y_i}{x_s} u_i(y_i,z_i) \simeq - \frac{\lambda x_s}{D_i^*} n_i(y_i,z_i) \tag{4.9}$$

The term $\frac{y_i}{x_s} u_i(y_i,z_i)$ is given by equation (4.9) with the absolute error equal to the sum of the two neglected terms $v_i(y_i,z_i)$ and $\frac{y_i z_i}{x_s^2} w_i(y_i,z_i)$. This may again cause large relative errors in the calculated $\frac{y_i}{x_s} u_i(y_i,z_i)$ term in those regions of the specimen surface where this term is small or equal to zero. From equation (4.9) $u_i(y_i,z_i)$ is calculated as

$$u_i(y_i,z_i) \simeq - \frac{\lambda x_s^2}{D_i^*} \frac{n_i(y_i,z_i)}{y_i} \qquad y_i \neq 0 \tag{4.10a}$$

Equation (4.10a) relates the out-of-plane displacement field $u_i(y_i,z_i)$ to the fringe pattern function $n_i(y_i,z_i)$. The in-plane displacements v_i and w_i remain undetermined. Due to the peculiar form of equation (4.10a), a small error in $n_i(y_i,z_i)$ may cause a large error in the calculated u_i when y_i is small.

For the case of $\phi = 0^o$ equation (4.10a) becomes

$$u(y,z) \simeq - \frac{\lambda x_s^2}{D} \frac{n(y,z)}{y} \qquad y \neq 0 \tag{4.10b}$$

Equation (4.10b) relates the out-of-plane displacement field u(y,z) to the fringe pattern function n(y,z). The in plane displacements v and w remain undetermined. Similar considerations pertaining to accuracy that were made about equation (4.10a) apply to equation (4.10b). There are certainly other "special" cases where one or two photographs taken by DASC may be used to calculate some components of the specimen deformation. However, the general case and the two special cases ought to demonstrate sufficiently the use of

DASC as an experimental testing device. To test the validity of equation (3.20) and get the "feeling" for DASC several experiments were performed with a known specimen deformation. These experiments and the numerical results obtained from the photographs taken by DASC are presented in Chapter 6.

4.5 Use of DASSC to Measure Specimen Deformation - Theoretical Considerations

The fringes are formed by DASSC according to equations (3.26) or (3.29), depending on the size of the lateral shear used. We shall restrict our attention to the more practical case of $\Delta y_s > D_{ss}$, for which equation (3.26) is applicable.

$$n(y,z) = -\frac{D}{\lambda X_s}\left(\frac{y}{x_s}u + v - \frac{yz}{x_s^2}w\right) - \frac{\Delta y_s}{\lambda}\left[(1+\cos\theta_x)u_{,y} - \right.$$

$$\left. - \left(\frac{y-y_A}{x_s} - \cos\theta_y\right)v_{,y} - \left(\frac{z}{x_s} - \cos\theta_z\right)w_{,y}\right] \qquad (3.26)$$

Equation (3.26) relates the surface displacements and strains to the fringe pattern function n(y,z) and for $\Delta y_s = 0$, it reduces to equation (3.20) . Equation (3.26) may be written in the form similar to equation (4.1) as

$$\frac{y}{x_s}u + v - \frac{yz}{x_s^2}w + \frac{\Delta y_s X_s}{D}(1+\cos\theta_x)u_{,y} - \frac{\Delta y_s X_s}{D}\left(\frac{y-y_A}{x_s} - \cos\theta_y\right)v_{,y} -$$

$$- \frac{\Delta y_s X_s}{D}\left(\frac{z}{x_s} - \cos\theta_z\right)w_{,y} = -\frac{\lambda X_s}{D}n(y,z) \qquad (4.11)$$

A set of apertures rotated by ϕ_i with respect to the y,z coordinate system produces a fringe pattern according to

$$\frac{y_i}{x_s}u_i + v_i - \frac{y_i z_i}{x_s^2}w_i + \frac{\Delta y_{si}X_{si}}{D_i^*}(1+\cos\theta_{xi})u_{i,yi} - \frac{\Delta y_{si}X_{si}}{D_i^*}\left(\frac{y_i - y_{Ai}}{x_s} - \right.$$

$$\left.\cos\theta_{yi}\right)v_{i,yi} - \frac{\Delta y_{si}X_{si}}{D_i^*}\left(\frac{z_i}{x_s} - \cos\theta_{zi}\right)w_{i,yi} = \frac{\lambda X_{si}}{D_i^*}n_i(y_i,z_i)$$

This may be written in a more compact form as

$$A_i u_i + B_i v_i + C_i w_i + D_i u_{i,yi} + F_i v_{i,yi} + H_i w_{i,yi} = N_i(y_i, z_i) \qquad (4.12)$$

where the coefficients A_i ,...., H_i are defined as

$$A_i = \frac{y_i}{x_s}$$

$$B_i = 1$$

$$C_i = -\frac{y_i z_i}{x_s^2}$$

$$D_i = S_i(1 + \cos\theta_{xi})$$

$$F_i = S_i\left(\cos\theta_{yi} - \frac{y_i - y_{Ai}}{x_s}\right)$$

$$H_i = S_i\left(\cos\theta_{zi} - \frac{z_i}{x_s}\right)$$

$$N_i = -\frac{\lambda X_{si}}{D_i^*} n_i(y_i, z_i)$$

and S_i is defined as $\qquad S_i = \dfrac{\Delta y_{si} X_{si}}{D_i^*}$

In Appendix T it is shown that, when all quantities in equation (4.12) are transformed in the y,z system, equation (4.12) becomes

$$a_i u + b_i v + c_i w + d_i u,_y + e_i u,_z + f_i v,_y + \\ + g_i v,_z + h_i w,_y + k_i w,_z = N_i(y,z) \qquad (4.13)$$

In equation (4.13) the coefficients a_i, b_i, c_i are given by equation (4.5) and the coefficients $d_i, \ldots, k_i$ are given by

$$d_i = S_i(1 + \cos\theta_{xi})\cos\phi_i$$

$$e_i = S_i(1 + \cos\theta_{xi})\sin\phi_i$$

$$f_i = S_i\left[(r - \cos\theta_{zi})\sin\phi_i - (s - \cos\theta_{yi})\cos\phi_i\right]\cos\phi_i$$

$$g_i = S_i\left[(r - \cos\theta_{zi})\sin\phi_i - (s - \cos\theta_{yi})\cos\phi_i\right]\sin\phi_i$$

$$h_i = - S_i\left[(r - \cos\theta_{zi})\cos\phi_i + (s - \cos\theta_{yi})\sin\phi_i\right]\cos\phi_i$$

$$k_i = - S_i\left[(r - \cos\theta_{zi})\cos\phi_i + (s - \cos\theta_{yi})\sin\phi_i\right]\sin\phi_i$$

$$N_i = - \frac{\lambda X_{si}}{D_i^*} n_i(y_i, z_i)$$

with r and s defined as $r = \dfrac{z_i}{x_s}$

$$s = \frac{y_i - y_{Ai}}{x_s}$$

Due to a lack of equipment or for other reasons a situation may arise where the specimen illumination is in the x,y plane, i.e. $\theta_z = 90^\circ$ and $\cos\theta_z = 0$. For this special, but important, case of specimen illumination the coefficients f_i, g_i, h_i, k_i reduce to the following simpler forms as is shown in Appendix U.

$$f_i = S_i(r\sin\phi_i - s\cos\phi_i - \sin\theta_{xi})\cos\phi_i$$

$$g_i = S_i(r\sin\phi_i - s\cos\phi_i - \sin\theta_{xi})\sin\phi_i$$

$$h_i = - S_i(r\cos\phi_i + s\sin\phi_i)\cos\phi_i$$

$$k_i = - S_i(r\cos\phi_i + s\sin\phi_i)\sin\phi_i$$

Since $\left|\dfrac{y_i}{x_s}\right|, \left|\dfrac{z_i}{x_s}\right| < \dfrac{1}{5}$, it is obvious that the coefficients h_i and k_i will probably be very small (especially near origin) when compared to the other coefficients, consequently, the DASSC using the in-plane illumination will be relatively insensitive to the strains $w,_y$ and $w,_z$.

There are three displacements and six strain components in equation (4.13) and, if the specimen deformation is general in nature, all nine terms

contribute significantly. Equation (4.13) may be solved in two possible ways. One way is to regard strains and displacements as mutually independent and, consequently, nine equations (photographs) are needed to solve for the unknowns. The other way is to take advantage of the fact that equation (4.13) is really a set of partial differential equations and, if the required boundary conditions are readily available, a set of three equations (photographs) is sufficient to solve for all nine unknowns. The most advantageous approach to solving equation (4.13) depends greatly on a particular test situation but, in general, the first "algebraic" method of solving equation (4.13) should be undertaken only for special cases, and when there is no point or line of known displacements (boundary condition) on the specimen surface. When there is a point or a line of known displacements on the specimen surface the second method should be used.

4.6 Use of DASSC to Measure General Deformation (Algebraic Solution)

Nine independent equations (photographs) could be obtained by using a number of aperture sets of different inclination to the y-axis and by using different illuminating beams associated with each aperture set, etc. In principle, the resultant set of nine independent equations (4.13) could be solved for the nine displacements and strains; however, because of the unavoidable errors in the determination of the camera parameters and in the location of the fringes, this method of solution of equation (4.13) is so inaccurate as to be of little practical use. The method is reasonably accurate only when the specimen deformation is of a special kind, or only if the strains along a particular direction are to be calculated, since under such circumstances fewer photographs need to be "taken" and processed.

Using three aperture sets inclined by the same angle ϕ_1 to the y-axis, three illuminating beams, each associated with one aperture set, and two

photographic plates in series, one may calculate the three strain components from four photographs. Three of these photographs are recorded on one photographic plate and one photograph is recorded on the other plate. Fringe patterns in these photographs satisfy equation (4.12) as

$$R(y_1,z_1) + D_i u_{1,y_1} + F_i v_{1,y_1} + H_i w_{1,y_1} = N_i(y_1,z_1) \quad i = 1,2,3,4 \qquad (4.14a)$$

Equation (4.14a) may be solved for the three strains and the "displacement sum" $R(y_1,z_1)$ defined as

$$R(y_1,z_1) = A_1 u_1 + B_1 v_1 + C_1 w_1$$

When the illumination is in the x,y plane and the aperture sets are in the $\phi = 0^o$ position, the camera is insensitive to w and $w_{,y}$ for small values of z; if the term $H_i w_{1,y_1}$ is negligible, equation (4.14a) reduces to

$$R(y,z) + D_i u_{,y} + F_i v_{,y} = N_i(y,z) \quad i = 1,2,3 \qquad (4.14b)$$

Equation (4.14b) may be solved for the two strains $u_{,y}$, $v_{,y}$ and the "displacement sum" R(y,z) from three independent photographs, with the absolute error being most likely of the same order as the terms that were neglected.

4.7 Use of DASSC to Measure Plane Strain and Plane Stress Deformation (Algebraic Solution)

In the case of plane stress or strain where $|u_1| << |v_1|, |w_1|$, and v_1 and w_1 are such that $|v_1| >> \left| \frac{y_1 z_1}{x_s^2} w_1 \right|$ over most of the specimen surface being photographed, the displacement sum $R(y_1,z_1)$ to v_1. Therefore, in addition to the three strains, a reasonably accurate $v_1(y_1,z_1)$ is also calculated by solving the set of four equations (4.14). If the magnitudes of the in-plane strains are of similar order such that $|v_{,y}| > |w_{,y}|$, and if the illuminating beams are in the x,y plane and the aperture set rotations

ϕ are equal to zero, the term $H_i w,_y$ is so small that it may be neglected and equation (4.14b) is then closely approximated by

$$v + D_i u,_y + F_i v,_y = N_i(y,z) \qquad i = 1,2,3 \tag{4.15}$$

In this case, three independent photographs are sufficient for the solution of $v, u,_y$, and $v,_y$. At those points of the specimen surface where $v, v,_y$ or $u,_y$ are small or zero, these variables will be calculated from equation (4.15) with a large relative error, but are likely to be determined everywhere with an acceptable absolute error.

4.8 Use of DASSC to Measure Out-of-Plane Bending (Algebraic Solution)

In this case of specimen deformation the out-of-plane displacements and strains are usually much larger than the in-plane displacements and strains, so that

$$\left|\frac{y_1}{x_s} u_1\right| >> |v_1|, \left|\frac{y_1 z_1}{x_s^2} w_1\right| \qquad \text{(except for } y_1 \text{ small)}$$

$$|u_1,_{y_1}| >> |v_1,_{y_1}|, |w_1,_{y_1}|$$

and equation (4.12) may be closely approximated by

$$A_i u_1 + D_i u_1,_{y_1} = N_i(y_1, z_1) \qquad i = 1,2 \tag{4.16}$$

By using two independent photographs, one may calculate u_1 and $u_1,_{y_1}$ from equation (4.16) with the absolute error being probably of the same magnitude as the terms that were neglected. Due to the peculiar form of the coefficient A_i, a large error in u_1 should be expected where y_1 is small.

4.9 Use of DASSC to Measure General Deformation

The main purpose of deriving equation (4.13) was to show that a photograph taken through a set of rotated apertures displays a fringe pattern

which is due to a combination of the three displacements u,v, and w and the partial derivatives of these displacements with respect to both y and z. By using three aperture sets, each with different rotation ϕ, and by using three illuminating beams (at least one of them not in the x,y plane), three independent photographs may be obtained. If there is a line of known displacements u,v, and w (boundary condition) on the specimen surface it is possible, in principle, to solve the set of equations (4.13). For this the finite difference equations will be used.

The forward finite difference analogs for first order derivatives are

$$u,_y(y,z) = \frac{u(y + \Delta,z) - u(y,z)}{\Delta} \qquad u,_z(y,z) = \frac{u(y,z + \Delta) - u(y,z)}{\Delta}$$

where Δ is the grid spacing in both y and z directions. By replacing the partial derivatives with these finite difference analogs equation (4.13) becomes

$$\left(a_i - \frac{d_i}{\Delta} - \frac{e_i}{\Delta}\right) u(y,z) + \frac{d_i}{\Delta} u(y + \Delta,z) + \frac{e_i}{\Delta} u(y,z + \Delta) + \ldots.$$

$$= N_i(y,z) \qquad i = 1,2,3 \qquad (4.17)$$

If the displacements u,v, and w are known, for example, along the line $z = z_0$ then the displacements may be found row by row from

$$e_i u(y,z + \Delta) + g_i v(y,z + \Delta) + k_i w(y,z + \Delta) =$$

$$N_i - (a_i\Delta - d_i - e_i)u(y,z) - \ldots\ldots \qquad i = 1,2,3 \qquad (4.18)$$

$$\begin{vmatrix} e_1 & g_1 & k_1 \\ e_2 & g_2 & k_2 \\ e_3 & g_3 & k_3 \end{vmatrix} \neq 0$$

Similar equations could be written for the case of the boundary condition being a line $y = y_0$ or an inclined straight line. A set of three photographs

obtained by a computer simulation of the DASSC was solved by using equation (4.18) and it was found that solution tended to diverge rather quickly with increasing distance from the boundary condition line. In contrast to this, a finite difference scheme based on equation (4.12) was found to be much more accurate and only slowly diverging. As equation (4.12) involves partial derivatives with respect to y_i only, the integration starts at a point on the boundary condition line and progresses away along a line z_i = constant as is shown in Fig. 4.4 .

The partial derivatives in equation (4.12) are replaced by their backward difference analogs and, with these, equation (4.12) may be written as

$$(A_i\Delta + D_i)u_i(y_1,z_1) + (B_i\Delta + F_i)v_1(y_1,z_1) + (C_i\Delta + H_i)w_1(y_1,z_1) = R_i \quad i = 1,2,3 \qquad (4.19)$$

where R_i is defined as

$$R_i = N_i(y_1,z_1)\Delta + D_i u_1(y_1 - \Delta,z_1) + F_i v_1(y_1 - \Delta,z_1) + H_i w_1(y_1 - \Delta,z_1)$$

$$\begin{vmatrix} (A_1\Delta + D_1) & (B_1\Delta + F_1) & (C_1\Delta + H_1) \\ (A_2\Delta + D_2) & (B_2\Delta + F_2) & (C_2\Delta + H_2) \\ (A_3\Delta + D_3) & (B_3\Delta + F_3) & (C_3\Delta + H_3) \end{vmatrix} \neq 0 \qquad (4.20)$$

To satisfy equation (4.20) three illuminating beams are needed and the DASSC shutter must have three sets of apertures inclined at the angle ϕ_1 with respect to the y axis. The advantage of this approach is that the boundary condition line C need not be straight and, since the finite differences are along a line, it is possible to vary line spacing as well. A further advantage of this approach is the smaller size of the equations and the fact that all three coefficients D_i, F_i, and H_i may be adjusted to be of the same magnitudes by a suitable choice of the aperture

rotation angle ϕ_1 . The programming of this scheme is also simple.

If some of the displacement fields u,v, and w are known or determined by other means, the terms containing the known displacement and its derivative are put on the right side of the equations and the reduced set is then solved; for example, if u is known, equation (4.19) is reduced to

$$(B_i\Delta + F_i)v_1(y_1,z_1) + (C_i\Delta + H_i)w_1(y_1,z_1) = R_i \qquad i = 1,2 \qquad (4.21)$$

where R_i is now defined as

$$R_i = N_i(y_1,z_1)\Delta - A_i\Delta u_1(y_1,z_1) - D_i\Delta u_{1,y_1}(y_1,z_1) + F_i v_1(y_1,z_1) + H_i w_1(y_1,z_1)$$

$$\begin{vmatrix} (B_1\Delta + F_1) & (C_1\Delta + H_1) \\ (B_2\Delta + F_2) & (C_2\Delta + H_2) \end{vmatrix} \neq 0$$

Once u_1,v_1 and w_1 are found over the specimen area these displacements may be transformed into the y,z coordinate system to u,v and w , and through numerical differentiation (using central finite differences for example) the strains $u,_y$,$u,_z$ ..., $w,_z$ are obtained.

There may be other methods or choices of DASSC parameters which would permit solution of either equation (4.12) or equation (4.13) for a general case of deformation but, before any of these methods are used, their sensitivity to the inaccuracies in measurement of DASSC parameters and fringe locations should be established. In practice, the fringe locations and the size of DASSC parameters may be determined with only a limited accuracy, a fact which may make some numerical schemes rather useless.

4.10 Use of DASSC to Measure $u,u,_y$,v, and $v,_y$ from Two Photographs

When a specimen illumination is in the x,y plane and the aperture sets are at zero inclination to the y-axis ($\phi = 0^o$), the terms in equation (4.12) involving w and $w,_y$ are often so small that they may be neglected (especially

for z small) and it is then possible to solve for u and v from two independent photographs as follows:

$$\frac{y}{x_s} u + v - \underbrace{\cancel{\frac{yz}{x_s^2} w}}_{\simeq 0} + d_j u_{,y} + f_j v_{,y} + \underbrace{\cancel{h_j w_{,y}}}_{\simeq 0} = N_j \qquad j = 1,2 \tag{4.22}$$

Replace equations (4.22) by a set of finite difference equations, using the forward finite difference analogs of the first derivatives which may be written, using finite difference notation as

$$u_{,yi} = \frac{u_{i+1} - u_i}{\Delta} \qquad\qquad v_{,yi} = \frac{v_{i+1} - v_i}{\Delta}$$

With these analogs equation (4.22) becomes

$$\frac{y_i}{x_s} u_i + v_i + d_j \frac{u_{i+1} - u_i}{\Delta} + f_j \frac{v_{i+1} - v_i}{\Delta} = N_j \qquad j = 1,2 \tag{4.23}$$

Equation (4.23) is solved for the unknowns u_{i+1} and v_{i+1}

$$\begin{aligned} u_{i+1} &= U_{1i} + U_{2i} u_i + U_{3i} v_i \\ v_{i+1} &= V_{1i} + V_{2i} u_i + V_{3i} v_i \end{aligned} \tag{4.24}$$

where the coefficients U_{1i} ..., V_{3i} are given by

$$U_{1i} = -r(N_1 f_2 - N_2 f_1) \qquad\qquad V_{1i} = r(N_1 d_2 - N_2 d_1)$$

$$U_{2i} = -r(f_1 - f_2)\frac{y_i}{x_s} + 1 \qquad\qquad V_{2i} = r(d_1 - d_2)\frac{y_i}{x_s}$$

$$U_{3i} = -r(f_1 - f_2) \qquad\qquad V_{3i} = r(d_1 - d_2) + 1$$

with r defined as $\qquad r = \Delta/(f_1 d_2 - f_2 d_1)$

In equation (4.24) the coefficients U_{1i} ..., V_{3i} are evaluated at $y = y_i$. If, at some point $y = y_j$, both displacements u and v are known, then u and

v may be found elsewhere by starting at this point and evaluating the displacements at the point $y = y_{j+1}$ by using equation (4.24). This procedure is repeated until the displacements at all points to the right of y_j are found. To find the displacements to the left of y_j one must solve equation (4.23) for u_i and v_i

$$\begin{aligned} u_i &= \underline{U}_{1i} + \underline{U}_{2i}u_{i+1} + \underline{U}_{3i}v_{i+1} \\ v_i &= \underline{V}_{1i} + \underline{V}_{2i}u_{i+1} + \underline{V}_{3i}v_{i+1} \end{aligned} \tag{4.25}$$

where the coefficients $\underline{U}_{1i}$ ..., $\underline{V}_{3i}$ are given by

$$\underline{U}_{1i} = s\left|N_2(\Delta - f_1) - N_1(\Delta - f_2)\right| \qquad \underline{V}_{1i} = s\left[N_1\left(\Delta\frac{y_i}{x_s} - d_2\right) - N_2\left(\Delta\frac{y_i}{x_s} - d_1\right)\right]$$

$$\underline{U}_{2i} = s\left(d_1 - d_2 + \frac{1}{r}\right) \qquad \underline{V}_{2i} = -\,s\,\frac{y_i}{x_s}(d_1 - d_2)$$

$$\underline{U}_{3i} = s(f_1 - f_2) \qquad \underline{V}_{3i} = s\left(\frac{1}{r} - \frac{y_i}{x_s}(f_1 - f_2)\right)$$

with s defined as $\quad s = 1/\left(r + d_i - d_2 - \frac{y_i}{x_s}(f_1 - f_2)\right)$

In equation (4.25) the coefficients $\underline{U}_{1i}$ ..., $\underline{V}_{3i}$ are evaluated at $y = y_i$. By setting $i + 1 = j$ the displacements to the left of y_j are found by successive applications of equation (4.25).

In the actual experimental work a situation may arise when the two displacements u and v are known at two different locations; for example, u is known at $y = y_j$ and v is known at $y = y_k$. This case is handled as follows:

At point i + 2 equation (4.24) becomes

$$\begin{aligned} u_{i+2} &= U_{1i+1} + U_{2i+1}u_{i+1} + U_{3i+1}v_{i+1} \\ &= (U_{1i+1} + U_{2i+1}U_{1i} + U_{3i+1}V_{1i}) + (U_{2i+1}U_{2i} + U_{3i+1}V_{2i})u_i + \\ &\qquad + (U_{2i+1}U_{3i} + U_{3i+1}V_{3i})v_i \end{aligned}$$

and a similar expression could be written for v_{i+2}. This process is repeated n times until i + n = k whereupon we get

$$u_{i+n} = u_k = \bar{U}_{1k-1} + \bar{U}_{2k-1}u_i + \bar{U}_{3k-1}v_i$$
$$v_{i+n} = v_k = \bar{V}_{1k-1} + \bar{V}_{2k-1}u_i + \bar{V}_{3k-1}v_i \qquad (4.26)$$

The coefficients $\bar{U}_{1k-1}, \ldots, \bar{V}_{3k-1}$ are obtained by repeated use of the recursion relationship between coefficients U_{1i+1} and U_{1i}, V_{1i}, U_{2i+1}, V_{2i+1} and so on. From equation (4.26) it is possible to solve for any of u_i, v_i, u_k, or v_k if any two of these are known and, once two displacements at the same point are determined, displacements u and v may be calculated elsewhere by using equations (4.24) and (4.25). The slopes and strains may then be calculated numerically by using the central finite differences

$$u,_{yi} = \frac{u_{i+1} - u_{i-1}}{2\Delta} \qquad v,_{yi} = \frac{v_{i+1} - v_{i-1}}{2\Delta}$$

If the out-of-plane displacement u is small, it is possible to solve equation (4.22) for v and $v,_y$ as follows:

$$\frac{y}{x_s}u + v + d_1u,_y + f_1v,_y = N_1$$
$$\frac{y}{x_s}u + v + d_2u,_y + f_2v,_y = N_2 \qquad (4.22)$$

By multiplying the first equation by d_2 and the second equation by $(-d_1)$ and adding the two equations we get

$$(d_2 - d_1)\frac{y}{x_s}u + (d_2 - d_1)v + (f_1d_2 - f_2d_1)v,_y = N_1d_2 - N_1d_2$$

By choosing the parameters of DASSC such that the term $|d_2 - d_1|$ is as small as possible and the term $|f_1d_2 - f_2d_1|$ is as large as possible, we may closely approximate the above equation by

$$(d_2 - d_1)v + (f_1 d_2 - f_2 d_1)v,_y \simeq N_1 d_2 - N_2 d_1$$

which may be written as $$v,_y + p(y)v = q(y) \tag{4.27}$$

with p(y) and q(y) defined as $$p(y) = \frac{d_2 - d_1}{f_1 d_2 - f_2 d_1}$$

$$q(y) = \frac{N_1 d_2 - N_2 d_1}{f_1 d_2 - f_2 d_1}$$

$$f_1 d_2 - f_2 d_1 \neq 0$$

Equation (4.27) is an ordinary, first order differential equation with a variable coefficient; its solution [63] is

$$v(y) = \frac{1}{\mu(y)} \left(\int_{y_o}^{y} \mu(t)\, q(t)\, dt + \mu(y_o) v(y_o) \right) \tag{4.28}$$

where $\mu(y)$ is the integrating factor $$\mu(y) = \exp\left(\int^{y} p(t)\, dt \right)$$

In equation (4.28) $v(y_o)$ is a known displacement v at one point on the specimen surface on the line ($z = z_o$ = constant) upon which v(y) is sought. Once v(y) isfound, the strain $v,_y(y)$ may be obtained by the numerical differentiation of v(y) or calculated from equation (4.27). After v and $v,_y$ are determined, the two remaining quantities u and $u,_y$ are found from equations (4.22).

4.11 Use of DASSC to Measure Out-of-Plane Bending

In the cases where the out-of-plane displacements and strains are much greater than the in-plane displacements and strains, equation (4.16) is again applicable. Equation (4.16) may be written in the standard form given by equation (4.29) and, since equation (4.29) is of the same type as equation (4.27), it is also solved in the same way, with the solution given by equation (4.30).

$$u_{1,y_1} + p_1(y_1)u_1 = q_1(y_1) \tag{4.29}$$

where $p_1(y_1)$ and $q_1(y_1)$ are defined as $\quad p_1(y_1) = \dfrac{A}{D_1}$

$$q_1(y_1) = \frac{N_1(y_1,z_1)}{D_1} \qquad D_1 \neq 0$$

$$u_1(y_1) = \frac{1}{\mu_1(y_1)}\left[\int_{y_{10}}^{y_1} \mu_1(t)q_1(t)\,dt + \mu_1(y_{10})u_1(y_{10})\right] \tag{4.30}$$

where the integrating factor $\mu_1(y_1)$ is given by $\quad \mu_1(y_1) = \exp\left[\int^{y_1} p_1(t)\,dt\right]$

In equation (4.30) $u_1(y_{10})$ is the known out-of-plane displacement u_1 at y_{10} on a line ($z_1 = z_{10}$ = constant) in the rotated coordinate system y_1, z_1 where $u_1(y_1)$ is being sought.

If the out-of-plane displacement at one point of the beam surface is not available then two photographs are necessary for an approximate solution of u_1 and u_{1,y_1} . If we use two sets of apertures at $\phi = 0^o$, the two fringe patterns are given by equation (4.13) as

$$\frac{y}{x_s}u + v - \frac{yz}{x_s^2}w + d_i u_{,y} + f_i v_{,y} + h_i w_{,y} = N_i \qquad i = 1,2 \tag{4.31}$$

If the second of these equations is subtracted from the first we get

$$(d_1 - d_2)u_{,y} + (f_1 - f_2)v_{,y} + (h_1 - h_2)w_{,y} = N_1 - N_2$$

By an appropriate choice of the DASSC parameters the term $|(d_1 - d_2)u_{,y}|$ may be made much larger than the other two terms, and an approximate value of $u_{,y}$ is then given by equation (4.33):

$$\text{if} \quad |(d_1 - d_2)u_{,y}| \gg |(f_1 - f_2)v_{,y}|, |(h_1 - h_2)w_{,y}| \tag{4.32}$$

$$u,_y = \frac{N_1 - N_2}{d_1 - d_2} \qquad d_1 - d_2 \neq 0 \tag{4.33}$$

Once $u,_y$ is calculated by using equation (4.33) it is substituted back in equation (4.31) and an approximate solution for u (except near the origin) is found by neglecting small terms involving $v, v,_y, w,$ and $w,_y$.

In some tests, the out-of-plane bending of the specimen may be accompanied by quite large in-plane displacements and strains of its illuminated surface. By the use of specimen illumination in the x,y, plane and the aperture sets rotated by $\phi = 0^o$ the camera is made insensitive to w and $w,_y$ and, consequently, the terms involving w and $w,_y$ in equation (4.12) are often negligible. When this is the case, equation (4.12) reduces to equation (4.22), the solution of which was derived and discussed in Section 4.10 .

4.12 Use of DASSC to Measure Plane Stress and Plane Strain Deformation

When the specimen deformation is of the plane stress or plane strain type, the out-of-plane displacement component u_i is usually very small or zero. If the terms involving u_i and its derivative(s) are so small that they do not contribute significantly to the fringe formation, these terms may be neglected in equations (4.12) and (4.13), and the displacement components v_i and w_i can be determined from only two photographs. These photographs could be obtained, for example, by DASSC with two illuminating beams, each beam being used with one of the two aperture sets which are rotated by the same angle ϕ_i . Use of the finite difference scheme discussed in Section 4.9 allows v_1 and w_1 to be calculated from equation (4.21) with u_1 and $u_1,_{y1}$ set equal to zero.

As mentioned in Section 4.10, when the specimen illumination is in the x,y plane and the aperture sets are in $\phi_i = 0^o$ position, the terms in

equation (4.12) involving w and $w,_y$ are often negligible; and, when it is possible, equation (4.12) with the u, $u,_y$,w, and $w,_y$ terms neglected reduces to

$$v + f_i v,_y = N_i$$

which may be written as

$$v,_y + p(y)v = q(y) \tag{4.34}$$

where p(y) and q(y) are defined as

$$p(y) = \frac{1}{f_i}$$

$$q(y) = \frac{N_i}{f_i}$$

Equation (4.34) is of the same type as equation (4.27) and, hence, it is solved in the same way, with the solution given by equation (4.28) and the integrating factor given by

$$\mu(y) = \exp\left(\int^{y} p(t)\, dt\right)$$

Unfortunately in most practical testing, while it is often possible to neglect the terms involving w and $w,_y$, the term $d_i u,_y$ is not sufficiently small and may not be neglected. If this is the case, equation (4.12) reduces to equation (4.22), the solution of which was discussed in Section 4.10.

5. EXPERIMENTAL APPARATUS AND PROCEDURE

In the first part of this chapter the various apparatus used in the experimental work is described and discussed in the following order: the camera; the recording system; the filtering system; the specimen loading systems; and finally the various specimens themselves. The latter part of the chapter contains a description of the experimental procedure which was used.

5.1 The Camera

The photograph of the camera is shown in Fig. 5.1 and its schematic in Fig. 5.2 . The camera may function as either DASC or DASSC, depending on the position of the photographic plate upon which the specimen is imaged. The position of the photographic plate may be varied along the x-axis with the use of the adjustable slide. The sub-assembly of the photographic plate holder and the slide is shown in Fig. 5.3 . The slide, lens assembly, and shutter assembly are each mounted on ½ in. diameter steel rods fitting into holes in the camera frame. These holes, spaced 1 in. apart, are along the full length of the frame, and are located precisely in the centre of the frame to ensure the axial alignment of the camera components while allowing their mounting at desired heights and spacings. The lens assembly, uncorrected for spherical aberration, consists of three high quality lenses mounted in a tabular frame. The shutter assembly shown in Fig. 5.4 is positioned in front of the lens assembly and utilizes a rotating shutter to open or close various aperture sets as required in a particular experiment. The stationary part of the shutter assembly accomodates a number of interchangeable aperture plates each having apertures of various diameters. The camera enclosure is used to prevent any unwanted light from reaching the photographic plate.

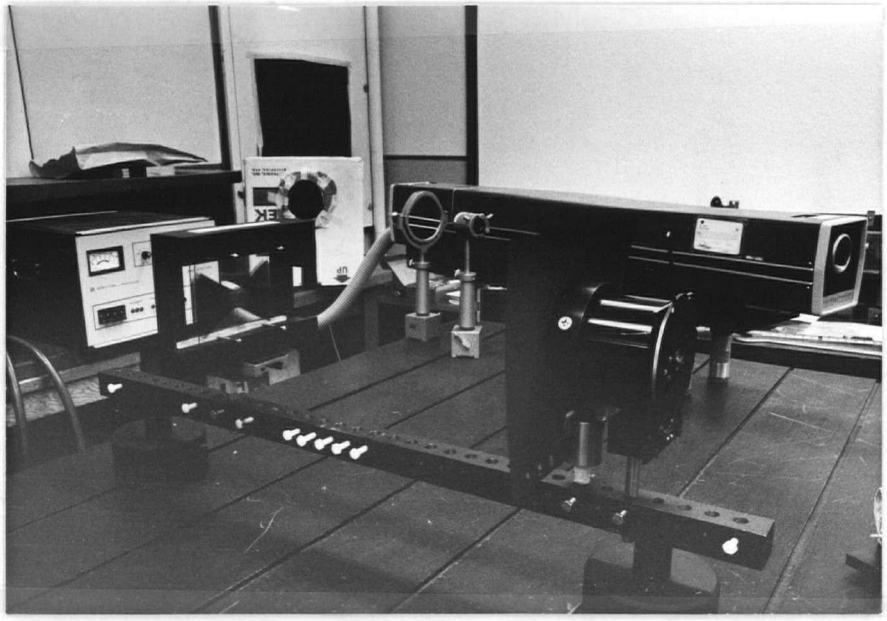

Fig. 5.1 Double aperture speckle shearing camera (DASSC).

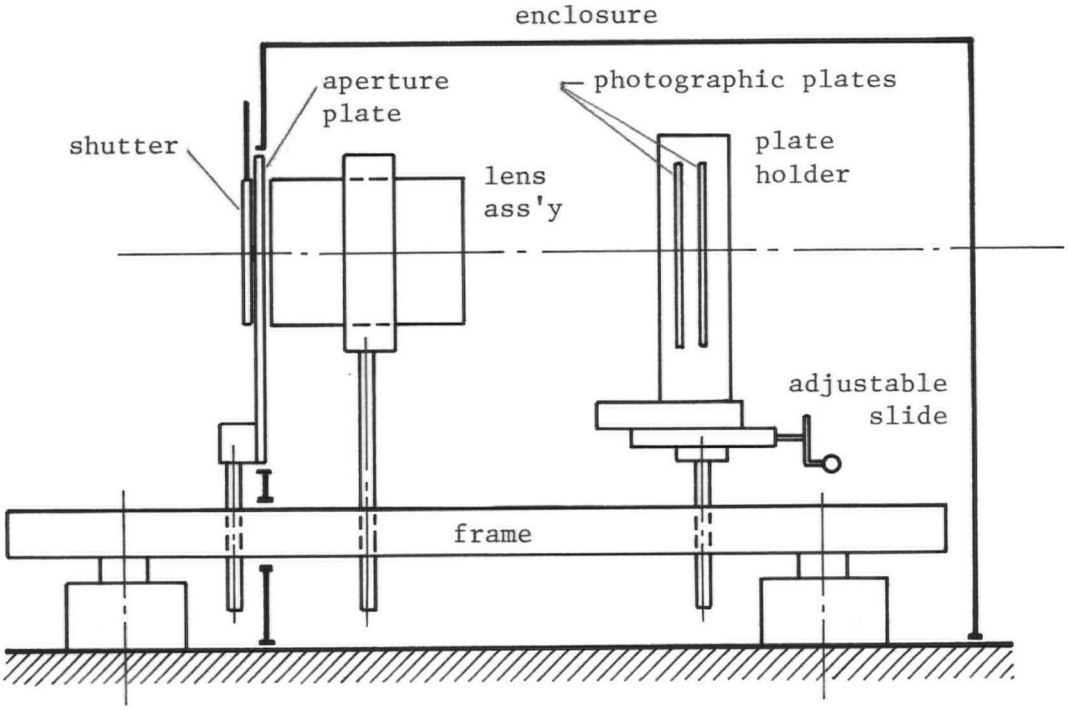

Fig. 5.2 Schematic of DASSC.

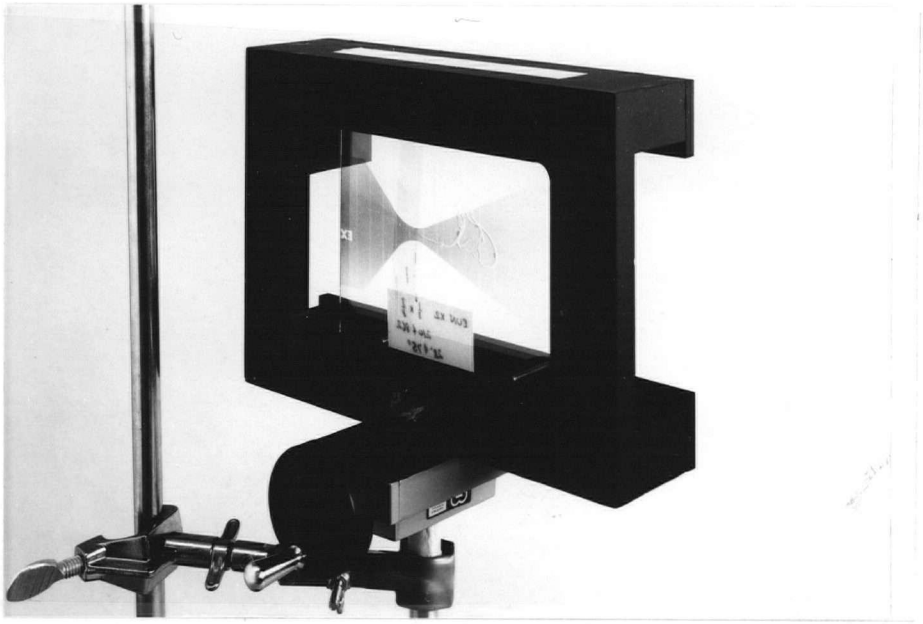

Fig. 5.3 Photographic plate holder assembly.

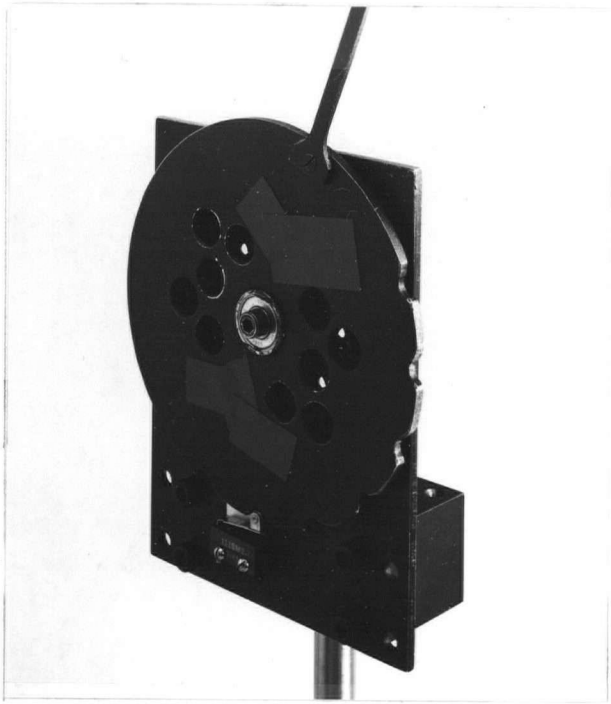

Fig. 5.4 Shutter assembly

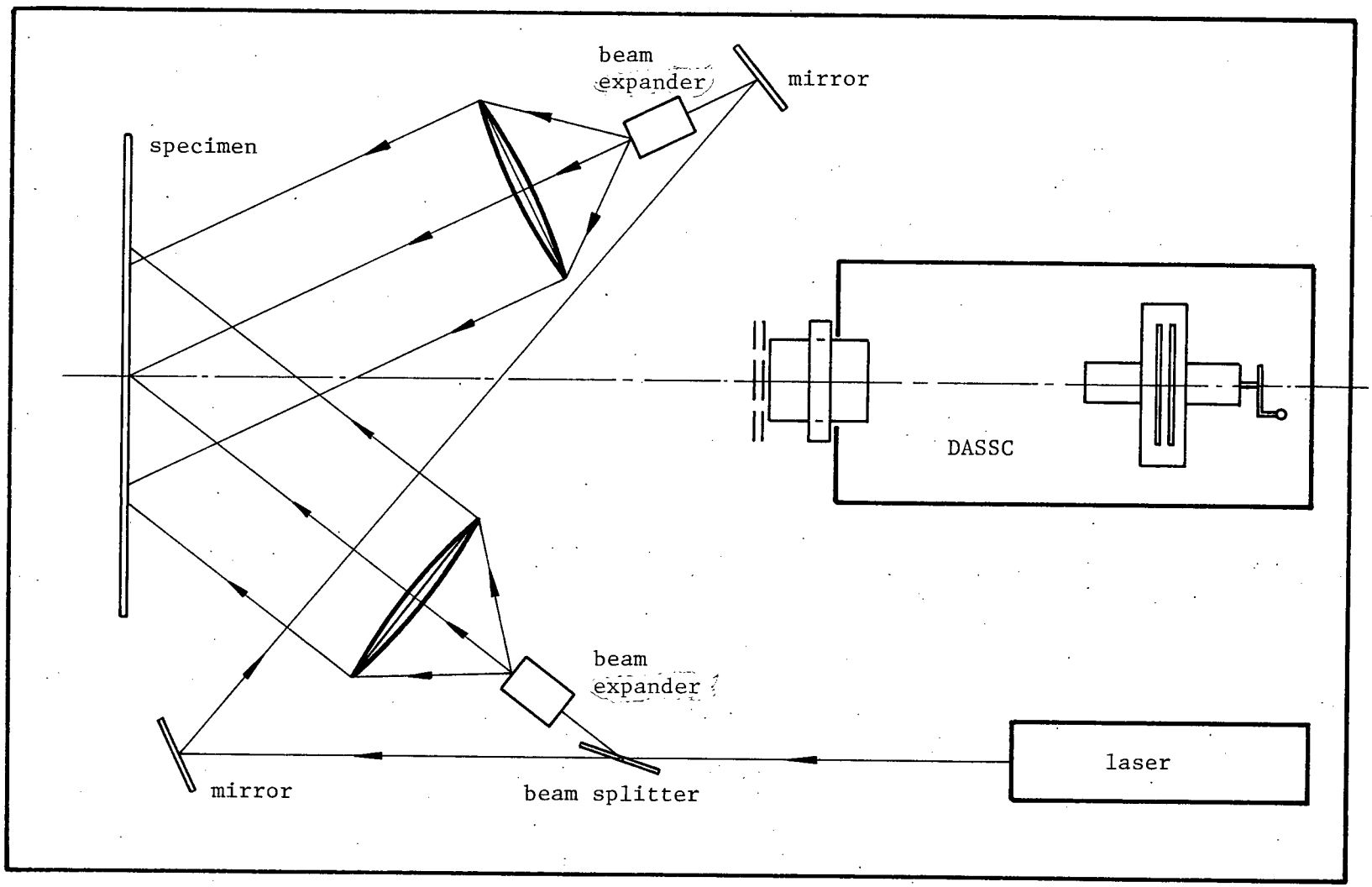

Fig. 5.5 Schematic of the recording system.

Fig. 5.6 Recording system.

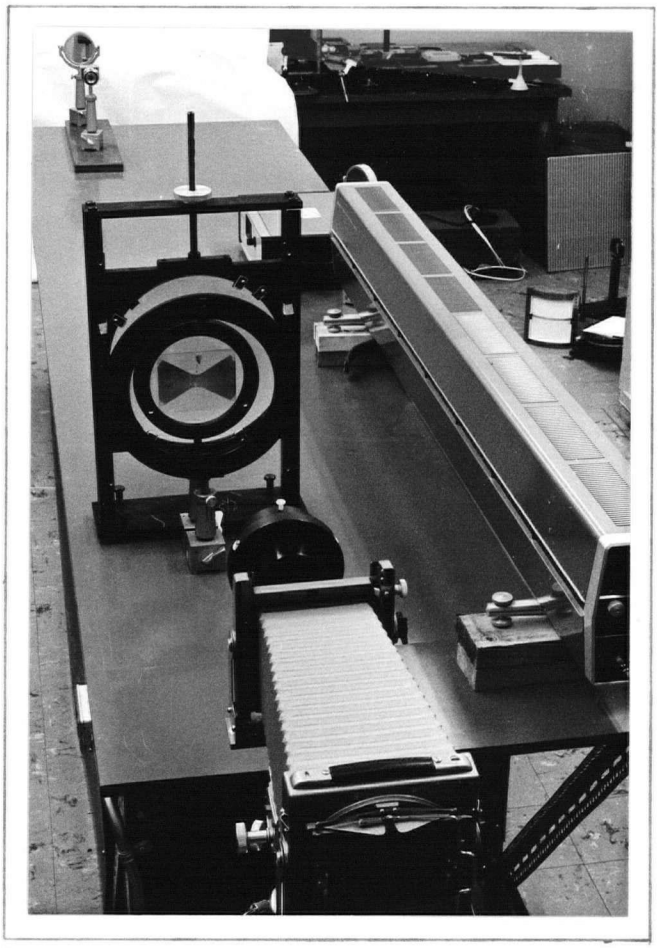

Fig. 5.7 Filtering system.

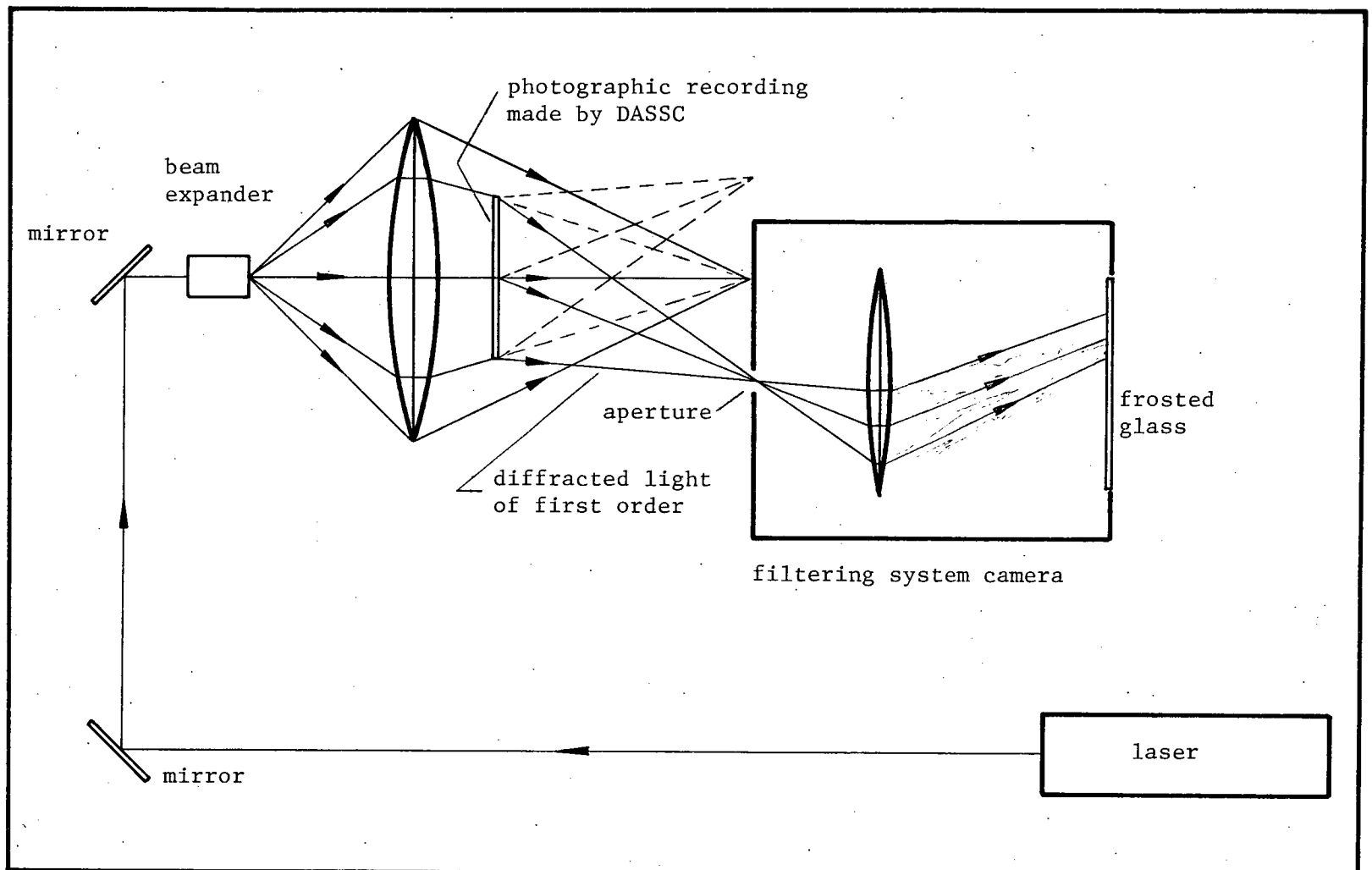

Fig. 5.8 Schematic of the filtering system.

5.2 The Recording System

A typical recording system is pictured in Fig. 5.6 and its schematic in Fig. 5.5 . The system consists of the camera, the optical components, the laser providing the specimen illumination, and the loading apparatus with the specimen. The camera was described in the previous section and the loading system will be described in Section 5.4 . The laser used is an argon laser providing a source of coherent light of wavelength 5140 Å delivered at a maximum continuous power of approximately .6 watts. The laser beam of approximately .1 in. diameter is directed by the adjustable mirrors and divided by the beam splitters. Once the laser beam has been properly oriented, it is expanded by the beam expander and then collimated by a large diameter lens. Depending on the experiment, one or two specimen illuminating beams were obtained in this way. The purpose of the recording system is to produce one or two photographic plates storing information about the specimen deformation that took place between the two recorded exposures. The emulsion of the photographic plate, once it is developed, contains two speckle grids, each corresponding to one exposure; as described in Chapter 3, the two speckle grids add and thus form a resultant grid of variable diffractive efficiency.

5.3 The Filtering System

Once the photographic, double exposure recording of the specimen deformation is made and subsequently developed, it must be "processed" in the filtering system so that the various fringe patterns may be separated, displayed and recorded. The filtering system, shown in Figs. 5.7 and 5.8, uses again the laser as a source of light and mirrors to direct the laser beam. After properly oriented, the laser beam is expanded by the beam expander and, upon reaching a sufficient diameter, is made to converge

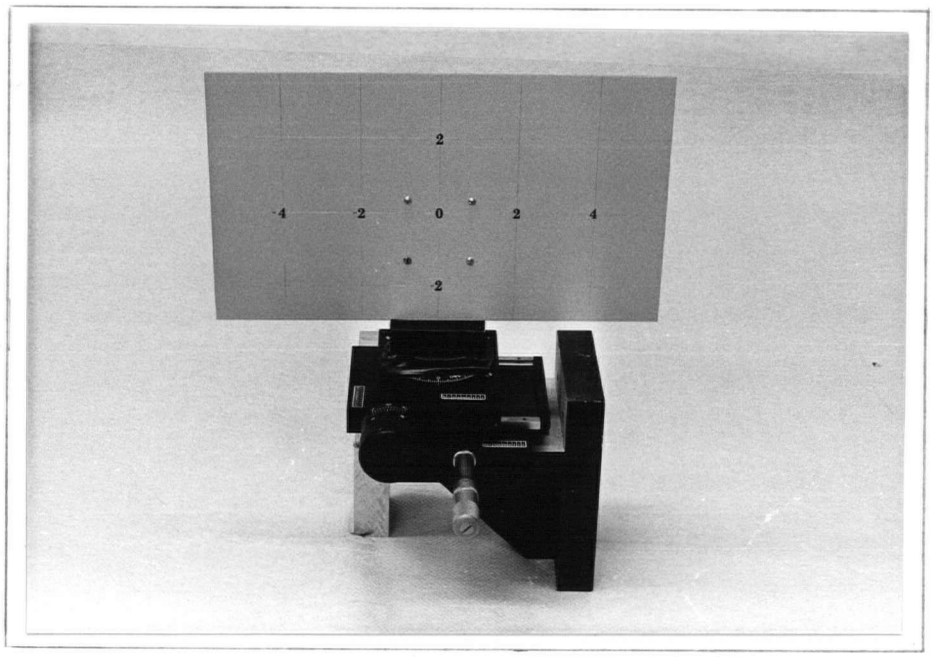

Fig. 5.9 Plate specimen positioned on translation and rotary tables.

Fig. 5.10
The arrangement in bending of the beam experiments.

by use of a large lens. The photographic plate containing the recording made by DASSC is placed in the converging light and, because it contains a speckle grid, the recording diffracts light in a direction depending on the speckle grid density and orientation. An opaque screen upon which the diffracted light orders are focused is placed in the focal plane of the lens. A circular aperture in the screen permits one of these diffracted light orders to pass through and be focused by the lens of the filtering system camera onto the frosted glass where the specimen image may be viewed and recorded. As was mentioned in the previous section, the speckle grid has variable diffractive efficiency over the area of the recorded image of the specimen, and this causes the intensity of the specimen image (formed by the diffracted light) to vary in some systematic manner. This last image of the specimen (appearing on the frosted glass) is, of course, the fringe pattern n(y,z).

5.4 The Specimen Loading Systems

In the experiments to be described in sections 6.2 and 6.3, involving the out-of-plane rigid body translation and the in-plane rotation of a plate specimen respectively, a Kinematic micro translation table (model TT-102) coupled with a rotary table (model RT-200) was used to impose displacements to within an accuracy of ± .00025 in. and rotations to within an accuracy of ± .1 min. . The assembly with the plate specimen is shown in Fig. 5.9 .

The schematic of the experimental apparatus used in the out-of-plane beam bending experiments is given in Fig. 6.16 and its photograph is shown in Fig. 5.10 . Two C-clamps at each end of the beam were used to clamp it to an aluminum channel of much greater bending stiffness than the beam. A small circular hole was machined at the center of the channel so that the

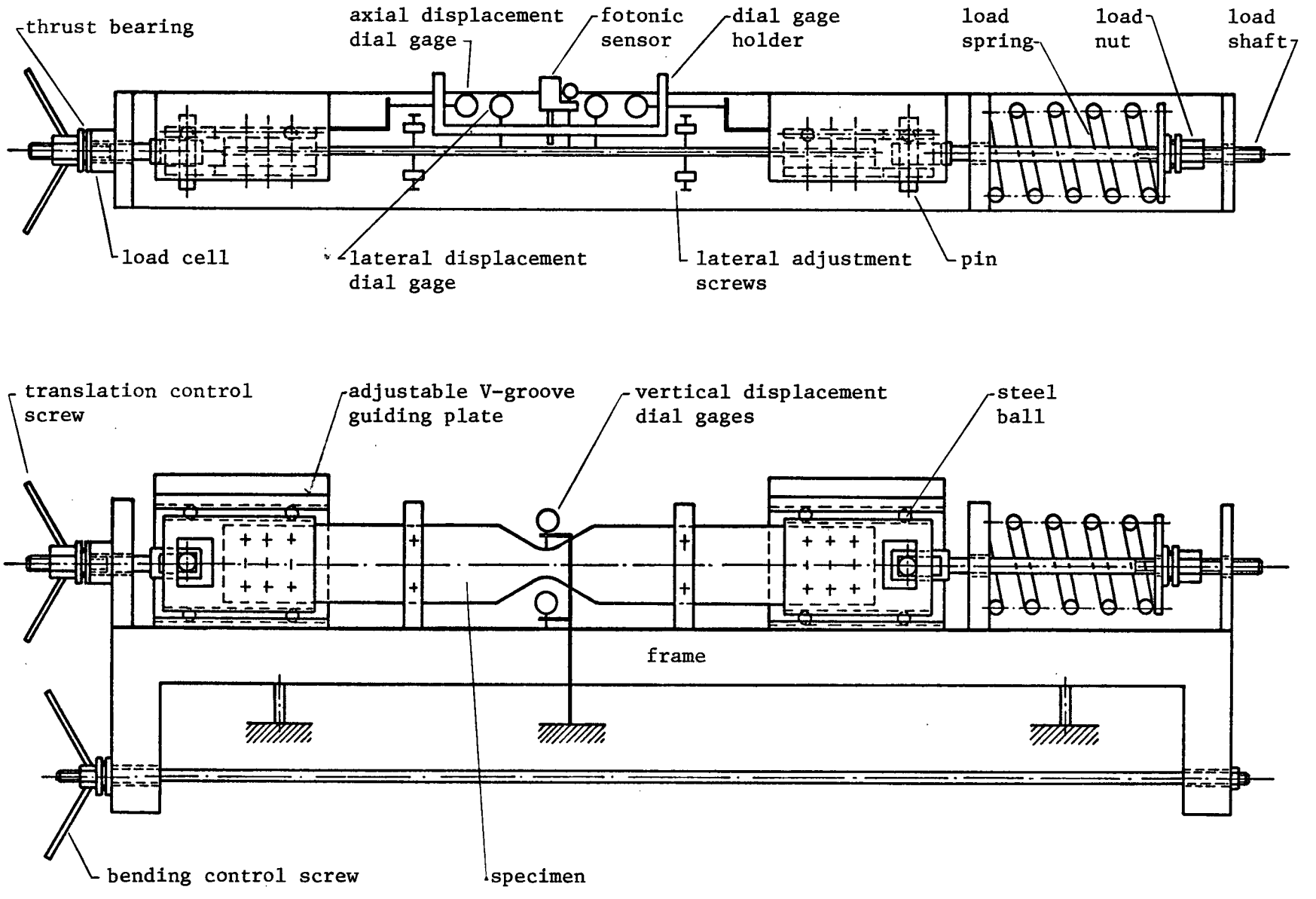

Fig. 5.11 Schematic of the tensile loading apparatus.

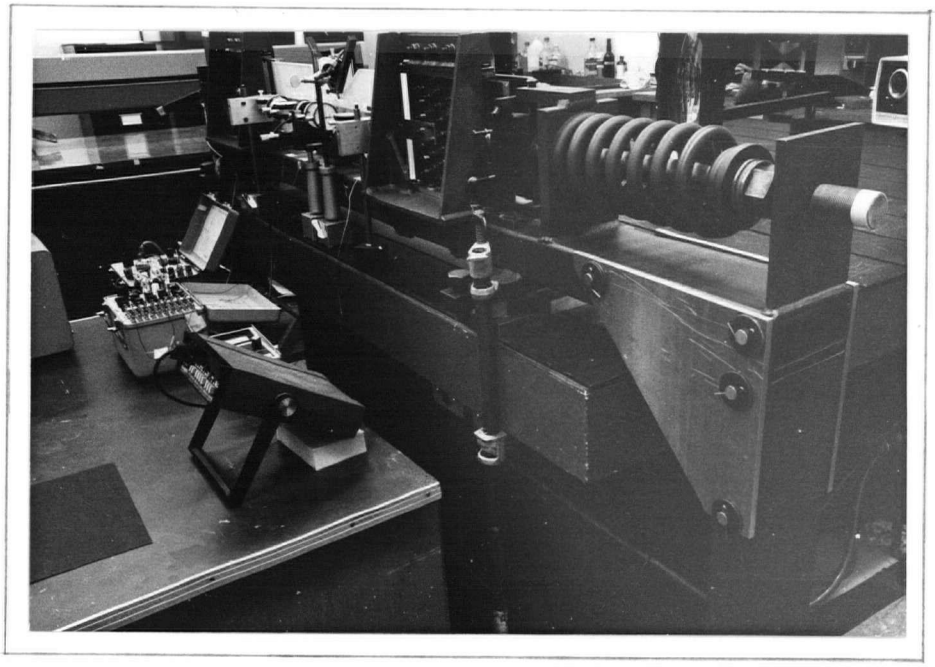

Fig. 5.12 Right side view of the loading apparatus.

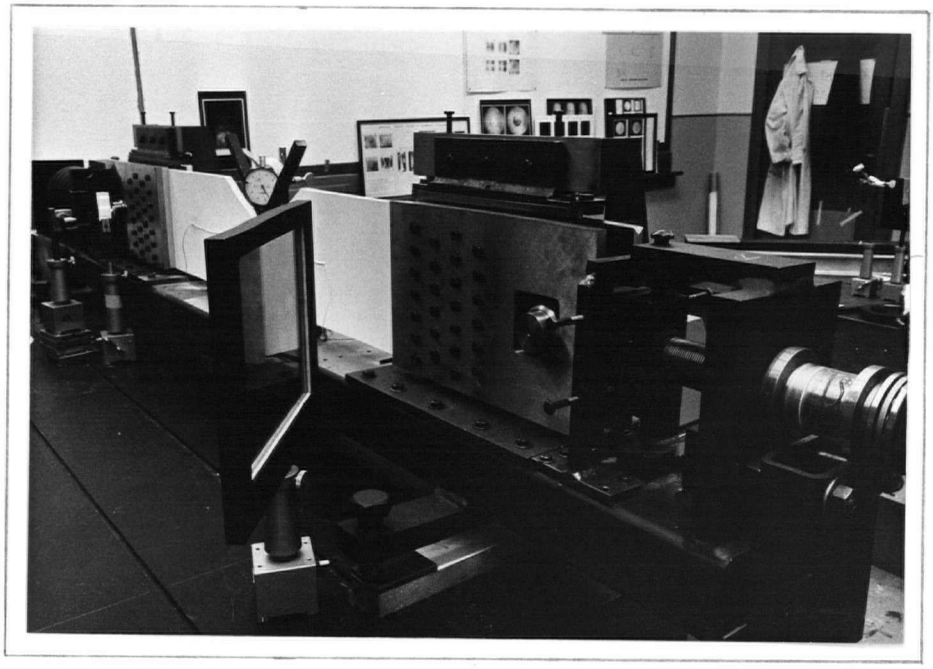

Fig. 5.13 Left side view of the loading apparatus.

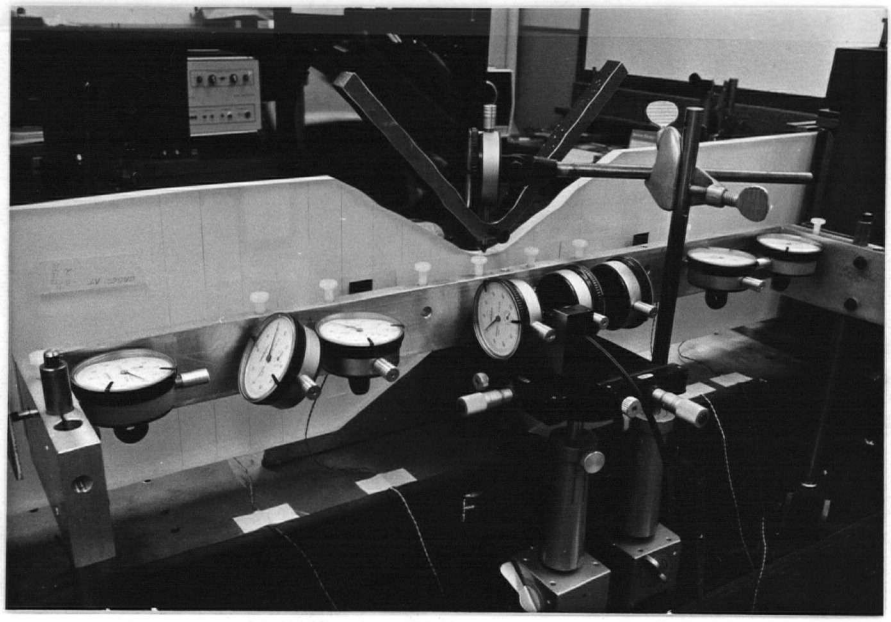

Fig. 5.14 Measurement of displacements u(y,0) by dial gages.

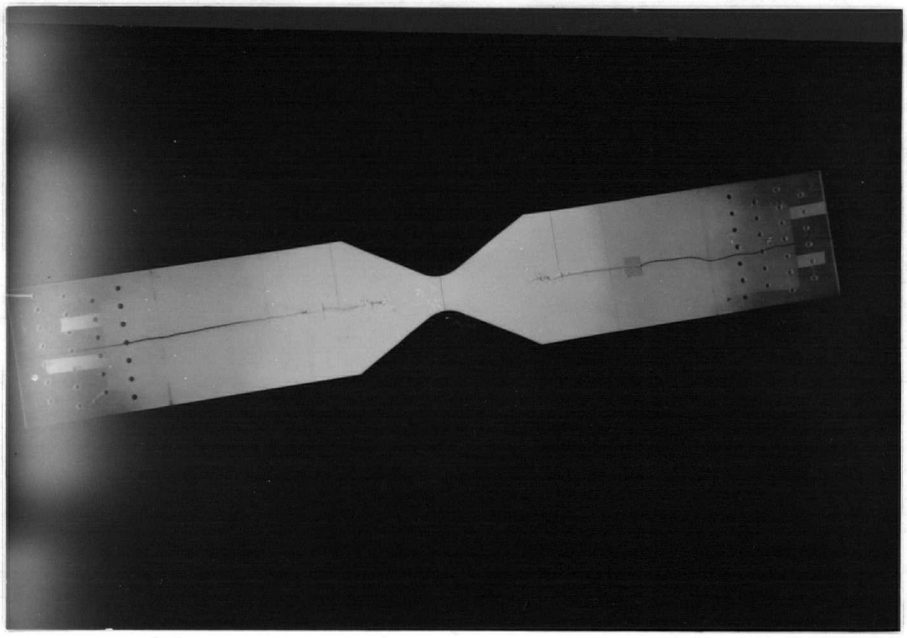

Fig. 5.15 Variable cross-section specimen.

micrometer tip could contact and displace the center of the beam out of the plane by a known amount to within an accuracy of approximately ± .00025 in.

In all the remaining experiments (to be described in sections 6.5 through 6.7) the loading apparatus shown in Figs. 5.11 , 5.12 and 5.13 was used. It was designed so that adjustments of the specimen shape and position could be made while the specimen was being subjected to as much as 6000 lbs. of static tensile axial load. The load was imposed by turning the loading nut which in turn compressed a coil spring. The load was transmitted to the specimen through a load shaft, pin, and clamps which were constrained to move axially by steel balls fitting into V grooves made in the frame and in the side of the clamps. Such an arrangement permitted an axial movement with a minimum amount of "play" in other directions. The loading, however, often resulted in an unwanted axial translation of the specimen. This axial translation was monitored at one point by a displacement transducer (Fotonic Sensor) mounted on a kinematic table so that the Sensor probe could be kept at a constant distance from the specimen surface. By making adjustments with the translation control screw and observing the Fotonic Sensor reading, we could zero out the axial displacement of this particular point. The initial crookedness of the specimen or a small misalignment of the clamps also caused a small lateral displacement of the specimen. This undesirable displacement was measured by a number of dial gages, shown in Fig. 5.14, and minimized by adjustments made with the lateral adjustment screws. In addition to the axial tensile load, the specimen was also subjected to some bending caused by the asymmetry of the loading apparatus. To minimize this bending deformation, a dial gage was used to measure the vertical displacement of the centre of the supporting frame and this displacement was then zeroed with the bending control screw. Once all these adjustments were completed, the load increment and the instrument

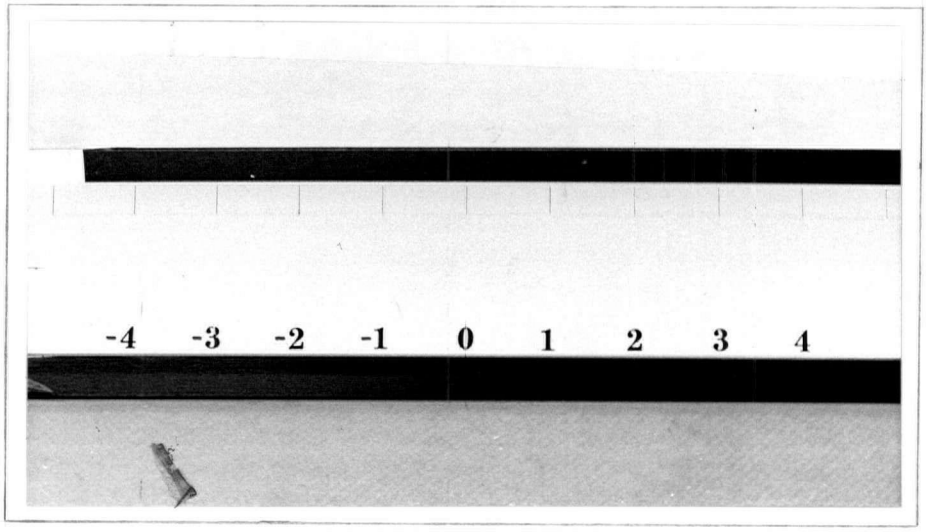

Fig. 5.16 Central part of the beam used in the beam bending experiments.

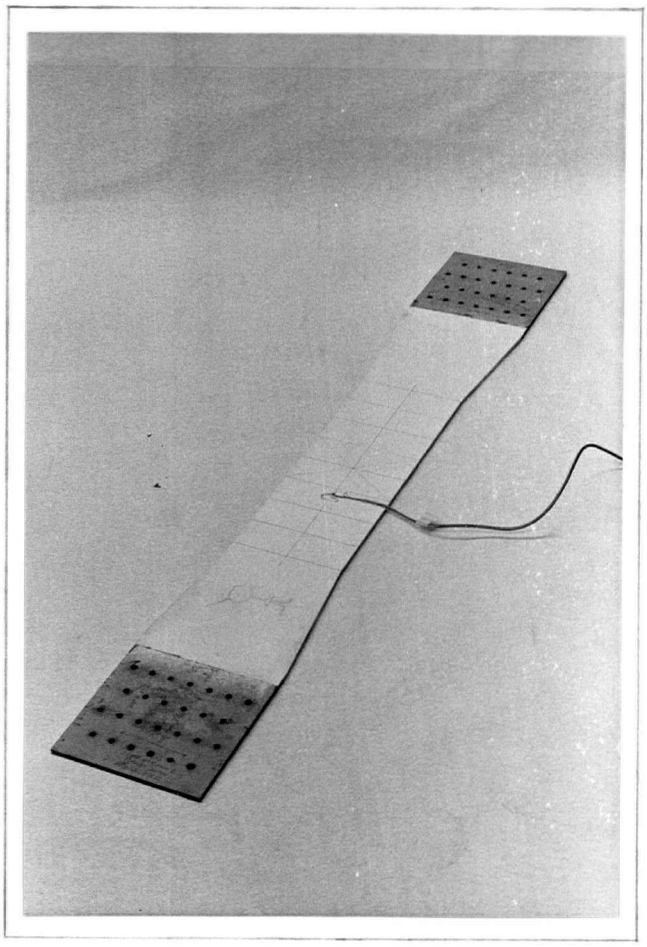

Fig. 5.17 Tensile specimen with the uniform cross-section.

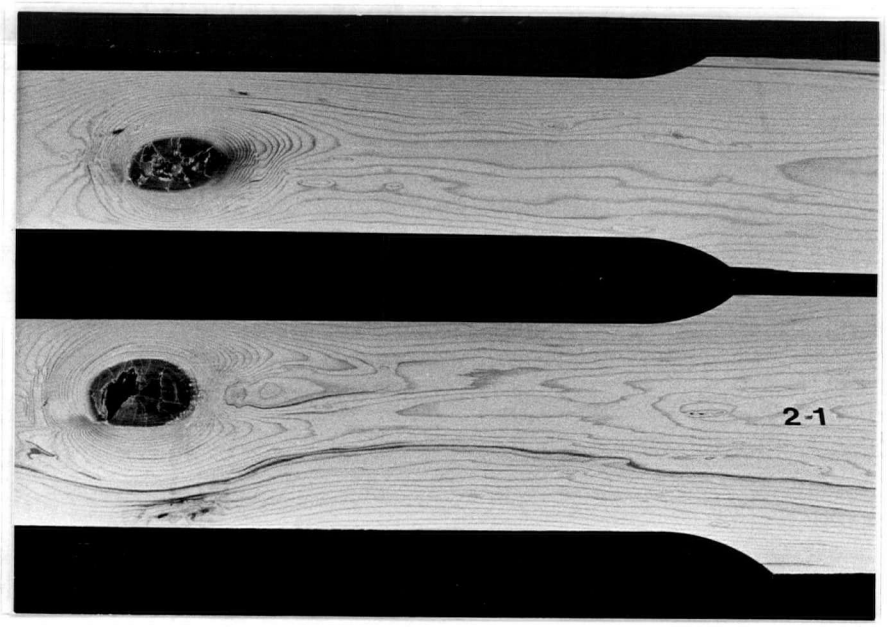

Fig. 5.18 Wooden beam specimen.

readings were recorded and the second exposure of the specimen surface was made.

5.5 Specimens

All specimens, including the wooden beam were coated with a flat white enamel paint to provide a diffusely reflecting surface. Detailed descriptions of the specimens are in Chapter 6; the plate specimen used in the experiments of sections 6.2 and 6.3 is shown in Fig. 5.9 and the remaining specimens are shown in Figs. 5.15 through 5.18 .

5.6 Experimental Procedure

The work performed in all the experiments described in Chapter 6 followed, in general, the same pattern whether DASC or DASSC was used. The experimental procedure can be outlined in the following steps:

a) Using knowledge that the camera forms fringes according to equation (3.20) or (3.26) and having some idea about the size of the specimen deformation in the intended testing, the parameters of the camera were chosen so that a desired number of independent recordings having desirable fringe densities could be made.

b) The specimen was coated with white enamel paint to reflect the laser light diffusely over the area of interest with approximately the same intensity. It was then clamped or attached in the loading apparatus which had been previously set up to accommodate the specimen.

c) Various sensors and dial gages were positioned and their initial (first exposure) readings were recorded. With the use of a telescope with dual cross-hairs or some laser alignment technique the center of the frame of DASSC was made to lie in the x,z plane of the specimen coordinate system. The optical components that make up the camera were then mounted at the

required height and orientation so that they were aligned along the x-axis. An aluminum ruler coated with flat black paint and having scratch marks made at 1 in. increments was positioned next to the specimen (usually just below) so that its plane was coincident with the y,z plane. A frosted glass plate was inserted in the plate holder of the camera and the specimen with the ruler was illuminated by one of the collimated laser beams. The image of the specimen and the ruler made by light passing through a particular aperture set was viewed on the frosted glass, and the size of the lateral shear Δy_i was adjusted by positioning the plate holder with the adjustable slide and observing the amount by which the bright images of the ruler scratch marks doubled.

d) With both the room lights and the laser turned off and in the near or total darkness one or, if desired, two photographic plates were inserted in the plate holder and the camera was then covered with the enclosure. The specimen was then illuminated by one illuminating beam at a time for the required exposure period at an appropriate shutter setting. Once the desired number of first exposures was made the laser was turned off and the specimen was loaded. After all the specimen adjustments described in Section 5.4 were made, the readings of the dial gages and other sensors were recorded. The specimen was again illuminated and the second exposures were made using the same illuminating beams and shutter settings as in the first exposures. All exposures were usually of the same duration.

e) The laser was turned off and the photographic plates were removed from the holder and developed according to manufacturers specifications.

f) After development, the photographic plates were inserted in the filtering system (described in Section 5.3) where the fringe patterns corresponding to the specimen deformation could be viewed and permanently recorded on the film.

g) The lateral shear Δy_i was measured on a traversing microscope either from the photographic plate or preferably from the film recording; using the film recording was easier because each recording had only one lateral shear corresponding to a particular aperture set. In contrast to this, the photographic plate contained all the images of the ruler scratch marks making it difficult to identify and measure the various lateral shears.

h) With the aid of a microdensitometer the film negatives with the fringe patterns were scanned and, by scanning the image of the ruler too, it was possible to establish the location of the fringes on the specimen surface.

i) With the known fringe locations and DASSC parameters as the input data, an appropriate computer program was used to calculate the unknown specimen deformation.

6. EXPERIMENTAL WORK

6.1 Preliminary Remarks

This chapter consists essentially of two parts. The first part is devoted to the description and discussion of the results of a number of relatively simple experiments, the purpose of which was to verify experimentally the validity and accuracy of the equations governing the fringe formation of DASC and DASSC. The second part of this chapter deals with several fairly complicated experiments which served to test the feasibility and accuracy of DASSC for measurement of displacements and strains in applications similar to those encountered in the practical testing of materials. In contrast to the other chapters, in this chapter all figures are placed at its end so that the continuity of reading may not be interrupted by their excessive number.

6.2 Rigid Body, Out-of-Plane Translation of a Plate Specimen

The purpose of this experiment was to verify the formation of fringes by DASC and DASSC due to the out-of-plane displacement of the specimen surface. For the rigid body, out-of-plane translation of the specimen surface, that is for $u = u_0$, and for other displacements and strains being identically zero, both equations (4.4) and (4.13) governing the fringe formation by DASC and DASSC respectively reduce to

$$a_i u_0 = N_i(y,z) \tag{6.1}$$

By using the definitions (4.5a) for a_i and (4.5d) for N_i , we may write equation (6.1) as equation (6.2) for DASC and as equation (6.3) for DASSC.

$$\frac{y\cos\phi_i + z\sin\phi_i}{x_s} u_0 = -\frac{\lambda x_s}{D} n_i(y\cos\phi_i + z\sin\phi_i \ , \ -y\sin\phi_i + z\cos\phi_i) \tag{6.2}$$

$$\frac{y\cos\phi_i + z\sin\phi_i}{x_s} u_0 = -\frac{\lambda X_s}{D} n_i(y\cos\phi_i + z\sin\phi_i \ , \ -y\sin\phi_i + z\cos\phi_i) \tag{6.3}$$

Two aperture sets, one rotated by 0° and the other by 90°, were used to photograph the out-of-plane displacements u_0 of the plate. The plan view of the experimental setup for DASC is shown in Fig. 6.1 .

One way to verify the fringe formation by the two cameras is to compare the predicted and actual fringe positions and spacings. From equations (6.2) and (6.3) the predicted fringe patterns for this experiment are given by

DASC: $\phi = 0^o$ $$n(y,z) = -\frac{D}{\lambda x_s^2} u_0 y \tag{6.4a}$$

$\phi = 90^o$ $$n(y,z) = -\frac{D}{\lambda x_s^2} u_0 z \tag{6.4b}$$

DASSC $\phi = 0^o$ $$n(y,z) = -\frac{D}{\lambda x_s X_s} u_0 y \tag{6.5}$$

The DASC parameters for Experiment (Exp.) 19 ($\phi = 0^o$) and for Exp. 22 ($\phi = 90^o$) were

$x_s = 38$ in.

$D = 2.5$ in.

$u_0 = .025$ in.

For these parameters the fringe patterns are calculated from equations (6.4a) and (6.4b) as

Exp. 19: $n(y,z) = -2.164\ y$

Exp. 22: $n(y,z) = -2.164\ z$

Hence, for Exp. 19 the fringes are predicted to be parallel to the z-axis and spaced .462 in. apart, and for Exp. 22 the fringes are predicted to be parallel to the y-axis and also spaced .462 in. apart. The actual fringe patterns for these two experiments are shown in Fig. 6.2 and Fig. 6.4 . From the microdensitometer traces of Fig. 6.2 and Fig. 6.4 the actual

fringe spacing was found to be .45 in. in both cases, which is close to the predicted spacing of .462 in. To show a typical microdensitometer trace, we have presented in Fig. 6.3 the trace of the fringe pattern of Exp. 19 shown in Fig. 6.2 .

The DASSC parameters for Exp. 17 and Exp. 18 ($\phi = 0^{o}$) were

x_s = 38 in.

u_0 = .025 in.

Exp. 17: D = 1.25 in , Δy_s = - .0257 in. , X_s = 37.22 in.

Exp. 18: D = 2.50 in. , Δy_s = - .0453 in. , X_s = 37.31 in.

The fringe patterns are determined by equation (6.5) as

Exp. 17: $n(y,z) = -1.105\ y$

Exp. 18 $n(y,z) = -2.204\ y$

Hence, for Exp. 17 the fringes are expected to be parallel to the z-axis and spaced .905 in.apart; for Exp. 18 the fringes are also expected to be parallel to the z-axis but spaced .454 in. apart. The fringe patterns for these two cases, obtained with DASSC, are shown in Fig. 6.5 and Fig. 6.6 . Note the "doubling" or "shearing" of lines and numbers in these two figures caused by the defocussing of the system. From the microdensitometer traces and after an appropriate scaling, the actual fringe spacing in Exp. 17 was found to be approximately .89 in., and in Exp. 18 the actual fringe spacing was found to be approximately .46 in. . Again the agreement between the predicted fringe spacing and the actual fringe spacing is acceptable.

A computer program, WONLY.S, to calculate u from equations (6.4) and (6.5) was written; it calculates u from data consisting of the parameters of DASC or DASSC and fringe center numbers and positions obtained from the microdensitometer trace. For example, the numerical data for Exp. 19 read

off Fig. 6.3 are given in Table 6.1

Fringe Location (in.)	Fringe Number
- 2.56	5.50
- 2.32	5.00
- 2.06	4.5o
- 1.88	4.00
- 1.60	3.50
- 1.40	3.00
- 1.14	2.50
- .94	2.00
- .68	1.50
- .50	1.00
- .24	.50
.04	.00
.24	- .50
.42	- 1.00
.68	- 1.50
.85	- 2.00
1.14	- 2.50
1.32	- 3.00
1.60	- 3.50
1.80	- 4.00
2.02	- 4.50
2.24	- 5.00
2.48	- 5.50
2.68	- 6.00
2.96	- 6.50

Table 6.1 Fringe data of Exp. 19

The fringe function n is approximated by a piecewise continuous cubic based on the above numerical data. For Exp. 19 this fringe function is compared to

the fringe function predicted by equation (6.4a) in Fig. 6.7 . The two functions are in good agreement and the actual difference between them is shown by the third curve. This third curve has its ordinate on the right side of the graph and the scale of the "difference" curve is usually highly exaggerated. The reason for the exaggerated scale is that often the plots of predicted and experimental (i.e. obtained with the use of DASC or DASSC) curves are so close together that it would be difficult to establish the actual numerical difference between them. The plot of the displacement, $u = u_0$ vs. u, calculated by WONLY.S is shown in Fig. 6.8 . Note that the two displacements are very close except near the origin where even a very small error in the fringe position produces a large error in the calculated displacement. The reason for this is obvious from the form of equation

$$u(y,z) = -\frac{\lambda x_s^2}{D}\frac{n(y,z)}{y} \qquad y \neq 0 \qquad (4.10b)$$

Therefore, if DASC or DASSC is used to measure the out-of-plane displacement it is essential to align the camera perfectly and to extrapolate the displacement at the origin from the displacements calculated nearby.
The result of this experiment agree very well with the theoretical predictions and confirm the validity of the coefficient a in equations (4.4) and (4.13).

6.3 Rigid Body, In-Plane Rotation of a Plate Specimen

The purpose of this experiment was to verify the formation of fringes by the two cameras due to the in-plane displacements of the specimen surface. The in-plane displacements v and w are produced by the rigid body rotation, α, of a plate about the x-axis as is shown in Fig. 6.9 . A point which was initially in the y,z plane at (0,y,z) was displaced between the two exposures

to the $(0,y^*,z^*)$ position. The displacements v and w are related to the coordinates (y,z) of an arbitrary point by

$$u = u,_y = u,_z = 0 \tag{6.6a}$$

$$v = y^* - y = y(\cos\alpha - 1) - z\sin\alpha \tag{6.6b}$$

$$w = z^* - z = z(\cos\alpha - 1) + y\sin\alpha \tag{6.6c}$$

The partial derivatives of these displacements are

$$v,_y = w,_z = \cos\alpha - 1 \tag{6.6d}$$

$$v,_z = - w,_y = - \sin\alpha \tag{6.6e}$$

All partial derivatives are constant and, for a small angle of rotation α as in the case, the terms in equation (4.13) involving these derivatives are negligible. For the angle of rotation, $\alpha = 2$ minutes, the numerical values of the displacements and strains are

$$v(y,z) = - 1.7 \times 10^{-7} y - 5.82 \times 10^{-4} z \tag{6.7a}$$

$$w(y,z) = - 5.82 \times 10^{-4} y - 1.7 \times 10^{-7} z \tag{6.7b}$$

$$v,_y = w,_z = - 1.7 \times 10^{-7} \tag{6.7c}$$

$$v,_z = - w,_y = - 5.82 \times 10^{-4} \tag{6.7d}$$

A schematic diagram for the experiments done in this section is shown in Fig. 6.10 . DASC with three aperture sets rotated by 0°,45°, and 90° was used to photograph the rotation of the plate which caused the displacements u,v and w given by equations (6.6). For these displacements equation (4.1); which governs the fringe formation by DASC, becomes

$$\phi = 0^o \quad : \qquad v - \frac{yz}{x_s^2} w = - \frac{\lambda x_s}{D} n(y,z) \tag{6.8a}$$

$$\phi = 45^o \quad : \quad \left(\frac{1}{\sqrt{2}} + \frac{z^2 - y^2}{2\sqrt{2}\, x_s^2}\right) v + \left(\frac{1}{\sqrt{2}} - \frac{z^2 - y^2}{2\sqrt{2}\, x_s^2}\right) w = - \frac{\lambda x_s}{D} n(y,z) \tag{6.8b}$$

$$\phi = 90^{\circ} : \qquad -\frac{yz}{x_s^2} v + w = -\frac{\lambda x_s}{D} n(y,z) \tag{6.8c}$$

The actual values of displacements v and w given by equations (6.7a) and (6.7b) are substituted in equations (6.8) and, using the fact that the viewing angle in these experiments was such that $\left|\frac{y}{x_s}\right|, \left|\frac{z}{x_s}\right| < \frac{1}{10}$, we may neglect some small terms. Once this was done, the equations were solved for the fringe functions n(y,z) as

Exp. 24 ($\phi = 0^{\circ}$) : $\quad n(y,z) \simeq (5.82 \times 10^{-4}) \frac{D}{\lambda x_s} z$

Exp. 25 ($\phi = 45^{\circ}$) : $\quad n(y,z) \simeq (5.82 \times 10^{-4}) \frac{D}{\lambda x_s} \frac{z - y}{\sqrt{2}}$

Exp. 26 ($\phi = 90^{\circ}$) : $\quad n(y,z) \simeq (5.82 \times 10^{-4}) \frac{-D}{\lambda x_s} y$

Thus for Exp. 24 the fringes are predicted to be parallel to the y-axis, for Exp. 25 the fringes are predicted to be straight and inclined at 45° to the y-axis, and for Exp. 26 the fringes are predicted to be parallel to the z-axis.

The DASC parameters used for the three experiments were

x_s = 39 in.

D = 2.5 in.

With these parameters the predicted fringe spacing is .536 in. - the same for all three experiments. The actual fringe patterns obtained by DASC are shown in Figs. 6.11, 6.12 and 6.13 . The fringes are oriented as predicted and, from the microdensitometer traces of these figures, the fringe spacing was found to be .55 in., close to the predicted spacing of .536 in.

Let us now predict the positions and spacing of fringes formed by DASSC,

which for Exp. 2 considered here had the following parameters:

$x_s = 32$ in.

$D = 2.5$ in.

$\theta_x = 20^o$, $\theta_y = 110^o$, $\theta_z = 90^o$

$\Delta y_s = .0608$ in.

$\phi = 0^o$

The displacements and strains given by equations (6.7) are substituted in equation (4.11); we can make use of the fact that the viewing angle was again such that $\left|\frac{y}{x_s}\right|, \left|\frac{z}{x_s}\right| < \frac{1}{10}$ to neglect many small terms and solve the equation for the fringe function n(y,z) as

Exp. 2 : $n(y,z) \simeq 2.328\ z$.

For this experiment the fringes are predicted to be parallel to the y-axis and spaced .429 in. apart. The actual fringe pattern is shown in Fig. 6.14 . The fringes are parallel to the y-axis and the fringe spacing was found from the microdensitometer trace to be .42 in. which compares well with the predicted spacing of .429 in.

A computer program, UONLY.S, was written to calculate v from equation (6.8a) with the w term neglected, or to calculate w from equation (6.8c) with the v term neglected. It computes the displacements from the given parameters of DASC or DASSC and from the fringe center numbers and positions obtained from the microdensitometer trace. The plot of the exact displacement v(z) and the plot of v calculated by UONLY.S, using data obtained by DASC, is shown in Fig. 6.15 .

The results of these experiments confirm that the response of both DASC and DASSC to the in-plane displacements is accurately described by equations (4.4) and (4.13). In particular, the accuracy of the coefficients b_i and c_i

of equations (4.4) and (4.13) was verified.

6.4 Out-of-Plane Bending of a Thin Beam with a Rectangular Cross-Section

The purpose of this experiment was to verify the formation of fringes by DASSC due to the variable out-of-plane displacement of a specimen surface. A diagram of the experiment is shown in Fig. 6.16 . A thin alluminum beam with a rectangular cross-section was clamped at the ends and its center was displaced, by use of a micrometer, a known distance δ out of the plane.

In Appendix V strength of materials theory was used to derive expressions closely approximating the actual displacements and strains that occur in the visible surface of the beam. The strains in the z direction were not derived as the beam deformation will be viewed through an aperture set(s) at zero inclination to the y-axis.

The parameters of DASSC used in the beam bending experiments considered in this section were similar to those of Exp. 101C given here as

beam: $\frac{1}{4}$ x 2 x 50 in. $\nu = .25$

$x_s = 39.75$ in. , $\Delta y_s = -.12$ in. , $X_s = 37.84$ in.

$D = 2.5$ in.

$\theta_x = 76.8^o$, $\theta_y = 166.8^o$, $\theta_z = 90^o$

With these parameters equation (4.11) becomes

$$\frac{y}{39.75} u + v - \frac{yz}{1580} w - 2.23\, u,_y + 1.82 \left(\frac{y - 1.25}{39.75} - .919\right) v,_y +$$

$$+ 1.82 \frac{z}{39.75} w,_y = - .00032\, n(y,z)$$

With the displacements and strains derived in Appendix T the above equation becomes

$$\underbrace{2.5 \times 10^{-2}\, y \left[1 - 3\left(\frac{y}{25}\right)^2 + 2\left(\frac{y}{25}\right)^3\right]}_{u} + \underbrace{1.2 \times 10^{-3}\, y\left(1 + \frac{y}{25}\right)}_{v} +$$

$$\underbrace{1.9 \times 10^{-7}\, yz^2 \left[1 - 2\left(\frac{y}{25}\right)\right]}_{w} + \underbrace{2.1 \times 10^{-2}\, y\left(1 - \frac{y}{25}\right)}_{u,y} +$$

$$\underbrace{2.2 \times 10^{-3} \left(\frac{y - 1.25}{39.75} - .919\right)\left[1 - 2\left(\frac{y}{25}\right)\right]}_{v,y} + \underbrace{1.1 \times 10^{-6}\, z^2}_{w,y} = -\frac{.00032}{\delta}\, n$$

It is obvious that, in the case of out-of-plane bending of beams, the fringe equation may be approximated by only two terms involving u and $u,_y$. A more accurate approximation would involve $u, u,_y, v$ and $v,_y$ terms. Note that for a beam these four quantities are closely approximated by functions of y only.

Let us first consider the use of DASC to determine the beam deformation. In the beam bending experiments considered here, the term involving u is so much larger than the terms involving v and w that equation (4.10b) determines u with sufficient accuracy.

$$u(y,z) \simeq -\frac{\lambda x_s^2}{D}\frac{n(y,z)}{y} \qquad y \neq 0 \tag{4.10b}$$

In Exp. 16 considered here the DASC parameters were

beam: $\frac{1}{8} \times 2 \times 55$ in.

$x_s = 29.5$ in.

$D = 2.5$ in.

$\delta = .50$ mm $= .019685$ in.

The fringe pattern of this experiment is shown in Fig. 6.17 . Once the fringe centers are correctly numbered and their coordinates are read off the microdensitometer trace, the displacement u is obtained by the use of

equation (4.10). A computer program, BEAM1.S, was written to calculate u(y,z) this way, and u determined by BEAM1.S and u obtained from the strength of materials theory are both plotted in Fig. 6.18. The two displacements correlate quite well.

When DASSC is used to "photograph" the out-of-plane bending of the beam, a number of ways to determine the out-of-plane displacement and slope is available. We shall consider several of these and point out their advantages and disadvantages.

It was shown in Section 4.8 that, for the beam bending experiments considered here, equation (4.11) may be accurately approximated by keeping only the terms involving u and u, ; hence, equation (4.11) reduces to equation (4.16), which for $\phi = 0^{o}$ becomes

$$au + du,_{y} = N(y,z) \tag{6.9}$$

In the case of beam bending, u and $u,_{y}$ are essentially functions of y only and, therefore, the partial derivative in equation (6.9) may be replaced by an ordinary derivative. After some rearranging we obtain

$$\frac{du}{dy} + \frac{a}{d} u = \frac{N(y)}{d} \tag{6.10}$$

In Section 4.11 is shown that, if the out-of-plane displacement at one point, $y = y_0$ is known, the solution to equation (6.10) is given by equation (4.32) with $p = a/d$ and $q = N(y)/d$. This approach was used to solve for u and $u,_{y}$ in Exp. 101C. The DASSC parameters used in Exp. 101C are given on page 118 and the fringe pattern is shown in Fig. 6.19 . A program, OUT1M.S, which was written solves equation (6.10) according to equation (4.30) with $\phi = 0^{o}$. The program accepts the system parameters, displacement at one point, and fringe centers as data and calculates u and $u,_{y}$. The graphs of

predicted u and $u,_y$ vs. the actual u and $u,_y$ obtained by DASSC and OUTIM.S are shown in Figs. 6.20 and 6.21 . Note that in both cases the agreement between predicted and actual values is quite good.

In the out-of-plane displacement u is not known at any point of the visible part of the beam, the two photographs must be taken and use made of the approach of Section 4.8 . Quantities u and $u,_y$ are determined from equation (4.16) which for the aperture set rotation $\phi = 0^o$ becomes

$$A_i u + D_i u,_y = N_i(y,z) \qquad i = 1,2 \tag{6.11}$$

A program, BEAM2.S, which solves equation (6.11) was written to determine u and $u,_y$ for Exp. 101; the system parameters were as follows:

beam: ¼ x 2 x 50 in.

x_s = 39.75 in. (illumination in x,y plane)

D = 2.5 in.	$\theta_x = 76.8^o$	Δy_s = - .012 in.	Exp. 101A
D = 1.75 in.	$\theta_x = 26^o$	Δy_s = - .097 in.	Exp. 101B
D = 2.5 in	$\theta_x = 76.8^o$	Δy_s = - .12 in	Exp. 101C

The two fringe patterns for Exp. 101A and Exp. 101B are shown in Figs. 6.22 and 6.23 . The plots of the predicted u and $u,_y$ and the experimentally found u and $u,_y$ (calculated by BEAM2.S) are shown in Fig.6.24 and 6.25 . Again the agreement between the predicted and the experimental results is good. It is important to note that it is not enough to know that $|u|, |u,_y| >> |v|, |v,_y|, |w|, |w,_y|$ and to ensure that $d_1 - d_2 \neq 0$; equation (4.32) must be satisfied as well to obtain accurate solutions for u and $u,_y$. For example, the combination of Exp. 101A and Exp. 101B satisfies this requirement while the combination of Exp. 101B and Exp. 101C does not.

The experiments described in this section have confirmed that DASSC forms fringes according to equation (4.13) for the case of out-of-plane

bending and have thus verified the accuracy of coefficients a_i and d_i of equation (4.13).

6.5 In-Plane Stretching of a Thin Beam with a Rectangular Cross-Section

The purpose of this experiment was to verify the formation of fringes by DASSC due to the in-plane displacement and straining of the specimen surface. The schematic diagram of the experiment is shown in Fig. 6.26 . A thin, fairly wide, acrylic beam with a rectangular cross-section was clamped at its ends, and a tensile load was applied between the two exposures in such a way that the center of the beam remained stationary while its ends were displaced a known amount. Due to the initial crookedness of the beam, the poisson effect, and some misalignment of the system, the beam was also displaced out-of-plane by a small amount. This out-of-plane displacement was monitored at the z = 0 line by a number of dial gages. At the point (-t/2,0,h/2) there was also a dial gage which measured the displacement of this point in the z direction; this last displacement was caused mainly by the poisson effect. A strain gage was cemented to the illuminated surface of the beam and its reading served as a standard against which the strain determined experimentally by DASSC was compared.

The beam deformation is essentially a special case of the plane stress, and the strains of the neutral surface are related to the imposed increase V in the length L of the beam by

$$\varepsilon_{y0} = \frac{V}{L}$$

$$\varepsilon_{x0} = -\nu\varepsilon_{y0} = -\nu\frac{V}{L}$$

Since the in-plane stretching is accompanied by a small unknown out-of-plane displacement u , the displacements and strains of the illuminated surface of the specimen are given as

$$v,_y = \varepsilon_y = \varepsilon_{y0} - \frac{t}{2} u,_{yy} = \frac{V}{L} - \frac{t}{2} u,_{yy}$$

$$v = y\frac{V}{L} - \frac{t}{2} u,_y \qquad v(0,z) = 0$$

$$w,_z = \varepsilon_z = -\nu\varepsilon_y = -\nu\left(\frac{V}{L} - \frac{t}{2} u,_{yy}\right)$$

$$w = -\nu\left(\frac{V}{L} - \frac{t}{2} u,_{yy}\right)z \qquad w(y,0) = 0$$

$$w,_y = \nu z\frac{t}{2} u,_{yyy}$$

The deformation of the beam was photographed by DASSC with the apertures at $\phi = 0^o$, and the field of view was such that $\left|\frac{y}{x_s}\right| < \frac{1}{9}$, $\left|\frac{z}{x_s}\right| < \frac{1}{15}$. For these parameters and the assumed form of the displacements and strains, and the specimen illumination in x,y plane equation (4.11) reduces to

$$\underbrace{\frac{y}{x_s} u}_{u} + \underbrace{\left(y\frac{V}{L} - \frac{t}{2} u,_y\right)}_{v} - \underbrace{\frac{yz}{x_s^2}\nu\left(-\frac{V}{L} + \frac{t}{2} u,_{yy}\right)z}_{w} + \frac{\Delta y_{si}X_{si}}{D_i}\left[\underbrace{(1 + \cos\theta_{xi})u,_y}_{u,_y} - \underbrace{\left(\frac{y - D_i/2}{x_s} - \cos\theta_{yi}\right)\left(\frac{V}{L} - \frac{t}{2} u,_{yy}\right)}_{v,_y} - \underbrace{\frac{z}{x_s}\nu z\frac{t}{2} u,_{yyy}}_{w,_y}\right] = -\frac{\lambda X_{si}}{D_i} n_i$$

The out-of-plane displacement u caused by the initial crookedness of the beam or by a misalignment of the loading mechanism was quite small, and its shape was found to be smooth and sinusoidal-like with one half period over the beam length. Because of these characteristics, and since the beam was thin (t = .25 in.), the terms $\frac{1}{2}tu,_y$,$\frac{1}{2}tu,_{yy}$ and $\frac{1}{2}tu,_{yyy}$ are very small. Thus the terms involving w and $w,_y$ may be neglected from the last equation and for this case equation (4.11) reduces to the form

$$\frac{y}{x_s} u + v + d_i u,_y + f_i v,_y = N_i \tag{4.22}$$

If u and $u,_y$ are very small, so that they are also negligible, equation (4.22) reduces to the simple form

$$v + f_i v,_y = N_i \tag{6.13}$$

Equation (6.13) is analogous to equation (4.34) and can be solved for v in the same manner. Unfortunately, in the actual testing the term $d_i u,_y$ was found to be large in magnitude and equation (6.13) could not be used. However, by a careful alignment of the loading mechanism it was possible to limit the out-of-plane displacement u to magnitudes less than . 0015 in. and for such a small value of u, the term $\frac{y}{x_s}$ u is very small, and it is then possible to solve for $u, u,_y, v$, and $v,_y$ from equation (4.22) in the manner discussed in Section 4.10 . A computer program PLATE2.S was written to solve equation (4.22) this way and was used to calculate the displacements and strains from the data of Exp. 114C and Exp. 114D which had the following parameters:

beam: ¼ x 6 x 32 in.

x_s = 45 in.

D = 2.5 in.

Δy_s = .07 in. X_s = 46.26 in. Exp. 114B

θ_x = - 21.2° θ_y = 68.8° θ_z = 90°

D = 1.75 in.

Δy_s = .14 in. X_s = 48.6 in. Exp. 114C

θ_x = - 21.2° θ_y = 68.8° θ_z = 90°

D = 2.5 in.

Δy_s = .23 in. X_s = 49.1 in. Exp. 114D

θ_x = 23.7° θ_y = 113.7° θ_z = 90°

v(- 3,0) = 0

u(- 1,0) = - .00102 in.

$v,_y(-3.625,0) = 413 \times 10^{-6}$

The fringe patterns obtained by DASSC are shown in Fig. 6.27 and Fig.6.28 . The computer plots of predicted and experimental displacements and strains done by PLATE2.S are shown in Figs. 6.29 through Fig. 6.32 . The value of $v,_y(-3.625,0)$ calculated by the program from the two fringe patterns is 419×10^{-6}, which compares favorably with the strain gage reading of 413×10^{-6} there.

If we do not wish to neglect the out-of-plane displacement and strain, then three independent and properly chosen photographs are needed to solve for the displacements and strains. A computer program, PLATE3.S, which solves equation (4.14b) for $u,_y$ and $v,_y$ in the way discussed in Section 4.6 (and for u and v by numerical intergration), was used to calculate these unknowns for Exp. 114B, Exp. 114C and Exp. 114D. The fringe pattern of Exp. 114B is shown in Fig. 6.33 and the displacements and strains calculated by PLATE3.S are shown in Figs. 6.34 through Fig. 6.37 . This time the experimentally determined strain at y = -3.625 in. is 414×10^{-6} , which again compares well with the strain gage reading of 413×10^{-6} there. It should be realized, however, that it is a coincidence that the two strains are this close at y = -3.625 in., as usually the two strains differ elsewhere by as much as five percent or more.

Alternatively, the two displacements u and v and the strains $u,_y$ and $v,_y$ may be calculated by the finite difference method discussed in Section 4.10 . A computer program, FD2, based on equations (4.23), (4.24), and (4.25) was written and used to calculate $u,v,u,_y$, and $v,_y$ from the fringe patterns of Exp. 114C and Exp. 114D. Since the program required one boundary condition on u and another on v, u(-1,0) (measured by one of the dial gages) and v(-3,0) were used. Figures 6.38 through 6.41 show the comparison of the actual and calculated displacements and strains. The experimentally determined strain

at y = -3.625 in. is 420 x 10^{-6} vs. 413 x 10^{-6} measured by the strain gage there.

All three approaches used to calculate the displacements and strains for this particular example yield reasonably accurate solutions. If the displacements $u(y_0,0)$ and $v(y_0,0)$ are available, the program FD2 should be used as it is, in general, more accurate, easier to write and more efficient than the program PLATE2.S. If the displacements $u(y_0,0)$ and $v(y_0,0)$ are not available, then one must, of necessity, use the program PLATE3.S. to determine the two strains and the "displacement sum".

These experiments have demonstrated the feasibility of using DASSC in testing involving primarily the plane stress deformation and in particular the accuracy of the coefficient f was verified.

6.6 In-Plane Stretching of a Beam with a Variable Cross-Section

The purpose of this experiment was to determine the performance of DASSC in a more "practical" type of investigation and to test the accuracy of the two-dimensional solution scheme(s) for displacements and strains. Unfortunately, at the time this experiment was done, the theory of the fringe formation by the DASSC had not yet been fully developed and, hence, the experiment was not set up in the way which would allow accurate determination of all displacements and strains. In particular, the effect of the displacement w and its two derivatives, $w,_y$ and $w,_z$, on the fringe formation by DASSC was not known.

The dimensions of the acrylic specimen used in this experiment are shown in Fig. 6.42. Two strain gages were cemented to the illuminated surface of the beam at the (-3,0) and (5,0) locations to measure the surface strains there for later comparison with the strains obtained with DASSC. An axial tensile load was imposed on the specimen by the use of the same loading apparatus as the one described in the preceeding section and shown in Fig.6.26.

The out-of-plane displacements of the beam were measured by a set of dial gages. The beam center, coincident with the coordinate origin, was kept in the same position during the two exposures with the aid of the Fotonic Sensor.

DASSC used in this experiment was equipped with the shutter shown in Fig. 6.43 so that it was possible to use two illuminating beams in the x,y plane in such a way that one illuminating beam was used with the inner aperture sets and the other illuminating beam was used with the outer aperture sets. We know now that the use of illumination in the x,y plane was unfortunate, as it makes DASSC insensitive to the strains $w,_y$ and $w,_z$.

In this experiment DASSC was used to take four photographs with the following parameters:

x_s = 45 in.

D = 1.75 in

Δy_s = .0914 in. Exp. 122S1

$\theta_x = -20.5^o$ $\theta_y = 69.5^o$ $\theta_z = 90^o$

$\phi = 0^o$

D = 2.50 in

Δy_s = .162 in. Exp. 122S2

$\theta_x = 24^o$ $\theta_y = 114^o$ $\theta_z = 90^o$

$\phi = 0^o$

D = 1.75 in.

Δy_s = .104 in Exp. 122S3

$\theta_x = -20.5^o$ $\theta_y = 69.5^o$ $\theta_z = 90^o$

$\phi = 135^o$

D = 2.5 in.

Δy_s = .171 in Exp. 122S6

$\theta_x = 24^o$ $\theta_y = 114^o$ $\theta_z = 90^o$

$\phi = 135^o$

The computer program FD2, based on equations (4.24), and (4.26), was used to calculate u(y,0) and v(y,0) from the photographs of Exp. 122S1 and Exp. 122S2 shown in Figs. 6.44 and 6.45. The two displacements, u(y,0) and v(y,0), and their derivatives calculated by FD2 are compared to those displacements and their derivatives determined from the dial gages and also to the finite element solution of this problem. These comparisons are shown in Figs. 6.46 through 6.49 and as can be seen from the graphs, the displacements and strains agree quite well.

We would now like to calculate u(y,z), v(y,z) and w(y,z). To do this, we need three "independent" photographs taken by DASSC having three aperture sets and three illuminating beams with at least one of them not being in the x,y plane. The three displacements may then be calculated with the use of the scheme discussed in Section 4.9 and based on equation (4.19). However, as was already mentioned, when this experiment was done DASSC was equipped with two aperture sets and two illuminating beams in the x,y plane were used. Thus, only two independent photographs are available, and therefore the scheme based on equation (4.23) must be used to calculate v(y,z) and w(y,z), with u(y,z) assumed to be known.

The displacement field u(y,z) was set equal to u(y,0) as calculated by FD2 and this has introduced a small but negligible error as, obviously, $u(y,z) \neq u(y,0)$ for $z \neq 0$. The error is expected to be small because u(y,z) is caused mainly by the out-of-plane bending due to a system misalignment and by the crookedness of the specimen and hence the out-of-plane displacement was most likely the same for all points on lines y = constant. The variation in u(y,z), for y = constant, is caused by the reduction of the specimen thickness due to the poisson effect, but this variation is small enough so that it may be neglected. Since the boundary condition w(y,0) could not be found, it was therefore set equal to the dial gage reading at the point (0,1) and corrected

for the poisson reduction of the beam half-width there.

Using the fringe patterns of Exp. 122S3 and Exp. 122S6, shown in Fig. 6.50 and Fig. 6.51, and the solution scheme based on equation (4.21), we may calculate the displacements $v(y,z)$ and $w(y,z)$ over a part of one quarter of the beam surface shown in Fig. 6.52 . Since the specimen illumination was in the x,y plane, $w(y,z)$ was not calculated accurately enough and is not shown. The displacement $v(y,z)$ and its partial derivative $v,_y(y,z)$ are compared to the finite element solution in Figs. 6.53 trough 6.55 . So that we might see the effect of the accuracy of the boundary condition on $v(y,z)$, two solutions for $v(y,z)$ and $v,_y(y,z)$ were found. We obtained one solution by using $u(y,0)$ and $v(y,0)$ as calculated by FD2, and the other solution by using $u(y,0)$ and $v(y,0)$ as given by the finite element solution and dial gage readings. From the two plots it is obvious that either of the two boundary conditions yields reasonably accurate $v(y,z)$ and $v,_y(y,z)$.

The result of this particular experiment confirm that the two dimensional computing schemes can produce accurate solutions for $v(y,z)$ and $v,_y(y,z)$. Had the experiment been set up properly - and the computer simulation of the experiment confirms this - all displacements and strains could be calculated with acceptable accuracy.

6.7 In-Plane Stretching of a Wooden Beam

The aim of this experiment was to test the possibility of using DASC or DASSC to measure the surface deformation of specimens made of materials such as wood. The wooden beam used in this experiment shown in Fig.5. ;was 4 in. wide, ½ in. thick, and 48 in. long, with a knot of approximately 1 in. diameter located at the center of the beam. The beam was subjected to an axial tensile load using the same experimental setup as is shown in Fig. 6.26. The beam center, which was coincident with the coordinate origin, was

maintained stationary during the two exposures with the aid of the Fotonic Sensor. The out-of-plane displacement u(-.5,y,0) of the shadow side of the beam was measured by a number of dial gages. Due to the lack of time, and also because of inadequate control over boundary conditions, no numerical calculations of displacements and strains were performed. Still, the photographs which were taken provide useful information about the application of DASC and DASSC in the testing of highly inhomogeneous materials like wood.

DASC used to produce the photographs of Exp. 132D1 and Exp. 132D2 (shown in Fig. 6.56 and Fig. 6.57) had the following parameters:

x_s = 45 in.

D = 1.75 in.

$\theta_x = -22.5^o$ $\theta_y = 67.5^o$ $\theta_z = 90^o$ Exp. 132D1

$\phi = 0^o$

D = 2.5 in.

$\theta_x = 24.3^o$ $\theta_y = 114.3^o$ $\theta_z = 90^o$ Exp. 132D2

$\phi = 0^o$

The axial load increment between the two exposures was approximately 200 lb., from 1600 lb. to 1800 lb.; this corresponds to the increase of 100 lb/in^2 in tensile stress. The axial load caused some out-of-plane bending which was monitored by the dial gages with the results

v(-.5,0,0) = .0 in.

v(0,16,0) = .00226 in.

v(0,-16,0) = -.00307 in.

u(-.5,-7,0) = .0 in.

u(-.5,-5,0) = -.0000787 in.

u(-.5,-2,0) = -.0000787 in.

u(-.5,1,0) = -.000315 in.

$u(-.5,4,0) = -.000394$ in.

$u(-.5,7,0) = -.000866$ in.

$w(-.25,0,2) = .0$ in.

The fringe patterns in photographs taken by DASC are fairly simple and show that DASC works quite well in testing specimens having highly nonuniform material properties.

DASSC was used to produce the photographs shown in Fig. 6.58 and Fig.6.59, corresponding to Exp. 132S2 and Exp. 132S1, for which it had the parameters:

$x_s = 45$ in.

$D = 1.75$ in.

$\Delta y_s = .0488$ in. Exp. 132S1

$\theta_x = -22.5^o$ $\theta_y = 67.5^o$ $\theta_z = 90^o$

$\phi = 0^o$

$D = 2.5$ in.

$\Delta y_s = .0878$ in. Exp. 132S2

$\theta_x = 24.3^o$ $\theta_y = 114.3^o$ $\theta_z = 90^o$

$\phi = 0^o$

The two fringe patterns obtained by DASSC are extremely complex, which suggest that the tensile loading of the wooden beam causes a complicated strain field in the illuminated surface of the beam. This is most likely due to the "aligning" process of the wood fibers involving large changes in surface slopes to which DASSC is most sensitive. In this particular experiment, the lateral shear Δy_s was obviously set too large, thus making DASSC too sensitive; the resultant fringe patterns were of such complexity as to be of no use in the quantitive analysis, since there was no hope of successfully numbering the fringes in these patterns.

In future experiments of this type, the sensitivity of DASSC would have

to be decreased or the load increment would have to be smaller to produce fringe patterns which could be interpreted. An inclusion of some simple boundary condition, such as a clamped end, would also be helpful.

6.8 Error Analysis

The results of the experiments discussed in this chapter have ascertained that the fringe formation of DASC and DASSC is described with sufficient accuracy for an ordinary laboratory testing by equations (3.20) and (3.26), or their equivalent forms given by equations (4.4) and (4.13).

$$a_i u + b_i v + c_i w = N_i \tag{4.4}$$

$$a_i u + b_i v + \ldots + k_i w_{,z} = N_i \tag{4.13}$$

By using either of the two cameras in a particular experiment we obtain a number of fringe patterns from which the displacements and strains of the specimen surface may then be determined by making use of the various solution schemes derived and discussed in Chapter 4. However, it must be realized that these displacements and strains can be calculated with only a limited accuracy because of the following errors:

1. Errors caused by the approximations made in the derivation of equations (4.4) and (4.13). In the first approximation the real cameras were replaced by the physical models shown in Fig. 3.5 and Fig. 3.11. The second approximation involved deletion of the high order terms throughout the derivation of equations (4.4) and (4.13). To assign a numerical bound on the errors due to these two approximations is very difficult. In principle, it could be done by comparing the results obtained from equations (4.4) and (4.13) with those determined from some "exact" equations derived for more accurate

physical models of the two cameras. It was, however, more convenient to do this experimentally, and by a computer simulation (not discussed in this thesis) of the two cameras, with the results indicating that these errors are less significant than those discussed in the subsequent paragraphs.

2. Errors in coefficients $a_i, \ldots, k_i$ caused by the inaccuracies in the measurement of the parameters of the two cameras. These parameters were usually determined with the following accuracies:

$$D \ldots \pm.005 \text{ in.}$$

$$x_s \ldots \pm.5 \text{ in.}$$

$$\theta_x, \theta_y, \theta_z \ldots \pm 1^{\circ}$$

$$\Delta y_s \ldots \pm.001 \text{ in.}$$

3. Errors in N_i (related to the Moire fringe numbers n_i) caused by a limited accuracy with which the location of the fringe centers may be determined. In the work presented in this thesis the fringe centers were usually located within ±.02 in. from the microdensitometer traces.

4. Errors in the calculated displacements and strains caused by the approximate nature of some of the solution schemes for the displacements and strains. The size of these errors depends on the particular solution scheme, and also on the actual location (y,z) on the specimen surface where the displacements and strains are being calculated.

From the experiments and calculations that were done, and from the computer analysis of the two cameras, it appears that the errors discussed in paragraph 2. are the greatest source of errors in the calculated displacements and strains. In particular, the inaccuracies in the measurements

of Δy_s and somewhat ambiguous parameter x_s cause the largest errors. This problem could be alleviated by making a large number of measurements of Δy_s and then calculating and using its average value; the parameter x_s could be determined more accurately from a number of simple experiments, or the problem with this parameter could be avoided altogether by using a more elaborate models of the two cameras. Such models would include two x-coordinates, one for the aperture plane and the other for the lens, instead of using x_s to approximate both of these coordinates. The simplest, and possibly the only practical way of determining the error caused by the inaccuracies in the camera parameters would involve the repeated use of the appropriate solution scheme, each time with the parameters being slightly changed within their range of accuracy. By examining the set of so calculated numerical values of the displacements and strains an estimate of the accuracy of the results could be obtained.

The comparison of the actual displacements and strains with those obtained through the use of the two cameras in the experiments described in this chapter indicates that all the errors discussed here are usually quite small and hence equations (4.4) and (4.13) need not be altered, although by implementing the suggestions made in this section, still more accurate results could presumably be obtained.

To get some idea about the effect of experimental errors on the accuracy of the calculated displacements and strains, the upper and lower bounds on these quantities are determined. The errors are caused by inaccuracies in the measurement of the camera parameters and fringe locations, and by using their extreme values in the calculations the bounds may be established. This was done at one "typical" point of the specimen surface for the experiments 26 and 114.

In the case of the experiment 26, the displacement w(0.,.547) at the point (0.,.547) is given by equation (6.8c) as

$$w(0.,.547) = -\frac{\lambda x_s}{D} n(0.,.547) \tag{6.14}$$

The parameters of DASC that was used were measured as

λ = .000020256 in.

x_s = 39.0 ± .5 in.

D = 2.500 ± .005 in.

The centers of the fringes shown in Fig. 6.13 were located with accuracy of ± .02 in., and from the plot of n(0,z) (not shown) it was found that n(0.,.547) = 1.00 ± .05. By substituting the parameters λ, x_s, D and n(0.,.547) in equation (6.14), the displacement w(0.,.547) was found as

$$-.000337 \text{ in.} < w(0.,.547) < -.000296 \text{ in.}$$

With the mean value of w(0.,.547) equal to -.000316 in. this displacement may be written as w(0.,.547) = -.000316 ± .000021 in. The bound on w(y,z) was found to be of the same magnitude at the other points of the specimen surface.

Similar calculations were done for experiment 114 which involved the use of DASSC. By varying the camera parameters and the fringe locations within their range of accuracy, and using the computer program FD2 the bounds on the displacements and strains were found at the point (1.0,0.0) as

u(1.0,0.0) = -.00119 ± .00002 in.

v(1.0,0.0) = ..00172 ± .00005 in.

$u_{,y}$(1.0,0.0) = .000946 ± .000094

$v_{,y}$(1.0,0.0) = .000431 ± .000017

At other points on the y-axis the bounds on these displacements and strains were found to be similar to those at the point (1.0,0.0).

The errors in the results of the two experiments that were examined are reasonably small and should provide some indication about the accuracy of the two cameras. In the actual calculations the errors would most likely be even smaller due to some cancellation of errors. The errors in the other experiments were not calculated but should be similar to those in the experiments 26 and 114.

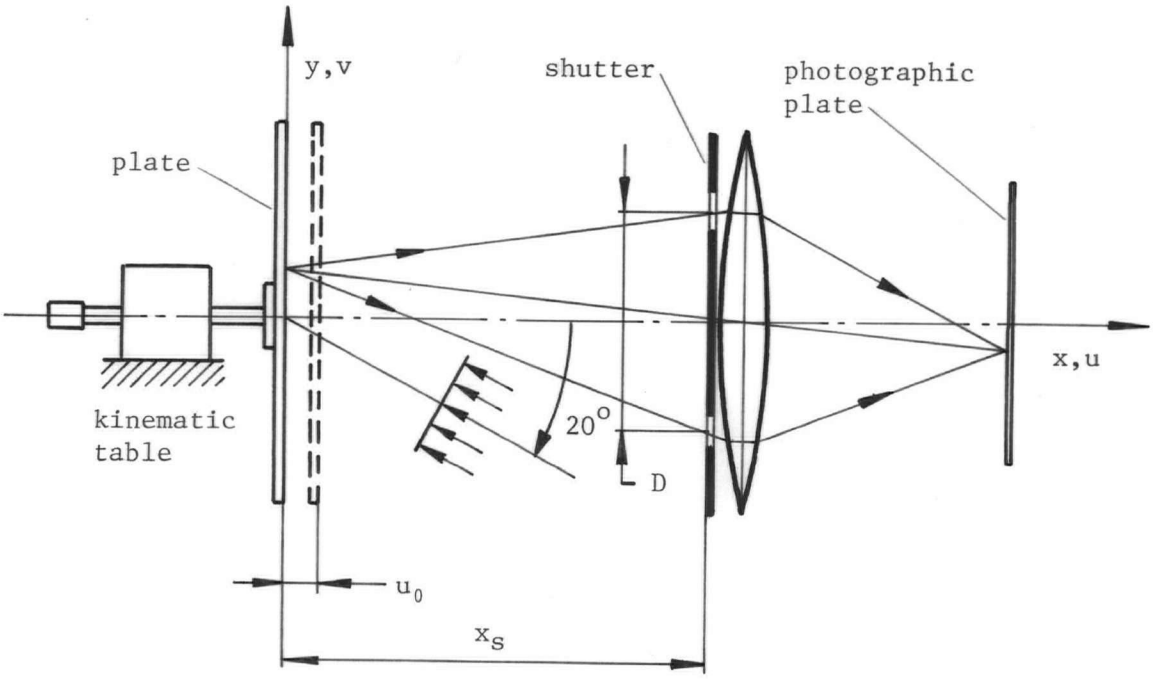

Fig. 6.1 Measurement of the out-of-plane displacement u_0 by DASC.

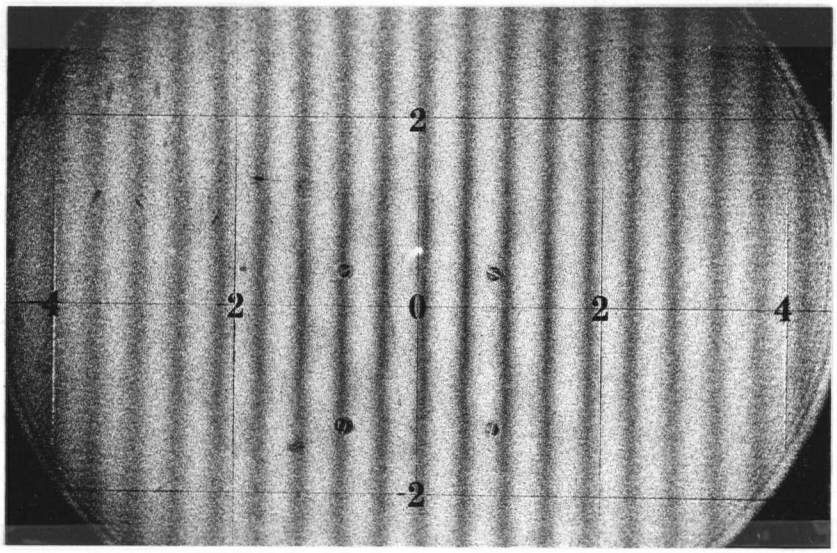

Fig. 6.2 Fringe pattern of Exp. 19.

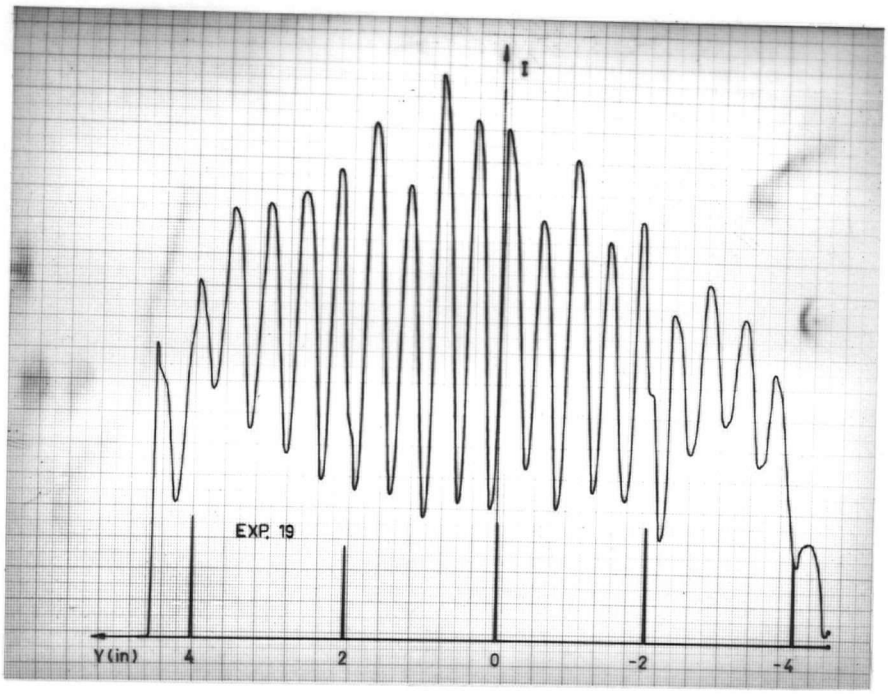

Fig. 6.3 Microdensitometer trace of Exp. 19.

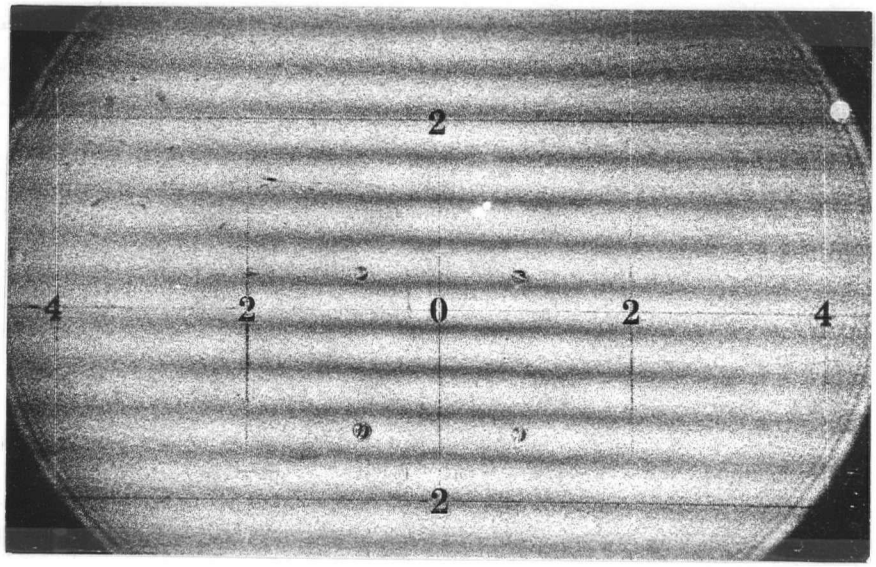

Fig. 6.4 Fringe pattern of Exp. 22.

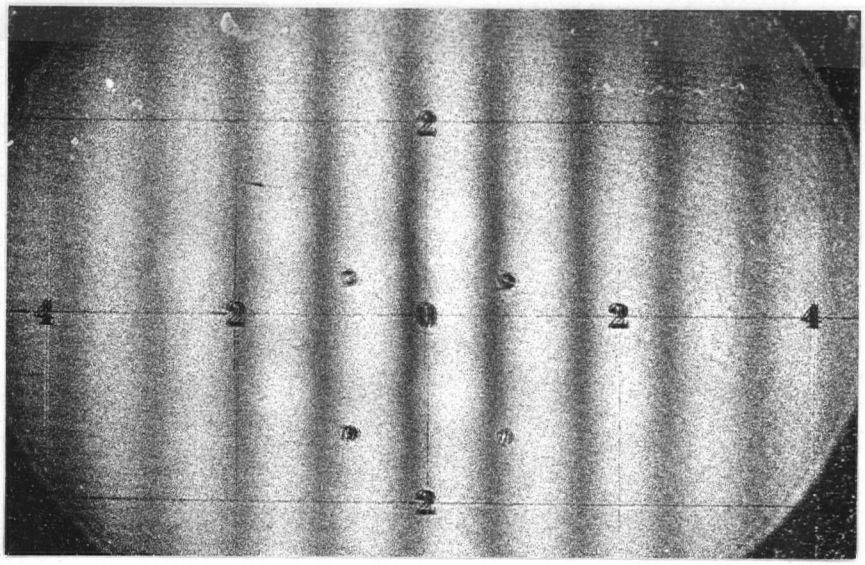

Fig. 6.5 Fringe pattern of Exp. 17.

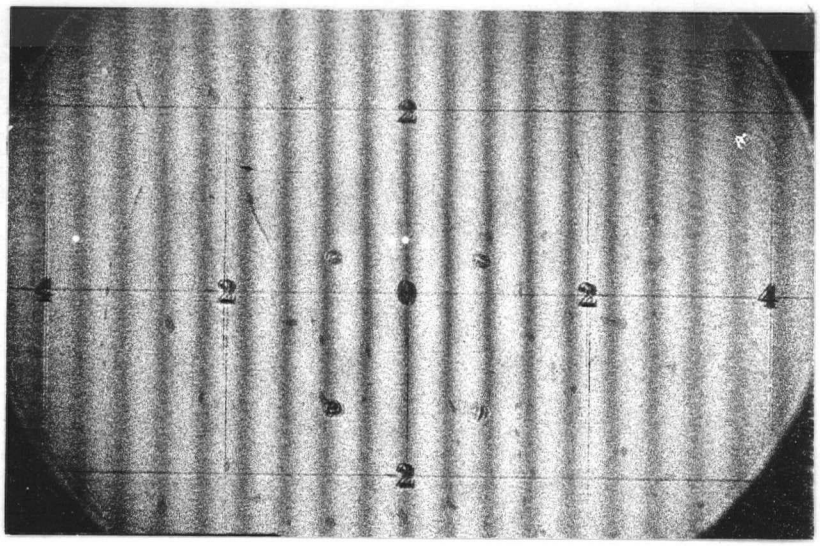

Fig. 6.6 Fringe pattern of Exp. 18.

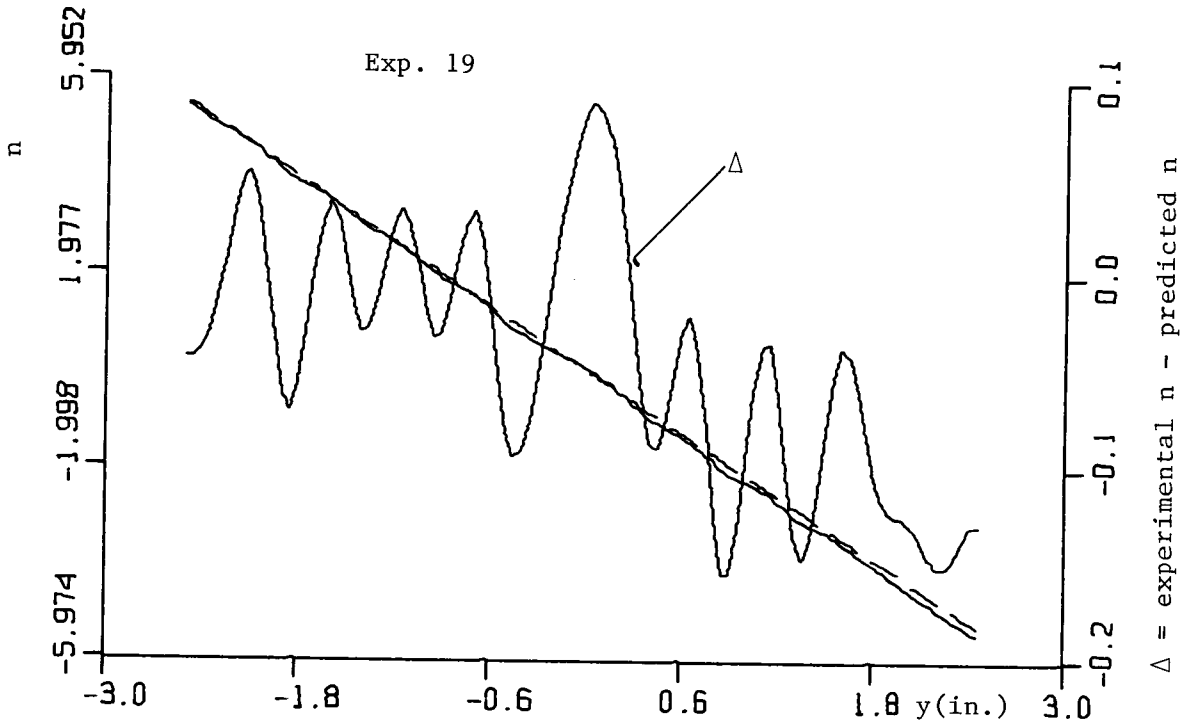

Fig. 6.7 Predicted n (dashed line) vs. experimental n (solid line).

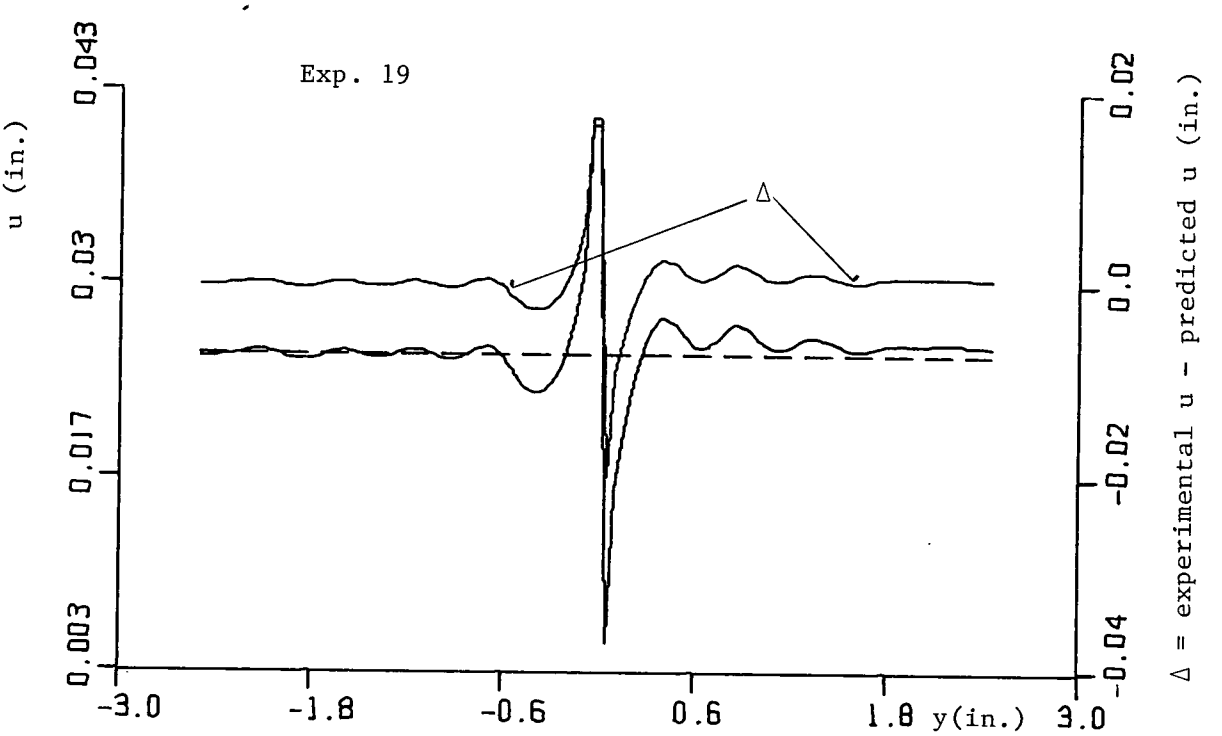

Fig. 6.8 Predicted u (dashed line) vs. experimental u (solid line).

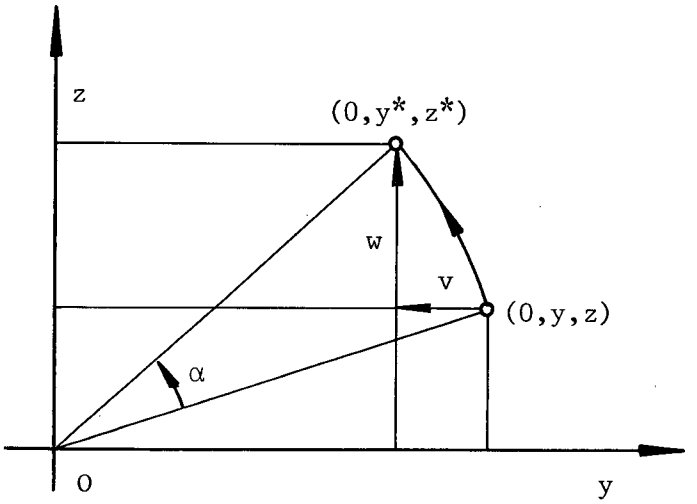

Fig. 6.9 Rotation of a plate about x-axis.

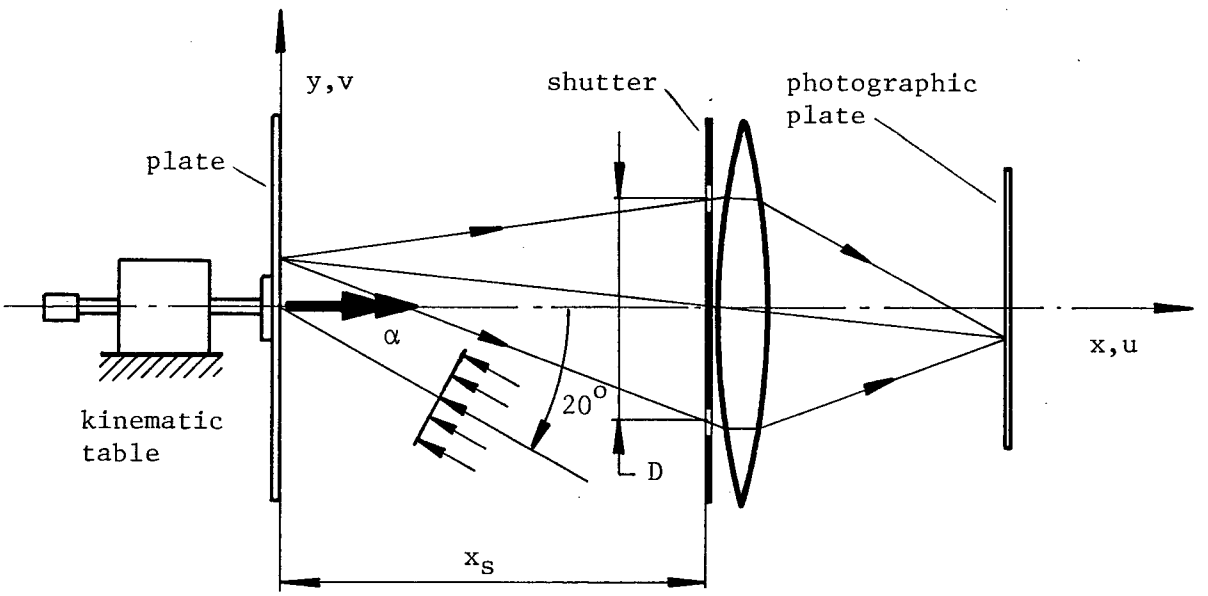

Fig. 6.10 Measurement of the in-plane displacements v and w by DASC.

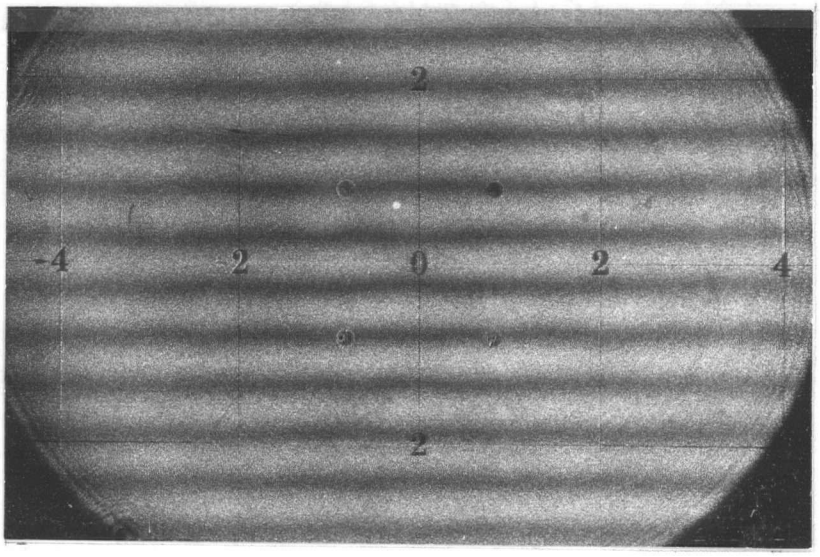

Fig. 6.11 Fringe pattern of Exp. 24.

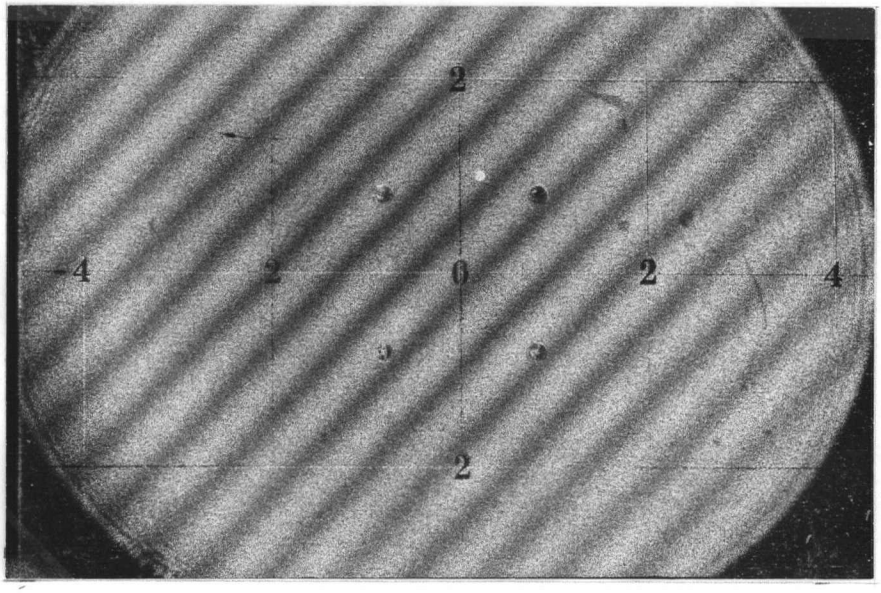

Fig. 6.12 Fringe pattern of Exp. 25.

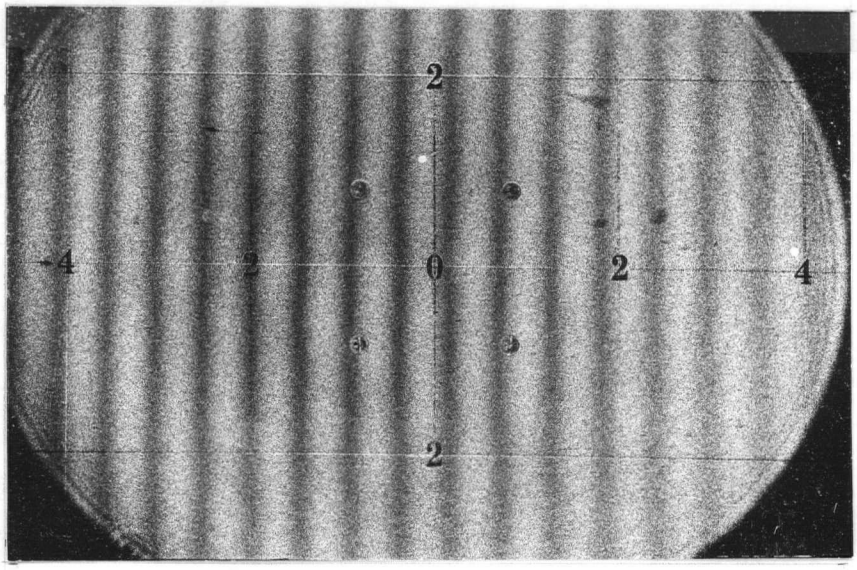

Fig. 6.13 Fringe pattern of Exp. 26.

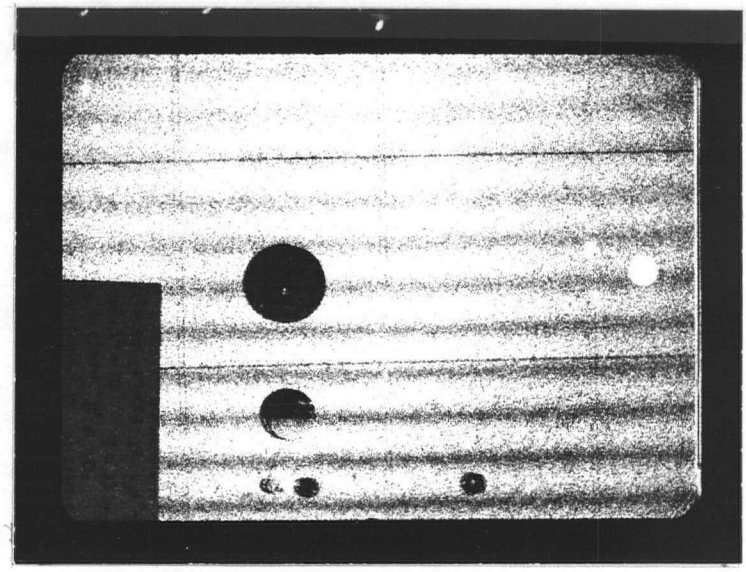

Fig. 6.14 Fringe pattern of Exp. 2.

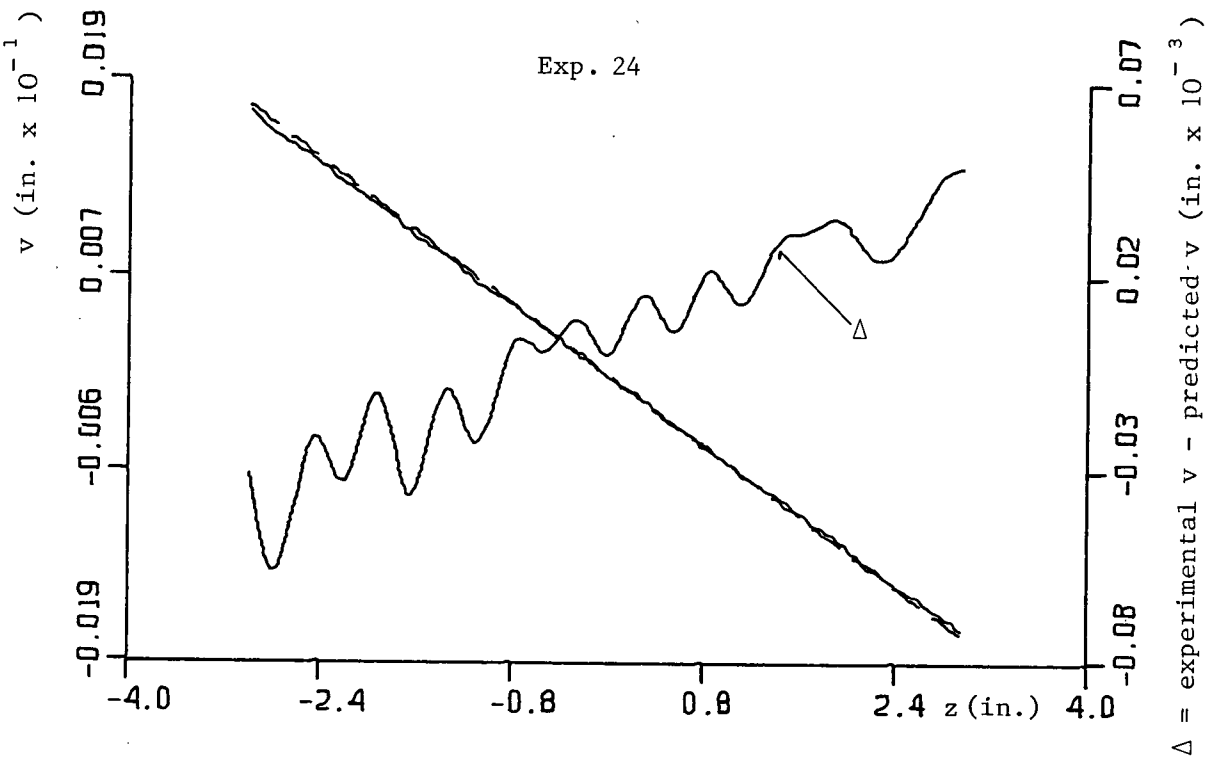

Fig. 6.15 Predicted v (dashed line) vs. experimental v (solid line).

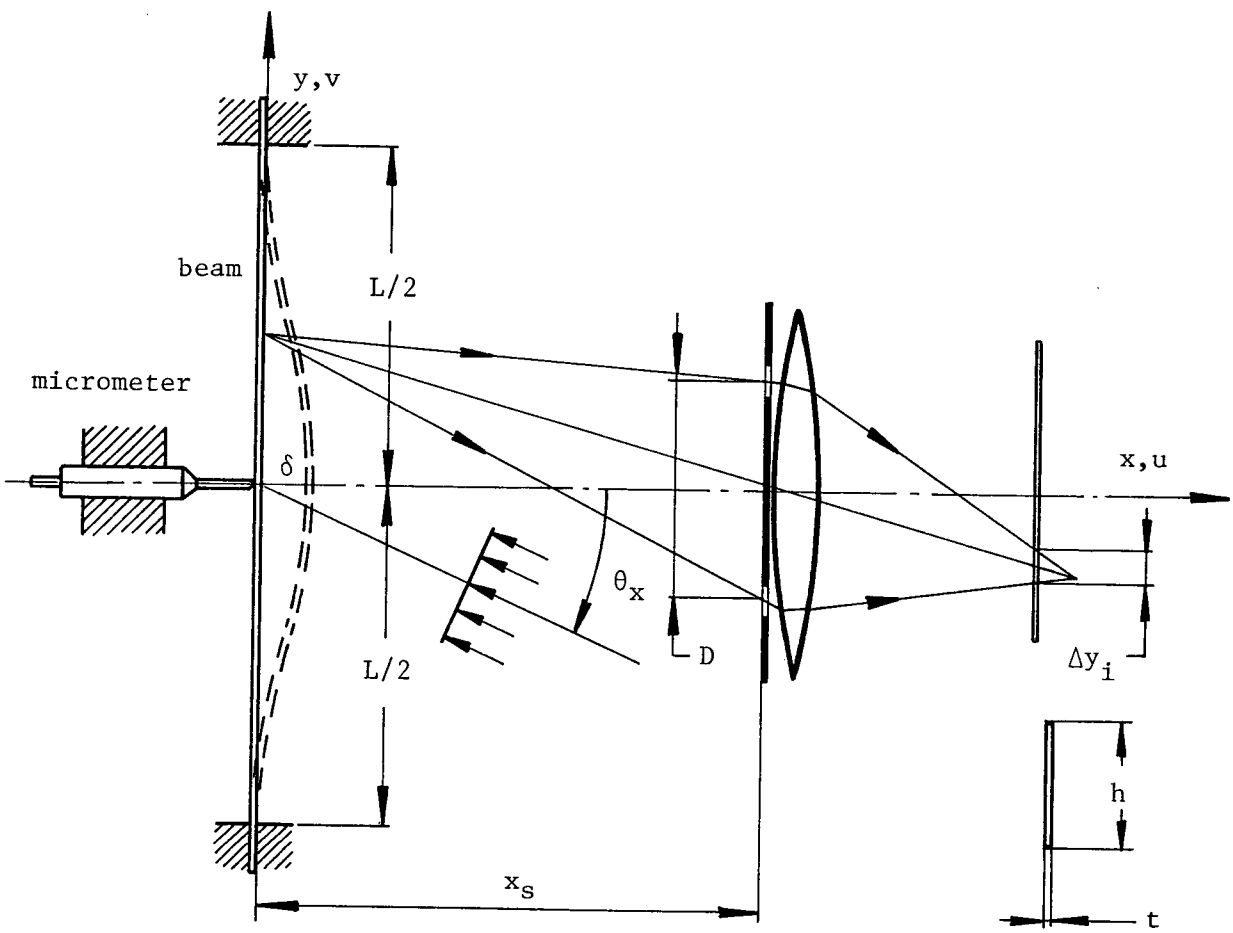

Fig. 6.16 Measurement of the out-of-plane displacement by DASSC.

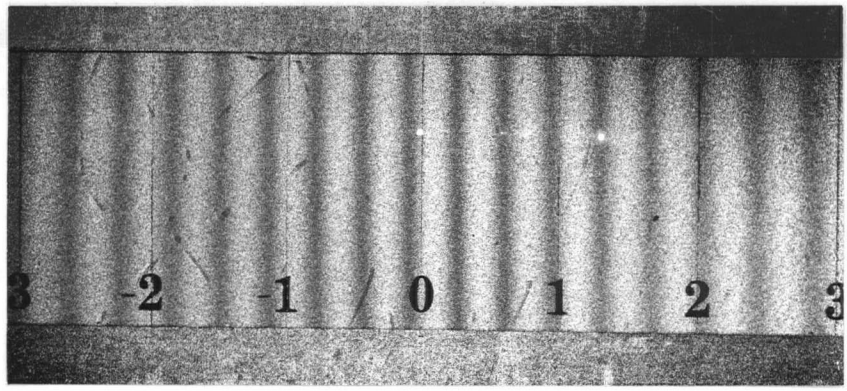

Fig. 6.17 Fringe pattern of Exp. 16.

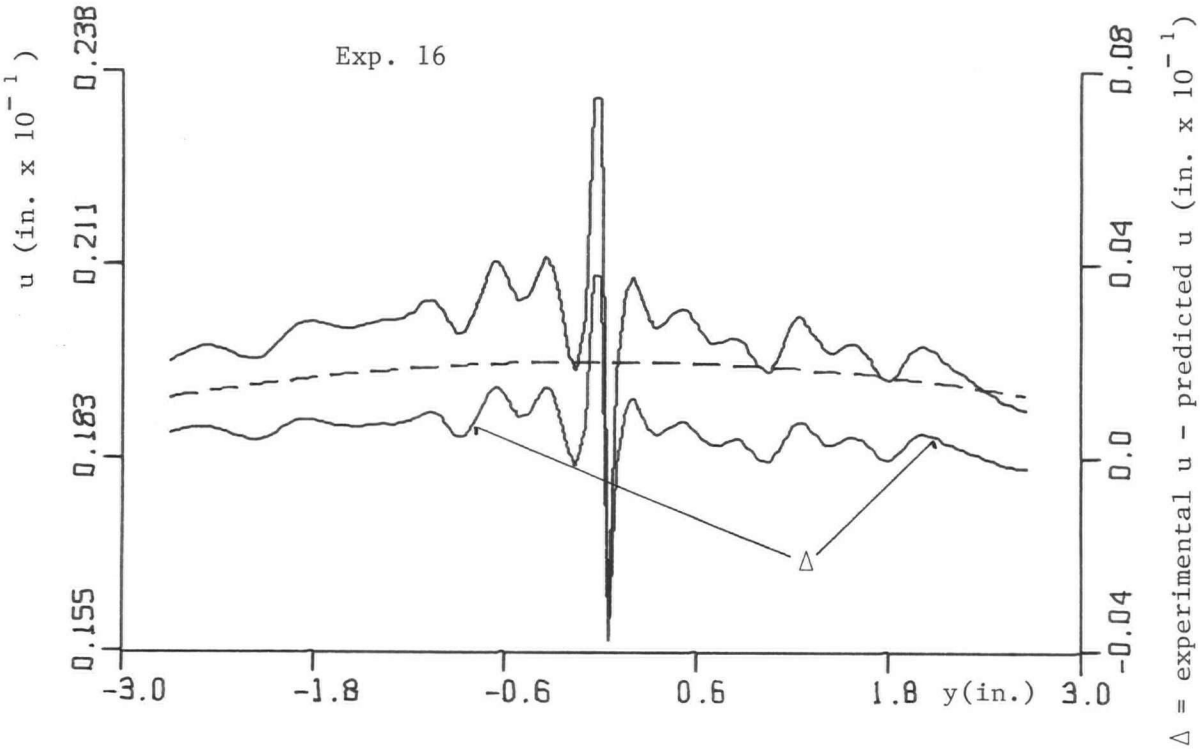

Fig. 6.18 Predicted u (dashed line) vs. experimental u (solid line).

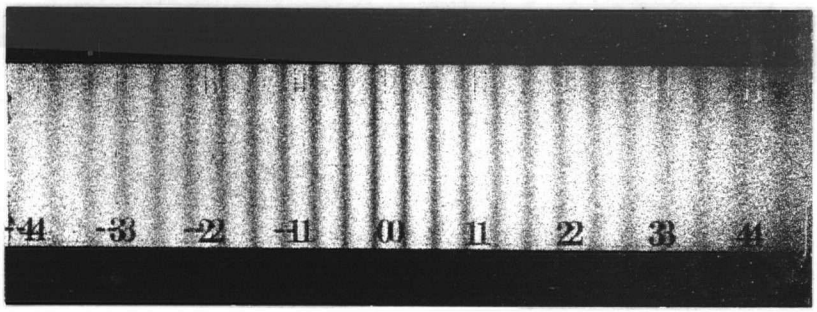

Fig. 6.19 Fringe pattern of Exp. 101C

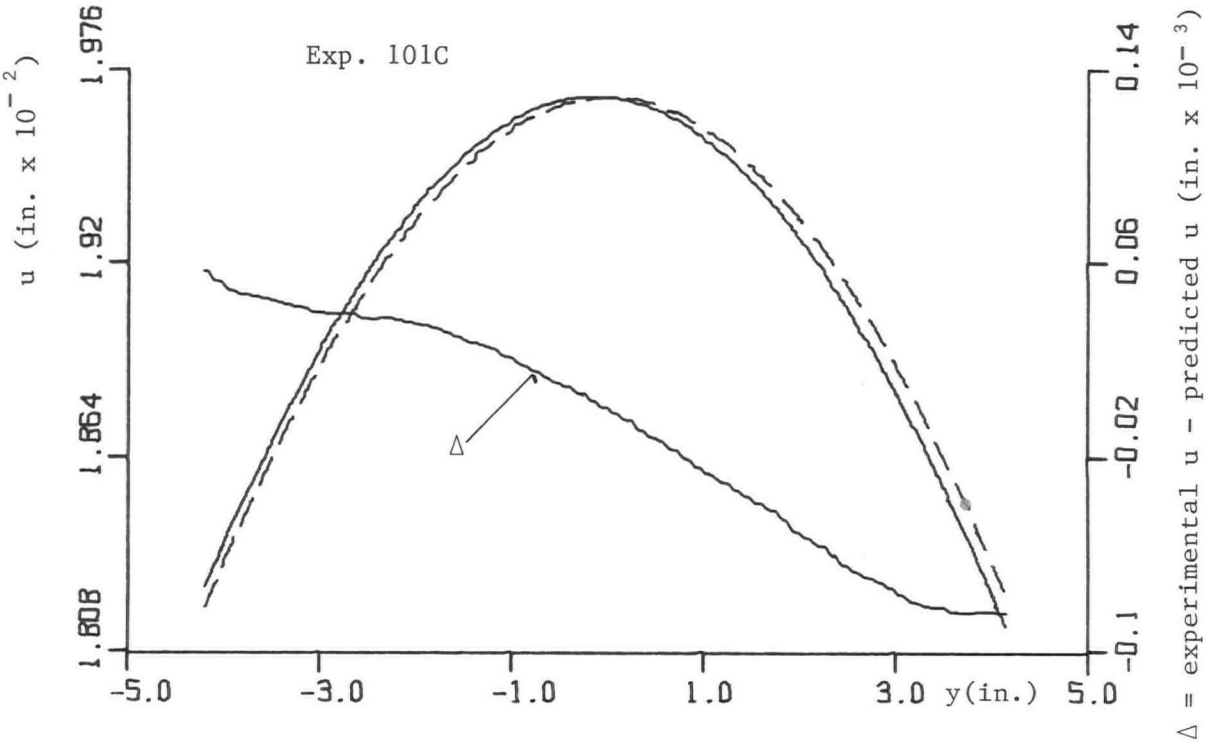

Fig. 6.20 Predicted u (dashed line) vs. experimental u (solid line).

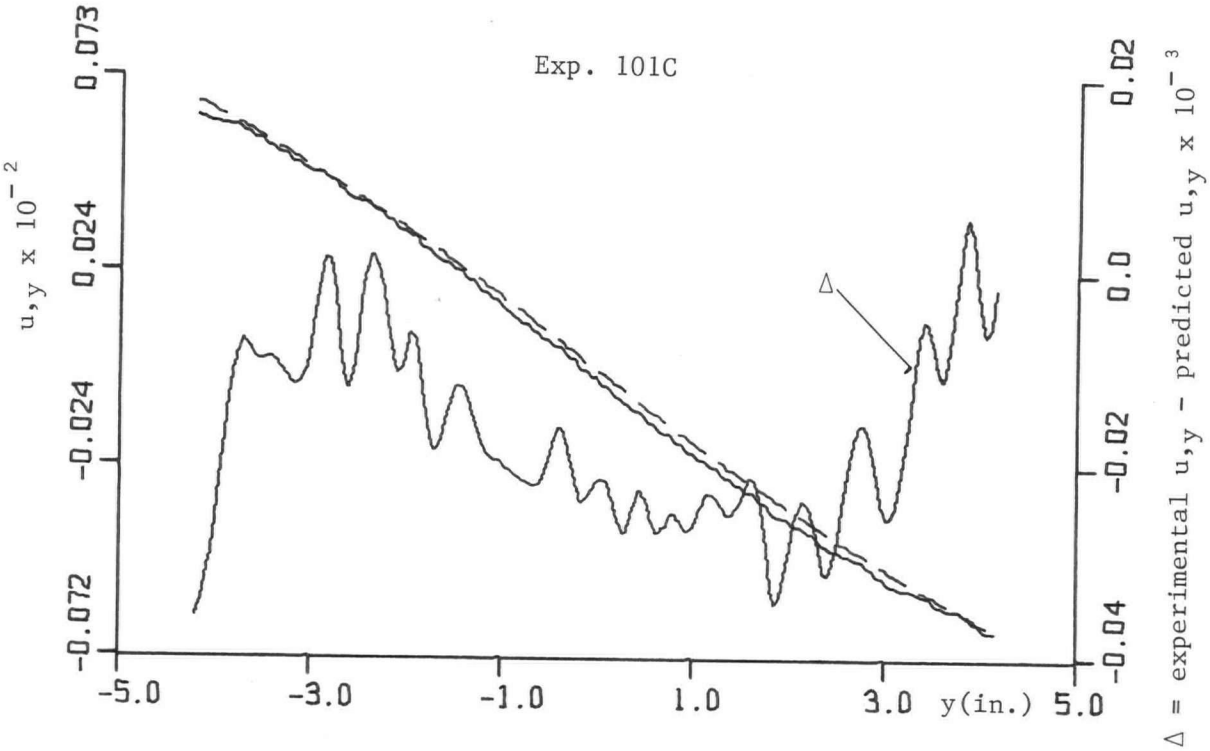

Fig. 6.21 Predicted $u_{,y}$ (dashed line) vs. experimental $u_{,y}$ (solid line).

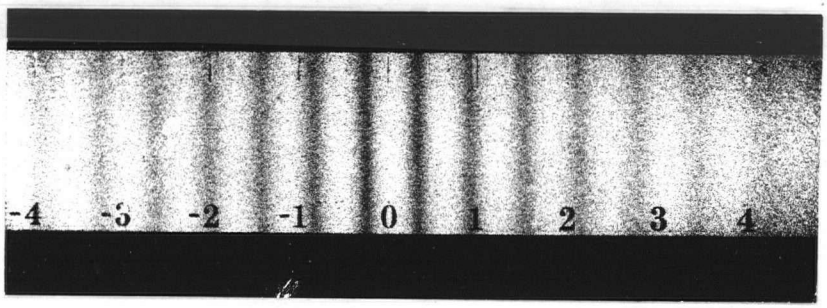

Fig. 6.22 Fringe pattern of Exp. 101A

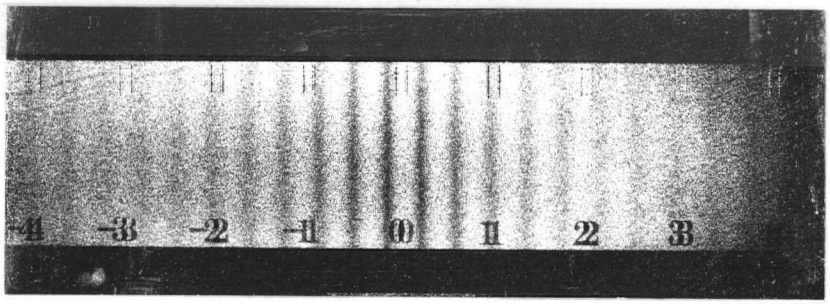

Fig. 6.23 Fringe pattern of Exp. 101B

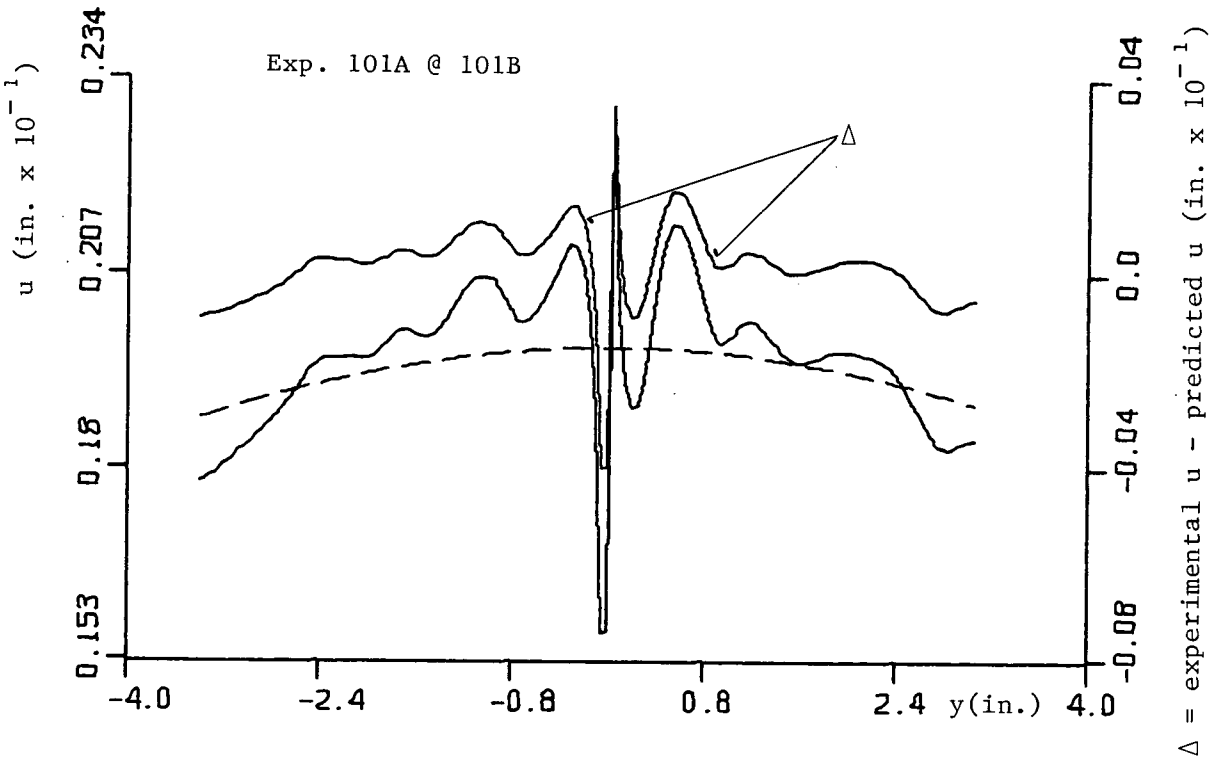

Fig. 6.24 Predicted u (dashed line) vs. experimental u (solid line).

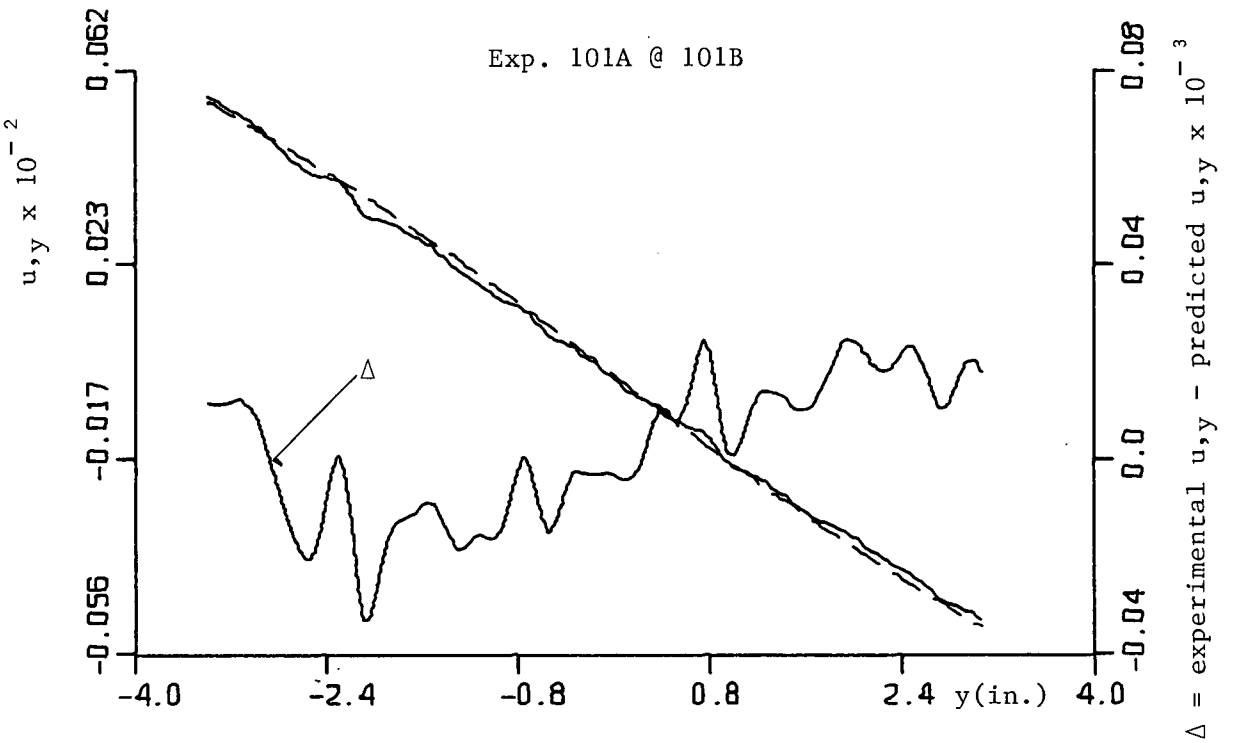

Fig. 6.25 Predicted $u,_y$ (dashed line) vs. experimental $u,_y$ (solid line).

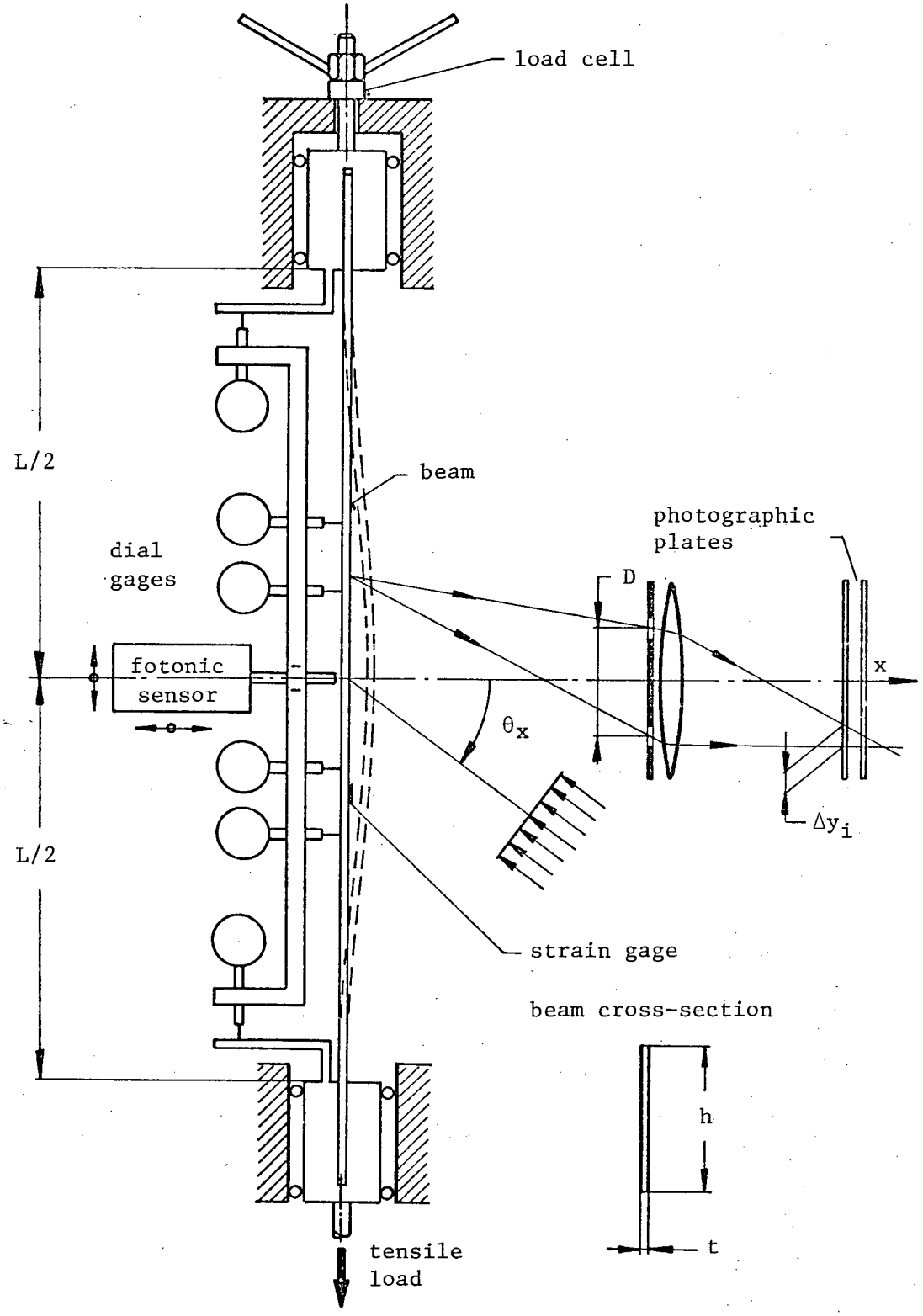

Fig. 6.26 Measurement of the in-plane deformation by DASSC.

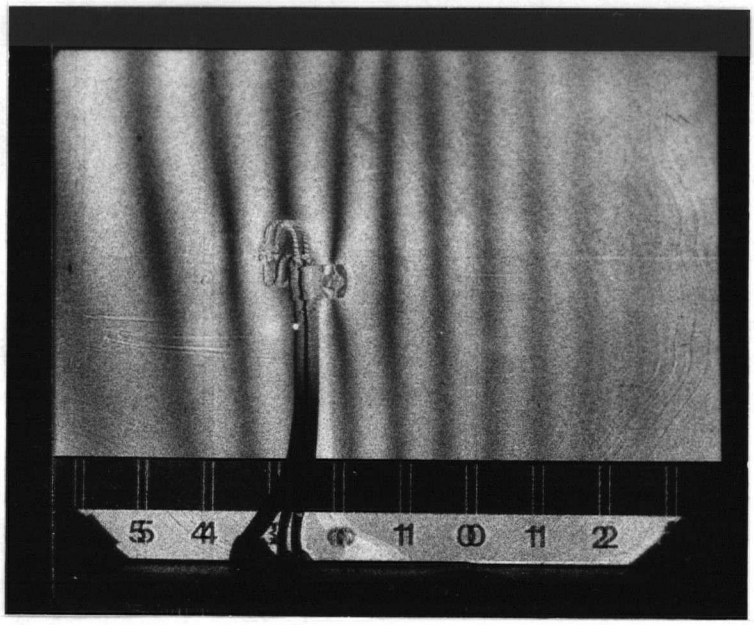

Fig. 6.27 Fringe pattern of Exp. 114C

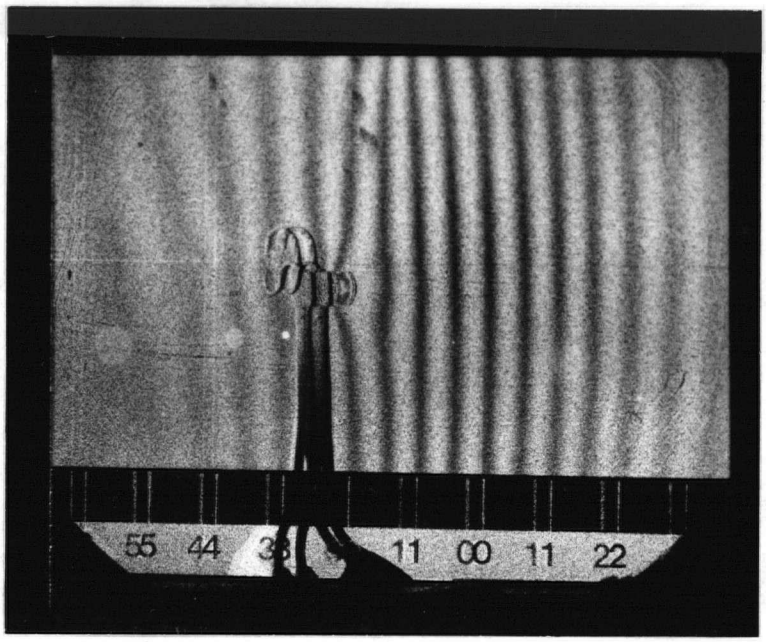

Fig. 6.28 Fringe pattern of Exp. 114D

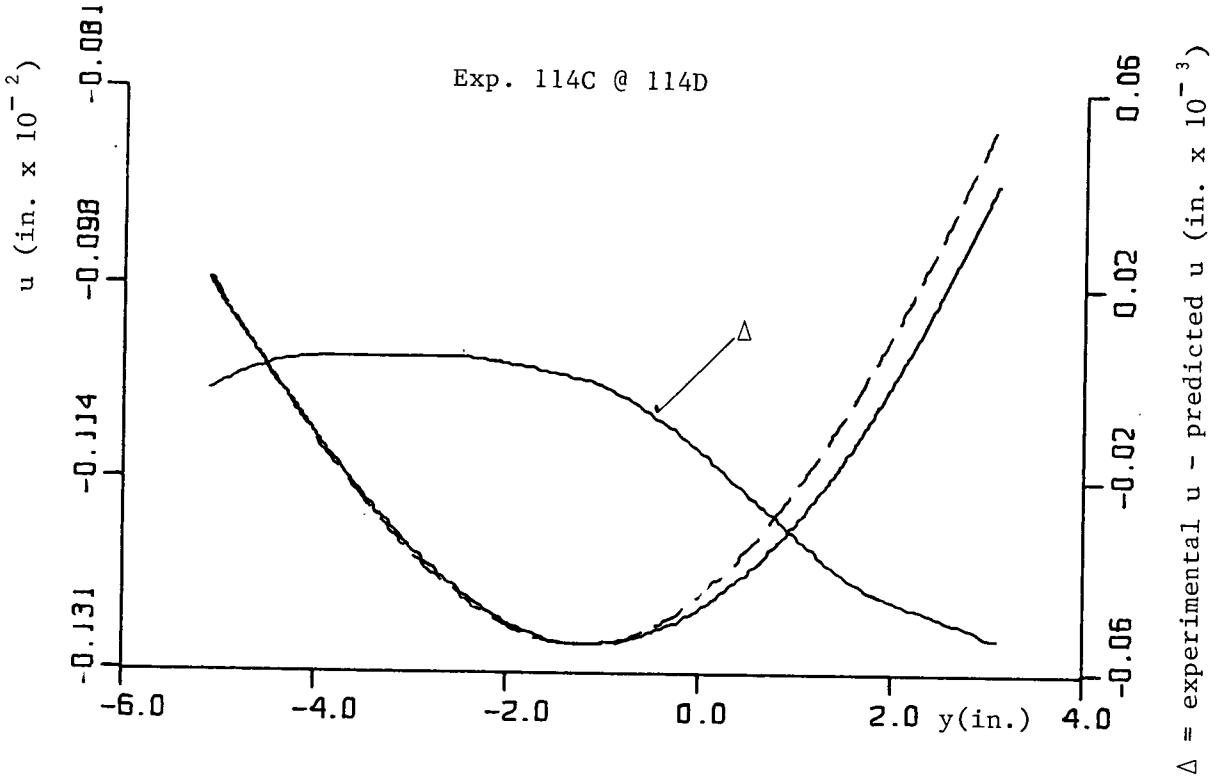

Fig. 6.29 Predicted u (dashed line) vs. experimental u (solid line).

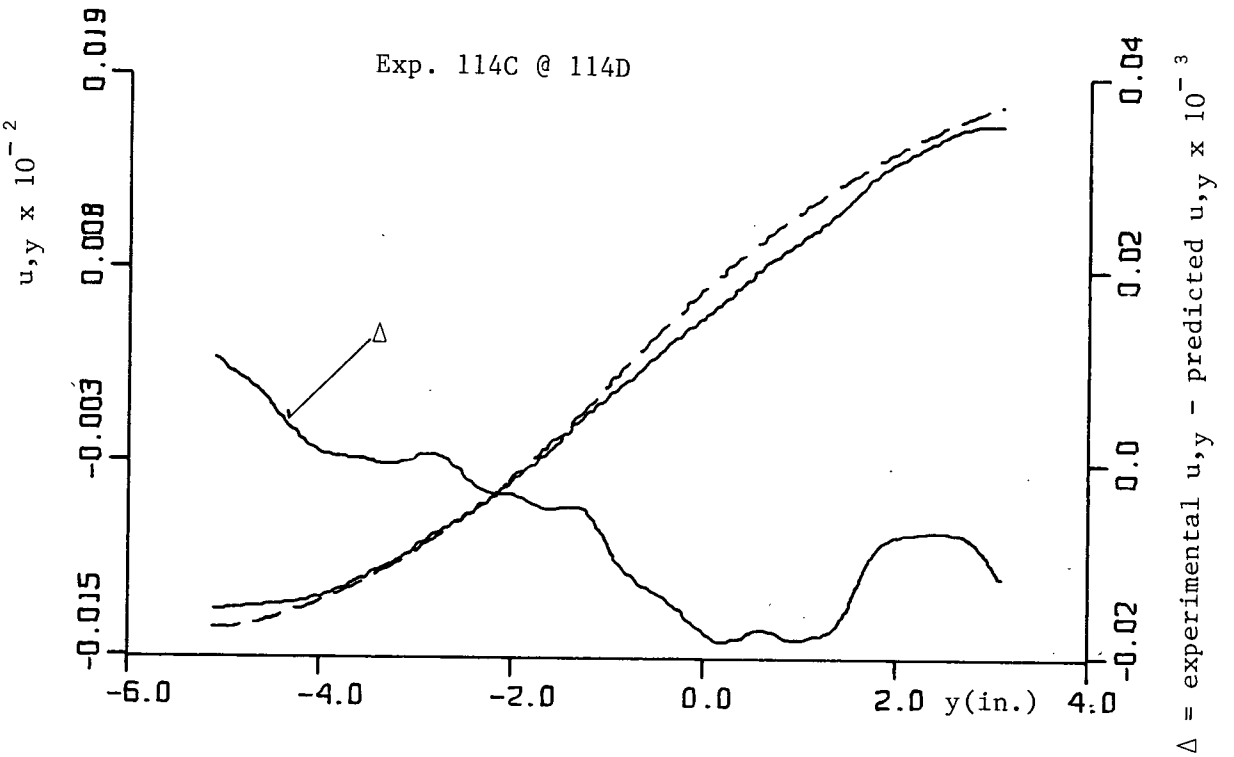

Fig. 6.30 Predicted $u_{,y}$ (dashed line) vs. experimental $u_{,y}$ (solid line).

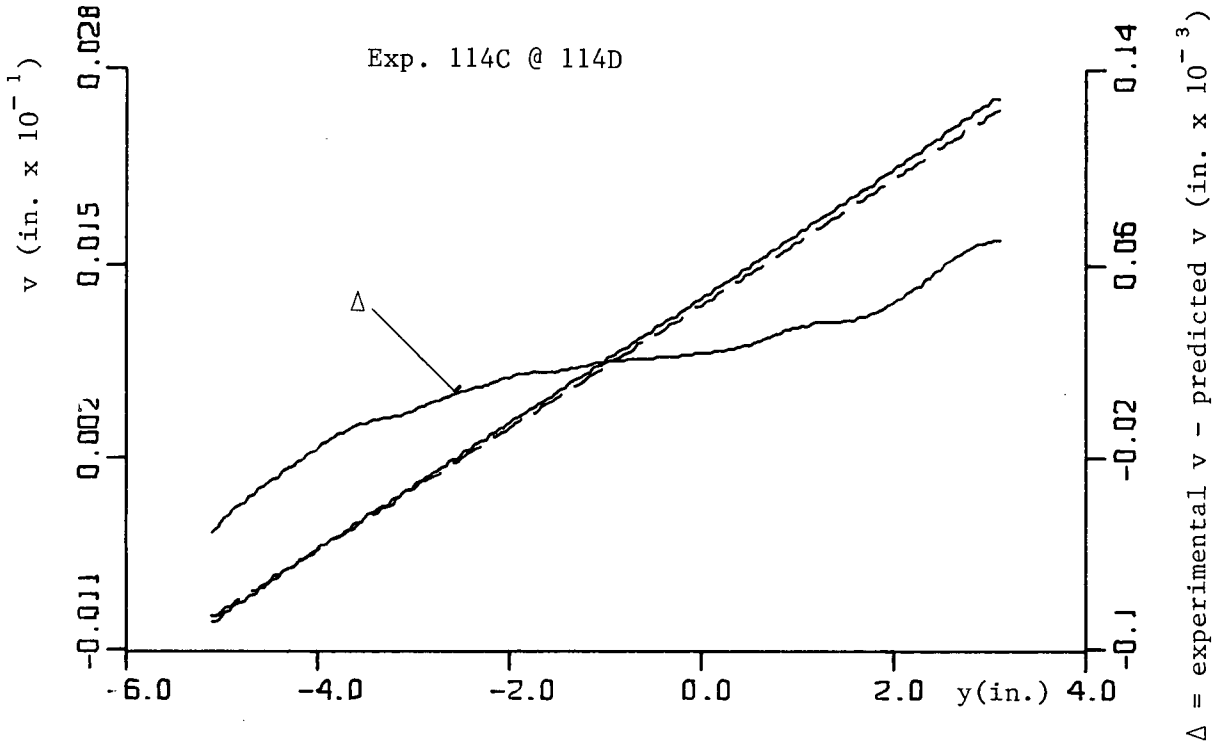

Fig. 6.31 Predicted v (dashed line) vs. experimental v (solid line).

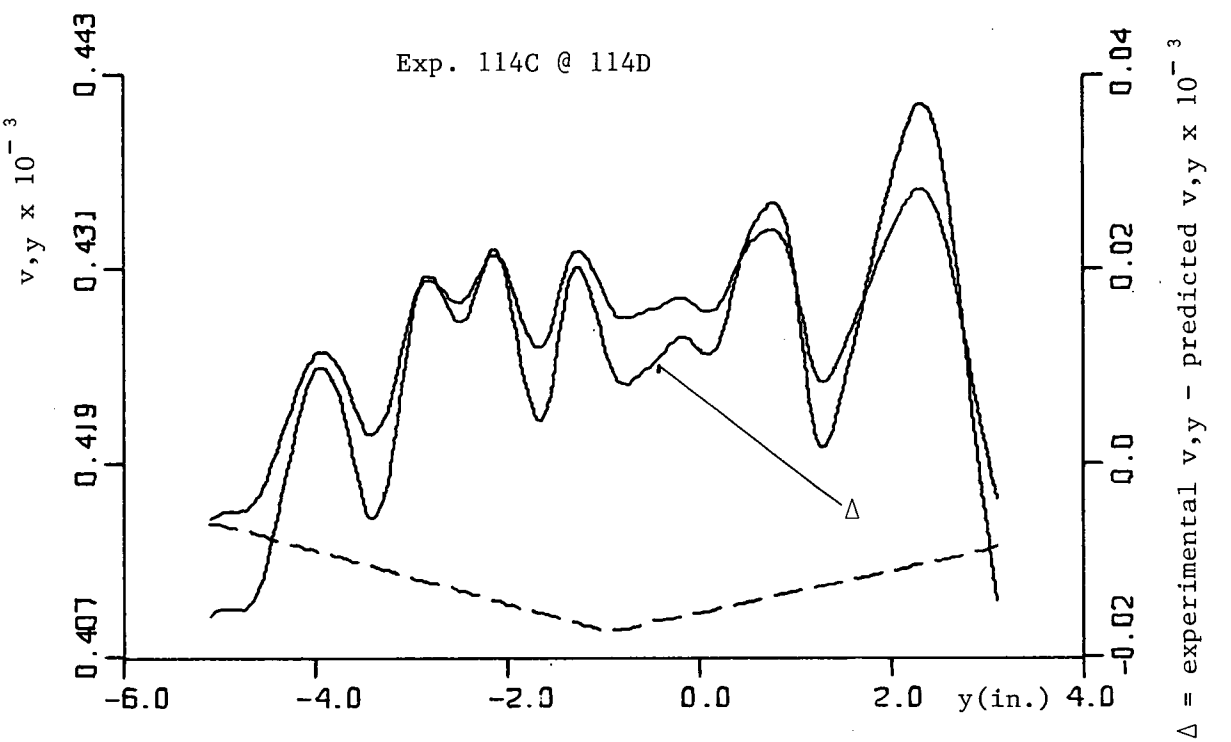

Fig. 6.32 Predicted $v_{,y}$ (dashed line) vs. experimental $v_{,y}$ (solid line).

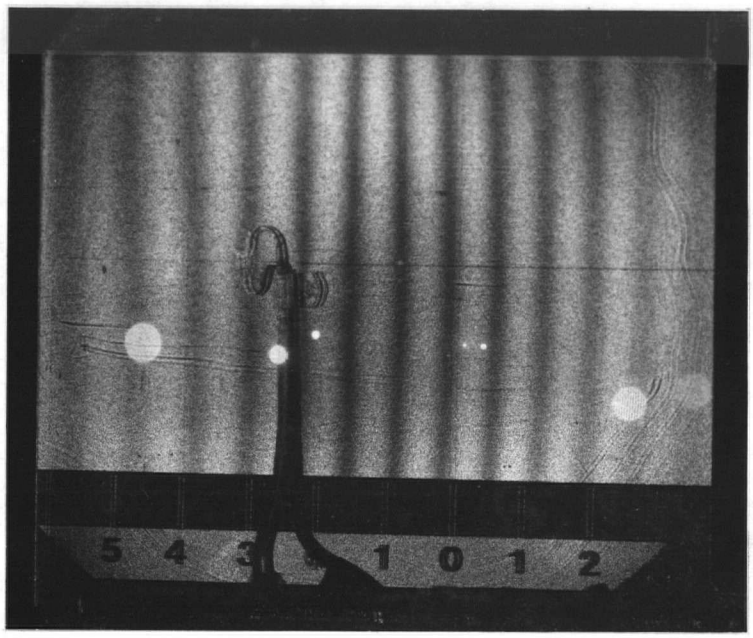

Fig. 6.33 Fringe pattern of Exp. 114B

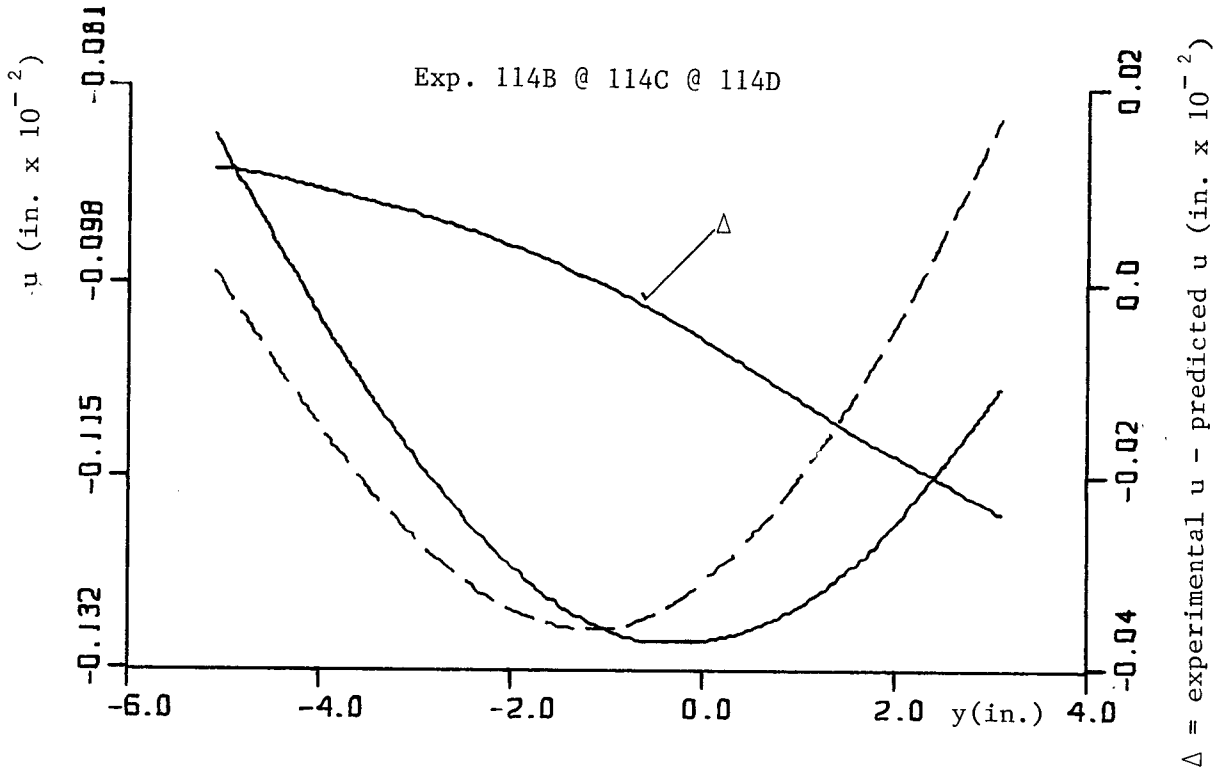

Fig. 6.34 Predicted u (dashed line) vs. experimental u (solid line).

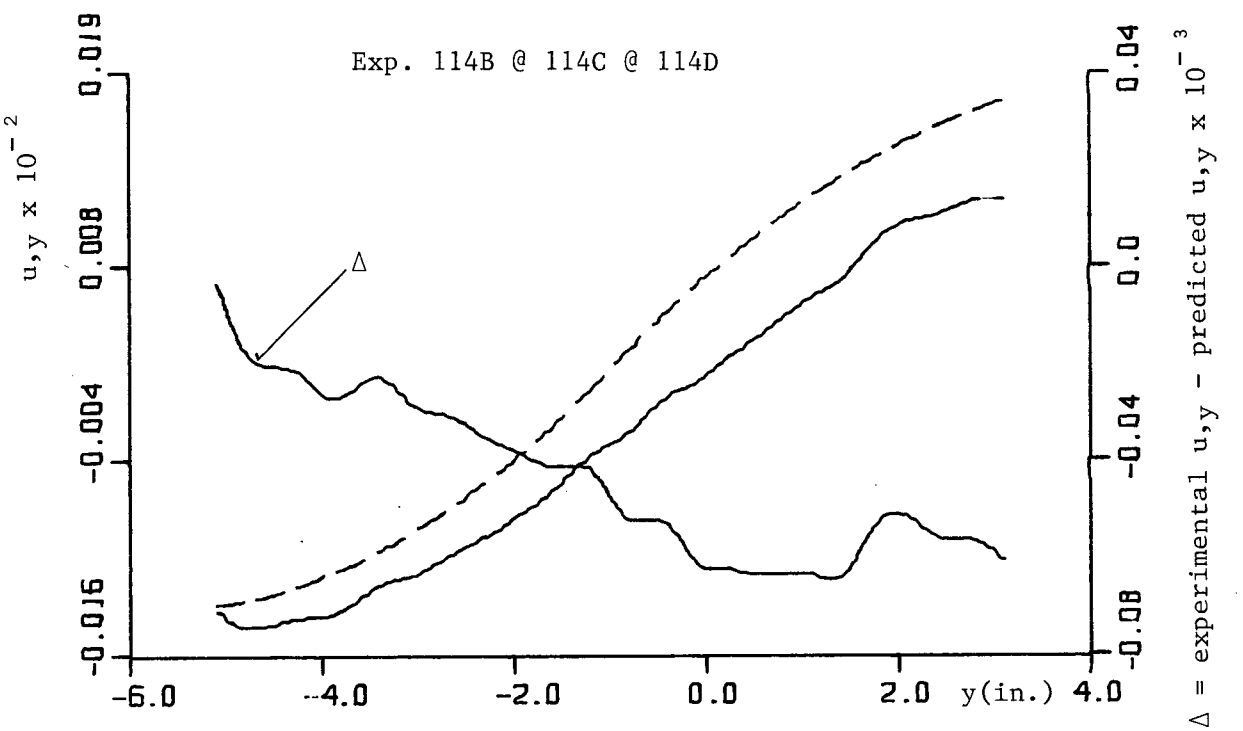

Fig. 6.35 Predicted $u_{,y}$ (dashed line) vs. experimental $u_{,y}$ (solid line).

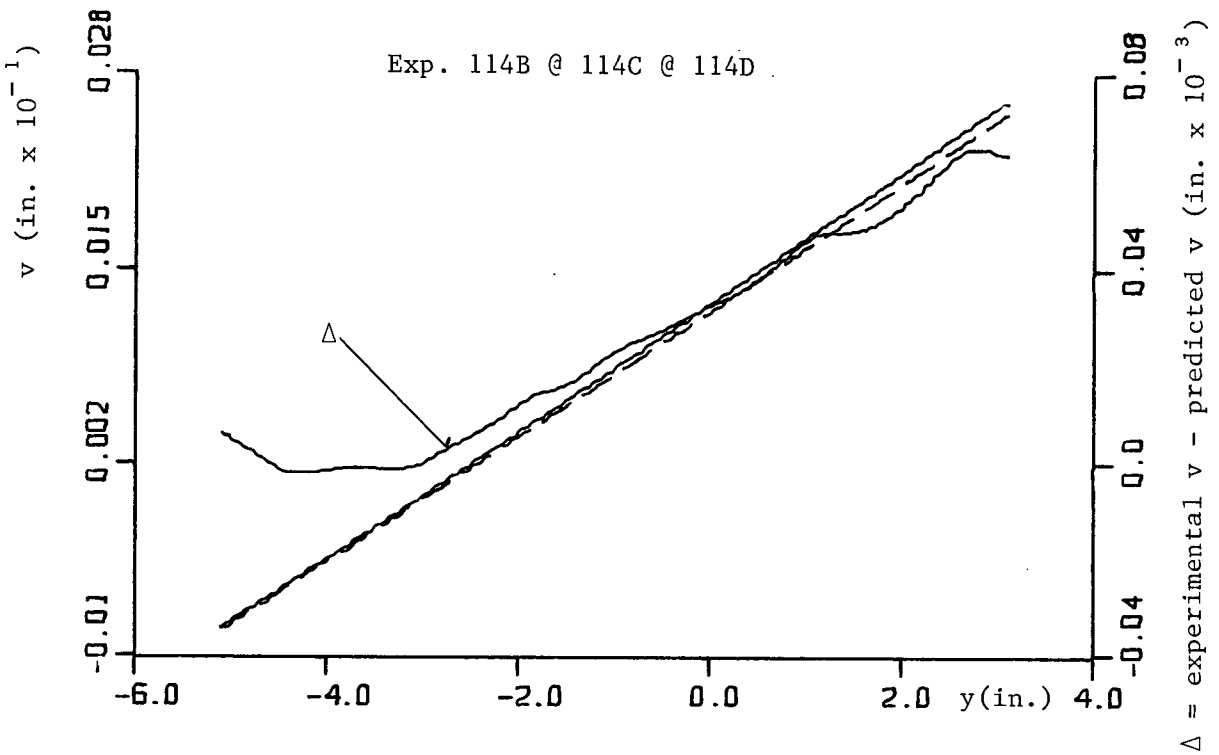

Fig. 6.36 Predicted v (dashed line) vs. experimental v (solid line).

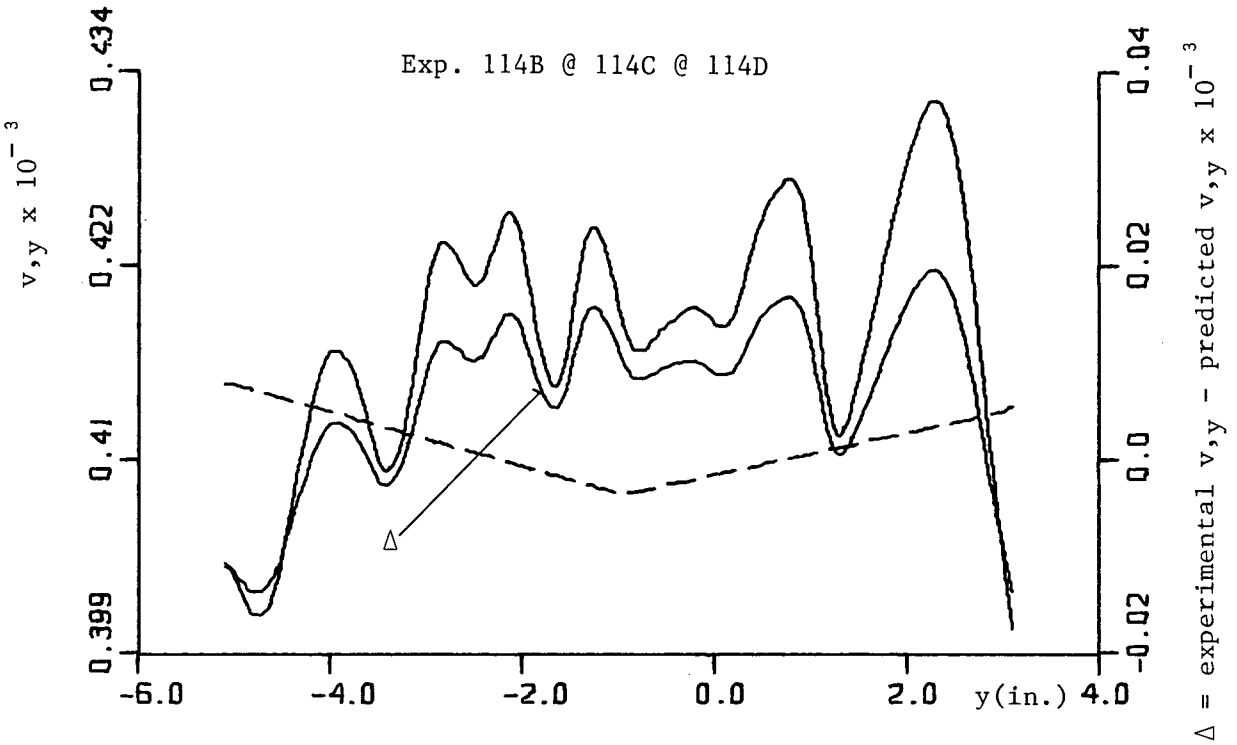

Fig. 6.37 Predicted $v_{,y}$ (dashed line) vs. experimental $v_{,y}$ (solid line).

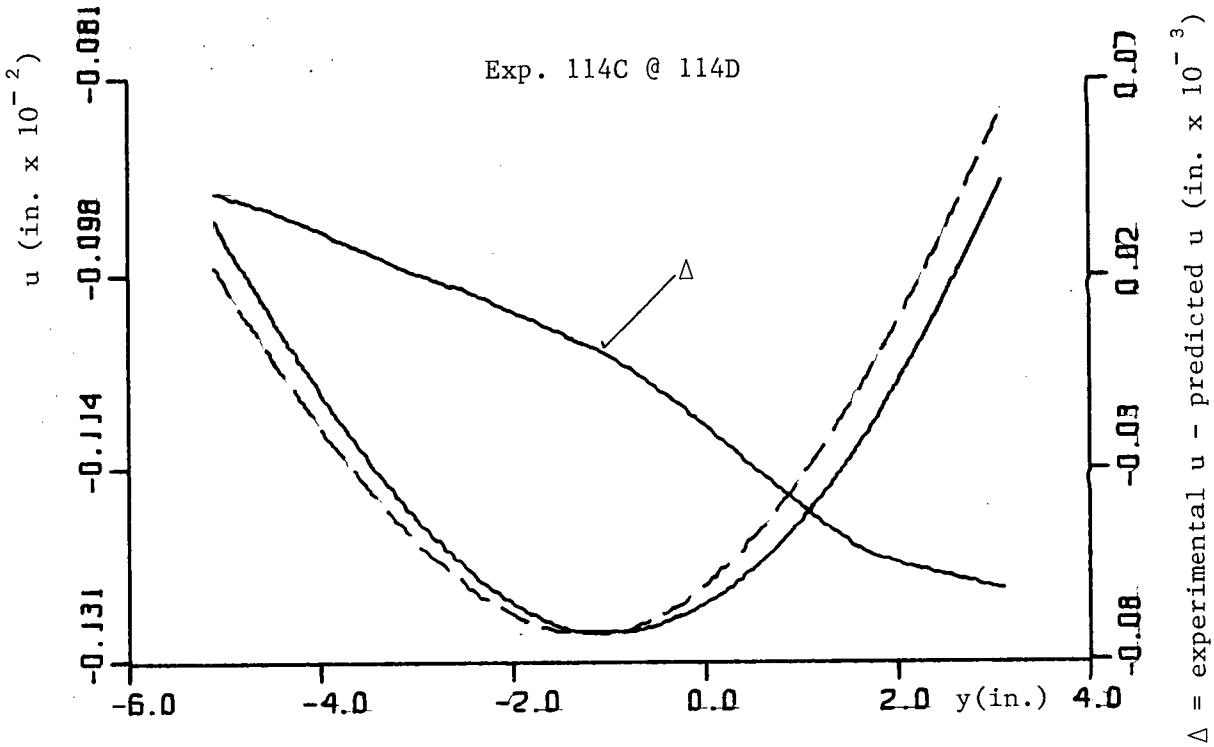

Fig. 6.38 Predicted u (dashed line) vs. experimental u (solid line).

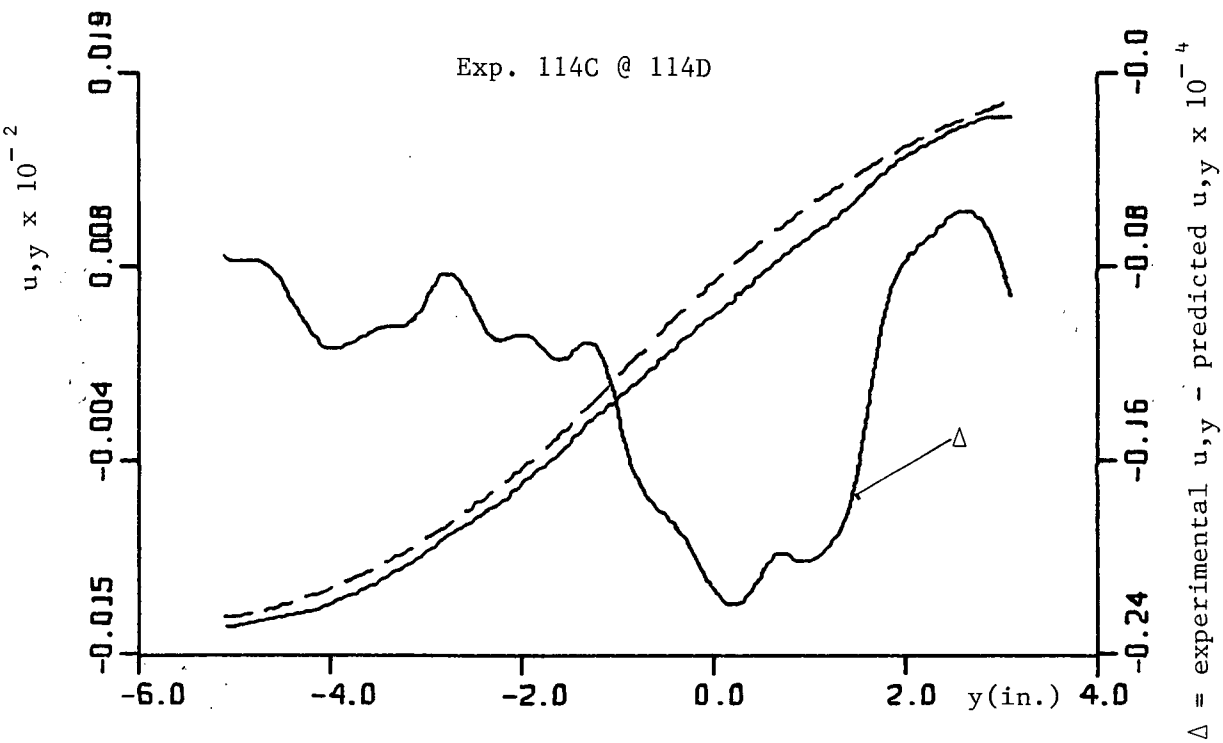

Fig. 6.39 Predicted $u_{,y}$ (dashed line) vs. experimental $u_{,y}$ (solid line).

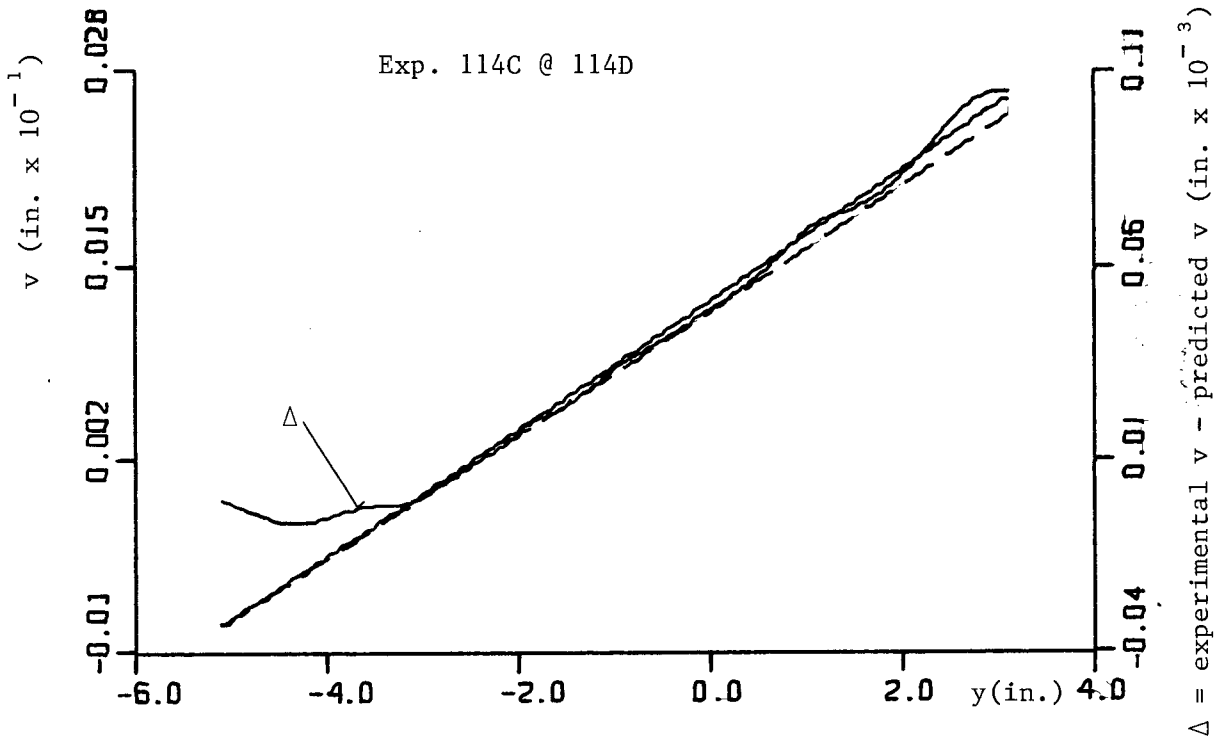

Fig. 6.40 Predicted v (dashed line) vs. experimental v (solid line).

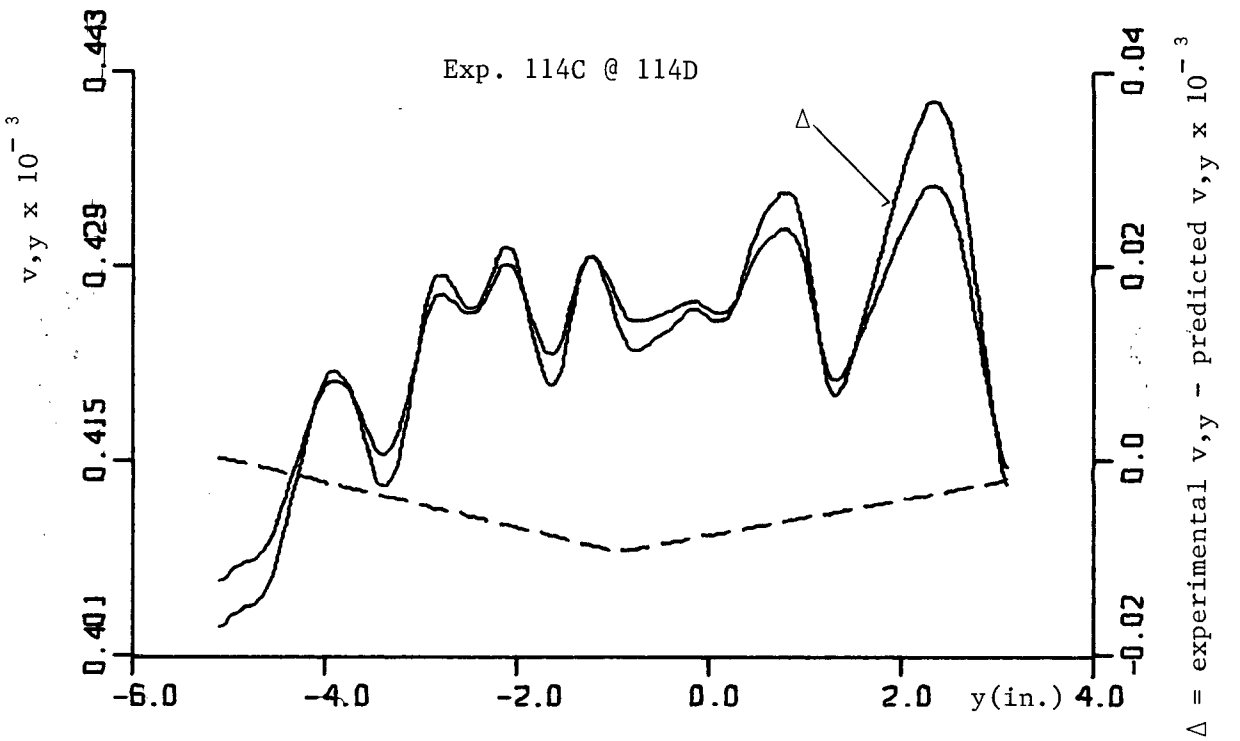

Fig. 6.41 Predicted $v,_y$ (dashed line) vs. experimental $v,_y$ (solid line).

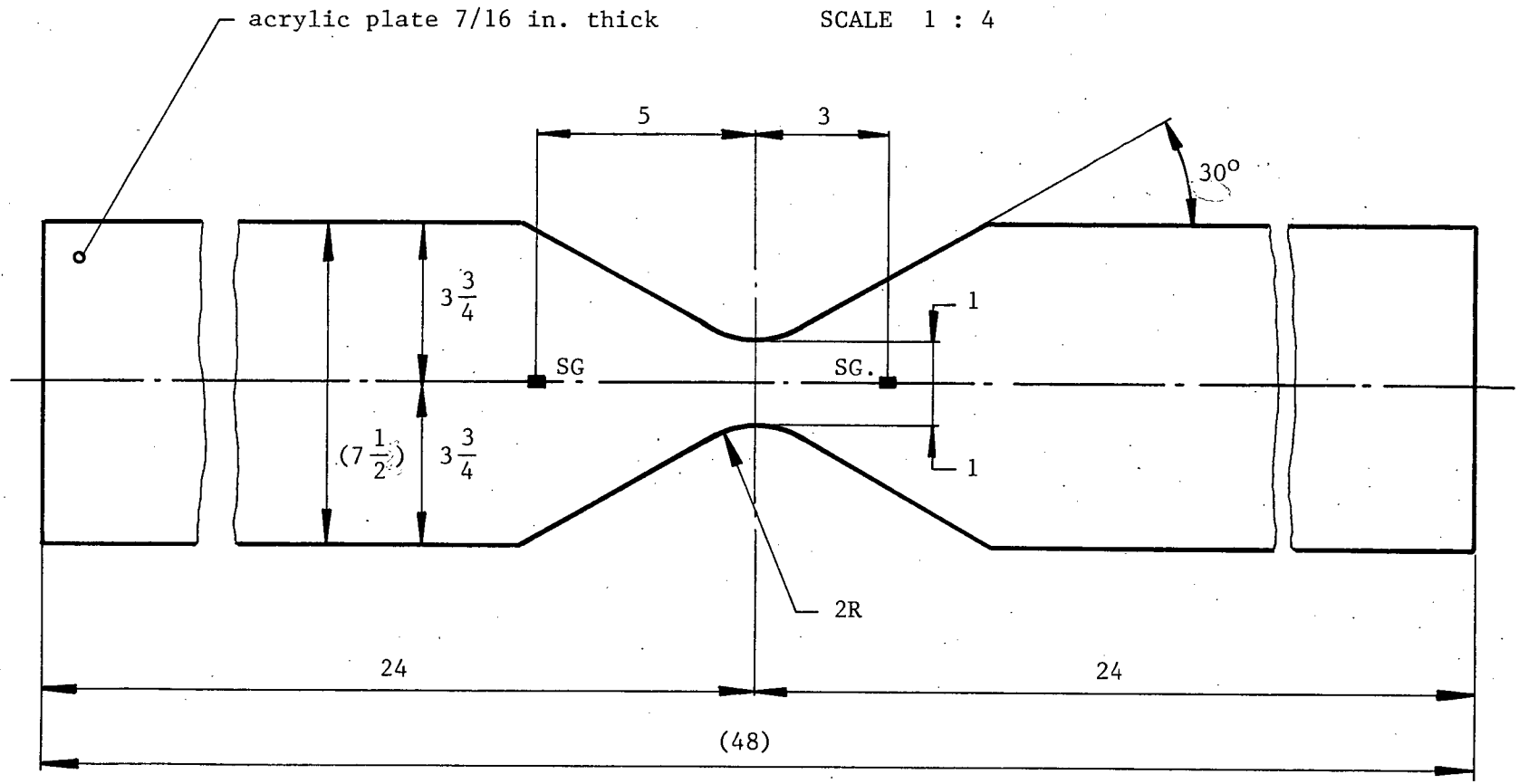

Fig. 6.42 Tensile specimen of Exp. 122.

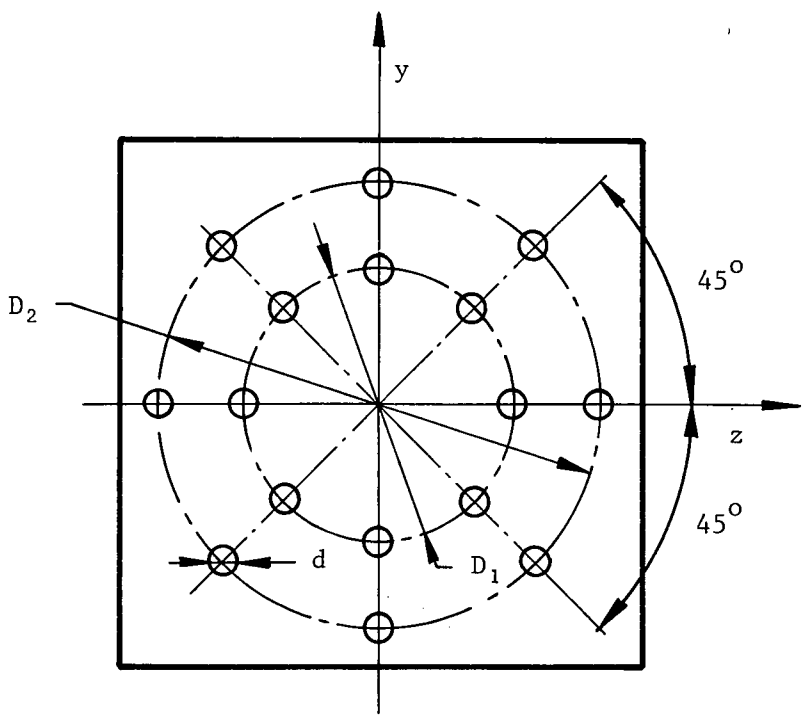

Fig. 6.43 Normal view of the aperture screen.

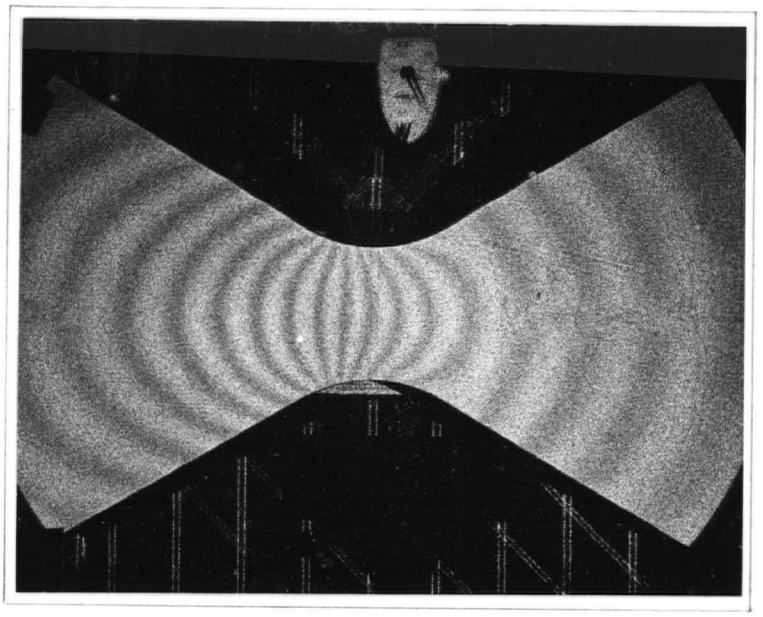

Fig. 6.44 Fringe pattern of Exp. 122S1

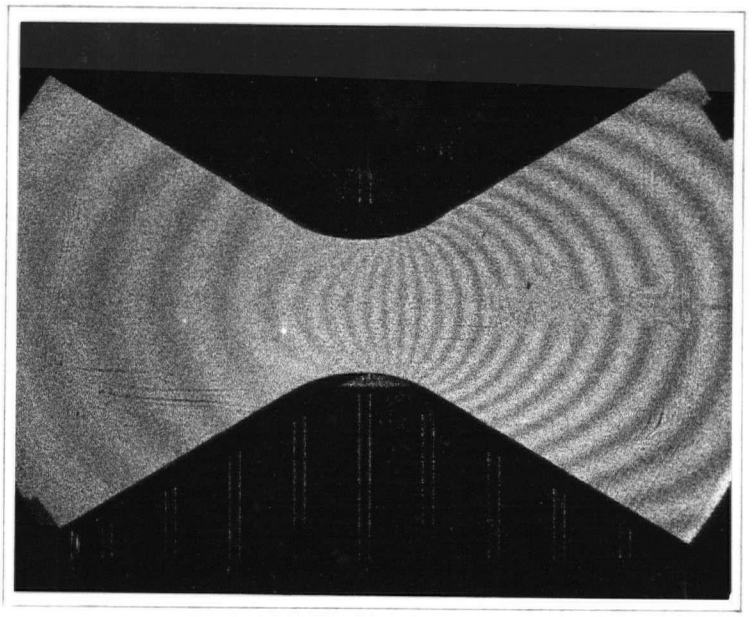

Fig. 6.45 Fringe pattern of Exp. 122S2

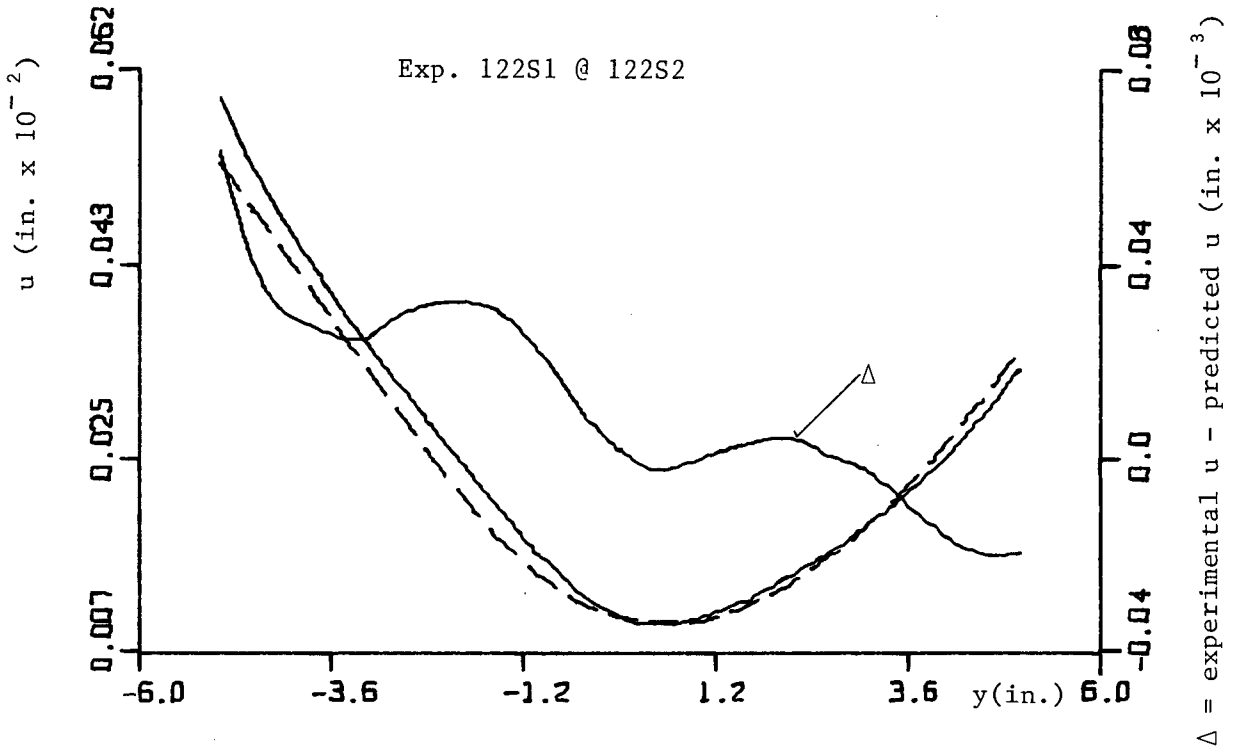

Fig. 6.46 Predicted u (dashed line) vs. experimental u (solid line).

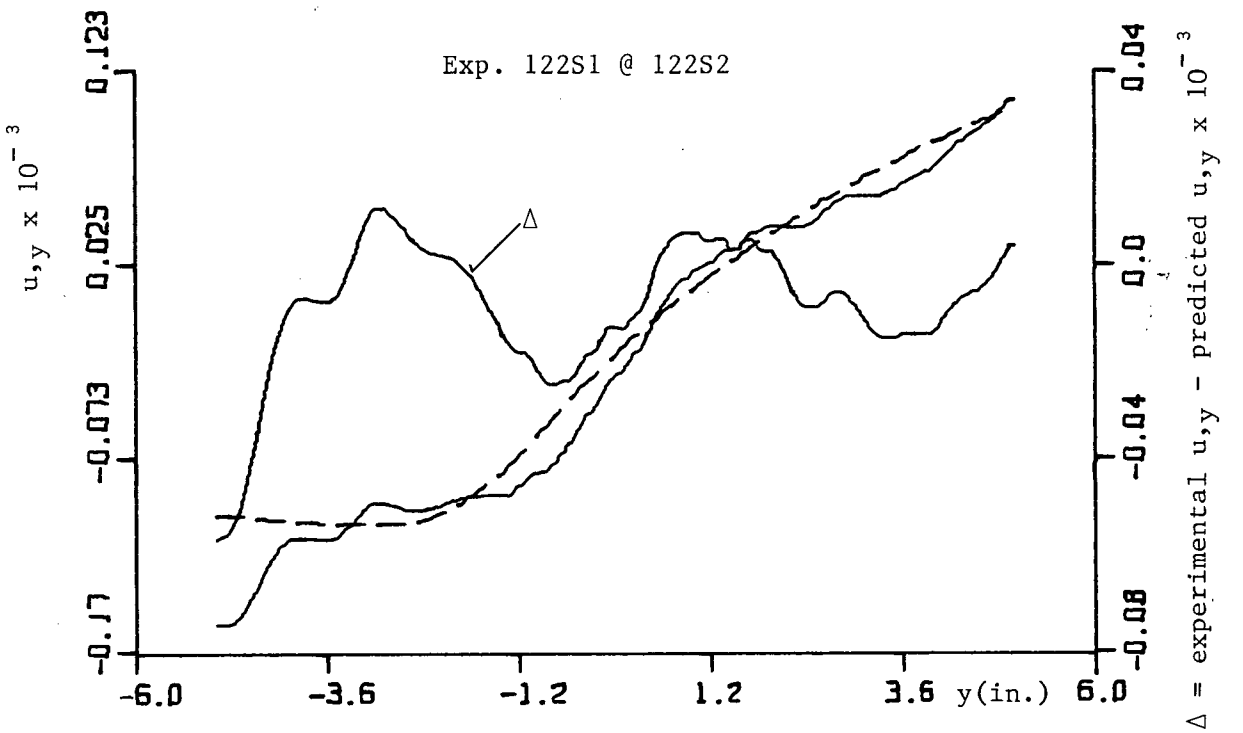

Fig. 6.47 Predicted $u_{,y}$ (dashed line) vs. experimental $u_{,y}$ (solid line).

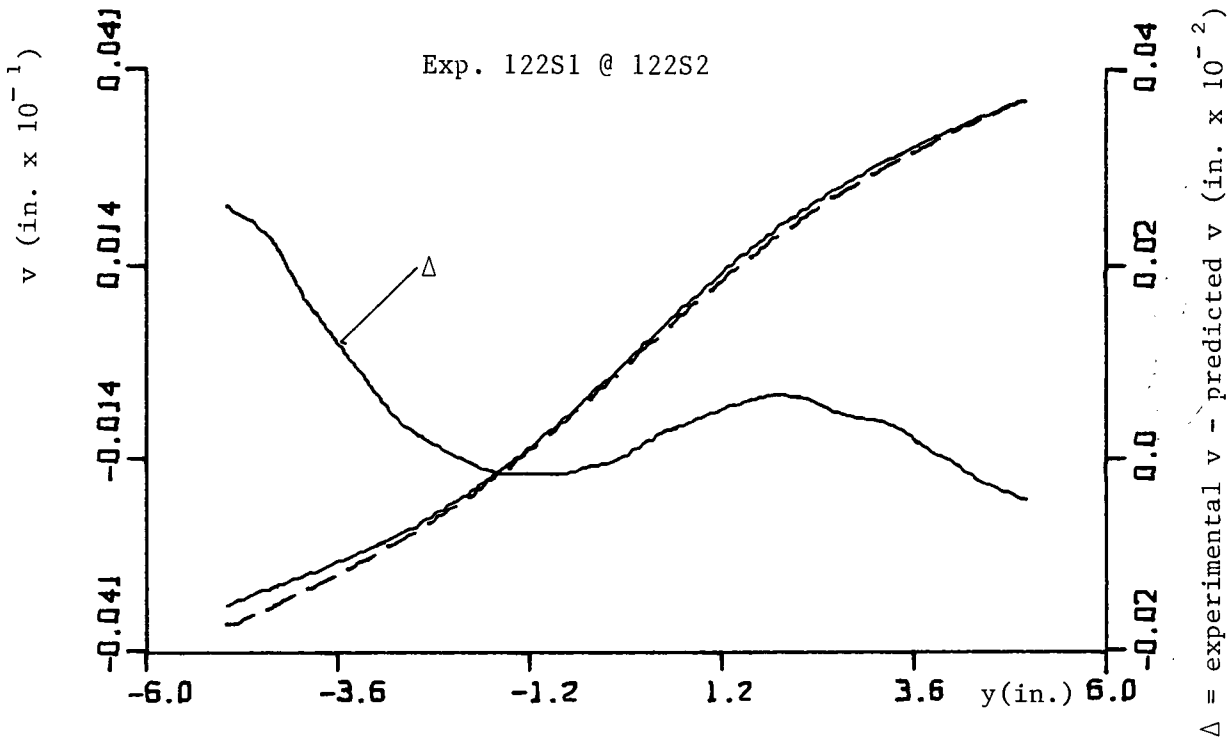

Fig. 6.48 Predicted v (dashed line) vs. experimental v (solid line).

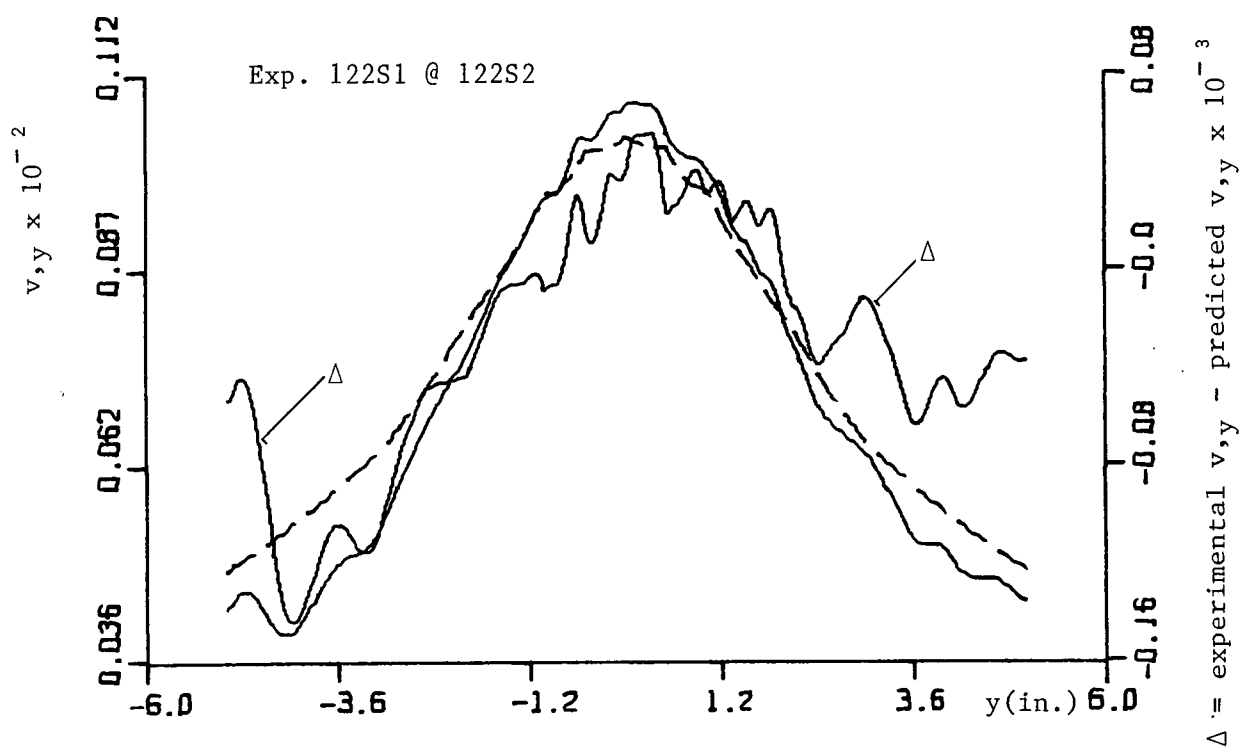

Fig. 6.49 Predicted $v_{,y}$ (dashed line) vs. experimental $v_{,y}$ (solid line).

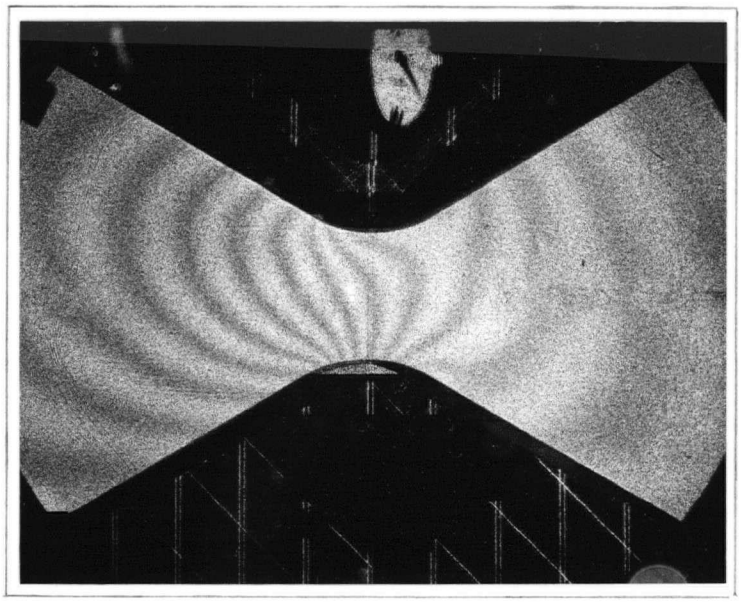

Fig. 6.50 Fringe pattern of Exp. 122S3

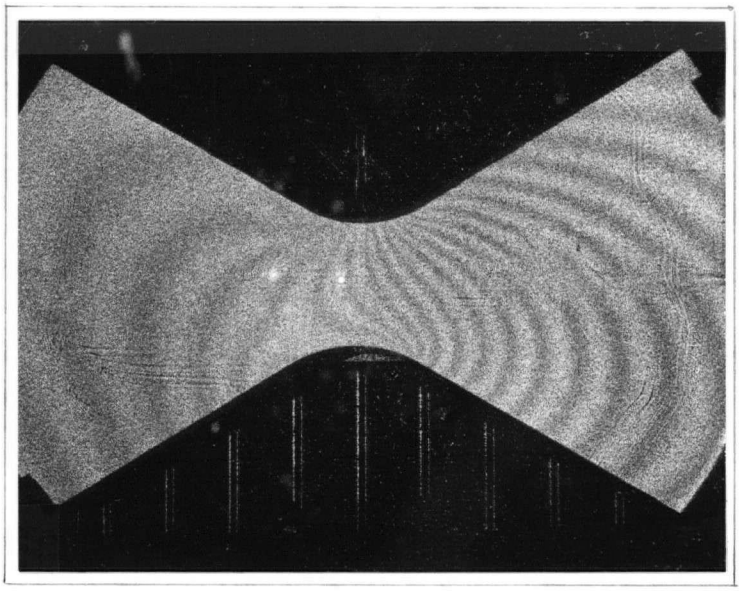

Fig. 6.51 Fringe pattern of Exp. 122S6

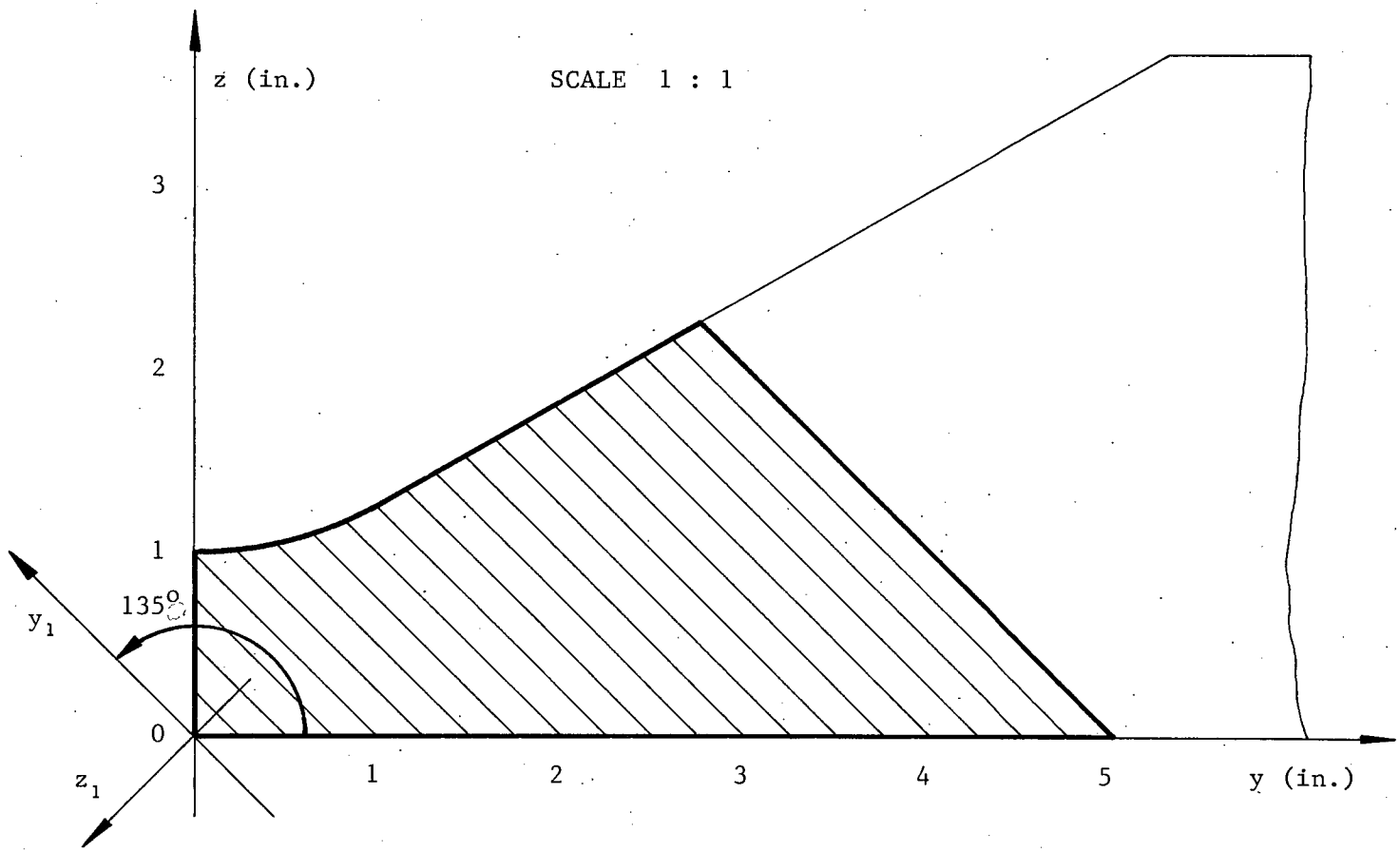

Fig. 6.52 The part of the specimen surface where the displacements and strains were calculated.

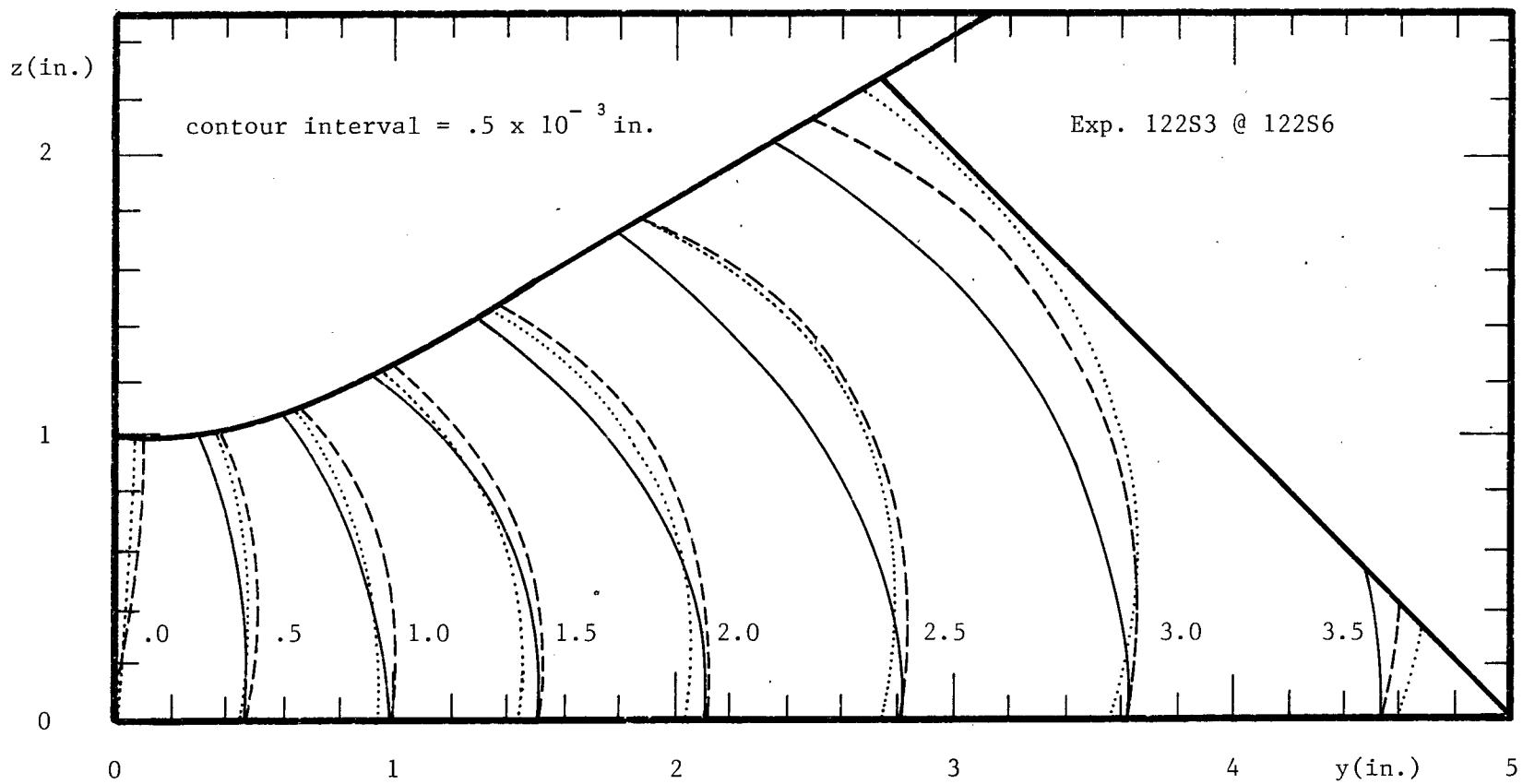

——— finite element solution

— — — experimental solution using the finite element u(y,0) and v(y,0) as boundary conditions

.... experimental solution using the experimental u(y,0) and v(y,0) as boundary conditions

Fig. 6.53 Contours of constant displacement v(y,z) in the variable cross-section specimen.

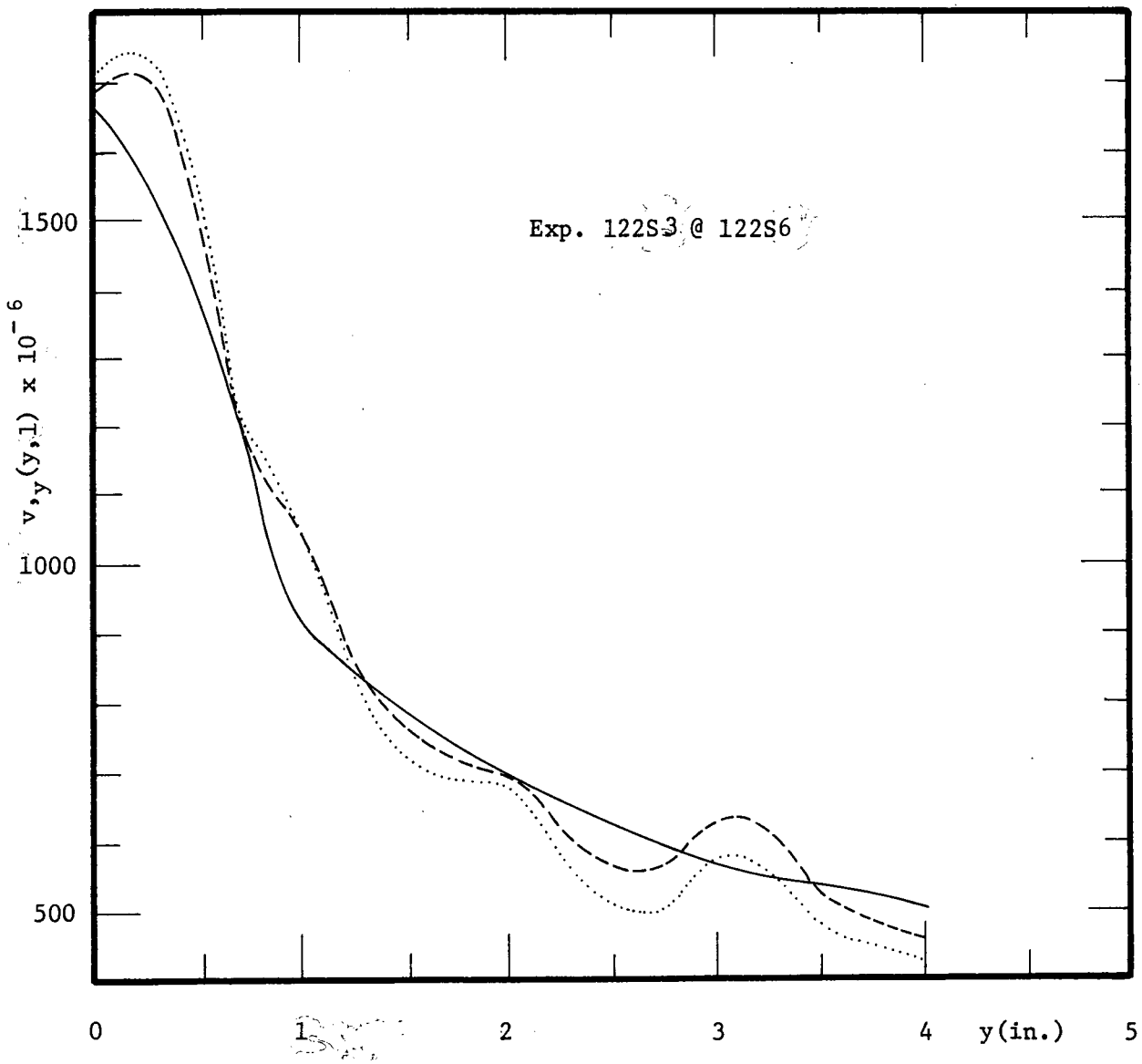

—— finite element solution

— — experimental solution using the finite element u(y,0) and v(y,0) as boundary conditions

.... experimental solution using the experimental u(y,0) and v(y,0) as boundary conditions

Fig. 6.54 Strain $v_{,y}(y,1)$ in the variable cross-section specimen.

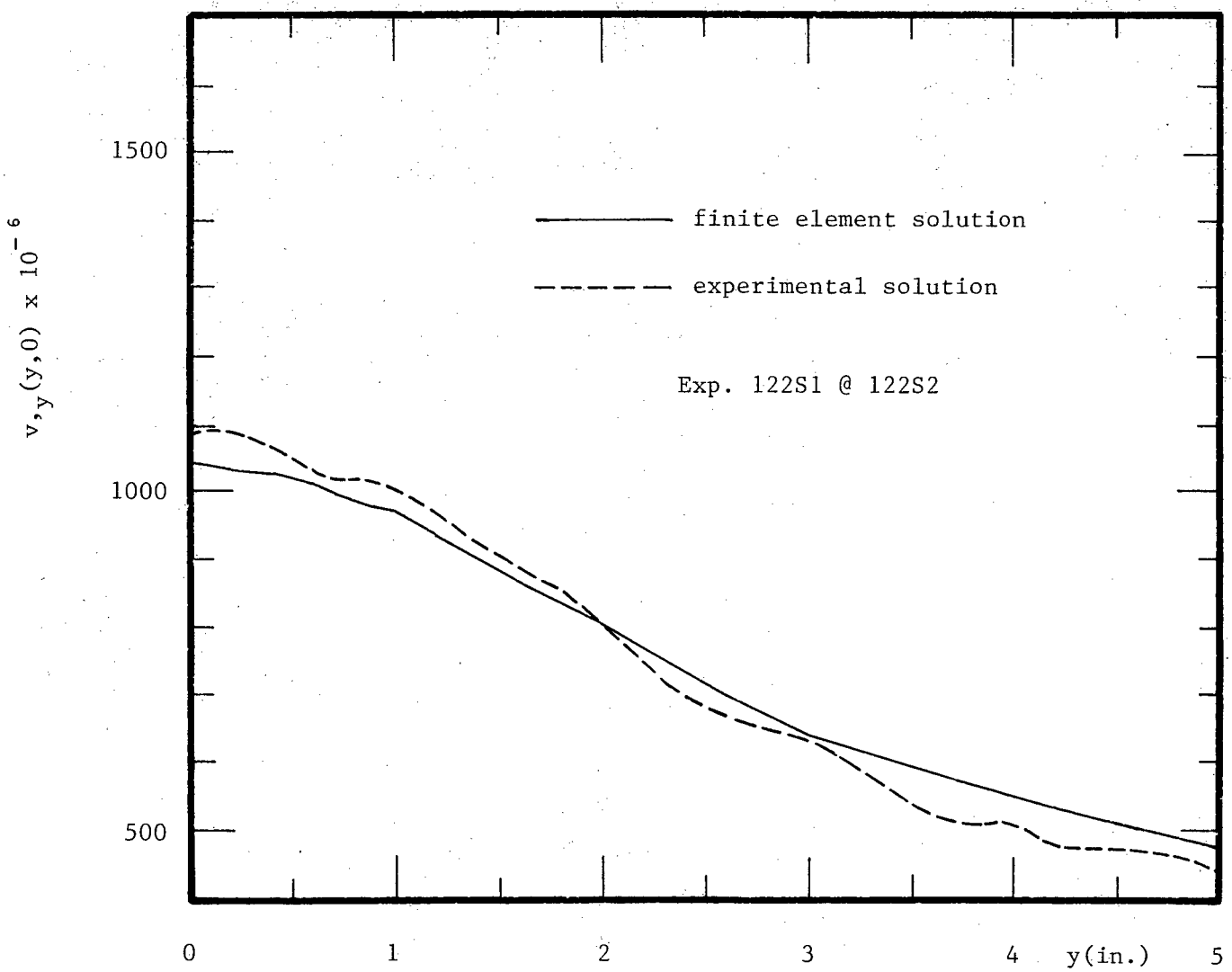

Fig. 6.55 Strain $v_{,y}(y,0)$ in the variable cross-section specimen.

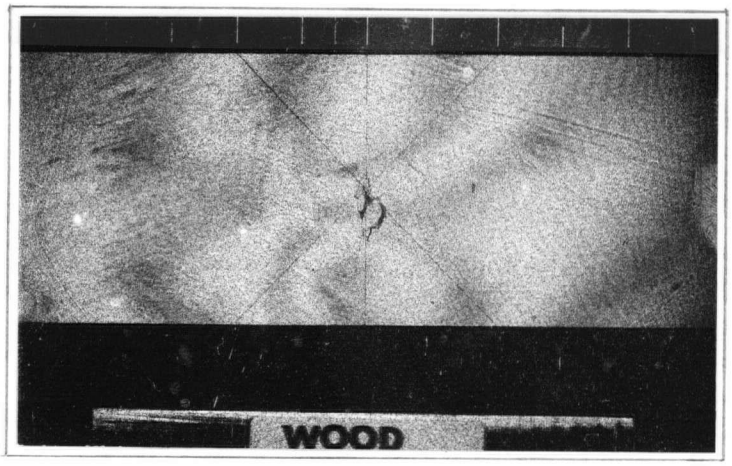

Fig. 6.56 Fringe pattern of Exp. 132D1

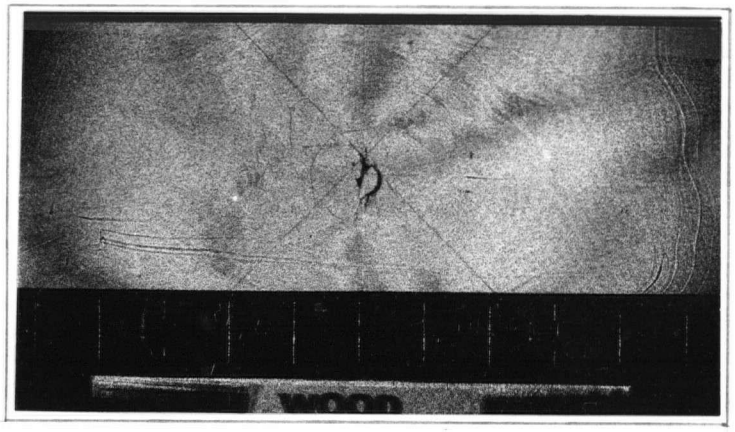

Fig. 6.57 Fringe pattern of Exp. 132D2

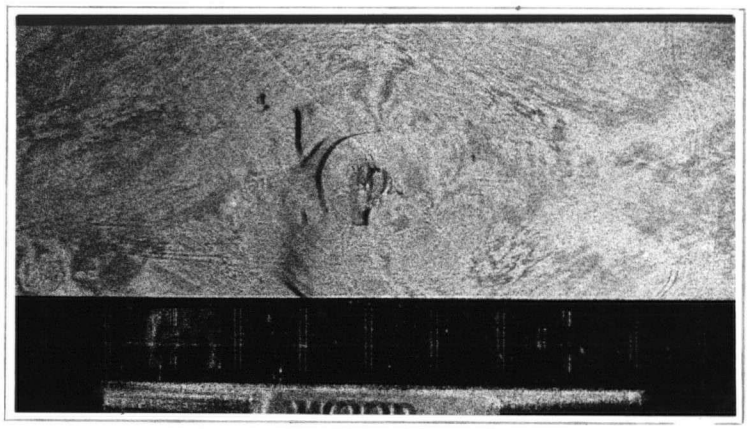

Fig. 6.58 Fringe pattern of Exp. 132S2

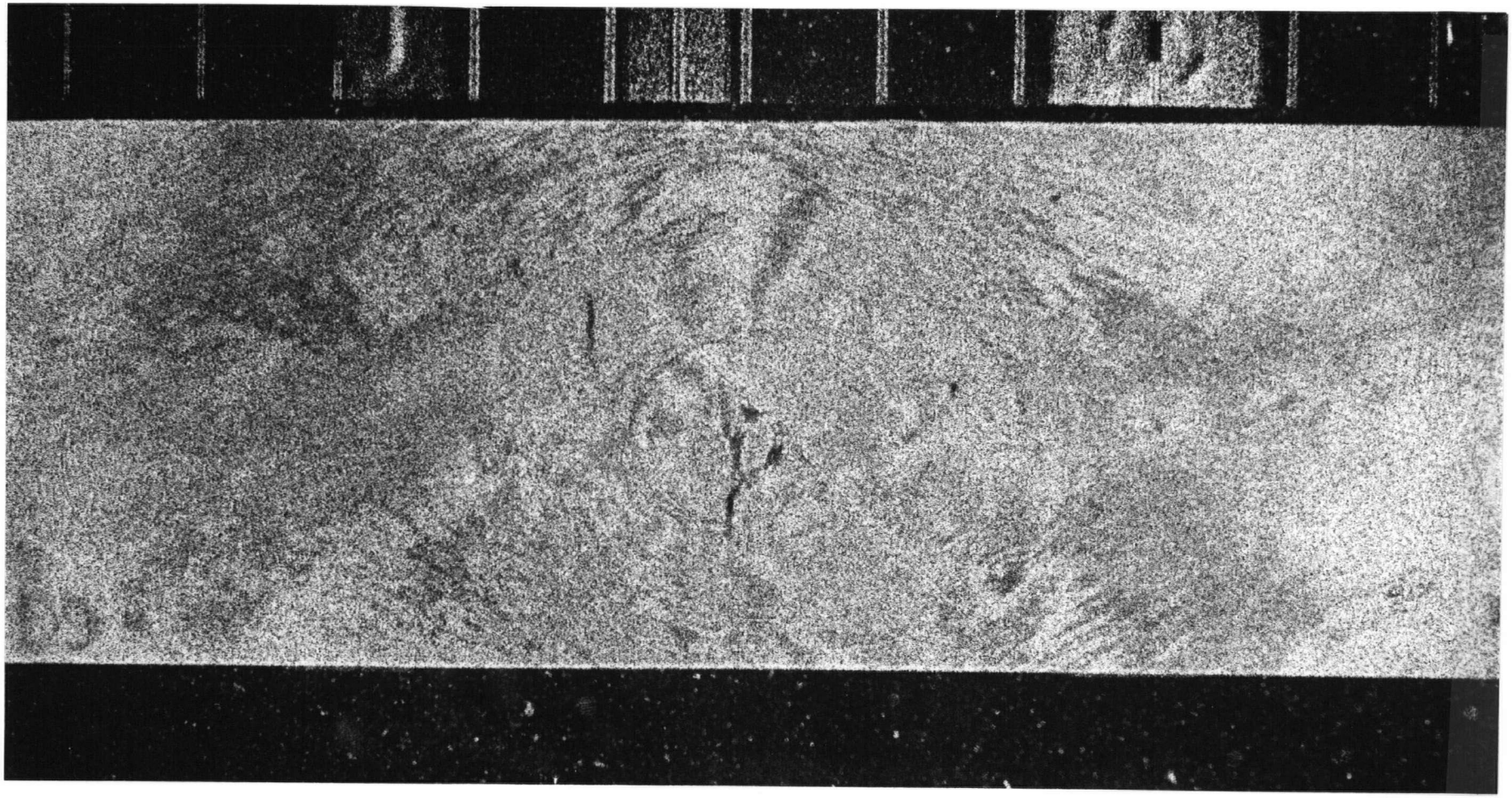

Fig. 6.59 Fringe pattern of Exp. 132S1.

7. CONCLUSIONS

7.1 Summary and Conclusions

A fairly involved theoretical analysis of the image and fringe formation by DASC and DASSC has been undertaken. The accuracy of the resulting equations relating the Moire fringe number to the deformed surface displacements and strains was verified by several simple and controlled experiments. Each experiment was set up to ascertain the accuracy of one or two coefficients of the fringe equations. The subsequent and more complicated experiments have proven the feasibility of the two cameras in experiments similar to those encountered in the typical laboratory testing of materials or structural components. With some exceptions the agreement between the optically determined and actual displacements and strains was good.

It was easier to use DASC than DASSC since the fringes formed by DASC are due to the displacements only; thus, the numbering of the fringes was relatively easy. In fact, in some special cases the fringes are related directly to only one displacement component. When DASC is used no boundary conditions are required to calculate the displacements, and the calculation involves the solution of a set of at most three algebraic equations, a process which is straightforward and easy to program. That DASC is insensitive to the out-of-plane displacements of the specimen surface near the coordinate origin may be considered an advantage if the measurement of in-plane displacements is desired, but it may make DASC potentially useless if the out-of-plane displacements near the coordinate origin are to be measured. The main disadvantage of DASC stems from its relative inflexibility as the sensitivity may be varied only by changing D, λ or x_s, the possibilities of which exist only in a rather narrow range.

The attractiveness of DASSC stems from its great flexibility since the sign and the size of the lateral shear may be set by an appropriate

positioning of the photographic plate with the adjustable slide. Thus, if the specimen deformation is approximately known before the test, the lateral shear may be chosen so that the density of the resultant fringe pattern is suitable for processing. The camera is sensitive to the surface displacements and strains (actually to partial derivatives) and, hence, the fringe patterns could be used qualitatively to identify those areas of the surface where stress concentrations occur. The calculation of the displacements in special cases often involves a solution of an ordinary linear differential equation or, in the general case, a solution of a set of partial differential equations for which the finite difference approach was found suitable. The solution requires a point boundary condition for the particular displacement in special cases and, in the general case, a line boundary condition for the three displacements. The solution schemes for DASSC are usually more complicated than those for DASC. If the required boundary conditions are available, the results obtained by DASSC are usually superior to those obtained by DASC.

Both DASC and DASSC were found to be useful and reasonably accurate instruments for measurement of displacements and strains. Which of the two cameras is to be used depends greatly on the particular circumstances of the proposed test. If the boundary conditions are readily available, then DASSC should be used as it is likely to provide a more accurate solution. When all displacements and strains are to be determined the illumination not coincident with the x,y plane must be provided and the researcher should be ready to do a rather large amount of programming to interpret the fringe patterns obtained by DASSC. On the other hand, if the boundary conditions are not available or if a researcher wishes to minimize the amount of experimental work and computing effort, then the use of DASC should be considered.

The approximation of the fringe function $n(y,z)$ by a continuous cubic

based on fringe centers (multiplies of .50) along a line $z = z_0$ = constant was found to be satisfactory where solutions along a line $z = z_0$ were sought. If a two-dimensional approximation of n(y,z) was necessary, then it was found to be sufficient to scan the fringe pattern along a number of lines z = constant and to approximate n(y,z) along these "scan" lines by a continuous cubic. The fringe number n(y,z) anywhere else was then found by fitting a continuous cubic along a line y = constant through the points where this line intersects already approximated scan lines.

7.2 Suggestions for Future Research

Mainly due to a lack of time two solution schemes were not tested and, hence, their accuracy remains yet to be experimentally verified. The first experiment should be such that none of the displacements u,v or w may be neglected and that these three displacements should be determined from three independent fringe patterns obtained with the use of DASC. The second experiment would be similar, but DASSC with at least one illuminating beam not in x,y plane would be used to take three independent photographs. A line boundary condition would have to be available and the three displacements u,v and w could then be calculated from the three fringe patterns by using the proposed finite difference scheme.

The experimental work done in this thesis was restricted to specimens with one planar surface. There is no reason why DASSC could not be used to measure displacements and strains in specimens having shallow curved surfaces or surfaces consisting of planar and curved surfaces. It would only be necessary to relate the lateral shear Δy_s to the third, i.e. the x, dimension of the curved surface. This dependence of the lateral shear on the (y,z) coordinates could be easily incorporated in the computer programs of the finite difference schemes used to calculate displacements and strains.

The "depth" of the specimen surface along the x-direction would, of course, have to be reasonably small so that the lateral shear would not be excessively large.

Numbering of the fringes could be made easier, in some cases, if one more photograph were processed than the minimum number required. With the knowledge of the deformations on the line boundary the fringe numbers at the boundary could be calculated and the fringe numbers at the neighbouring points could, in principle, be determined by finding that fringe number which would satisfy the overdetermined system of equations at those points. This process would be repeated until the fringe numbers of all points would be known; in fact, numbering of the fringe centers would probably be sufficient.

BIBLIOGRAPHY

1. Duffy "Moire Gauging of In-plane Displacement Using Double Aperture Imaging" Applied Optics, 1778-1781, Aug., 1972.

2. Duffy, D., "Measurement of Surface Displacement Normal to the Line of Sight", Experimental Mechanics, Vol. 14, No. 9, pp. 378-384 (1974).

3. Hung, Y. Y. and Taylor, C. E., "Speckle-Shearing Interferometric Camera - A Tool for Measurement of Derivatives of Surface-Displacements," Proceedings of Society of Photo-Optical Instrumentation Engineers, Vol. 41, pp. 169-175 (1973).

4. Hung, Y. Y., "A Speckle-Shearing Interferometer", Optics Communications, Vol. 11, p. 732,(1974).

5. Hung, Y. Y., Hu, C. P. and Taylor, C. E., "Speckle-Moire Interferometry - A Tool for Complete Measurement of In-plane Surface-Displacements", Proceedings of Seventh Southeastern Conference on Theoretical and Applied Mechanics, pp. 497-505 (1974).

6. Hung, Y. Y., Rowlands, R. E. and Daniel, I. M., "Speckle-Shearing Interferometric Technique: A Full-Field Strain Gauge", Applied Optics, Vol. 14, No. 3, pp. 618-622 (1975).

7. Dally, J. W. and Riley, F. W., "Experimental Stress Analysis", McGraw-Hill, New York, 1965.

8. O'Regan, R., "A New Method for Determining Strain on the Surface of a Body with Photoelastic Coatings", Experimental Mechanics, Vol. 5, No. 8, 241-242 (1965).

9. Theocaris, "Moire Fringes in Strain Analysis", Pergamon Press, N. Y., 1969.

10. Durelli, A. J. and Parks, V. J., "Moire Analysis of Strains", Prentice-Hall, Inc. (1970).

11. Boone, P. M., "A Method for Directly Determining Surface Strain Fields Using Diffraction Gratings", Experimental Mechanics, Vol. 11, No. 11, 481-489 (1971).

12. Powell, R. L. and Stetson, K. A., "Hologram Interferometry", J. Opt. Soc. Am. 56, 1161-1167 (1966).

13. Archbold, et al, "Visual Observation of Surface Vibration Nodal Patterns", Nature, 222 (5190), 263 (April 1969).

14. Archbold E. and Ennos, A. C., "Observation of Surface Vibration Modes by Stroboscopic Hologram Interferometry", Nature, 217, 942, 1968.

15. Monahan, M. A. and Bromley, K., "Vibration Analysis by Holographic Interferometry", J.Aconst. Soc. Am, 44, 1225, 1968.

16. Neuman, D. B., Jacobson, C. F., and Brown, G. M., "Holographic Technique for Determining the Phase of Vibrating Objects", Applied Optics, Vol. 9, No. 6, 1357, 1970.

17. Aleksoff, C. C., "Time Average Holography Extended", Applied Physics Letters, Vol. 14, No. 1, 23, 1969.

18. Vest, C. M. and Sweeney, D. W., "Measurement of Vibrational Amplitude by Modulation of Projected Fringes", Applied Optics, Vol. 11, No. 2, 449, 1972.

19. Stetson, K. A., "Hologram Interferometry of Nonsinusoidal Vibrations Analyzed by Density Functions", J. Opt. Soc. Amer. 61, 1359 (1971).

20. Hiroyoshi, S., et al, "Application of Holographic Interferometry to Mechanical Experiment", Presented at U.S.-Japan Seminar on Information Processing by Holography, Washington, D.C., (Oct. 1969).

21. Tsuruta, T., Shiotake, N. and Itoh, Y., "Formation and Localization of Holographically Produced Interference Fringes", Optica Acta, Vol. 16, No. 6, 723-733 (1969).

22. Nils-Erik M. and Stetson, K. A., "Measurement of Fringe Loci and Localization in Holographic Interferometry", Optik, 31 (1970).

23. Robertson, E. R. and Harvey, J. M. (editors). The engineering uses of holography, 1970 (Cambridge University Press).

24. Sollid, J. E., "Holographic Interferometry Applied to Measurement of Small Static Displacements of Diffusely Reflecting Surfaces", Applied Optics, 8, 1587-1595, (1969).

25. Aprahamian, R., Evensen, D. A., Mixon, J. S. and Wright, J. E., "Application of Pulsed Holographic Interferometry to the Measurement of Propagating Transverse Waves in Beams", Experimental Mechanics, 11 (7), 309-314 (1971).

26. Aprahamian, R., Evensen, D. A., Mixon, J. S. and Jacoby, J. A., "Holographic Study of Propagating Transverse Waves in Plates", Experimental Mechanics, 11 (8), 357-362 (1971).

27. Boone, P. M., "Holographic Determination of In-Plane Deformation", Opt. Technol. 2, 94 (1970); Proc. Int. Symp. Holography, Besancon 5-1 (1970).

28. Wadsworth, N. J., Marchant, M. J. N. and Billing, B. F., "Real-Time Observation of In-Plane Displacements of Opaque Surfaces", Opt. Laser Technol. 5, 119 (1973).

29. Hovanesian and Varner, "Methods for Determining the Bending Moments in Normally Loaded Thin Plates by Hologram Interferometry", Strathclyde Symposium on the Engineering Uses of Holography (1968).

30. Sollid, J. E., "Holographic Interferometry Applied to Measurements of Small Static Displacements of Diffusely Reflecting Surface", Appl. Opt., 8, 1587 (1969).

31. Sollid, J. E., "Translation Displacement Versus Deformation Displacement in Holographic Interferometry", Opt. Commun. 2 (6)

32. Boone, P. M. and Verbiest, R., "Application of Hologram Interferometry to Plate Deformation and Translation Measurement", Opt. Acta. 16 (1969).

33. Wilson, A. D., "In-plane Displacement of a Stressed Membrane with a Hole Measurement by Holographic Interferometry", Appl. Opt., 10, 908-912 (1971).

34. Ennos, A. E., "Measurement of In-plane Surface Strain by Hologram Interferometry", J. of Scientific Instruments, (Journal of Physics E), Series 2, 1.

35. Aleksandrov, E. B. and Bonch-Bruevich, A. M., "Investigation of Surface Strains by the Hologram Technique", Soviet Physics - Technical Physics 12 (2) (1967).

36. Schumann, W., "Some Aspects of the Optical Techniques for Strain Determination", Experimental Mechanics, 13 (8), 225-231 (1973).

37. Hovanesian, J. D. and Hung, Y. Y., "Moire Contour-Sum Contour-Difference, and Vibration Analysis of Arbitrary Objects", Applied Optics, Vol. 10, No. 12, 1971.

38. Meadows, D. M., et al. "Generation of Surface Contours by Moire Patterns", Appl. Opt., 7, 942 (1970).

39. Hildebrand, B. P. and Haines, K. A., "Multiple-wavelength and Multiple-sources Holography Applied to Contour Generation", J. Opt. Soc. Am., 57, 155 (1967).

40. Brooks, R. E. and Heflinger, L. O., "Moire Gaging Using Optical Interference Patterns, Appl. Opt., 8, 935-939 (1969).

41. Post, D., "New Optical Methods of Moire-fringe Multiplication", Experimental Mechanics, 8 (12), 63-68 (1968).

42. Sciammarella, C. A., "Moire-fringe Multiplication by Means of Filtering and a Wave-front Reconstruction Process", Experimental Mechanics, 9 (4), 179-185 (1969).

43. Dainty, J. C., "Laser Speckle and Related Phenomena", Springer-Verlag, New York, (1975).

44. Fernelius, N. and Tome, C., "Vibration-Analysis Studies Using Changes of Laser Speckle", J. Of Opt. Soc. Am. Vol. 61, No. 5, 566-572, 1971.

45. Tiziani, H. J., "Application of Speckling for In-Plane Vibration Analysis", Optica Acta, 18, 1971.

46. Archbold, E., Burch, J. M. and Ennos, A. E., "Recording of In-Plane Displacement by Double-Exposure Speckle Photography", Optica Acta, 17, 883-898 (1970).

47. Groh, g., "Engineering Uses of Laser-produced Speckle Patterns", Strathclyde Symposium on the Engineering Uses of Holography, Cambridge University Press (1969).

48. Archbold, A. E. Ennos: J. Strain Analysis 9, 10 (1974)

49. Leendertz, J. A., "Interferometric Displacement Measurement on Scattering Surface Utilizing Speckle Effect", J. of Phys. E. Sc. Inst.,3 (1970)

50. Monk, G. S., "Light-Principles and Experiments", Dover, New York, 1963.

51. F. A. Jenkins and H. E. White., "Fundamentals of Optics", McGraw-Hill, New York, 1957.

52. Stroke, G. W., "An Introduction to Coherent Optics and Holography", Academic Press, New York, 1969.

53. Williams, C. E. and Becklund, O. A., "Optics: A Short Course for Engineers and Scientist", Wiley-Interscience, New York, 1972.

54. Yu, F. T. S., "Introduction to Diffraction, Information Processing, and Holography", The MIT Press, Massachusetts, 1973.

55. Cathey, W. T., "Optical Information Processing and Holography", Wiley, New York, 1974.

56. Fowles, G. R., "Introduction to Modern Optics", Holt, Rinehart and Winston, Inc., New York, 1968.

57. Fox, L., "Numerical Solution of Ordinary and Partial Differential Equations", Pergamon Press, London, 1962.

58. Smith, G. D., "Numerical Solution of Partial Differential Equations", Oxforh University Press, Toronto, 1975.

59. vonRosenberg, D. U., "Methods for the Numerical Solution of Partial Equations", American Elsevier Publishing Co., New York, 1969.

60. Crawford, F. S., "Waves", Berkley Physics Course-Volume 3, McGraw-Hill, New York, 1968.

61. Born, M., "Principles of Optics - Electromagnetic Theory of Propagation, Interference and Diffraction of Light", Pergamon Press, Toronto, 1975.

62. Canadian Institute of Steel Construction, "Handbook of Steel Construction", 2nd edition, Universal Offset Ltd., Don Mills, Ontario, 1970.

63. Hildebrand, F. B., "Advanced Calculus for Applications", Prentice-Hall, New Jersey, 1962, p. 7

APPENDIX A

DERIVATION OF EQUATION (2.9)

$$I(t) = |\bar{E}_1|^2 + |\bar{E}_2|^2 + 2\bar{E}_1 \cdot \bar{E}_2$$

$$= \left(\frac{a_1}{r_1}\right)^2 \cos^2(kr_1 - \omega t + \psi_1) + \left(\frac{a_2}{r_2}\right)^2 \cos^2(kr_2 - \omega t + \psi_2) +$$

$$2\left(\frac{a_1}{r_1}\right)\left(\frac{a_2}{r_2}\right)(\hat{e}_1 \cdot \hat{e}_2)\cos(kr_1 - \omega t + \psi_1)\cos(kr_2 - \omega t + \psi_2)$$

$$I_r = \int_0^T I(t)\, dt$$

$$= \left(\frac{a_1}{r_1}\right)^2 \int_0^T \cos^2(kr_1 - \omega t + \psi_1)\, dt + \left(\frac{a_2}{r_2}\right)^2 \int_0^T \cos^2(kr_2 - \omega t + \psi_2)\, dt +$$

$$2\left(\frac{a_1}{r_1}\right)\left(\frac{a_2}{r_2}\right)(\hat{e}_1 \cdot \hat{e}_2) \int_0^T \cos(kr_1 - \omega t + \psi_1)\cos(kr_2 - \omega t + \psi_2)\, dt$$

Let us now evaluate the three integrals and approximate the results by making use of the fact that $T \gg \tau$.

$$\int_0^T \cos^2(kr_1 - \omega t + \psi_1)\, dt = \frac{T}{2} - \frac{\tau}{8\pi}\left[\sin 2(kr_1 - \omega T + \psi_1) - \sin 2(kr_1 + \psi_1)\right] \simeq \frac{T}{2}$$

$$\int_0^T \cos^2(kr_2 - \omega t + \psi_2)\, dt \simeq \frac{T}{2}$$

$$\int_0^T \cos(kr_1 - \omega t + \psi_1)\cos(kr_2 - \omega t + \psi_2)\, dt = \frac{T}{2}\cos(kr_1 - kr_2 + \psi_1 - \psi_2) -$$

$$\frac{\tau}{8\pi}\left[\sin(kr_1 + kr_2 + \psi_1 + \psi_2 - 2\omega T) - \sin(kr_1 + kr_2 + \psi_1 + \psi_2)\right]$$

$$\simeq \frac{T}{2}\cos(kr_1 - kr_2 + \psi_1 - \psi_2)$$

With these integrals, I_r is given by equation (2.9).

APPENDIX B

DERIVATION OF EQUATIONS (2.18) AND (2.19)

$$\cos\left[kr(y,z) - \omega t + \psi\right] = \cos(kr_0 - \omega t + \psi)\cos kr_e - \sin(kr_0 - \omega t + \psi)\sin kr_e$$

$$I(t) = \left| E_r(t) \right|^2$$

$$= \left(\frac{a}{r_0}\right)^2 \left(\int_A \left[\cos(kr_0 - \omega t + \psi)\cos kr_e - \sin(kr_0 - \omega t + \psi)\sin kr_e\right] dA \right)^2$$

Let us define the integrals $E_1 = \int_A \cos kr_e(y,z)\, dA$

and $E_2 = \int_A \sin kr_e(y,z)\, dA$

With E_1 and E_2 , $I(t)$ becomes

$$I(t) = \left(\frac{a}{r_0}\right)^2 \left[E_1\cos(kr_0 - \omega t + \psi) - E_2\sin(kr_0 - \omega t + \psi)\right]^2$$

The recorded intensity I_r is given by

$$I_r = \int_0^T I(t)\, dt = \left(\frac{a}{r_0}\right)^2 \left(E_1^2 \int_0^T \cos^2(kr_0 - \omega t + \psi)\, dt + E_2^2 \int_0^T \sin^2(kr_0 - \omega t + \psi)\, dt \right.$$

$$\left. - 2E_1E_2 \int_0^T \sin 2(kr_0 - \omega t + \psi)\, dt \right.$$

In Appendix A it was shown that $\int_0^T \cos^2(kr_0 - \omega t + \psi)\, dt \simeq \frac{T}{2}$

and similarly it could be shown that $\int_0^T \sin^2(kr_0 - \omega t + \psi)\, dt \simeq \frac{T}{2}$

$$\int_0^T \sin 2(kr_0 - \omega t + \psi)\, dt = \frac{\tau}{4\pi}\left[\cos 2(kr_0 - \omega t + \psi) - \cos 2(kr_0 + \psi)\right] << \frac{T}{2}$$

With these integrals I_r is closely approximated by equation (2.18).

With the use of complex notation equation (2.18) may be written as equation (2.19), as is shown:

$$\int_A e^{ikr_e(y,z)} dA = \int_A \cos kr_e(y,z)\, dA + i \int_A \sin kr_e(y,z)\, dA$$

$$\int_A e^{-ikr_e(y,z)} dA = \int_A \cos kr_e(y,z)\, dA - i \int_A \sin kr_e(y,z)\, dA$$

$$\left(\int_A e^{ikr_e(y,z)} dA \right) \left(\int_A e^{-ikr_e(y,z)} dA \right) = \left(\int_A \cos kr_e(y,z)\, dA \right)^2 + \left(\int_A \sin kr_e(y,z)\, dA \right)^2$$

$$I_r = \left(\frac{a}{r_0} \right)^2 \frac{T}{2} \left(\int_A e^{ikr_e(y,z)} dA \right) \left(\int_A e^{-ikr_e(y,z)} dA \right) \qquad (2.19)$$

APPENDIX C

DERIVATION OF EQUATION (3.5)

The equations of the source (sw) and diffracted (dw) spherical wavefronts shown in Fig. C.1 are given as

dw: $$x^2 + (y - y_D)^2 + (z - z_D)^2 = x_s^2 + (y_D - y_A)^2 + z_D^2 \qquad (C.1)$$

sw: $$x^2 + (y - y_S)^2 + (z - z_S)^2 = x_s^2 + (y_S - y_A)^2 + z_S^2 \qquad (C.2)$$

The equation of the diffracted ray is the equation of the line from the "apparent" source point $D(0,y_D,z_D)$ to the point (x_s,y_a,z_a) in the aperture.

diffracted ray: $$y = \frac{y_a - y_D}{x_s} x + y_D \qquad (C.3a)$$

$$z = \frac{z_a - z_D}{x_s} x + z_D \qquad (C.3b)$$

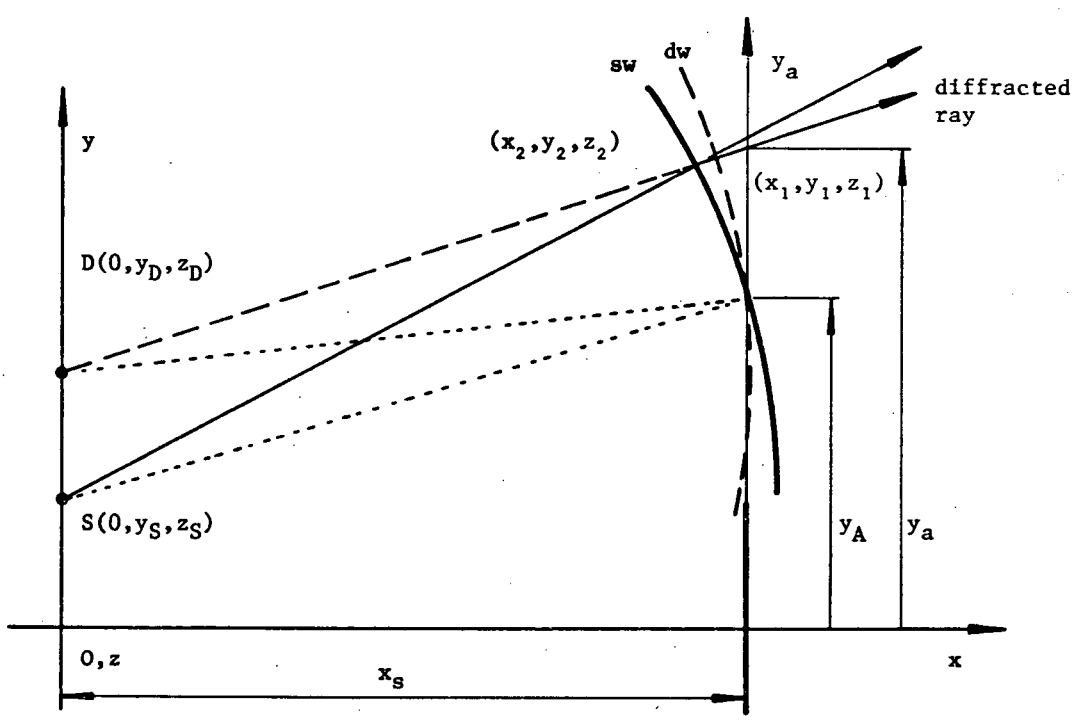

Fig. C.1 Diffraction in a single aperture camera.

Huygen's principle permits us to assume that the diffracted ray originates from the source wavefront at the point (x_2, y_2, z_2) and reaches the diffracted wavefront at the point (x_1, y_1, z_1). Therefore the diffracted wavefront "leads" the source wavefront by the distance $r_e(y_a, z_a)$ given by

$$r_e(y_a, z_a) = \sqrt{(x_1 - x_2)^2 + (y_1 - y_2)^2 + (z_1 - z_2)^2} \qquad (C.4)$$

The magnitudes of the parameters of DASC that is to be used are such that

$x_S > 30$ in.

$D < 2.5$ in. , $y_A < 1.25$ in.

$\lambda \simeq 2 \times 10^{-5}$ in.

$|y_D - y_S|, |z_D - z_S| < D_{ss} = 2.44 \dfrac{\lambda x_S}{d}$ hence $|\Delta y|, |\Delta z| < 4 \times 10^{-4}$

The field of view is such that $\left|\dfrac{y}{x_S}\right|, \left|\dfrac{z}{x_S}\right| < \dfrac{1}{5}$

Let us now define the following quantities:

$$a = \left(\frac{y_a - y_D}{x_S}\right)^2 + \left(\frac{z_a - z_D}{x_S}\right)^2 \qquad |a| < 4 \times 10^{-2}$$

$$b = \left(\frac{y_D - y_A}{x_S}\right)^2 + \left(\frac{z_D}{x_S}\right)^2 \qquad |b| < 4 \times 10^{-2}$$

$$c = \frac{y_A - y_D}{x_S} \Delta y - \frac{z_D}{x_S} \Delta z \qquad |c| < 1.6 \times 10^{-4}$$

$$\beta = \frac{\underline{r}}{x_S} \qquad |\beta| < 2 \times 10^{-3}$$

$$d^* = \beta(\Delta y \cos\theta + \Delta z \sin\theta) \qquad |d^*| < 1.6 \times 10^{-6}$$

It is convenient to introduce a polar coordinate system of the circular aperture, as is shown in Fig. 3.3 , so that we may write y_a and z_a as

$$y_a = y_A + \underline{r} \cos\theta \qquad z_a = \underline{r} \sin\theta$$

The equations (C.1) and (C.3) are evaluated at the point (x_1, y_1, z_1) and the equations (C.2) and (C.3) are evaluated at the point (x_2, y_2, z_2). By combining these equations and using the quantities that have been defined we get a quadratic equation in (r_e/x_s)

$$\left(\frac{r_e}{x_s}\right)^2 - 2\left(\frac{r_e}{x_s}\right)\left(\sqrt{G} + \frac{c + d^*}{\sqrt{F}}\right) + 2\left(\frac{\sqrt{G}}{\sqrt{F}}(c + d^*) - c\right) = 0 \qquad \text{(C.5)}$$

where F and G are defined as

$$F = 1 + a$$

$$G = 1 + b$$

The solution of equation (C.5) for r_e is given by equation (3.5). Its derivation is quite tedious as Taylor's series for the square root and several fractions must be used to determine r_e with the desired accuracy of $\lambda/10$. By making use of equation (3.5) it may be shown that $|r_e/x_s| < 1.5 \times 10^{-6}$ With the magnitude of r_e known, we see that if r_e is to be determined with $\lambda/10$ accuracy (or r_e/x_s with 6.7×10^{-8} accuracy), the quadratic term in equation (C.5) is so small that it may be neglected. This was done and it was found, that the solution of the resultant linear equation is still given by equation (3.5). The latter solution is much less tedious and therefore this approach is used in the subsequent appendices whenever possible.

APPENDIX D

DERIVATION OF EQUATION (3.7)

Let us define the following terms:

$$D_1 = \left(1 - \frac{3y_S^2}{2x_S^2}\right)\Delta y - \frac{z_S y_S}{x_S^2}\,\Delta z \tag{D.1}$$

$$D_2 = \left(1 - \frac{3z_S^2}{2x_S^2}\right)\Delta z - \frac{z_S y_S}{x_S^2}\,\Delta y \tag{D.2}$$

$$\rho = \frac{kd}{2}\sqrt{D_1^2 + D_2^2} \tag{D.3}$$

Using equations (D.1),(D.2) and (3.5) we may write

$$kr_e(\underline{r},\theta) = k\underline{r}(D_1\cos\theta + D_2\sin\theta) \tag{D.4}$$

The recorded intensity I_r is evaluated by using equations (2.19) and (D.4) as

$$I_r = \left(\frac{a}{r_0}\right)^2 \frac{T}{2}\left[\int_0^{d/2}\int_0^{2\pi} e^{ik\underline{r}(D_1\cos\theta + D_2\sin\theta)}\,\underline{r}\,d\underline{r}\,d\theta \;\bullet \int_0^{d/2}\int_0^{2\pi} e^{-ik\underline{r}(D_1\cos\theta + D_2\sin\theta)}\,\underline{r}\,d\underline{r}\,d\theta\right] \tag{D.5}$$

Since $$\int_0^{d/2}\int_0^{2\pi} e^{\pm ik\underline{r}(D_1\cos\theta + D_2\sin\theta)}\,\underline{r}\,d\underline{r}\,d\theta = \frac{\pi d^2}{4}\,\frac{2J_1(\rho)}{\rho} \tag{D.6}$$

$$I_r = \left(\frac{a}{r_0}\right)^2 \frac{T}{2}\left(\frac{\pi d^2}{4}\right)^2 \left(\frac{2J_1(\rho)}{\rho}\right)^2 \tag{D.7}$$

Using I_0 given by equation (3.8), I_r may be written as

$$I_r = I_0\left(\frac{2J_1(\rho)}{\rho}\right)^2 \tag{3.7}$$

APPENDIX E

DERIVATION OF EQUATIONS (3.10) AND (3.11)

Using equations (D.1),(D.2) and (D.3) we may write the following:

$$\left(\frac{2}{kd}\,\rho\right)^2 = D_1^2 + D_2^2 \simeq \Delta y^2 + \Delta z^2$$

With Δy and Δz defined by equation (3.6), the above equation may be written as

$$(y_D - y_S)^2 + (z_D - z_S)^2 = \left(\frac{2x_S}{kd}\,\rho\right)^2 \qquad \text{(E.1)}$$

Equation (E.1) is the equation of a circle of the radius $\left(\frac{2x_S}{kd}\,\rho\right)$, and with the center at (y_S, z_S) in the specimen plane. By making use of equation (2.12) we may put equation (E.1) in the form

$$(y_i - y_{ic})^2 + (z_i - z_{ic})^2 = \left(\frac{2x_i}{kd}\,\rho\right)^2 \qquad \text{(E.2)}$$

This time equation (E.2) is the equation of a circle of the radius $\left(\frac{2x_i}{kd}\,\rho\right)$ and with the center at (y_{ic}, z_{ic}) in the image plane. From equation (E.2) it is apparent that I_r is circular with its center at the geometric image $R(y_{ic}, z_{ic})$ of the source point $S(y_S, z_S)$. As shown in Fig. 3.4 , I_r varies as $\left(\frac{2J_1(\rho)}{\rho}\right)^2$; it has the maximum at $\rho = 0$, and its first minimum at $\rho = 3.832$. The area of the circle of the radius $\left(\frac{2x_i}{kd}\,3.832\right) \simeq 1.22\,\lambda\frac{x_i}{d}$ is known as the Airy disk and it will be referred to as the "speckle" . The diameter of the speckle in the image plane will be called D_s and the diameter of the apparent speckle in the specimen plane will be called D_{ss} . The two diameters are given as

$$D_s = 2.44\,\lambda\frac{x_i}{d} \qquad (3.10)$$

$$D_{ss} = 2.44\,\lambda\frac{x_s}{d} \qquad (3.11)$$

APPENDIX F

In this appendix it is shown that the unit electric field vectors of all rays reaching a point in the image plane are nearly parallel so that the vector nature of the rays may be neglected in the calculation of I_r.

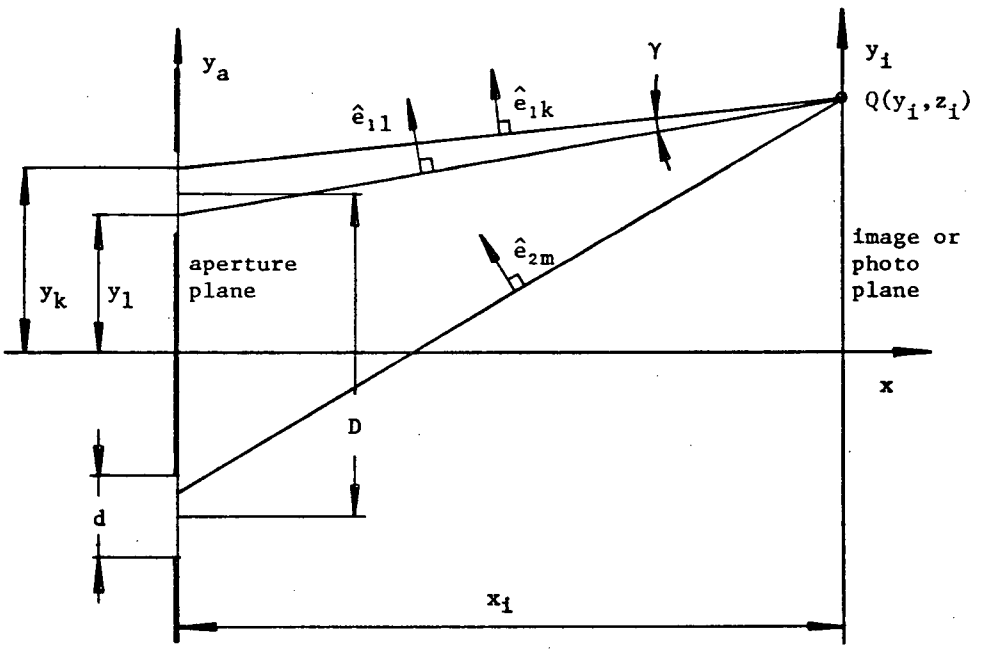

Fig. F.1 Unit vectors of electric fields.

$$\gamma \simeq \tan\gamma \simeq (y_k - y_l)/x_i$$

$$\hat{e}_{mk}\cdot\hat{e}_{nl} = |\hat{e}_{mk}||\hat{e}_{nl}|\cos\gamma = \cos\gamma = 1 - \frac{\gamma^2}{2} + \ldots$$

For the single aperture camera $\gamma < \frac{d}{x_i} < \frac{.0625}{12} = .0052$ and hence $\hat{e}_{mk}\cdot\hat{e}_{nl} \simeq 1$ with the error being smaller than $.0052^2/2 = 1.4 \times 10^{-5}$.

When DASC or DASSC is considered, $\gamma < \frac{D + d}{x_i} < \frac{2.5 + .0625}{12} = .214$ and this time $\hat{e}_{mk}\cdot\hat{e}_{nl} \simeq 1$ with the error being smaller than $.214^2/2 = .023$ which is still sufficiently small.

(the dimensions of d,D and x_i are in inches)

APPENDIX G

DERIVATION OF r_{e1} AND r_{e2} FOR DASC DURING THE FIRST EXPOSURE.

The optical path lengths from the apparent point source S to the point Q, in the image plane , are given by

through aperture 1 : $\overline{S-Q} = \overline{S-sw_1} + \overline{dw_1-sw_1} + \overline{dw_1-Q} = r_1$

through aperture 2 : $\overline{S-Q} = \overline{S-sw_2} + \overline{dw_2-sw_2} + \overline{dw_2-Q} = r_2$

In a focused system the optical path lengths from the point D to its geometric image Q are all equal, and therefore we may write

$$\overline{D-dw_1} + \overline{dw_1-Q} = \overline{D-dw_2} + \overline{dw_2-Q}$$

$$\overline{dw_2-Q} = \overline{D-dw_1} - \overline{D-dw_2} + \overline{dw_1-Q}$$

Using the last equation the optical path length through aperture 2 is given as

$$\overline{S-Q} = \overline{S-sw_2} + \overline{dw_2-sw_2} + \overline{D-dw_1} - \overline{D-dw_2} + \overline{dw_1-Q} + (\overline{S-sw_1} - \overline{S-sw_1})$$

We define the mean optical path length r_0 as

$$r_0 = \overline{S-sw_1} + \overline{dw_1-Q}$$

With r_0 now defined the total optical path lengths are given as

$$r_1 = r_0 + \overline{dw_1-sw_1}$$

$$r_2 = r_0 + \overline{dw_2-sw_2} + (\overline{D-dw_1} - \overline{S-sw_1}) - (\overline{D-dw_2} - \overline{S-sw_2})$$

The variations in the two optical path lengths are then given by

$$r_{e1} = r_1 - r_0 = \overline{dw_1-sw_1} \qquad \text{(G.1)}$$

$$r_{e2} = r_2 - r_0 = \overline{dw_2-sw_2} + (\overline{D-dw_1} - \overline{S-sw_1}) - (\overline{D-dw_2} - \overline{S-sw_2}) \qquad \text{(G.2)}$$

We must now express r_{e1} and r_{e2} in terms of system parameters. The equations of the source and diffracted spherical wavefronts are given as

$$dw_1 : \quad x^2 + (y - y_D)^2 + (z - z_D)^2 = x_s^2 + (y_D - y_A)^2 + z_D^2 \qquad (G.3)$$

$$dw_2 : \quad x^2 + (y - y_D)^2 + (z - z_D)^2 = x_s^2 + (y_D + y_A)^2 + z_D^2 \qquad (G.4)$$

$$sw_1 : \quad x^2 + (y - y_S)^2 + (z - z_S)^2 = x_s^2 + (y_S - y_A)^2 + z_S^2 \qquad (G.5)$$

$$sw_2 : \quad x^2 + (y - y_S)^2 + (z - z_S)^2 = x_s^2 + (y_S + y_A)^2 + z_S^2 \qquad (G.6)$$

The equations of the diffracted ray are the same as before and are given by equations (C.3) . Note that the equations of dw_2 and sw_2 are the same those of dw_1 and sw_1 except for the sign of y_A .

r_{e1} has been derived in Appendix C (where r_{e1} is called r_e), and is given by equation (3.5) . An examination of that equation reveals that r_e is not a function of y_A and hence we may write

$$r_{e1} = \overline{dw_1 - sw_1} = \overline{dw_2 - sw_2} = r_e \qquad (G.7)$$

$$r_{e2} = \overline{dw_2 - sw_2} + (\overline{D - dw_1} - \overline{S - sw_1}) - (\overline{D - dw_2} - \overline{S - sw_2})$$

$$= r_e + \sqrt{x_s^2 + (y_D - y_A)^2 + z_D^2} - \sqrt{x_s^2 + (y_S - y_A)^2 + z_S^2}$$

$$- \sqrt{x_s^2 + (y_D + y_A)^2 + z_D^2} + \sqrt{x_s^2 + (y_S + y_A)^2 + z_S^2} \qquad (G.8)$$

Let us now define the following parameters:

$$X_{s0}^2 = x_s^2 + y_S^2 + z_S^2 + y_A^2$$

$$\Delta = (y_D^2 - y_S^2 + z_D^2 - z_S^2)/X_{s0}^2 \qquad |\Delta| < 3 \times 10^{-4}$$

$$e = 2y_A(y_D - y_S)/X_{s0}^2 \qquad |e| < 3 \times 10^{-5}$$

$$f = 2y_A y_S/X_{s0}^2 \qquad |f| < 1.3 \times 10^{-2}$$

With these parameters and using the Taylor's series expansion for the square roots in equation (G.8) and by neglecting terms smaller than $\lambda/30$ we get

$$r_{e2} = r_e - \left(e - \frac{\Delta f}{2}\right) X_{s0}$$

The last equation may be accurately approximated by

$$r_{e2} = r_e - D\delta \tag{G.9}$$

where δ is given by

$$\delta = \left(1 - \frac{y_S^2}{X_{S0}^2}\right)\frac{y_D - y_S}{X_{S0}} - \frac{y_S z_S}{X_{S0}^2}\,\frac{z_D - z_S}{X_{S0}} \tag{G.10}$$

Note that a small change in y_D alters δ much more than the same change in z_D would; because of this, and using equation (2.12) δ is accurately approximated as

$$\delta \simeq -\frac{y_i - y_{ic}}{x_i} \tag{3.13}$$

APPENDIX H

DERIVATION OF EQUATION (3.12) - THE FIRST EXPOSURE I_r

$$I_r = \left(\frac{a}{r_0}\right)^2 \frac{T}{2}\left[\int_0^{d/2}\int_0^{2\pi} e^{ikr_e}\, \underline{r}\, d\underline{r}\, d\theta + \int_0^{d/2}\int_0^{2\pi} e^{ik(r_e - D\delta)}\, \underline{r}\, d\underline{r}\, d\theta\right] \cdot$$

$$\left[\int_0^{d/2}\int_0^{2\pi} e^{-ikr_e}\, \underline{r}\, d\underline{r}\, d\theta + \int_0^{d/2}\int_0^{2\pi} e^{-ik(r_e - D\delta)}\, \underline{r}\, d\underline{r}\, d\theta\right]$$

$$= \left(\frac{a}{r_0}\right)^2 \frac{T}{2}\left(1 + e^{-ikD\delta}\right)\left(1 + e^{ikD\delta}\right)\left[\int_0^{d/2}\int_0^{2\pi} e^{ikr_e}\, \underline{r}\, d\underline{r}\, d\theta\right] \cdot$$

$$\left[\int_0^{d/2}\int_0^{2\pi} e^{-ikr_e}\, \underline{r}\, d\underline{r}\, d\theta\right] \qquad \text{(H.1)}$$

The values of the integrals in the above equation are given by equation (D.6) and with

$$\left(1 + e^{-ikD\delta}\right)\left(1 + e^{ikD\delta}\right) = 4\cos^2 kD\delta$$

equation (H.1) becomes

$$I_r = \left(\frac{a}{r_0}\right)^2 \frac{T}{2}\left(2\,\frac{\pi d^2}{4}\right)^2 \left(\frac{2J_1(\rho)}{\rho}\right)^2 \cos^2\frac{kD\delta}{2} \qquad \text{(H.2)}$$

With I_0 given by equation (3.8), I_r may be written as

$$I_r = 4I_0\left(\frac{2J_1(\rho)}{\rho}\right)^2 \cos^2\frac{kD\delta}{2} \qquad (3.12)$$

APPENDIX I

DERIVATION OF EQUATIONS (3.14) AND (3.15)

The minima of I_r given by equation (3.12) occur when either of the terms $\frac{2J_1(\rho)}{\rho}$ or $\cos^2\frac{kD\delta}{2}$ is zero. The first term has already been discussed in Appendix E where it is shown that I_r may be approximated by the Airy disk of diameter D_s in the image plane, and of diameter D_{ss} in the specimen plane. The second, cosine, term modulates the first term so that in this case the resultant I_r looks as is shown in Fig. 3.7 . The period of the modulation is called the speckle grid pitch G_s and it is calculated from two consecutive zeros of the cosine term.

for $y_i - y_{ic} = G_s$: $$\frac{kD\delta}{2} \simeq -\frac{kD(y_i - y_{ic})}{2x_i} = \frac{kDG_s}{2x_i} = \pi$$

since $k = 2\pi/\lambda$ $$G_s = \frac{\lambda x_i}{D} \tag{3.14}$$

By using equation (2.12) the apparent speckle grid pitch G_{ss} is determined from the last equation as

$$G_{ss} = \frac{\lambda x_s}{D} \tag{3.15}$$

APPENDIX J

DERIVATION OF r_{e1} AND r_{e2} FOR DASC DURING THE SECOND EXPOSURE

Due to a general deformation of a specimen, the point S representing the specimen surface is displaced to S^* , and its coordinates change between the two exposures as

$$S(0,y_S,z_S) \rightarrow S^*(u,y_S + v,z_S + w)$$

The equations of the diffracted wavefronts dw_1 and dw_2 , as well as those of the diffracted rays remain unchanged and are given by equations (G.3), (G.4) and (C.3) respectively. The equations of the source wavefronts sw_1 and sw_2 must be modified to account for the altered, second exposure position of S .

$$sw_1 : \quad (x - u)^2 + \left[y - (y_S + v)\right]^2 + \left[z - (z_S + w)\right]^2 = (x_s - u)^2 + \left[(y_S + v) - y_A\right]^2 + (z_S + w)^2 \quad (J.1)$$

$$sw_2 : \quad (x - u)^2 + \left[y - (y_S + y)\right]^2 + \left[z - (z_S + w)\right]^2 = (x_s - u)^2 + \left[(y_S + v) + y_A\right]^2 + (z_S + w)^2 \quad (J.2)$$

Calculations completely analogous to those presented in Appendix C will again be done. The diffracted wavefronts lead the source wavefronts by the distance $r_e(y_a,z_a)$ given by equation (C.4).

We now define U,V and W as

$$U = \frac{u}{x_s} \qquad |U| < 1.3 \times 10^{-3} \qquad \text{for } |u| < 1 \text{ mm} \simeq .04 \text{ in.}$$

$$V = \frac{v}{x_s} \qquad |V| < 4 \times 10^{-4} \qquad \text{for } |v| < .012 \text{ in.}$$

$$W = \frac{w}{x_s} \qquad |W| < 4 \times 10^{-4} \qquad \text{for } |w| < .012 \text{ in.}$$

r_{e1} , the optical path length variation of the rays passing through aperture 1 , will be determined first. The equations (G.3) and (C.3) are evaluated at the point (x_1, y_1, z_1) and equations (J.1) and (C.3) are evaluated at the point (x_2, y_2, z_2). All these equations are combined and we eventually get a quadratic equation in (r_{e1}/x_s)

$$\left(\frac{r_{e1}}{x_s}\right)^2 - 2\left(\frac{r_{e1}}{x_s}\right)\left[\sqrt{G} + \frac{1}{\sqrt{F}}\left(\frac{y_A - y_D}{x_s}(\Delta y - V) - \frac{z_D}{x_s}(\Delta z - W) - U\right) + \right.$$

$$\left. + \frac{\beta}{\sqrt{F}}\left((\Delta y - V)\cos\theta + (\Delta z - W)\sin\theta\right)\right] + 2\frac{\sqrt{G}}{\sqrt{F}}\left[\frac{y_A - y_D}{x_s}(\Delta y - V) - \frac{z_D}{x_s}(\Delta z - W) - \right.$$

$$\left. - U + \beta\left((\Delta y - V)\cos\theta + (\Delta z - W)\sin\theta\right)\right] + 2\Delta y\,\frac{y_D - y_A}{x_s} + 2\Delta z\,\frac{z_D}{x_s} -$$

$$- 2V\,\frac{y_D - y_A}{x_s} - 2W\,\frac{z_D}{x_s} + 2U = 0 \qquad \text{(J.3)}$$

In Appendix C it was shown that the quadratic term may be neglected when r_{e1} is to be determined to $\lambda/10$ (or in fact to $\lambda/30$) accuracy and this was done here too. Using Taylor's series expansions for square roots and fractions, the solution of equation (J.3) (with the quadratic term neglected) is found to accuracy of $\lambda/30$ as

$$r_{e1} = \underline{r}\left[\left[\left(1 - \frac{3y_S^2}{2x_S^2}\right)(\Delta y - V) - \frac{y_S z_S}{x_S^2}(\Delta z - W) - \left(1 - \frac{3y_S^2 + 3z_S^2}{2x_S^2}\right)\frac{y_S - y_A}{x_S}U\right]\cos\theta + \right.$$

$$\left. + \left[\left(1 - \frac{3z_S^2}{2x_S^2}\right)(\Delta z - W) - \frac{y_S z_S}{x_S^2}(\Delta y - V) - \left(1 - \frac{3y_S^2 + 3z_S^2}{2x_S^2}\right)\frac{z_S}{x_S}U\right]\sin\theta\right] \qquad \text{(J.4)}$$

Since $r_{e1} = \overline{dw_1 - sw_1}$ is this time a function of y_A , we must replace y_A in equation (J.4) by $-y_A$ to get $\overline{dw_2 - sw_2}$, and r_{e2} is then calculated as

$$r_{e2} = r_{e1}(y_A \to -y_A) + (\overline{D-dw_1} - \overline{S-sw_1}) - (\overline{D-dw_2} - \overline{S-sw_2})$$

$$r_{e2} = r_{e1}(-y_A) + \sqrt{x_s^2 + (y_D - y_A)^2 + z_D^2} - \sqrt{(x_s - u)^2 + \left[(y_S + v) - y_A\right]^2 + (z_S + w)^2}$$
$$- \sqrt{x_s^2 + (y_D + y_A)^2 + z_D^2} + \sqrt{(x_s - u)^2 + \left[(y_S + v) + y_A\right]^2 + (z_S + w)^2} \qquad (J.5)$$

Using Taylor's series expansions for the square roots in the above equation, r_{e2} , accurate to $\lambda/30$ was found as

$$r_{e2} = r_{e1}(-y_A) - D(\delta - \xi) \qquad (J.6)$$

where ξ is given by equation (3.16). With D_1 and D_2 defined by equations (D.1) and (D.2) we define E_1 ,E_2 and F as

$$E_1 = D_1 - \left(1 - \frac{3y_S^2}{2x_s^2}\right)\frac{v}{x_s} + \frac{y_S z_S}{x_s^2}\frac{w}{x_s} - \left(1 - \frac{3y_S^2 + 3z_S^2}{2x_s^2}\right)\frac{y_S}{x_s}\frac{u}{x_s}$$

$$E_2 = D_2 - \left(1 - \frac{3z_S^2}{2x_s^2}\right)\frac{w}{x_s} + \frac{y_S z_S}{x_s^2}\frac{v}{x_s} - \left(1 - \frac{3y_S^2 + 3z_S^2}{2x_s^2}\right)\frac{z_S}{x_s}\frac{u}{x_s}$$

$$F = \left(1 - \frac{3y_S^2 + 3z_S^2}{2x_s^2}\right)\frac{D/2}{x_s}\frac{u}{x_s}$$

We can now write equations (J.4) and (J.6) as

$$r_{e1} = \underline{r}\left[(E_1 + F)\cos\theta + E_2\sin\theta\right] \qquad (J.7)$$

$$r_{e2} = \underline{r}\left[(E_1 - F)\cos\theta + E_2\sin\theta\right] - D(\delta - \xi) \qquad (J.8)$$

APPENDIX K

DERIVATION OF EQUATION (3.17) - THE SECOND EXPOSURE I_r

The substitution of the second exposure optical path length variations r_{e_1} and r_{e_2} , given by equations (J.7) and (J.8), in equation (2.19) gives the second exposure recorded intensity as

$$I_r = \left(\frac{a}{r_0}\right)^2 \frac{T}{2}\left[\int_0^{d/2}\int_0^{2\pi} e^{ikr_{e_1}}\,\underline{r}\,d\theta\,d\underline{r} + \int_0^{d/2}\int_0^{2\pi} e^{ikr_{e_2}}\,\underline{r}\,d\theta\,d\underline{r}\right]\cdot$$

$$\left[\int_0^{d/2}\int_0^{2\pi} e^{-ikr_{e_1}}\,\underline{r}\,d\theta\,d\underline{r} + \int_0^{d/2}\int_0^{2\pi} e^{-ikr_{e_2}}\,\underline{r}\,d\theta\,d\underline{r}\right] \qquad (K.1)$$

We define ρ_1 and ρ_2 as

$$\rho_1 = \frac{kd}{2}\sqrt{(E_1 + F)^2 + E_2^2} \qquad (K.2)$$

$$\rho_2 = \frac{kd}{2}\sqrt{(E_1 - F)^2 + E_2^2} \qquad (K.3)$$

The integrals of equation (K.1) are evaluated as

$$\int_0^{d/2}\int_0^{2\pi} e^{\pm r_{e_1}}\,\underline{r}\,d\theta\,d\underline{r} = 2\,\frac{\pi d^2}{4}\,\frac{J_1(\rho_1)}{\rho_1} \qquad (K.4)$$

$$\int_0^{d/2}\int_0^{2\pi} e^{\pm r_{e_2}}\,\underline{r}\,d\theta\,d\underline{r} = 2\,\frac{\pi d^2}{4}\,\frac{J_1(\rho_2)}{\rho_2}\,e^{\mp ikD(\delta - \xi)} \qquad (K.5)$$

Using these results equation (K.1) becomes

$$I_r = \left(\frac{a}{r_0}\right)^2 \frac{T}{2}\left(2\,\frac{\pi d^2}{4}\right)^2 \left(\frac{J_1(\rho_1)}{\rho_1} + e^{-ikD(\delta - \xi)}\,\frac{J_1(\rho_2)}{\rho_2}\right)\left(\frac{J_1(\rho_1)}{\rho_1} + e^{ikD(\delta - \xi)}\,\frac{J_1(\rho_2)}{\rho_2}\right)$$

$$= \left(\frac{a}{r_0}\right)^2 \frac{T}{2}\left(2\,\frac{\pi d^2}{4}\right)^2 \left[\left(\frac{J_1(\rho_1)}{\rho_1} - \frac{J_1(\rho_2)}{\rho_2}\right)^2 + \left(\frac{2J_1(\rho_1)}{\rho_1}\right)\left(\frac{2J_1(\rho_2)}{\rho_2}\right)\cos^2\frac{kD(\delta - \xi)}{2}\right]$$

(3.17)

APPENDIX L

DERIVATION OF EQUATIONS (3.19) AND (3.20)

From the form of the second exposure I_r it is apparent that the speckle grid has been shifted with respect to its first exposure position. This shift produces Moire fringes and it will be now related to the camera parameters and the displacements u,v and w. Using equations (G.10) and (3.16) defining δ and ξ respectively we write

$$\frac{kD(\delta - \xi)}{2} = \frac{kD}{2}\left[\left(1 - \frac{y_S^2}{X_{S0}^2}\right)\frac{y_D - y_S}{X_{S0}} - \frac{y_S z_S}{X_{S0}^2}\frac{z_D - z_S}{X_{S0}} - \frac{u}{X_{S0}}\left[\frac{y_S}{X_{S0}}\left(\frac{x_S}{X_{S0}} + \frac{u}{X_{S0}}\right) - \right.\right.$$

$$\left.\left. - \frac{2}{D}\frac{x_S}{X_{S0}}\left(v\frac{y_S}{X_{S0}} + w\frac{z_S}{X_{S0}}\right)\right] - \frac{v}{X_{S0}}\left(1 - \frac{y_S^2}{X_{S0}^2}\right) + \frac{w}{X_{S0}}\frac{y_S z_S}{X_{S0}^2}\right] \qquad (L.1)$$

During the first exposure the speckle grid "passed" through the center of the speckle, and hence we may write $y_{sg_1} = y_S$, where y_{sgj} is analogous to y_{igj} ; it denotes the y-coordinate of the "center", or the first maximum of the modulating term, of the apparent speckle grid in the j-th exposure. We find y_{sg_2} , the speckle grid "center" during the second exposure, on the line $z = z_S$ from

$$\frac{kD(\delta - \xi)}{2} = 0 \qquad (L.2)$$

where y_D is replaced by y_{sg_2} . The solution to equation (L.2) was found as

$$y_{sg_2} = y_S + v + \left(1 - \frac{y_S^2}{X_{S0}^2}\right)^{-1}\left[u\left(\frac{y_S}{X_{S0}}\frac{x_S + u}{X_{S0}} - \frac{2x_S}{D}\frac{vy_S + wz_S}{X_{S0}^2}\right) - w\frac{y_S z_S}{X_{S0}^2}\right] \qquad (L.3)$$

Equation (L.3) is accurately approximated as

$$y_{sg_2} \simeq y_S + v + \frac{y_S}{x_S}u - \frac{y_S z_S}{x_S^2}w \qquad (L.4)$$

The Moire fringe number n is found from equation (3.18) which by using equation (2.12) may be written as

$$y_{sg_2} - y_{sg_1} = y_{sg_2} - y_S = - nG_{ss} \tag{L.5}$$

n is determined from equations (L.3) and (L.5) as

$$n = - \frac{D}{\lambda x_s}\left[\left(1 - \frac{y_S^2}{X_{s0}^2}\right)^{-1}\left[u\left(\frac{y_S}{X_{s0}}\,\frac{x_s + u}{X_{s0}} - \frac{2x_s}{D}\,\frac{vy_S + wz_S}{X_{s0}^2}\right) - w\,\frac{y_S z_S}{X_{s0}^2}\right] + v\right] \tag{3.19}$$

Equation (3.19) may be closely approximated as

$$n \simeq - \frac{D}{\lambda x_s}\left(\frac{y_S}{x_s}\,u + v - \frac{y_S z_S}{x_s^2}\,w\right) \tag{3.20}$$

APPENDIX M

DERIVATION OF EQUATION (3.21)

The envelope of the speckle grid term of equation (3.17) is given by the product $\frac{2J_1(\rho_1)}{\rho_1}\frac{2J_1(\rho_2)}{\rho_2}$. The two terms are circularly symmetric about their respective maxima (centers) which occur when

$$\rho_1 = 0 \tag{M.1}$$

$$\rho_2 = 0 \tag{M.2}$$

Using equations (K.2) and (K.3) defining ρ_1 and ρ_2 the approximate solutions of equations (M.1) and (M.2) are given by

$\rho_1 = 0$:

$$y_D = y_{D1} = y_S + v + u\frac{y_S - y_A}{x_s} \tag{M.3a}$$

$$z_D = z_{D1} = z_S + w + u\frac{z_S}{x_s} \tag{M.3b}$$

$\rho_2 = 0$:

$$y_D = y_{D2} = y_S + v + u\frac{y_S + y_A}{x_s} \tag{M.4a}$$

$$z_D = z_{D2} = z_{D1} \tag{M.4b}$$

We denote the coordinates of the centers of the two speckles by (y_{ic1}, z_{ic1}) and (y_{ic2}, z_{ic2}) respectively. By making use of equation (2.12) these centers are determined from equations (M.3) and (M.4) as

$$y_{ic1} = -\frac{x_i}{x_s}y_{D1} = y_{ic} - v\frac{x_i}{x_s} + u\frac{y_{ic}}{x_s} + u\frac{x_i}{x_s}\frac{D}{2x_s} \tag{M.5a}$$

$$z_{ic1} = -\frac{x_i}{x_s}z_{D1} = z_{ic} - w\frac{x_i}{x_s} + u\frac{z_{ic}}{x_s} \tag{M.5b}$$

$$y_{ic2} = -\frac{x_i}{x_s}y_{D2} = y_{ic} - v\frac{x_i}{x_s} + u\frac{y_{ic}}{x_s} - u\frac{x_i}{x_s}\frac{D}{2x_s} \tag{M.6a}$$

$$z_{ic2} = -\frac{x_i}{x_s}z_{D2} = z_{ic1} \tag{M.6b}$$

where y_{ic} and z_{ic} are the coordinates of the first exposure speckle centre. The limit on the magnitude of the displacements u,v and w is obtained from the requirement that the first and the second exposure speckles must overlap so that Moire fringes may be formed. We write

$$\left[(y_{ic1} - y_{ic})^2 + (z_{ic1} - z_{ic})^2\right]^{\frac{1}{2}} < \frac{D_s}{2} \tag{M.7a}$$

$$\left[(y_{ic2} - y_{ic})^2 + (z_{ic2} - z_{ic})^2\right]^{\frac{1}{2}} < \frac{D_s}{2} \tag{M.7b}$$

Using equation (2.12) and by combining the two equations (M.7) we get

$$\left[\left(v + u\,\frac{y_S \pm D/2}{x_S}\right)^2 + \left(w + u\,\frac{z_S}{x_S}\right)^2\right]^{\frac{1}{2}} < \frac{D_{ss}}{2} = 1.22\,\lambda\,\frac{x_s}{d} \tag{3.21}$$

APPENDIX N

DERIVATION OF r_{eij} FOR DASSC DURING THE FIRST EXPOSURE

With r_0 defined by equation (3.22) as $r_0 = \overline{S_2\text{-}sw_{12}} + \overline{dw_1\text{-}Q}$ the four optical path lengths r_{ij} from the two point sources S_1 and S_2 to the point Q in the image plane are given as

$$r_{12} = \overline{S_2\text{-}sw_{12}} + \overline{dw_1\text{-}sw_{12}} + \overline{dw_1\text{-}Q} = r_0 + \overline{dw_1\text{-}sw_{12}} \tag{N.1}$$

$$r_{11} = \overline{S_1\text{-}sw_{11}} + \overline{dw_1\text{-}sw_{11}} + \overline{dw_1\text{-}Q} + (\overline{S_2\text{-}sw_{12}} - \overline{S_2\text{-}sw_{12}})$$

$$= r_0 + \overline{dw_1\text{-}sw_{11}} + (\overline{S_1\text{-}sw_{11}} - \overline{S_2\text{-}sw_{12}}) \tag{N.2}$$

$$r_{21} = \overline{S_1\text{-}sw_{21}} + \overline{dw_2\text{-}sw_{21}} + \overline{dw_2\text{-}Q} + (\overline{S_2\text{-}sw_{12}} - \overline{S_2\text{-}sw_{12}})$$

In Appendix G it was shown that $\overline{dw_2\text{-}Q} = \overline{D\text{-}dw_1} - \overline{D\text{-}dw_2} + \overline{dw_1\text{-}Q}$ and hence r_{21} may be written as

$$r_{21} = r_0 + \overline{dw_2\text{-}sw_{21}} + (\overline{D\text{-}dw_1} - \overline{S_2\text{-}sw_{12}}) - (\overline{D\text{-}dw_2} - \overline{S_1\text{-}sw_{21}}) \tag{N.3}$$

$$r_{22} = \overline{S_2\text{-}sw_{22}} + \overline{dw_2\text{-}sw_{22}} + \overline{dw_2\text{-}Q} + (\overline{S_2\text{-}sw_{12}} - \overline{S_2\text{-}sw_{12}})$$

$$= r_0 + \overline{dw_2\text{-}sw_{22}} + (\overline{D\text{-}dw_1} - \overline{S_2\text{-}sw_{12}}) - (\overline{D\text{-}dw_2} - \overline{S_2\text{-}sw_{22}}) \tag{N.4}$$

The optical path length variations r_{eij} are then given by

$$r_{e12} = r_{12} - r_0 = \overline{dw_1\text{-}sw_{12}} \tag{N.5}$$

$$r_{e11} = r_{11} - r_0 = \overline{dw_1\text{-}sw_{11}} + (\overline{S_1\text{-}sw_{11}} - \overline{S_2\text{-}sw_{12}}) \tag{N.6}$$

$$r_{e21} = r_{21} - r_0 = \overline{dw_2\text{-}sw_{21}} + (\overline{D\text{-}dw_1} - \overline{S_2\text{-}sw_{12}}) - (\overline{D\text{-}dw_2} - \overline{S_1\text{-}sw_{21}}) \tag{N.7}$$

$$r_{e22} = r_{22} - r_0 = \overline{dw_2\text{-}sw_{22}} + (\overline{D\text{-}dw_1} - \overline{S_2\text{-}sw_{12}}) - (\overline{D\text{-}dw_2} - \overline{S_2\text{-}sw_{22}}) \tag{N.8}$$

The four spherical source wavefronts have the centers at the points $S_1(0,y_{S1},z_S)$ and $S_2(0,y_{S2},z_S)$ and pass through the aperture centers at y_A and $-y_A$ respectively. The two spherical diffracted wavefronts have the center at the point $D(-\gamma,Y_D,Z_D)$ and pass through the aperture centers at $\pm y_A$. The diffracted ray appears to originate from $D(-\gamma,Y_D,Z_D)$ and passes

through the point (x_s, y_a, z_a) in the aperture. The equations of the source and diffracted wavefronts and of the diffracted ray are given as

$$dw_1 : \quad (x+\gamma)^2 + (y - Y_D)^2 + (z - Z_D)^2 = X_s^2 + (Y_D - y_A)^2 + Z_D^2 \tag{N.9}$$

$$dw_2 : \quad (x+\gamma)^2 + (y - Y_D)^2 + (z - Z_D)^2 = X_s^2 + (Y_D + y_A)^2 + Z_D^2 \tag{N.10}$$

$$sw_{12} : \quad x^2 + (y - y_{S2})^2 + (z - z_S)^2 = x_s^2 + (y_{S2} - y_A)^2 + z_S^2 \tag{N.11}$$

$$sw_{11} : \quad x^2 + (y - y_{S1})^2 + (z - z_S)^2 = x_s^2 + (y_{S1} - y_A)^2 + z_S^2 \tag{N.12}$$

$$sw_{21} : \quad x^2 + (y - y_{S1})^2 + (z - z_S)^2 = x_s^2 + (y_{S1} + y_A)^2 + z_S^2 \tag{N.13}$$

$$sw_{22} : \quad x^2 + (y - y_{S2})^2 + (z - z_S)^2 = x_s^2 + (y_{S2} + y_A)^2 + z_S^2 \tag{N.14}$$

diffracted ray :

$$y = \frac{y_a - Y_D}{X_s}(x+\gamma) + Y_D \tag{N.15a}$$

$$z = \frac{z_a - Z_D}{X_s}(x+\gamma) + Z_D \tag{N.15b}$$

The case $\Delta y_s > D_{ss}$ is considered first. In Section 3.5 an argument was made that in this case only the diffracted light from the source wavefronts sw_{12} and sw_{21} contributes significantly to I_r at Q. The positions of S, D, S_1 and S_2 are shown in Fig. 3.12 , with the coordinates of D being such that $|\overline{S-D}| < D_{ss}$. The position of the imaginary point source S was chosen so that (hopefully) the blurred and sheared images of the real point sources S_1 and S_2 would both be centered about the point R, the geometric image of S. The subsequent analysis has shown this choice to be correct.

The geometry of DASSC is such that the positions of S_1 and S_2 are related to the position of S by

$$y_{S_1} = Y_S - \frac{\gamma}{X_s}(Y_S + y_A)$$

$$y_{S_2} = Y_S - \frac{\gamma}{X_s}(Y_S - y_A)$$

$$z_S = \left(1 - \frac{\gamma}{X_s}\right) Z_S$$

Let us define (and redefine) the following parameters:

$$a = 1 + \left(\frac{y_a - Y_D}{X_s}\right)^2 + \left(\frac{z_a - Z_D}{X_s}\right)^2 \qquad |a| < 4 \times 10^{-2}$$

$$b = 1 + \left(\frac{Y_D - y_A}{X_s}\right)^2 + \left(\frac{Z_D}{X_s}\right)^2 \qquad |b| < 4 \times 10^{-2}$$

$$F = 1 + a$$

$$G = 1 + b$$

$$\beta_1 = \frac{\gamma}{X_s} \qquad |\beta_1| < 1 \times 10^{-1}$$

$$\Delta y = \frac{Y_D - Y_S}{X_s} \qquad |\Delta y| < 4 \times 10^{-4}$$

$$\Delta z = \frac{Z_D - Z_S}{X_s} \qquad |\Delta z| < 4 \times 10^{-4}$$

$$\beta = \frac{\underline{r}}{X_s} \qquad |\beta| < 2 \times 10^{-3}$$

The distances $\overline{dw_i\text{-}sw_{ij}}$ are determined in the same way as in Appendix C. The diffracted ray originates from the source wavefront at the point (x_2, y_2, z_2) and reaches the diffracted wavefront at the point (x_1, y_1, z_1) and therefore the distance r^*_{eij} by which the diffracted wavefront leads the source wavefront is given by

$$r^*_{eij} \equiv \overline{dw_i\text{-}sw_{ij}} = \sqrt{(x_1 - x_2)^2 + (y_1 - y_2)^2 + (z_1 - z_2)^2} \qquad \text{(N.16)}$$

We introduce the polar coordinate systems of the two apertures

aperture 1 : $y_a = y_A + \underline{r}\cos\theta$

$z_a = \underline{r}\sin\theta$

aperture 2 : $y_a = -\,y_A + \underline{r}\cos\theta$

$z_a = \underline{r}\sin\theta$

r_{e12} will be determined first. The equations (N.9) and (N.15) are evaluated

at the point (x_1, y_1, z_1) and the equations (N.11) and (N.15) are evaluated at the point (x_2, y_2, z_2) . From these equations and equation (N.16) a quadratic equation in (r_{e12}/X_s) is obtained as

$$\left(\frac{r_{e12}}{X_s}\right)^2 - 2\left(\frac{r_{e12}}{X_s}\right)\left[\sqrt{G} + \frac{1}{\sqrt{F}}\left[-\beta_1 + \frac{y_A - Y_D}{X_s}\left(\Delta y + \beta_1\frac{Y_S - y_A}{X_s}\right) - \frac{Z_D}{X_s}\left(\Delta z + \beta_1\frac{Z_S}{X_s}\right)\right] + \right.$$

$$\left. + \beta\left[\left(\Delta y + \beta_1\frac{Y_S - y_A}{X_s}\right)\cos\theta + \left(\Delta z + \beta_1\frac{Z_S}{X_s}\right)\sin\theta\right]\right] + 2\beta_1\left(1 - \frac{\sqrt{G}}{\sqrt{F}}\right) + 2\frac{\sqrt{G}}{\sqrt{F}}\left[\frac{y_A - Y_D}{X_s}\cdot\right.$$

$$\left.\left(\Delta y + \beta_1\frac{Y_S - y_A}{X_s}\right) - \frac{Z_D}{X_s}\left(\Delta z + \beta_1\frac{Z_S}{X_s}\right) + \beta\left[\left(\Delta y + \beta_1\frac{Y_S - y_A}{X_s}\right)\cos\theta + \left(\Delta z + \beta_1\frac{Z_S}{X_s}\right)\sin\theta\right]\right]$$

$$+ 2\frac{Y_D - y_A}{X_s}\Delta y + 2\frac{Z_D}{X_s}\Delta z + 2\beta_1\frac{(Y_S - y_A)(Y_D - y_A) + Z_D Z_S}{X_s^2} = 0 \qquad \text{(N.17)}$$

The small quadratic term is neglected and by making an extensive use of Taylor's series we obtain an approximate solution to equation (N.17), accurate to $\lambda/30$ as

$$r_{e12} = q\underline{r}^2 + \underline{r}(K_1\cos\theta + K_2\sin\theta) \equiv r_e \qquad \text{(N.18)}$$

where q, K_1 and K_2 are defined as

$$q = \frac{\beta_1}{2X_s}(1 + \beta_1)$$

$$K_1 = \left(1 - \frac{3Y_S^2}{2X_s^2}\right)\Delta y - \frac{Y_S Z_S}{X_s^2}\Delta z$$

$$K_2 = \left(1 - \frac{3Z_S^2}{2X_s^2}\right)\Delta z - \frac{Y_S Z_S}{X_s^2}\Delta y$$

We shall now determine r_{e21} . Since r_{e12} is not a function of y_A we may write $\overline{dw_2 - sw_{21}} = \overline{dw_1 - sw_{12}} = r_e$ and r_{e21} is then given as

$$r_{e21} = r_e + (\overline{D - dw_1} - \overline{S_2 - sw_{12}}) - (\overline{D - dw_2} - \overline{S_1 - sw_{21}})$$

$$r_{e21} = r_e + \sqrt{X_S^2 + (Y_D - y_A)^2 + Z_D^2} - \sqrt{x_S^2 + (y_S - y_A)^2 + z_S^2}$$
$$- \sqrt{X_S^2 + (Y_D + y_A)^2 + Z_D^2} + \sqrt{x_S^2 + (y_S + y_A)^2 + z_S^2} \qquad (N.19)$$

Using the Taylor's series expansion for the square roots in the equation above, an approximate solution for r_{e21} is found as

$$r_{e21} \simeq r_e - Dp \qquad (N.20)$$

where p is defined as

$$p = \left(1 - \frac{Y_S^2}{X_{S0}^2}\right)\frac{Y_D - Y_S}{X_{S0}} - \frac{Y_S Z_S}{X_{S0}^2}\frac{Z_D - Z_S}{X_{S0}} + \beta_1 \frac{Y_S}{X_{S0}} \qquad (N.21)$$

with X_{S0} redefined as $\quad X_{S0}^2 = X_S^2 + Y_S^2 + Z_S^2 + y_A^2 \qquad (N.22)$

When the case $\Delta y_s < D_{ss}$ is considered the parameter β_1 is such that $|\beta_1| < 6 \times 10^{-3}$ and consequently r_{e12} and r_{e21} may be further approximated as

$$r_{e12} = \underline{r}(K_1 \cos\theta + K_2 \sin\theta) \qquad (N.23)$$

$$r_{e21} = \underline{r}(K_1 \cos\theta + K_2 \sin\theta) - Dp \qquad (N.24)$$

To determine $r_{e11}^* = \overline{dw_1 - sw_{11}}$ we use equation (N.16) again. Equations (N.9) and (N.15) are evaluated at the point (x_1, y_1, z_1) and equations (N.12) and (N.15) are evaluated at the point (x_2, y_2, z_2). From these equations, and equation (N.16) we obtain a quadratic equation in (r_{e11}^*/X_S).

$$\left(\frac{r_{e11}^*}{X_S}\right)^2 - 2\left(\frac{r_{e11}^*}{X_S}\right)\left[\sqrt{G} + \frac{1}{\sqrt{F}}\left[-\beta_1 + \frac{y_A - Y_D}{X_S}\left(\Delta y + \beta_1 \frac{Y_S + y_A}{X_S}\right) - \frac{Z_D}{X_S}\left(\Delta z + \beta_1 \frac{Z_S}{X_S}\right)\right] + \right.$$
$$\left. + \frac{\beta}{\sqrt{F}}\left[\left(\Delta y + \beta_1 \frac{Y_S + y_A}{X_S}\right)\cos\theta + \left(\Delta z + \beta_1 \frac{Z_S}{X_S}\right)\sin\theta\right]\right] + 2\left(1 - \frac{\sqrt{G}}{\sqrt{F}}\right)\left(\beta_1 + \Delta y \frac{Y_D - y_A}{X_S} + \right.$$
$$\left. + \Delta z \frac{Z_D}{X_S} + \beta_1 \frac{(Y_D - Y_S)y_A - y_A^2 + Y_S Y_D + Z_S Z_D}{X_S^2}\right) + 2\beta \frac{\sqrt{G}}{\sqrt{F}}\left[\left(\Delta y + \beta_1 \frac{Y_S + y_A}{X_S}\cos\theta + \right.\right.$$
$$\left.\left. + \left(\Delta z + \beta_1 \frac{Z_S}{X_S}\right)\sin\theta\right]\right. = 0 \qquad (N.25)$$

With the small quadratic term neglected an approximate solution to equation (N.25) accurate to $\lambda/30$ was found as

$$r^*_{e11} = \underline{r}\left[\left(K_1 + \beta_1\frac{D}{X_S}\right)\cos\theta + K_2\sin\theta\right] \tag{N.26}$$

r_{e11} is calculated from equation (N.6) as

$$\begin{aligned} r_{e11} &= r^*_{e11} + \overline{S_1-sw_{11}} - \overline{S_2-sw_{12}} \\ &= r^*_{e11} + \sqrt{x_S^2 + (y_S - y_A)^2 + z_S^2} - \sqrt{x_S^2 + (y_S - y_A)^2 + z_S^2} \end{aligned}$$

An approximate solution to the equation above accurate to $\lambda/30$ is given by

$$r_{e11} = \underline{r}\left[\left(K_1 + \beta_1\frac{D}{X_S}\right)\cos\theta + K_2\sin\theta\right] - \alpha_A + \alpha_s \tag{N.27}$$

where α_A and α_s are defined as

$$\alpha_A = 2y_A\beta_1\left(\frac{Y_S}{X_{S0}} - \frac{y_A^2 Y_S}{X_{S0}^3}\right)$$

$$\alpha_s = 2y_A\beta_1\frac{y_A}{X_{S0}}\left(1 + \beta_1 - \frac{Y_S^2}{X_{S0}^2}\right)$$

$r^*_{e22} \equiv \overline{dw_2-sw_{22}}$ is obtained by replacing y_A in equation (N.26) by $-y_A$, and r_{e22} is then found from equation (N.8) .

$$\begin{aligned} r_{e22} &= r^*_{e11}(y_A \to -y_A) + (\overline{D-dw_1} - \overline{S_2-sw_{12}}) - (\overline{D-dw_2} - \overline{S_2-sw_{22}}) \\ &= r^*_{e11}(y_A \to -y_A) + \sqrt{X_S^2 + (Y_D - y_A)^2 + Z_D^2} - \sqrt{x_S^2 + (y_S - y_A)^2 + z_S^2} \\ &\quad - \sqrt{X_S^2 + (Y_D + y_A)^2 + Z_D^2} + \sqrt{x_S^2 + (y_S + y_A)^2 + z_S^2} \end{aligned}$$

An approximate solution of the last equation accurate to $\lambda/30$ was found as

$$r_{e22} = \underline{r}\left[\left(K_1 - \beta_1\frac{D}{X_S}\right)\cos\theta + K_2\sin\theta\right] - Dp + \alpha_A + \alpha_s \tag{N.28}$$

APPENDIX O

DERIVATION OF EQUATIONS (3.23) AND (3.24) - THE FIRST EXPOSURE I_r

The first exposure recorded intensity for the case $\Delta y_s > D_{ss}$ is determined first. In this case I_r is produced essentially by the interference of the light radiated by S_2 and passing through aperture 1 with the light radiated by S_1 and passing through aperture 2. Using equation (2.19) I_r is given by

$$I_r = \left(\frac{a}{r_0}\right)^2 \frac{T}{2}\left(\int_0^{d/2}\int_0^{2\pi} e^{ikr_{e12}} \underline{r}\, d\theta\, d\underline{r} + \int_0^{d/2}\int_0^{2\pi} e^{ikr_{e21}} \underline{r}\, d\theta\, d\underline{r}\right)$$
$$\left(\int_0^{d/2}\int_0^{2\pi} e^{-ikr_{e12}} \underline{r}\, d\theta\, d\underline{r} + \int_0^{d/2}\int_0^{2\pi} e^{-ikr_{e21}} \underline{r}\, d\theta\, d\underline{r}\right) \qquad (0.1)$$

The two optical path length variations r_{e12} and r_{e21} are given by equations (N.18) and (N.20) and with these equations I_r is calculated as

$$I_r = \left(\frac{a}{r_0}\right)^2 \frac{T}{2}\left(1+e^{-ikDp}\right)\left(1+e^{ikDp}\right)\left(\int_0^{d/2}\int_0^{2\pi} e^{ikr_e} \underline{r}\, d\theta\, d\underline{r}\right)\left(\int_0^{d/2}\int_0^{2\pi} e^{-ikr_e} \underline{r}\, d\theta\, d\underline{r}\right)$$
$$= \left(\frac{a}{r_0}\right)^2 \frac{T}{2}\left[\left(\int_0^{d/2}\int_0^{2\pi} e^{ikr_e} \underline{r}\, d\theta\, d\underline{r}\right)\left(\int_0^{d/2}\int_0^{2\pi} e^{-ikr_e} \underline{r}\, d\theta\, d\underline{r}\right)\right] 4\cos^2\frac{kDp}{2} \qquad (3.23)$$

Using the integration by parts equation (3.23) may be written as

$$I_r = 4I_0\left(\left(\frac{2J_1(\rho)}{\rho}\right)^2 - 4\frac{\omega}{\rho}\left(\frac{2J_1(\rho)}{\rho}\right)\int_0^{\rho}\left(\frac{R}{\rho}\right)^3\left(\frac{2J_1(R)}{R}\right)\sin\omega\left(1-\frac{R^2}{\rho^2}\right)dR + 4\frac{\omega^2}{\rho^2}\left[\left[\int_0^{\rho}\left(\frac{R}{\rho}\right)^3 \cdot\right.\right.\right.$$
$$\left.\left.\left.\left(\frac{2J_1(R)}{R}\right)\cos\omega\frac{R^2}{\rho^2}dR\right]^2 + \left[\int_0^{\rho}\left(\frac{R}{\rho}\right)^3\left(\frac{2J_1(R)}{R}\right)\sin\omega\frac{R^2}{\rho^2}dR\right]^2\right]\right)\cos^2\frac{kDp}{2} \qquad (0.1b)$$

where R and ω are defined as $\quad R = \frac{\underline{r}}{d/2}\rho$

$$\omega = \frac{kqd^2}{4} \qquad |\omega| < 2$$

The first exposure recorded intensity for the case $\Delta y_s < D_{ss}$ is again calculated according to equation (2.19), but this time all the light radiated by the two sources contributes significantly to the resultant I_r and the intensity is therefore calculated as

$$I_r = \left(\frac{a}{r_0}\right)^2 \frac{T}{2}\left[\sum_{\substack{m=1,2\\n=1,2}} \int_0^{d/2} \int_0^{2\pi} e^{ikr_{emn}} \underline{r}\, d\theta\, d\underline{r}\right]\left[\sum_{\substack{m=1,2\\n=1,2}} \int_0^{d/2} \int_0^{2\pi} e^{-ikr_{emn}} \underline{r}\, d\theta\, d\underline{r}\right] \quad (0.2)$$

We now define ρ, ρ_{11} and ρ_{22} as

$$\rho = \frac{kd}{2}(K_1^2 + K_2^2)^{\frac{1}{2}} \quad (0.3)$$

$$\rho_{11} = \frac{kd}{2}\left[\left(K_1 + \beta_1 \frac{2y_A}{X_s}\right)^2 + K_2^2\right]^{\frac{1}{2}} \quad (0.4)$$

$$\rho_{22} = \frac{kd}{2}\left[\left(K_1 - \beta_1 \frac{2y_A}{X_s}\right)^2 + K_2^2\right]^{\frac{1}{2}} \quad (0.5)$$

The four r_{eij} are given by equations (N.23),(N.24),(N.27) and (N.28). By making use of equations (N.18),(N.20),(N.26) and (N.16) we may write equation (0.2) as

$$I_r = \left(\frac{a}{r_0}\right)^2 \frac{T}{2}\left(\int_A e^{ik(r^*_{e11} - \alpha_A + \alpha_s)} dA + \int_A e^{ikr_e} dA + \int_A e^{ik(r_e - Dp)} dA + \right.$$

$$\left. + \int_A e^{ik(r^*_{e22} + \alpha_A + \alpha_s - Dp)} dA\right)\left(\int_A e^{-ik(r^*_{e11} - \alpha_A + \alpha_s)} dA + \int_A e^{-ikr_e} dA + \right.$$

$$\left. + \int_A e^{-ik(r_e - Dp)} dA + \int_A e^{-ik(r^*_{e22} + \alpha_A + \alpha_s - Dp)} dA\right) \quad (0.6)$$

where A is the area of the circular aperture(s). Using equation (D.6) I_r is evaluated as

$$I_r = 4I_0\left(J_{11}e^{ik(\alpha_s - \alpha_A)} + J + Je^{-ikDp} + J_{22}e^{ik(\alpha_A + \alpha_s - Dp)}\right). \quad \rightarrow$$

$$\cdot\left(J_{11}e^{-ik(\alpha_s - \alpha_A)} + J + Je^{ikDp} + J_{22}e^{-ik(\alpha_A + \alpha_s - Dp)}\right) \qquad (0.7)$$

where J, J_{11} and J_{22} are defined as

$$J = \frac{J_1(\rho)}{\rho}$$

$$J_{11} = \frac{J_1(\rho_{11})}{\rho_{11}}$$

$$J_{22} = \frac{J_1(\rho_{22})}{\rho_{22}}$$

To interpret equation (0.7) we assume that all products $J_{mn}J_{kl}$ have approximately the same value over the speckle area, i.e. we let $J_{mn}J_{kl} \simeq J$. Equation (0.7) is then put in the form

$$I_r \simeq 16I_0\left(\frac{J_1(\rho)}{\rho}\right)^2\left(P_1 + P_2\cos^2\frac{k}{2}(Dp - \alpha_A)\right) \qquad (3.24)$$

where P_1 and P_2 are defined as

$$P_1 = 1 + \cos k\alpha_s \cos k\alpha_A - 2\cos\frac{k}{2}(\alpha_A + \alpha_s)\cos\frac{k}{2}(\alpha_A - \alpha_s) \qquad (0.8)$$

$$P_2 = 4\cos\frac{k}{2}(\alpha_A + \alpha_s)\cos\frac{k}{2}(\alpha_A - \alpha_s) \qquad (0.9)$$

APPENDIX P

DERIVATION OF r_{eij} FOR DASSC DURING THE SECOND EXPOSURE

As shown in Fig. 3.14 , when a specimen is deformed its surface is, in general, displaced and strained both in and out-of-plane. The deformation occurs between the two exposures and it changes the coordinates of the two point sources S_1 and S_2, representing the surface, as follows

$$S_1(0,y_{S1},z_S) \rightarrow S_1^*(u,y_{S1}+v,z_S+w)$$

$$S_2(0,y_{S2},z_S) \rightarrow S_2^*(u+\delta u,y_{S2}+v+\delta v,z_S+w+\delta w)$$

The equations of the diffracted wavefronts dw_1 and dw_2 , and of the diffracted ray(s) remain unchanged and are given by equations (N.9),(N.10) and (N.15) respectively. The equations of the source wavefronts sw_{ij} must be modified to account for the changed, second exposure positions of S_1 and S_2.

$$sw_{11}: \quad (x-u)^2 + [y-(y_{S1}+v)]^2 + [z-(z_S+w)]^2 = (x_s-u)^2 + [(y_{S1}+v)-y_A]^2 + (z_S+w)^2 \qquad (P.1)$$

$$sw_{12}: \quad [x-(u+\delta u)]^2 + [y-(y_{S2}+v+\delta v)]^2 + [z-(z_S+w+\delta w)]^2 = [x_s-(u+\delta u)]^2 + [(y_{S2}+v+\delta v)-y_A]^2 + [z_S+(w+\delta w)]^2 \qquad (P.2)$$

$$sw_{21}: \quad (x-u)^2 + [y-(y_{S1}+v)]^2 + [z-(z_S+w)]^2 = (x_s-u)^2 + [(y_{S1}+v)+y_A]^2 + (z_S+w)^2 \qquad (P.3)$$

$$sw_{22}: \quad [x-(u+\delta u)]^2 + [y-(y_{S2}+v+\delta v)]^2 + [z-(z_S+w+\delta w)]^2 = [x_s-(u+\delta u)]^2 + [(y_{S2}+v+\delta v)+y_A]^2 + [z_S+(w+\delta w)]^2 \qquad (P.4)$$

As is discussed in Section 3.6 , when DASSC is considered the changes in the distances between each of the point sources S_1 and S_2 and the laser must be included in the calculation of r_{eij}, and hence using equations (N.5) through (N.8) the second exposure r_{eij} are given by

$$r_{e12} = \overline{dw_1 - sw_{12}} + r_{L2} \tag{P.5}$$

$$r_{e11} = \overline{dw_1 - sw_{11}} + (\overline{S_1 - sw_{11}} - \overline{S_2 - sw_{12}}) + r_{L1} \tag{P.6}$$

$$r_{e21} = \overline{dw_2 - sw_{21}} + (\overline{D - dw_1} - \overline{S_2 - sw_{12}}) - (\overline{D - dw_2} - \overline{S_1 - sw_{21}}) + r_{L1} \tag{P.7}$$

$$r_{e22} = \overline{dw_2 - sw_{22}} + (\overline{D - dw_1} - \overline{S_2 - sw_{12}}) - (\overline{D - dw_2} - \overline{S_2 - sw_{22}}) + r_{L2} \tag{P.8}$$

The subsequent calculations of the second exposure r_{eij} are similar to the calculations of the first exposure r_{eij} presented in Appendix N. The diffracted ray originates from the source wavefront at the point (x_2, y_2, z_2) and reaches the diffracted wavefront at the point (x_1, y_1, z_1) with the distance r^*_{eij} by which the diffracted wavefront leads the source wavefront given by equation (N.16).

The case $\Delta y_s < D_{ss}$ is considered first. To determine r^*_{e12} equations (N.9) and (N.15) are evaluated at the point (x_1, y_1, z_1) and equations (P.2) and (N.15) are evaluated at the point (x_2, y_2, z_2). From these equations and equation (N.16) we obtain a quadratic equation in (r^*_{e12}/X_s) as

$$\left(\frac{r^*_{e12}}{X_s}\right)^2 - 2\left(\frac{r^*_{e12}}{X_s}\right)\left[\sqrt{G} + \frac{1}{\sqrt{F}}\left[-\beta_1 - U + \frac{y_A - Y_D}{X_s}\left(\Delta y + \beta_1\frac{Y_S - y_A}{X_s} - V\right) - \frac{Z_D}{X_s}\left(\Delta z + \right.\right.\right.$$
$$\left.\left.\left. + \beta_1\frac{Z_S}{X_s} - W\right)\right] + \frac{\beta}{\sqrt{F}}\left[\left(\Delta y + \beta_1\frac{Y_S - y_A}{X_s} - V\right)\cos\theta + \left(\Delta z + \beta_1\frac{Z_S}{X_s} - W\right)\sin\theta\right]\right] +$$
$$+ 2\left(1 - \frac{\sqrt{G}}{\sqrt{F}}\right)\left[\beta_1 + U + \frac{Y_D - y_A}{X_s}\left(\Delta y + \beta_1\frac{Y_S - y_A}{X_s} - V\right) + \frac{Z_D}{X_s}\left(\Delta z + \beta_1\frac{Z_S}{X_s} - W\right)\right] +$$
$$+ 2\beta\frac{\sqrt{G}}{\sqrt{F}}\left[\left(\Delta y + \beta_1\frac{Y_S - y_A}{X_s} - V\right)\cos\theta + \left(\Delta z + \beta_1\frac{Z_S}{X_s} - W\right)\sin\theta\right] = 0 \tag{P.9}$$

where U,V and W are defined as

$$U = \frac{u + \delta u}{X_s} \qquad |U| < 1.3 \times 10^{-3}$$

$$V = \frac{v + \delta v}{X_s} \qquad |V| < 4 \times 10^{-4}$$

$$W = \frac{w + \delta w}{X_s} \qquad |W| < 4 \times 10^{-4}$$

The small qadratic term in equation (P.9) is neglected and with an extensive use of Taylor's series we obtain an approximate solution, accurate to $\lambda/10$, for r^*_{e12} as

$$r^*_{e12} = \frac{\beta_1 \underline{r}^2}{2X_S} + \underline{r}\left[\left(\frac{Y_D - Y_S}{X_S} - \frac{Y_S - y_A}{X_S}\frac{u + \delta u}{X_S} - (1 + \beta_1)\frac{v + \delta v}{X_S}\right)\cos\theta + \right.$$

$$\left. + \left(\frac{Z_D - Z_S}{X_S} - \frac{Z_S}{X_S}\frac{u + \delta u}{X_S} - (1 + \beta_1)\frac{w + \delta w}{X_S}\right)\sin\theta\right] \qquad \text{(P.10)}$$

r^*_{e21} is obtained from equation (P.10) by replacing y_A by $-y_A$, and $u + \delta u$, $v + \delta v$ and $w + \delta w$ by u,v and w respectively.

$$r^*_{e21} = \frac{\beta_1 \underline{r}^2}{2X_S} + \underline{r}\left[\left(\frac{Y_D - Y_S}{X_S} - \frac{Y_S + y_A}{X_S}\frac{u}{X_S} - (1 + \beta_1)\frac{v}{X_S}\right)\cos\theta + \right.$$

$$\left. + \left(\frac{Z_D - Z_S}{X_S} - \frac{Z_S}{X_S}\frac{u}{X_S} - (1 + \beta_1)\frac{w}{X_S}\right)\sin\theta\right] \qquad \text{(P.11)}$$

In Section 3.6 it is shown that $\Delta r_{L2} = \Delta r_{L1} - \delta u \cos\theta_x - \delta v \cos\theta_y - \delta w \cos\theta_z$ and hence r_{e12} is given by

$$r_{e12} = r^*_{e12} + \Delta r_{L1} - \delta u \cos\theta_x - \delta v \cos\theta_y - \delta w \cos\theta_z \qquad \text{(P.12)}$$

r_{e21} is given by equation (P.7) as

$$r_{e21} = r^*_{e21} + (\overline{D-dw_1} - \overline{S_2-sw_{12}}) - (\overline{D-dw_2} - \overline{S_1sw_{21}}) + r_{L1}$$

$$= r^*_{e21} + r_{L1} + \left(X_S^2 + (Y_D - y_A)^2 + Z_D^2\right)^{\frac{1}{2}} - \left(X_S^2 + (Y_D + y_A)^2 + Z_D^2\right)^{\frac{1}{2}} +$$

$$+ \left((x_S - u)^2 + [(y_S + v) + y_A]^2 + (z_S + w)^2\right)^{\frac{1}{2}} - \left([x_S - (u + \delta u)]^2 + \right.$$

$$\left. + [(y_S + v + \delta v) - y_A]^2 + [z_S + (w + \delta w)]^2\right)^{\frac{1}{2}} \qquad \text{(P.13)}$$

An approximate solution of equation (P.13), accurate to $\lambda/10$, is obtained by using the Taylor's series expansions for the square roots with the result

$$r_{e21} = r^*_{e21} + \Delta r_{L_1} - D(p - \xi^*) \tag{P.14}$$

where ξ^* is defined as

$$\xi^* = \frac{u}{X_{s0}}\left(\frac{Y_S X_S}{X_{s0}^2} - \frac{Y_S \delta v}{DX_{s0}} - \frac{Z_S \delta w}{DX_{s0}}\right) + \frac{v}{X_{s0}}\left(1 - \frac{Y_S^2}{X_{s0}^2} - \frac{\delta v}{D}\right) - \frac{w}{X_{s0}}\left(\frac{Y_S Z_S}{X_{s0}^2} + \frac{\delta w}{D}\right) +$$

$$+ \frac{X_S}{D}\left(1 + \frac{DY_S}{2X_{s0}^2}\right)\frac{\delta u}{X_{s0}} - \frac{\delta v}{X_{s0}}\left[\frac{Y_S - D/2}{D}\left(1 + \frac{DY_S}{2X_{s0}^2}\right) + \frac{\delta v}{2D}\right] -$$

$$- \frac{\delta w}{X_{s0}}\left[\frac{Z_S}{D}\left(1 + \frac{DY_S}{2X_{s0}^2}\right) + \frac{\delta w}{2D}\right] \tag{P.15}$$

We shall now consider the case $\Delta y_s < D_{ss}$. Since now $|\beta_1| < 6 \times 10^{-3}$ r^*_{e12} and r^*_{e21} may be obtained from equations (P.10) and (P.11) by neglecting some small terms involving β_1 with the result

$$r^*_{e12} = \underline{r}\left[\left(\frac{Y_D - Y_S}{X_S} - \frac{Y_S - y_A}{X_S}\frac{u + \delta u}{X_S} - \frac{v + \delta v}{X_S}\right)\cos\theta +\right.$$

$$\left. + \left(\frac{Z_D - Z_S}{X_S} - \frac{Z_S}{X_S}\frac{u + \delta u}{X_S} - \frac{w + \delta w}{X_S}\right)\sin\theta\right] \tag{P.16}$$

$$r^*_{e21} = \underline{r}\left[\left(\frac{Y_D - Y_S}{X_S} - \frac{Y_S + y_A}{X_S}\frac{u}{X_S} - \frac{v}{X_S}\right)\cos\theta + \left(\frac{Z_D - Z_S}{X_S} - \frac{Z_S}{X_S}\frac{u}{X_S} - \frac{w}{X_S}\right)\sin\theta\right] \tag{P.17}$$

r_{e12} and r_{e21} are given by equations (P.12) and (P.14) with r^*_{e12} and r^*_{e21} given by equations (P.16) and (P.17) . $r^*_{e11} = \overline{dw_1 - sw_{11}}$ is determined from equation (N.16). Equations (N.9) and (N.15) are evaluated at the point (x_1, y_1, z_1) and equations (P.1) and (N.15) are evaluated at the point (x_2, y_2, z_2). From these equations and equation (N.16) we obtain a quadratic equation in (r^*_{e11}/X_s).

$$\left(\frac{r^*_{e11}}{X_s}\right)^2 - 2\left(\frac{r^*_{e11}}{X_s}\right)\left[\sqrt{G} + \frac{1}{\sqrt{F}}\left[-\beta_1 - U - \frac{Y_D - y_A}{X_s}\left(\Delta y + \beta_1\frac{Y_S + y_A}{X_s} - V\right) - \frac{Z_D}{X_s}\left(\Delta z +\right.\right.\right.$$

$$+ \beta_1 \frac{Z_S}{X_S} - W\Big)\Big] + \frac{\beta}{\sqrt{F}}\Big[\Big(\Delta y + \beta_1 \frac{Y_S + y_A}{X_S} - V\Big)\cos\theta + \Big(\Delta z + \beta_1 \frac{Z_S}{X_S} - W\Big)\sin\theta\Big]\Big] +$$

$$+ 2\Big(1 - \frac{\sqrt{G}}{\sqrt{F}}\Big)\Big[\beta_1 + U + \frac{Y_D - y_A}{X_S}\Big(\Delta y + \beta_1 \frac{Y_S + y_A}{X_S} - V\Big) + \frac{Z_D}{X_S}\Big(\Delta z + \beta_1 \frac{Z_S}{X_S} - W\Big)\Big] +$$

$$+ 2\beta \frac{\sqrt{G}}{\sqrt{F}}\Big[\Big(\Delta y + \beta_1 \frac{Y_S + y_A}{X_S} - V\Big)\cos\theta + \Big(\Delta z + \beta_1 \frac{Z_S}{X_S} - W\Big)\sin\theta\Big] = 0 \qquad \text{(P.18)}$$

where this time U,V and W are defined as

$$U = \frac{u}{X_S} \qquad |U| < 1.3 \times 10^{-3}$$

$$V = \frac{v}{X_S} \qquad |V| < 4 \times 10^{-4}$$

$$W = \frac{w}{X_S} \qquad |W| < 4 \times 10^{-4}$$

An approximate solution of equation (P.18), accurate to $\lambda/10$, was found as

$$r^*_{e11} = \underline{r}\Big[\Big(\frac{Y_D - Y_S}{X_S} - \frac{Y_S - y_A}{X_S}\frac{u}{X_S} - \frac{v}{X_S}\Big)\cos\theta + \Big(\frac{Z_D - Z_S}{X_S} - \frac{Z_S}{X_S}\frac{u}{X_S} - \frac{w}{X_S}\Big)\sin\theta\Big] \qquad \text{(P.19)}$$

r_{e11} is obtained from equation (P.6) as

$$r_{e11} = r^*_{e11} + r_{L1} + (\overline{S_1 - sw_{11}} - \overline{S_2 - sw_{12}})$$

$$= r^*_{e11} + r_{L1} + \Big((x_S - u)^2 + [(y_S + v) - y_A]^2 + (z_S + w)^2\Big)^{\frac{1}{2}} -$$

$$- \Big([x_S - (u + \delta u)]^2 + [(y_S + v + \delta v) - y_A]^2 + [z_S + (w + \delta w)]^2\Big)^{\frac{1}{2}} \qquad \text{(P.20)}$$

An approximate solution of equation (P.20), accurate to $\lambda/10$, is given by

$$r_{e11} = r^*_{e11} + r_{L1} - \alpha^* + \beta_{11} \qquad \text{(P.21)}$$

where α^* and β_{11} are defined as

$$\alpha^* = \alpha_A + u\Big(\frac{2\beta_1 y_A Y_S}{X_{S0}^2} + \frac{Y_S \delta v}{X_{S0}^2} + \frac{Z_S \delta w}{X_{S0}^2}\Big) + \frac{w\delta w}{X_{S0}} - \delta u \frac{X_S}{X_{S0}} + \delta v\Big(\frac{Y_S}{X_{S0}} + \frac{\delta v}{2X_{S0}}\Big) +$$

$$+ \delta w\Big(\frac{Z_S}{X_{S0}} - \frac{y_A Y_S Z_S}{X_{S0}^3} - \frac{\delta w}{2X_{S0}}\Big) \qquad \text{(P.22)}$$

$$\beta_{11} = \alpha_s - v\left(\frac{2\beta_1 y_A}{X_{s0}} + \frac{\delta v}{X_{s0}}\right) + \delta u\,\frac{y_A Y_S X_S}{X_{s0}^3} - \delta v\left(-\frac{y_A}{X_{s0}} + \frac{y_A Y_S^2}{X_{s0}^3} + \frac{y_A^2 Y_S}{X_{s0}^3}\right) \qquad \text{(P.23)}$$

r^*_{e22} is obtained from equation (P.19) by substituting $-y_A$ for y_A , and $u+\delta u$, $v+\delta v$ and $w+\delta w$ for u,v and w respectively.

$$r^*_{e22} = \underline{r}\left[\left(\frac{Y_D - Y_S}{X_s} - \frac{Y_S + y_A}{X_s}\,\frac{u+\delta u}{X_s} - \frac{v+\delta v}{X_s}\right)\cos\theta + \right.$$

$$\left. + \left(\frac{Z_D - Z_S}{X_s} - \frac{Z_S}{X_s}\,\frac{u+\delta u}{X_s} - \frac{w+\delta w}{X_s}\right)\sin\theta\right] \qquad \text{(P.24)}$$

r_{e22} is given by equation (P.8) as

$$r_{e22} = r^*_{e22} + \Delta r_{L2} + (\overline{D-dw_1} - \overline{S_2-sw_{12}}) - (\overline{D-dw_2} - \overline{S_2-sw_{22}})$$

$$= r^*_{e22} + \Delta r_{L2} + \left(X_s^2 + (Y_D - y_A)^2 + Z_D^2\right)^{\frac{1}{2}} - \left(X_s^2 + (Y_D + y_A)^2 + Z_D^2\right)^{\frac{1}{2}} +$$

$$+ \left([x_s - (u+\delta u)]^2 + [(y_S + v + \delta v) + y_A]^2 + [z_S + (w+\delta w)]^2\right)^{\frac{1}{2}} -$$

$$- \left([x_s - (u+\delta u)]^2 + [(y_S + v + \delta v) - y_A]^2 + [z_S + (w+\delta w)]^2\right)^{\frac{1}{2}} \qquad \text{(P.25)}$$

Using Taylor's series expansion for the square roots in the above equation we find an approximate solution, accurate to $\lambda/10$, for r_{e22} as

$$r_{e22} = r^*_{e22} + \Delta r_{L1} + \alpha^* + \beta_{22} - D(p - \xi^*) + \Delta^* \qquad \text{(P.26)}$$

where β_{22} and Δ^* are defined as

$$\beta_{22} = \alpha_s + u\,\frac{2y_A Y_S}{X_{s0}^2}\,\frac{u + 2\delta u}{X_{s0}} + \delta u\left[\frac{y_A Y_S X_s}{X_{s0}^3} + \frac{2y_A Y_S}{X_{s0}^2}\left(\frac{\delta u}{X_{s0}} + \beta_1\frac{X_s}{X_{s0}}\right)\right] +$$

$$+ \delta v\left(\frac{y_A}{X_{s0}} - \frac{y_A Y_S^2}{X_{s0}^3} - \frac{y_A^2 Y_S}{X_{s0}^3} + \beta_1\frac{2y_A}{X_{s0}}\right) \qquad \text{(P.27)}$$

$$\Delta^* = -\,\delta u\cos\theta_x - \delta v\cos\theta_y - \delta w\cos\theta_z \qquad \text{(P.28)}$$

APPENDIX Q

DERIVATION OF EQUATIONS (3.25) AND (3.28) - THE SECOND EXPOSURE I_r

The second exposure I_r for the case $\Delta y_s > D_{ss}$ is calculated according to equation (O.1). Once r_{e12} and r_{e21} given by equations (P.12) and (P.13) respectively are substituted in equation (O.1) and the indicated multiplication is done we get

$$I_r = \left(\frac{a}{r_0}\right)^2 \frac{T}{2}\left[\int_A e^{ikr^*_{e12}}dA \int_A e^{-ikr^*_{e12}}dA + \int_A e^{ikr^*_{e21}}dA \int_A e^{-ikr^*_{e21}}dA + \right.$$

$$\left. + e^{-i\Delta}\int_A e^{-ikr^*_{e12}}dA \int_A e^{ikr^*_{e21}}dA + e^{i\Delta}\int_A e^{ikr^*_{e12}}dA \int_A e^{-ikr^*_{e21}}dA\right] \qquad (Q.1)$$

where Δ is defined as $\Delta = k\left[D(p - \xi^*) + \Delta^*\right]$

Equation (Q.2) may be put in the form equivalent to equation (3.25)

$$I_r = \left(\frac{a}{r_0}\right)^2 \frac{T}{2}\left(R_1 + R_2\cos^2\frac{\Delta}{2} + R_3\sin\Delta\right) \qquad (Q.2)$$

R_1, R_2 and R_3 are defined as

$$R_1 = \int_A e^{ikr^*_{e12}}dA \int_A e^{-ikr^*_{e12}}dA + \int_A e^{ikr^*_{e21}}dA \int_A e^{-ikr^*_{e21}}dA -$$

$$2\int_A \cos kr^*_{e12}\, dA \int_A \cos kr^*_{e21}\, dA - 2\int_A \sin kr^*_{e12}\, dA \int_A \sin kr^*_{e21}\, dA \qquad (Q.3)$$

$$R_2 = 4\left[\int_A \cos kr^*_{e12}\, dA \int_A \cos kr^*_{e21}\, dA + \int_A \sin kr^*_{e12}\, dA \int_A \sin kr^*_{e21}\, dA\right] \qquad (Q.4)$$

$$R_3 = 2\left[\int_A \cos kr^*_{e12}\, dA \int_A \sin kr^*_{e21}\, dA - \int_A \cos kr^*_{e21}\, dA \int_A \sin kr^*_{e12}\, dA\right] \qquad (Q.5)$$

In the case $\Delta y_s < D_{ss}$, I_r is given by equation (O.2) with r_{e12} given by equations (P.12) and (P.16) , and r_{e21} given by equations (P.14) and (P.17) . r_{e11} and r_{e22} are given by equations (P.21) and (P.26) respectively.

When the indicated multiplication in equation (O.2) is done, we get

$$I_r = 4I_0\Big(J_{11}e^{ik(\beta_{11} - \alpha^*)} + J_{12}e^{ik\Delta^*} + J_{21}e^{-ikD(p - \xi^*)} + $$
$$+ J_{22}e^{ik[\alpha^* + \beta_{22} + \Delta^* - D(p - \xi^*)]}\Big)\Big(J_{11}e^{-ik(\beta_{11} - \alpha^*)} + J_{12}e^{-ik\Delta^*} +$$
$$+ J_{21}e^{ikD(p - \xi^*)} + J_{22}e^{-ik[\alpha^* + \beta_{22} + \Delta^* - D(p - \xi^*)]}\Big) \qquad (Q.6)$$

where J_{mn} is defined as $\qquad J_{mn} = \dfrac{J_1(\rho_{mn})}{\rho_{mn}}$

and ρ_{mn} are defined as

$$\rho_{11} = \frac{kd}{2}\left[\left(\frac{Y_D - Y_S}{X_S} - \frac{Y_S - y_A}{X_S}\frac{u}{X_S} - \frac{v}{X_S}\right)^2 + \left(\frac{Z_D - Z_S}{X_S} - \frac{Z_S}{X_S}\frac{u}{X_S} - \frac{w}{X_S}\right)^2\right]^{\frac{1}{2}}$$

$$\rho_{12} = \frac{kd}{2}\left[\left(\frac{Y_D - Y_S}{X_S} - \frac{Y_S - y_A}{X_S}\frac{u + \delta u}{X_S} - \frac{v + \delta v}{X_S}\right)^2 + \left(\frac{Z_D - Z_S}{X_S} - \frac{Z_S}{X_S}\frac{u + \delta u}{X_S} - \frac{w + \delta w}{X_S}\right)^2\right]^{\frac{1}{2}}$$

$$\rho_{21} = \frac{kd}{2}\left[\left(\frac{Y_D - Y_S}{X_S} - \frac{Y_S + y_A}{X_S}\frac{u}{X_S} - \frac{v}{X_S}\right)^2 + \left(\frac{Z_D - Z_S}{X_S} - \frac{Z_S}{X_S}\frac{u}{X_S} - \frac{w}{X_S}\right)^2\right]^{\frac{1}{2}}$$

$$\rho_{22} = \frac{kd}{2}\left[\left(\frac{Y_D - Y_S}{X_S} - \frac{Y_S + y_A}{X_S}\frac{u + \delta u}{X_S} - \frac{v + \delta v}{X_S}\right)^2 + \left(\frac{Z_D - Z_S}{X_S} - \frac{Z_S}{X_S}\frac{u + \delta u}{X_S} - \frac{w + \delta w}{X_S}\right)^2\right]^{\frac{1}{2}}$$

To interpret equation (Q.6) we assume that $J_{mn}J_{kl} \simeq J^2$ (and hence $\rho_{mn} \simeq \rho$) within the speckle area, and equation (Q.6) may then be written as

$$I_r \simeq 16I_0\left(\frac{J_1(\rho)}{\rho}\right)^2\left[Q_1 + Q_2\cos^2\frac{k}{2}\left(D(p - \xi^*) - \alpha^* + \frac{\beta_{11} - \beta_{22}}{2}\right)\right] \qquad (3.28)$$

where Q_1 and Q_2 are defined as

$$Q_1 = \frac{1}{4}\Big(1 + \cos\frac{k}{2}(\beta_{11} - \beta_{22} - 2\alpha^* - 2\Delta^*)\cos\frac{k}{2}(\beta_{11} - \beta_{22})$$
$$- 2\cos k(\alpha^* + \Delta^*)\cos k(\beta_{11} - \beta_{22})\Big)$$

$$Q_2 = \cos k(\alpha^* + \Delta^*)\cos k(\beta_{11} - \beta_{22})$$

APPENDIX R

DERIVATION OF EQUATIONS (3.26) AND (3.29)

The forms of the second exposure I_r , for the two cases of Δy_s considered, reveal that in each instance the speckle grid has been shifted with respect to its first exposure position. By comparing the modulating (cosine) terms of the first and the second exposure I_r the relative shift of the speckle grids may be related to the surface displacements and their increments, and to the camera parameters.

The case $\Delta y_s > D_{ss}$ is considered first. The two modulating terms are given by equations (3.23) and (3.25) as

first exposure : $\cos^2 \frac{kDp}{2}$

second exposure : $\cos^2 \frac{k}{2}\left[D(p - \xi^*) + \Delta^*\right]$

In a similar way as in Appendix L, the apparent speckle grid centers Y_{sg1} and Y_{sg2} , in the object plane, are found from the maxima of the two modulating terms. Y_{sg1} is found on the line $Z = Z_s$ from

$$\frac{kDp}{2} = 0 \tag{R.1}$$

with Y_{sg1} substituted for Y_D . Y_{sg2} is found on the line $Z = Z_S$ from

$$\frac{k}{2}\left[D(p - \xi^*) + \Delta^*\right] = 0 \tag{R.2}$$

with Y_{sg2} substituted for Y_D . The solutions of equations (R.1) and (R.2) are given by

$$Y_{sg1} = Y_S\left[1 - \beta_1\left(1 - \frac{Y_S^2}{X_{S0}^2}\right)^{-1}\right] \tag{R.3}$$

$$Y_{sg2} = Y_{sg1} + \left(1 - \frac{Y_S^2}{X_{S0}^2}\right)^{-1}\left(\xi^* + \frac{\Delta^*}{D}\right)X_{S0} \tag{R.4}$$

The Moire fringe number n is related to Y_{sg1} and Y_{sg2} by

$$Y_{sg2} - Y_{sg1} = n\lambda \frac{X_s}{D} \tag{R.5}$$

Equation (R.5) was solved for n with the result

$$n = \frac{D}{\lambda X_s}\left(1 - \frac{Y_S^2}{X_{S0}^2}\right)^{-1}\left[u\left(\frac{Y_S X_s}{X_{S0}^2} - \frac{Y_S \delta v}{D X_{S0}} - \frac{Z_S \delta w}{D X_{S0}}\right) + v\left(1 - \frac{Y_S^2}{X_{S0}^2} - \frac{\delta v}{D}\right) - w\left(\frac{Y_S Z_S}{X_{S0}^2} + \frac{\delta w}{D}\right) + \right.$$

$$+ \delta u \frac{X_s}{D}\left(\frac{X_{S0}}{X_s}\cos\theta_x + 1 + \frac{DY_S}{2X_{S0}^2}\right) + \delta v \frac{X_{S0}}{D}\left[\cos\theta_y - \frac{Y_S - D/2}{X_{S0}}\left(1 + \frac{DY_S}{2X_{S0}^2}\right) + \frac{\delta v}{2X_{S0}}\right] +$$

$$\left. + \delta w \frac{X_{S0}}{D}\left[\cos\theta_z - \frac{Z_S}{X_{S0}}\left(1 + \frac{DY_S}{2X_{S0}^2}\right) - \frac{\delta w}{2X_{S0}}\right]\right] \tag{R.6}$$

Once the definitions of $\delta u, \delta v$ and δw are substituted in equation (R.6) it may then be accurately approximated by equation (3.26)

When the case $\Delta y_s < D_{ss}$ is considered the modulating terms for the two exposures are obtained from equations (3.24) and (3.28) as

first exposure : $\cos^2\frac{k}{2}(Dp - \alpha_A)$

second exposure : $\cos^2\frac{k}{2}\left(D(p - \xi^*) - \alpha^* + \frac{\beta_{11} - \beta_{22}}{2}\right)$

Again the apparent speckle grid centers Y_{sg1} and Y_{sg2} are found from the maxima of the two modulating terms. These maxima occur when

$$\frac{k}{2}(Dp - \alpha) = 0 \tag{R.7}$$

$$\frac{k}{2}\left(D(p - \xi^*) - \alpha^* + \frac{\beta_{11} - \beta_{22}}{2}\right) = 0 \tag{R.8}$$

In equation (R.7) Y_{sg1} is substituted for Y_D and in equation (R.8) Y_{sg2} is substituted for Y_D . In both equations Z_D is set equal to Z_S . Equations (R.7) and (R.8) are solved with the result

$$Y_{sg1} = Y_S - \left(1 - \frac{Y_S^2}{X_{S0}^2}\right)^{-1}\left(\beta_1 Y_S - \alpha_A \frac{X_{S0}}{D}\right) \tag{R.9}$$

$$Y_{sg2} = Y_S - \left(1 - \frac{Y_S^2}{X_{S0}^2}\right)^{-1} \left[\beta_1 Y_S - X_{S0}\left(\xi^* + \frac{\alpha^*}{D} - \frac{\beta_{11} - \beta_{22}}{2D}\right)\right] \qquad (R.10)$$

The Moire fringe number n is obtained from equation (R.5) with Y_{sg1} and Y_{sg2} given by equations (R.9) and (R.10). An approximate solution for n is given by equation (3.29).

APPENDIX S

DERIVATION OF EQUATIONS (3.27a) AND (3.27b)

The amplitudes of the speckle grid terms for the case $\Delta y_S > D_{SS}$ are obtained from I_r recorded during the two exposures and described by equations (3.23) and (3.25) . The two amplitudes are given by

first exposure : $\int_A e^{ikr_e}\, dA \int_A e^{-ikr_e}\, dA$

second exposure : R_2

When the effect of the small nonlinear term $\frac{\beta_1 r^2}{2X_S}$ on the shapes of the speckle envelopes is neglected the amplitudes are proportional to $\left(\frac{J_1(\rho)}{\rho}\right)^2$ for the first exposure, and $\frac{J_1(\rho_{mn})}{\rho_{mn}} \frac{J_1(\rho_{kl})}{\rho_{kl}}$ for the second exposure. Using equations (N.18),(P.10) and (P.11) we define ρ, ρ_{12} and ρ_{21} as

$$\rho = \frac{kd}{2}(K_1^2 + K_2^2)^{\frac{1}{2}} \tag{S.1}$$

$$\rho_{12} = \frac{kd}{2}\left[\left(\frac{Y_D - Y_S}{X_S} - \frac{Y_S - y_A}{X_S}\frac{u+\delta u}{X_S} - (1+\beta_1)\frac{v+\delta v}{X_S}\right)^2 + \left(\frac{Z_D - Z_S}{X_S} - \frac{Z_S}{X_S}\frac{u+\delta u}{X_S} - (1+\beta_1)\frac{w+\delta w}{X_S}\right)^2\right]^{\frac{1}{2}} \tag{S.2}$$

$$\rho_{21} = \frac{kd}{2}\left[\left(\frac{Y_D - Y_S}{X_S} - \frac{Y_S + y_A}{X_S}\frac{u}{X_S} - (1+\beta_1)\frac{v}{X_S}\right)^2 + \left(\frac{Z_D - Z_S}{X_S} - \frac{Z_S}{X_S}\frac{u}{X_S} - (1+\beta_1)\frac{w}{X_S}\right)^2\right]^{\frac{1}{2}} \tag{S.3}$$

where K_1 and K_2 are defined in Appendix N. The limit on the size of displacements and strains is obtained from the requirement that all the speckles recorded in the two exposures overlap. Let us call the coordinates of the speckle centers (maxima) as (Y_1, Z_1) for the first exposure, and (Y_{12}, Z_{12}) and (Y_{21}, Z_{21}) for the second exposure. Since $\left(\frac{J_1(\rho_{mn})}{\rho_{mn}}\right)^2$ is maximum when $\rho_{mn} = 0$, the coordinates (Y_1, Z_1) are found from the equation

$\rho = 0$, with Y_1 and Z_1 substituted for Y_D and Z_D. An approximate solution was found as

$$Y_1 \simeq Y_S \tag{S.4a}$$

$$Z_1 \simeq Z_S \tag{S.4b}$$

When Y_{12} and Z_{12}, and Y_{21} and Z_{21} are substituted in the equation $\rho_{12} = 0$, and $\rho_{21} = 0$ respectively, for Y_D and Z_D, the approximate solutions of these equations are then found as

$$Y_{12} \simeq Y_S + \frac{Y_S - y_A}{X_S}(u + \delta u) + (1 + \beta_1)(v + \delta v) \tag{S.5a}$$

$$Z_{12} \simeq Z_S + \frac{Z_S}{X_S}(u + \delta u) + (1 + \beta_1)(w + \delta w) \tag{S.5b}$$

$$Y_{21} \simeq Y_S + \frac{Y_S + y_A}{X_S} u + (1 + \beta_1)v \tag{S.6a}$$

$$Z_{21} \simeq Z_S + \frac{Z_S}{X_S} u + (1 + \beta_1)w \tag{S.6b}$$

The distances between the speckle centers must be smaller than the speckle radius and hence we may write

$$\rho \text{ and } \rho_{12}: \qquad (Y_{12} - Y_1)^2 + (Z_{12} - Z_1)^2 < \left(\frac{D_{ss}}{2}\right)^2 \tag{S.7}$$

$$\rho \text{ and } \rho_{21}: \qquad (Y_{21} - Y_1)^2 + (Z_{21} - Z_1)^2 < \left(\frac{D_{ss}}{2}\right)^2 \tag{S.8}$$

$Y_1, Z_2, \ldots, Z_{21}$ given by equations (S.4a) through (S.6b) and the definitions of the displacement increments $\delta u, \delta v$ and δw are substituted in equations (S.7) and (S.8). Since $|\beta_1| << 1$, equations (S.7) and (S.8) may then be closely approximated by equations (3.27a) and (3.27b).

APPENDIX T

DERIVATION OF EQUATION (4.13).

DASSC using a set of apertures rotated by the angle ϕ_i forms fringes according to equation (4.12).

$$\frac{y_i}{x_s} u_i + v_i - \frac{y_i z_i}{x_s^2} w_i + \frac{\Delta y_{si} X_{si}}{D} (1 + \cos\theta_{xi}) u_{i,yi} - \frac{\Delta y_{si} X_{si}}{D}\left(\frac{y_i - y_A}{x_s} - \right.$$

$$\left. - \cos\theta_{yi}\right) v_{i,yi} - \frac{\Delta y_{si} X_{si}}{D}\left(\frac{z_i}{x_s} - \cos\theta_{zi}\right) w_{i,yi} = - \frac{\lambda X_{si}}{D} n_i(y_i, z_i) \qquad (4.12)$$

All terms in equation (4.12) will now be transformed into y,z coordinate system using the transformations

$$y_i = y\cos\phi_i + z\sin\phi_i \qquad y = y_i\cos\phi_i - z_i\sin\phi_i$$

$$z_i = - y\sin\phi_i + z\cos\phi_i \qquad z = y_i\sin\phi_i + z_i\cos\phi_i$$

The transformations of the displacement components are given by equations (4.3), and the strain components transform as

$$u_{i,yi}(y_i, z_i) = u_{,yi}(y,z) = u_{,y}(y,z) y_{,yi} + u_{,y}(y,z) z_{,yi}$$

$$= u_{,y}\cos\phi_i + u_{,z}\sin\phi_i \qquad (T.1a)$$

$$v_{i,yi}(y_i, z_i) = [v(y,z)\cos\phi_i + w(y,z)\sin\phi_i]_{,yi} =$$

$$= (v_{,y} y_{,yi} + v_{,z} z_{,yi})\cos\phi_i + (w_{,y} y_{,yi} + w_{,z} z_{,yi})\sin\phi_i =$$

$$= v_{,y}\cos^2\phi_i + v_{,z}\sin\phi_i\cos\phi_i + w_{,y}\sin\phi_i\cos\phi_i + w_{,z}\sin^2\phi_i \qquad (T.1b)$$

$$w_{i,yi}(y_i, z_i) = [- v(y,z)\sin\phi_i + w(y,z)\cos\phi_i]_{,yi} =$$

$$= - (v_{,y} y_{,yi} + v_{,z} z_{,yi})\sin\phi_i + (w_{,y} y_{,yi} + w_{,z} z_{,yi})\cos\phi_i =$$

$$= - v_{,y}\sin\phi_i\cos\phi_i - v_{,z}\sin^2\phi_i + w_{,y}\cos^2\phi_i + w_{,y}\sin\phi_i\cos\phi_i \qquad (T.1c)$$

By substituting the coordinate, displacement and strain transformations in equation (4.12) it becomes

$$\frac{y_i}{x_s} u + (v\cos\phi_i + w\sin\phi_i) - (- v\sin\phi_i + w\cos\phi_i) \frac{y_i z_i}{x_s^2} + \frac{\Delta y_{si} X_{si}}{D} (1 + \cos\theta_{xi})\cdot$$

$$\cdot(u,_y\cos\phi_i + u,_z\sin\phi_i) - \frac{\Delta y_{si} X_{si}}{D}\left(\frac{y_i}{x_s} - \cos\theta_{yi}\right)(v,_y\cos^2\phi_i + v,_z\sin\phi_i\cos\phi_i +$$

$$+ w,_y\sin\phi_i\cos\phi_i + w,_z\sin^2\phi_i) - \frac{\Delta y_{si} X_{si}}{D}\left(\frac{z_i}{x_s} - \cos\theta_{zi}\right)(- v,_y\sin\phi_i\cos\phi_i -$$

$$- v,_z\sin^2\phi_i + w,_y\cos^2\phi_i + w,_z\sin\phi_i\cos\phi_i) = - \frac{\lambda X_{si}}{D} n_i(y_i, z_i) \qquad \text{(T.2)}$$

With coefficients $a_i,\ldots,k_i$ and N_i defined in Section 4.5, equation (T.2) may be written as equation (4.13).

APPENDIX U

The coefficients $d_i,\ldots,k_i$ for the case of the specimen illumination in x,y plane ($\theta_z = 90^o$) are derived here. From Fig. 4.3 (where $\phi_i = \phi_1$) the unit vectors $\hat{i},\hat{j}$ and $\hat{i}_i,\hat{j}_i$ are related as

$$\hat{i} = \hat{i}_i$$

$$\hat{j} = \hat{j}_i\cos\phi_i - \hat{k}_i\sin\phi_i$$

For $\theta_z = 90^o$ the angles θ_x and θ_y are related by

$$\cos\theta_y = \cos(90^o + \theta_x) = -\sin\theta_x$$

The unit illumination vector $\hat{l}$ is written in the two coordinate systems as

$$\begin{aligned}\hat{l} &= \hat{i}\cos\theta_x + \hat{j}\cos\theta_y + \hat{k}\cos\theta_z \\ &= \hat{i}\cos\theta_x - \hat{j}\sin\theta_x \\ &= \hat{i}_i\cos\theta_x - (\hat{j}_i\cos\phi_i - \hat{k}_i\sin\phi_i)\sin\theta_x \\ &= \hat{i}_i\cos\theta_x - \hat{j}_i\sin\theta_x\cos\phi_i + \hat{k}_i\sin\theta_x\sin\phi_i \\ &= \hat{i}\cos\theta_{xi} + \hat{j}\cos\theta_{yi} + \hat{k}\cos\theta_{zi}\end{aligned}$$

From the last two equations we get

$$\cos\theta_{xi} = \cos\theta_x$$

$$\cos\theta_{yi} = -\sin\theta_x\cos\phi_i$$

$$\cos\theta_{zi} = \sin\theta_x\sin\phi_i$$

By substituting these relationships in the expressions for $d_i,\ldots,k_i$ in Section 4.5 the simpler forms of these coefficients are obtained.

APPENDIX V

DERIVATION OF THE DISPLACEMENTS AND STRAINS CAUSED BY THE OUT-OF-PLANE BENDING OF BEAMS

Handbook of Steel Construction [62] gives (after change of notation and the coordinate origin) the deflection of a neutral surface of a thin prismatic beam with clamped ends and a point load at its center as

$$-L/2 \leqslant y \leqslant 0 \qquad u(y) = \delta\left[1 - 3\left(\frac{y}{L/2}\right)^2 - 2\left(\frac{y}{L/2}\right)^3\right] \tag{V.1a}$$

$$0 \leqslant y \leqslant L/2 \qquad u(y) = \delta\left[1 - 3\left(\frac{y}{L/2}\right)^2 + 2\left(\frac{y}{L/2}\right)^3\right] \tag{V.1b}$$

where δ is the deflection of the beam centre and L is the beam length. u is not a function of z, and since we consider only a thin beam and small deformations, it may be assumed that the out-of-plane deflection of the illuminated surface of the beam is the same as that of the neutral surface. It is apparent from Fig. V.1 the bending of the beam gives rise to the in-plane displacement v as

$$v = -\frac{t}{2}\, u_{,y}$$

Using equations (V.1a) and (V.1b) v is given as

$$-L/2 \leqslant y \leqslant 0 \qquad v(y) = 12\,\frac{t}{2}\,\frac{\delta}{L}\,\frac{y}{L/2}\left(1 + \frac{y}{L/2}\right) \tag{V.2a}$$

$$0 \leqslant y \leqslant L/2 \qquad v(y) = 12\,\frac{t}{2}\,\frac{\delta}{L}\,\frac{y}{L/2}\left(1 - \frac{y}{L/2}\right) \tag{V.2b}$$

The surface strains $\varepsilon_y(y)$ and $\varepsilon_z(y)$ are given as

$$\varepsilon_y = v_{,y} = -\frac{t}{2}\, u_{,yy} \tag{V.3}$$

$$\varepsilon_z = w_{,z} = -\nu\varepsilon_y = \nu\,\frac{t}{2}\, u_{,yy} \tag{V.4}$$

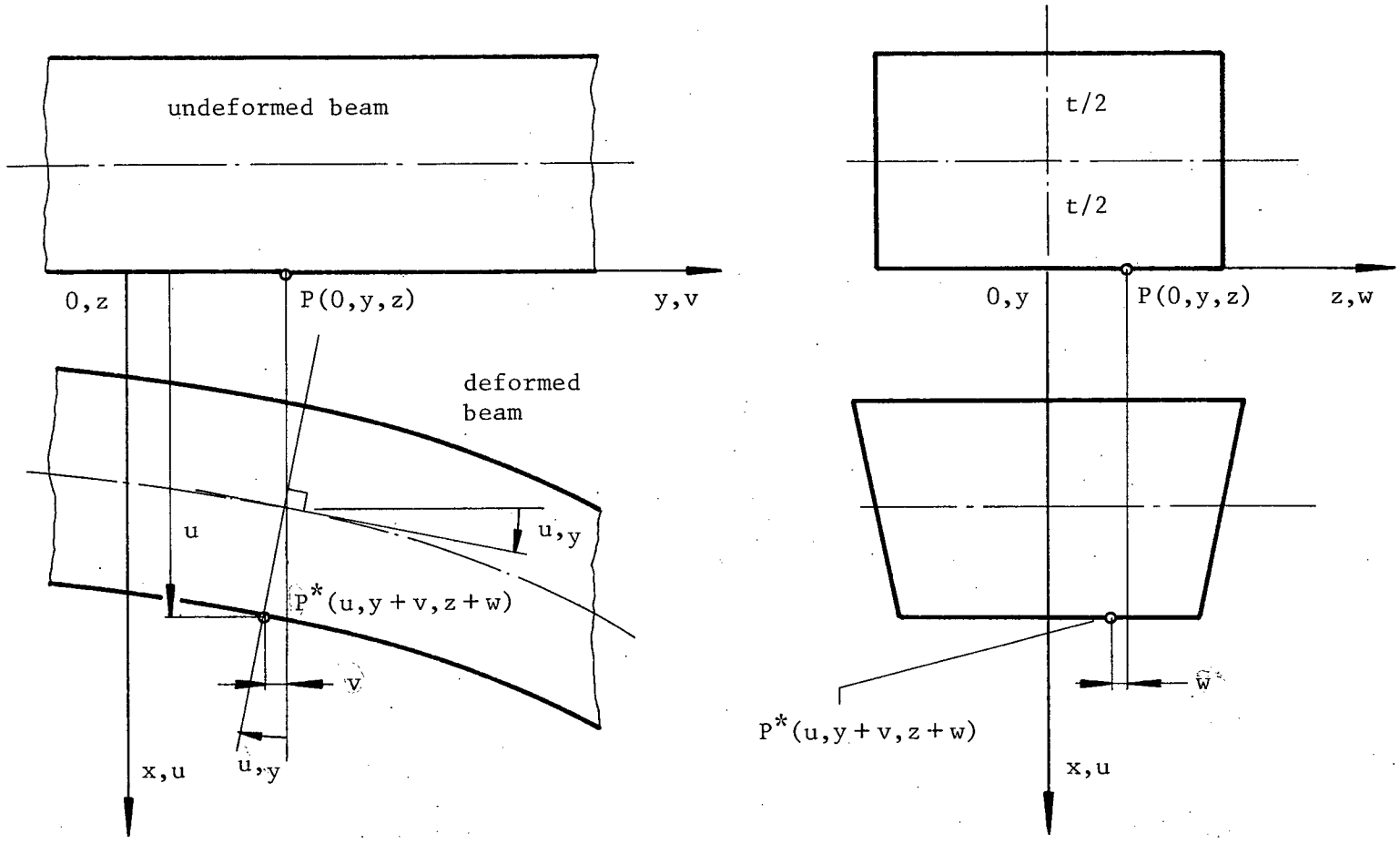

Fig. V.1 Out-of-plane bending of a prismatic beam.

where ν is Poisson's ratio. The displacement w is such that $w(y,z=0) = 0$, and hence $w(y,z)$ is obtained from equation (V.4) as

$$w(y,z) = \nu z \frac{t}{2} u_{,yy}$$

and using equations (V.1a) and (V.1b) $w(y,z)$ may be written as

$$-L/2 \leqslant y \leqslant 0 \qquad w(y,z) = -12\nu z \frac{t}{2} \frac{\delta}{L^2/2}\left(1 + \frac{2y}{L/2}\right) \tag{V.6a}$$

$$0 \leqslant y \leqslant L/2 \qquad w(y,z) = -12\nu z \frac{t}{2} \frac{\delta}{L^2/2}\left(1 - \frac{2y}{L/2}\right) \tag{V.6b}$$

The partial derivatives $u_{,y}$, $v_{,y}$ and $w_{,y}$ are given as

$$-L/2 \leqslant y \leqslant 0 \qquad u_{,y} = -12 \frac{\delta}{L} \frac{y}{L/2}\left(1 + \frac{y}{L/2}\right) \tag{V.7a}$$

$$v_{,y} = 12 \frac{t}{2} \frac{\delta}{L^2/2}\left(1 + \frac{2y}{L/2}\right) \tag{V.7b}$$

$$w_{,y} = -48\nu t \frac{\delta}{L^3} z \tag{V.7c}$$

$$0 \leqslant y \leqslant L/2 \qquad u_{,y} = -12 \frac{\delta}{L} \frac{y}{L/2}\left(1 - \frac{y}{L/2}\right) \tag{V.7d}$$

$$v_{,y} = 12 \frac{t}{2} \frac{\delta}{L^2/2}\left(1 - \frac{2y}{L/2}\right) \tag{V.7e}$$

$$w_{,y} = 48\nu t \frac{\delta}{L^3} z \tag{V.7f}$$